

Infrared Investigations of Circumstellar matter

A Thesis

submitted for the Award of Ph.D. degree of
MOHANLAL SUKHADIA UNIVERSITY

in the
Faculty of Science

By
Venkataraman.V



Under the supervision of

Dr. Rajesh Pandey
Emeritus Scientist - CSIR

&

Co-supervision of

Dr. P. Janardhan

Professor

Physical Research Laboratory, Ahmedabad

DEPARTMENT OF PHYSICS

FACULTY OF SCIENCE

MOHANLAL SUKHADIA UNIVERSITY

UDAIPUR (RAJ.)

Year of submission: 2015

DECLARATION

I, **Mr. Venkataraman.V**, S/o Mr. Veeman Pandaram, P., resident of D3, PRL Quarters, Vikram nagar, Ahmedabad 380058, hereby declare that the research work incorporated in the present thesis entitled, “**Infrared investigations of Circumstellar matter**” is my own work and is original. This work (in part or in full) has not been submitted to any University for the award of a Degree or a Diploma. I have properly acknowledged the material collected from secondary sources wherever required. I solely own the responsibility for the originality of the entire content.

Date:

Venkataraman.V
(Author)

CERTIFICATE

We feel great pleasure in certifying the thesis entitled, “**Infrared investigations of circumstellar matter**” by Mr. Venkataraman.V. He has completed the following requirements as per Ph.D regulations of the University.

- (a) Course work as per the university rules.
- (b) Residential requirements of the university.
- (c) Regularly submitted six monthly progress reports.
- (d) Presented his work in the departmental committee.
- (e) Published minimum of one research papers in a referred research journal.

We recommend the submission of thesis.

Date:

Prof. P. Janardhan

Professor,
Physical Research Laboratory,
Navrangpura,
Ahmedabad

Prof. Rajesh Pandey

Emeritus Scientist - CSIR,
Department of Physics,
Mohanlal Sukhadia University,
Udaipur

Countersigned by

Head of the Department

Dedicated
to my Beloved Father

Contents

List of Figures	xv
List of Tables	xix
Acknowledgements	xxi
Abstract	xxiii
1 Introduction	1
1.1 Evolution of Pre-main sequence stars	1
1.1.1 Spectral Energy Distribution of Protostellar stages	4
1.1.2 Eruptive young stars	4
1.1.2.1 FUors	6
1.1.2.2 EXors	7
1.1.3 Outburst mechanism	8
1.2 Post-main-sequence evolution	10
1.2.1 Red-Giant phase of evolution	10
1.2.2 Asymptotic Giant Branch (AGB) phase of evolution	12
1.2.3 Evolution of C/O during the AGB phase	14
1.2.4 Circumstellar matter in AGB stars	15
1.2.5 Post-AGB Evolution	17
1.2.6 IR spectra of Evolved Stars	18
1.2.6.1 Rotational-vibrational spectra of CO	19
1.2.6.2 Rotational spectra of H ₂	20
1.2.6.3 Polycyclic Aromatic Hydrocarbons (PAHs)	20

1.2.6.4	PAH formation	21
1.2.6.5	PAH emission mechanism	23
1.3	Organization of thesis	24
1.3.1	Chapter 1: Introduction	24
1.3.2	Chapter 2: Observations and Data analysis	24
1.3.3	Chapter 3: Infrared study of V1647 Ori and five other eruptive young stellar objects	25
1.3.4	Chapter 4: Infrared photometric and spectroscopic study of Asymptotic Giant Branch stars	25
1.3.5	Chapter 5: Infrared photometric and spectroscopic study of Post Asymptotic Giant Branch stars/Proto-Planetary Nebulae	25
1.3.6	Chapter 6: Summary and Future Work	26
2	Observations and Data analysis	27
2.1	Introduction	27
2.2	Mt. Abu Infrared Observatory	28
2.3	Detector principles	30
2.3.1	Mercury Cadmium Telluride (HgCdTe)	31
2.3.2	Detector performance	32
2.3.2.1	Dark current	32
2.3.2.2	Read noise	32
2.3.2.3	Readout time	32
2.3.2.4	Quantum efficiency	32
2.3.2.5	Linearity	33
2.3.2.6	Well capacity	33
2.3.2.7	Array size	33
2.3.3	Array Readouts	33
2.4	Near Infrared Camera and Multi-Object Spectrometer (NICMOS)	35
2.5	Near Infrared Camera and Spectrograph (NICS)	36
2.5.1	Optical layout	37

2.5.2	Photometric mode	40
2.5.3	Spectroscopic Mode	41
2.5.4	Detector Characteristics	43
2.5.4.1	Determination of Gain	43
2.5.4.2	Determination of read-out noise	43
2.5.4.3	Linearity test	44
2.6	Near-infrared Observations and data analysis	45
2.6.1	Photometric Observations	46
2.6.2	Spectroscopic Observations	47
2.6.3	NIR data reduction	47
2.6.3.1	Photometric data reduction	47
2.6.3.2	Spectroscopic data reduction	48
2.7	Infrared Space Observatory	48
2.7.1	ISO SWS data reduction	49
2.8	<i>Spitzer</i> Space Observatory	50
2.8.1	<i>Spitzer</i> archival data and analysis	50
3	Infrared study of V1647 Ori and five other eruptive young stellar objects	53
3.1	Introduction	53
3.2	Observations and data reduction	55
3.2.1	Near-infrared Photometric & Spectroscopic Observations	56
3.2.2	<i>Spitzer</i> archival Spectroscopic data	57
3.3	Results and Discussion	57
3.3.1	Near Infra-red photometry	57
3.3.2	Spectroscopic Variations	61
3.3.3	Variations in HH22 and the nebula around V1647 Ori . .	64
3.3.4	Modeling of Spectral Energy Distribution	67
3.4	Infrared investigations of other eruptive young stellar objects . .	70
3.4.1	IRAS 05426+0903 (FU Orionis)	71
3.4.2	IRAS 07013-1128 (Z CMa)	71

3.4.3	V1515 Cyg	75
3.4.4	V1057 Cyg	75
3.4.5	V1331 Cyg	77
3.4.6	Discussion	79
3.5	Conclusions	81
4	Infrared photometric and spectroscopic study of Asymptotic Giant Branch stars	83
4.1	Introduction	83
4.2	The Sample Stars	85
4.3	Near-Infrared Observations and analysis	85
4.4	Results and Discussion	86
4.4.1	Correlations and their implications:	88
4.4.2	Modeling of Infrared Spectral Energy Distribution:	92
4.5	Conclusions	95
5	Infrared photometric and spectroscopic study of Post Asymptotic Giant Branch stars/Proto-Planetary Nebulae	97
5.1	Introduction	97
5.2	The Sample Stars	99
5.3	NIR Observations of a sample of PAGB stars	100
5.3.1	Data reduction:	101
5.3.2	Spectral variations in some PAGB objects	101
5.3.3	Discussion	108
5.3.3.1	Evolutionary trends in the NIR spectra	110
5.4	<i>Spitzer</i> spectra of PAGB/PPNe objects	110
5.5	Modelling of SEDs	112
5.6	Variation of mid-IR spectral features with the evolution (T_*)	118
5.6.1	PAH modes:	119
5.6.2	H ₂ rotational lines:	122
5.6.3	Trends in the mass-loss rates	123
5.6.4	Unidentified mid-IR features	126

5.6.4.1	The 21 μm feature:	126
5.6.4.2	The 23- μm feature:	129
5.6.4.3	The 30- μm feature:	131
5.7	Identification of transition objects	132
5.8	Identification of Fullerenes	134
5.9	Conclusions	136
6	Summary and Future Work	139
6.1	Summary	139
6.1.1	Infrared studies of V1647 Ori and five other eruptive young stellar objects	139
6.1.2	Infrared studies on a sample of Asymptotic Giant Branch stars	140
6.1.3	Infrared studies on a sample of Post-AGB/Proto-Planetary Nebulae	141
6.2	Future Work	142
A	Near-infrared monitoring of V1647 Ori	183
B	Near-infrared spectroscopy of AGB stars	185
C	Infrared investigations of PAGB/PPNe candidates	191
D	LIST OF PUBLICATIONS	207
E	Reprints of research papers published in refereed journals	211

List of Figures

1.1	YSO classification	3
1.2	Mass accretion rate during the pre-main sequence evolution . . .	5
1.3	FU Ori light curve	6
1.4	EX Ori light curve	7
1.5	Post-main sequence evolution	11
1.6	Comparison of the observed spectra of PPNe with lab spectra of PAH	23
2.1	Mt. Abu IR Observatory	28
2.2	Infrared telescope at MIRO	29
2.3	NICS: Inside view and mounted at MIRO	38
2.4	Optical layout of NICS	39
2.5	Laboratory Hg CFL spectra obtained using NICS	42
2.6	Photon transfer curve of NICS	44
2.7	Illumination response curve of NICS	45
3.1	Light curve of V1647 Ori during 2004-2012	58
3.2	Time variation of A_V towards V1647 Ori	59
3.3	Color-color diagram of V1647 Ori	60
3.4	Br γ line variation of V1647 Ori	62
3.5	<i>JHK</i> spectra of V1647 Ori using NICS	63
3.6	<i>Spitzer</i> spectra of V1647 Ori	63
3.7	Color composite image of V1647 Ori and its circumstellar envi- ronment	65

3.8	Brightness variations of V1647 Ori against HH22	66
3.9	SED models for V1647 Ori	69
3.10	NIR and mid-IR spectra of FU Ori	72
3.11	NIR and mid-IR spectra of Z CMa	74
3.12	NIR and mid-IR spectra of V1515 Cyg	76
3.13	Mid-IR spectra of V1057 Cyg	77
3.14	NIR and mid-IR spectra of V1331 Cyg	78
4.1	<i>HK</i> spectra of M type stars	87
4.2	<i>HK</i> spectra of SR type stars	87
4.3	<i>HK</i> spectra of S type stars	88
4.4	Plots of the EWs between the first and second overtone bands of CO	89
4.5	Plot of the EWs of CO(3-0) & CO(2-0) with Period and Infrared colors for M and S type stars	90
4.6	Model SEDs of M type stars	93
4.7	Model SEDs of SR and S type stars	94
5.1	IRAS color-color diagram of the PAGB & PPNe stars	100
5.2	Spectral variability of IRAS 12538-2611	102
5.3	Spectral variability of IRAS 19399+2312	106
5.4	Spectral variability of IRAS 22272+5435	107
5.5	NIR correlation plots of PAGB stars	109
5.6	Typical <i>Spitzer</i> IRS spectra of the PPNe & PAGB stars	111
5.7	Model SEDs of PPNeS using single shell	114
5.8	Model SEDs of PAGB stars using single shell	115
5.9	Model SEDs of PPNeS using two shells for sources with PAH emission	116
5.10	Plot of dust temperature vs inner dust shell radius	117
5.11	Plot of central source temperature vs the ratio of inner dust shell radius and the central source radius	118

5.12	Plot of the PAH mode ratio $\log (EW(6.2)/EW(11.2))$ vs $\log (EW(7.6 + 7.8)/EW(11.2))$	119
5.13	Plot of PAH mode ratio $\log(EW(7.6 + 7.8)/EW(11.2))$ vs effective temperature	120
5.14	Plot of the PAH mode ratio $\log(EW(12.6)/EW(11.2))$ vs effective temperature	121
5.15	Plot of the peak wavelength $11.2 \mu\text{m}$ vs effective temperature .	122
5.16	Plot of the EWs of the rotational lines S(5) of H_2 vs effective and dust temperatures	123
5.17	Plot of gas mass loss rate vs optical depth at $0.55 \mu\text{m}$	124
5.18	Plot of gas mass loss rate vs dust temperature	124
5.19	Plot of mass loss rate vs mass loss index	125
5.20	Typical $21 \mu\text{m}$ feature observed in PAGB/PPNe candidates . .	127
5.21	Plot of the photospheric temperature vs peak wavelengths of the feature at $21 \mu\text{m}$	128
5.22	Continuum subtracted 23 & $30 \mu\text{m}$ feature of PPNe & PAGB stars	130
5.23	PPNe candidates with $30 \mu\text{m}$ MgS feature	131
5.24	Continuum subtracted spectra of transition objects with [NeII] emission at $12.8 \mu\text{m}$	133
5.25	<i>Spitzer</i> IRS spectra of sources with fullerene	135

List of Tables

1.1	Mid-IR emission features of PAH	22
2.1	Detector characteristics of NICMOS	35
2.2	Broad & narrow band filters in NICMOS	36
2.3	Description of filters in NICS	40
2.4	Detector characteristics of NICS	46
3.1	Model parameters for V1647 Ori in its quiescent and outburst phases	70
A.1	<i>JHK</i> magnitudes, colors and A_V (in mag) of V1647 Ori during 2004-2012	183
B.1	Photometric colors & NIR EWs observed in a sample of M type stars	186
B.2	Photometric colors & NIR EWs observed in a sample of S type stars	188
B.3	Photometric colors & NIR EWs observed in a sample of SR type stars	189
C.1	NIR spectral variability observed in a sample of PAGB/PPNe stars	191
C.2	EWs of PAH features observed in a sample of PPNe candidates	193
C.3	EWs of PAH features observed in a sample of PAGB candidates	196
C.4	Circumstellar parameters derived using DUSTY with single shell for a sample of PPNe candidates	198

C.5	Circumstellar parameters derived using DUSTY with single shell for a sample of PAGB candidates	200
C.6	Circumstellar parameters derived using DUSTY with two shells for a sample of PPNe candidates	201
C.7	Circumstellar parameters derived using DUSTY with two shells for a sample of PAGB candidates	203
C.8	EWs of H ₂ S(5) line observed in a sample of PAGB/PPNe can- didates	204
C.9	EWs of 23 & 30 μm features observed in a sample of PPNe candidates	204
C.10	EWs of 23 & 30 μm features observed in a sample of PAGB candidates	206

Acknowledgements

First of all, I express my sincere and deepest gratitude to Prof. B.G.Anandarao, who has introduced me to astronomy and under the guidance of whom, the work reported in this thesis has been carried out. His deep insight in the subject and vast experience helped me immensely in learning the subject. Discussion with him was a great pleasure as he always gave importance to my views and was always patient with me. It was a great experience to work with him. This thesis would not be possible without his constant encouragement and support. I also thank him for critically going through the thesis and making useful comments and suggestions.

I express my sincere gratitude to Prof. P.Janardhan for his guidance, help and for carefully reading the thesis and making useful suggestions. I feel deeply honored in expressing my sincere gratitude to Prof. Rajesh Pandey for his guidance and encouragement through out my research work.

I thank the A&A faculty members Prof. N.M. Ashok, Prof. D.P.K. Banerjee, Prof. Baliyan, Prof. T. Chandrasekhar, Prof. Hari Om Vats, Dr. A. K. Singal, Dr. Abhijit Chakraborty, Dr. Santhosh Vadawale, Dr. Sachindra Naik, Dr. Shashikiran Ganesh and Mr. A. B. Shah for their concern about my research work. I thank all the staff members of the Mt. Abu observatory, Mr. Rajesh Shah, Mathurbhai, Jineshbhai, Pethambarbhai, Purohitji, Nafeesbhai, Narayansinghji, Padamsinghji for their help and assistance during the observations. I thank Dr. Balamurugan Sivaraman for carefully reading my thesis and giving critical comments.

I would like to thank the Director PRL, Prof. Utpal Sarkar, past Director, Prof. J.N.Goswami and former Dean, Prof. Anjan Joshipura for their encouragements to carry out research work.

This work had made use of the archival data obtained with the Spitzer Space Telescope, which is operated by the Jet Propulsion Laboratory, California Institute of Technology under a contract with NASA. I would greatly acknowledge the meticulous work of the Infrared Spectrograph team in designing the instrument and make the data available for general public. This work also made use

of the Highly Processed Data Product (HPDP) available for public use in the Infrared Space Observatory (ISO) data archive. I would like to express my sincere gratitude to team members of 2MASS, MSX, COBE, IRAS, WISE, ISO, AKARI and SPITZER/GLIMPSE for providing the photometric data for the sources in the present study. I would like to sincerely thank Google, NASA-ADS, SIMBAD and VIZIER database for providing references and the basic data pertaining to the astronomical sources in the present study.

I would like to profoundly thank my family to whom I owe a great deal. I fondly remember my father, who was everything for me, and always wanted me to pursue research work. His absence has created a irrevocable void in my life. I miss him a lot for his abiding love and affection towards me. I wish he could have seen my thesis. I gratefully extend my heartfelt gratitude to my mother for her unceasing love and affection through out my life. She has made an untold number of sacrifices for my studies and never complained about my absence during difficult times when my support was badly needed for her. Hence, great appreciation and enormous thanks are due to her, for without her understanding, I am sure this thesis would never have been completed. I am also grateful to my sisters and in-laws for providing me support and encouragement through out the period.

Finally, without the support of my wife Punitha and my wonderful son Karunyan, I would never have succeeded in completing my thesis. Although they often had to endure my absence during my observations they seldom complained. I thank them for bearing with me and my mood swings and being my greatest supporters. I am very fortunate and blessed to have these two people in my life.

Venkataraman. V

ABSTRACT

Circumstellar environment of eruptive young pre-main sequence stars and that of evolved low mass stars offers a unique opportunity to study the underlying physical processes. Investigation of circumstellar matter around eruptive pre-main sequence stars gives insights into understanding the accretion process responsible for the observed episodic behavior, while that around evolved stars helps in understanding the mass loss processes.

The first part of the thesis (Chapter 3) deals with infrared (IR) investigations of the circumstellar matter around eruptive young low-mass stars. The eruptive events in such stars are classified as FUors and EXors depending on the duration of the outburst, which are believed to be caused by enhanced disk mass accretion. V1647 Ori is a young eruptive variable star that has caught the attention of astronomers since last decade on account of its peculiar behavior. It experienced two episodes of outbursts during 2004 and 2008. Here we report the IR monitoring at an unprecedented high cadence of V1647 Ori during 2004 to 2012 including the two outbursts flanking the brief quiescent period. The nature of the outburst and its similarity to the pre-main sequence eruptive types of both FUors and EXors makes V1647 Ori to be distinctive. The *JHK* color patterns during the 2008 outburst suggested the presence of colder dust in its circumstellar environment as compared to the 2004 outburst phase. The physical parameters obtained by modeling the spectral energy distribution (SED) of V1647 Ori during its outburst and quiescent phases showed marked differences in the disk accretion rates. The disk mass and disk accretion rate during the outburst phase are significantly greater than those in the quiescent phase. The envelope mass and accretion rate are higher during quiescent phase. The IR photometric and spectroscopic properties of V1647 Ori were compared with five other eruptive variables.

The second part of the thesis (Chapters 4 and 5) deals with the photometric and spectroscopic study of evolved stages of low and intermediate mass stars namely Asymptotic Giant Branch (AGB) stage and post-AGB (PAGB)/Proto-planetary nebule (PPNe) stage. Near-infrared (NIR) spectroscopy in the *H*

and K bands was done at Mt. Abu on a selection of 80 AGB stars of M, S and semiregular (SR) types. The NIR spectra of these stars showed CO vibration-rotation lines of first and second overtone bands ($\Delta v = 2$ and $\Delta v = 3$ respectively). The equivalent width (EW) of the second overtone band of CO correlated with IR colours, suggesting a possible relationship with mass-loss processes. Modeling of the SED showed an increase in the derived mass-loss rates for the M type as compared to that of SR and S types.

Investigations were also made on the transition phase between AGB and the Planetary Nebula (PN) stages, the so called PAGB or PPNe phase. Spectroscopic variability at NIR wavelengths was monitored for a sample of 14 PAGB candidates that are known to undergo episodic mass loss. Cooler PAGB stars showed variation in CO first overtone lines, while hotter stars showed variability in HI lines. The mid-IR spectra for a sample of 50 PPNe and 21 PAGB candidates were obtained from the *Spitzer* data archive. Investigations of such a large sample are not done earlier. The mid-IR spectra of these sample stars showed different spectral features that include emissions from polycyclic aromatic hydrocarbons (PAHs). The physical and circumstellar parameters for these sample stars were derived from the SED models. A trend of dependency is established between the EWs of various vibrational modes of PAHs with their photospheric temperature T_* of the sample objects. A few transition objects with low-excitation line emission of [NeII] were identified, which indicates their advanced stage of evolution. IR vibration modes of neutral fullerenes (C_{60}) were detected for the first time in the PAGB star IRAS 21546+4721 making it one of the very few evolved stars that showed the presence of fullerenes.

Keywords: Pre-main sequence stars - Eruptive young stellar objects: Circumstellar matter - Asymptotic Giant Branch stars - Proto-planetary Nebulae - mass-loss, Infrared Spectra - Spectral Energy Distribution - Polycyclic aromatic hydrocarbons

Chapter 1

Introduction

This thesis deals with the circumstellar environments of stars that are in different stages of stellar evolution. We consider here firstly, circumstellar matter around eruptive, young, low mass pre-main sequence stars to understand the accretion processes responsible for its outburst. Secondly, we also take up the study of circumstellar environments around mass-losing, evolved intermediate mass stars. In both the cases viz. young low mass pre-mainsequence stars and evolved intermediate mass stars the evolution of circumstellar matter is rather rapid and in itself forms an interesting case study; although phenomenological differences do exist in these two environments. In this chapter, we give an introduction to (i) the mass *accretion* phenomenon in low mass young stellar objects and the scenario of eruptions; and (ii) the *mass loss* processes in evolved stars that lead to the circumstellar matter around such stars.

1.1 Evolution of Pre-main sequence stars

Stars are formed by the gravitational contraction of dense clumps that are formed within molecular clouds. These clumps subsequently give rise to protostellar cores that are in hydrostatic equilibrium. These protostellar cores accrete matter from the parent molecular cloud. While high mass stars ($M \geq 8 M_{\odot}$, where M_{\odot} is 1 solar mass) are known to form in Giant Molecular Clouds

(GMC; typical size 20 - 100 pc, and masses between 10^4 - $10^6 M_{\odot}$), low mass stars ($M \leq 3 M_{\odot}$) may form either in GMCs or in dwarf clouds (typical size 2 to 5 parsec with masses 10^3 and $10^4 M_{\odot}$) (Stahler and Palla, 2005).

We consider as a starting point, a low mass ($\leq 1 - 2 M_{\odot}$) protostellar core accreting mass from a surrounding accretion disk which is in turn fed by an enclosing envelope. Such protostars contain ionised hydrogen (their central temperature is about $\sim 10^5$ K), whose mass is a few tenths of $1 M_{\odot}$ and whose size is a few solar radii (Stahler and Palla, 2005). These protostars form in about 10^4 years after the start of the gravitational collapse. Due to the substantial rotation of the protostellar core, material cannot fall directly on to its surface (Adams and Shu, 1986) and a disk-like structure called an accretion disk is formed with matter slowly spiraling inwards. In agreement with the theory, observations show that the circumstellar material surrounding young stars having dispersed envelopes are not spherically distributed, but concentrated into a disk (e.g. Cohen and Schwartz (1983); Appenzeller, Oestreicher and Jankovics (1984)) from which material is slowly spiraling inwards. The evolution of a deeply embedded protostellar core into a main sequence star involves various stages (Lada, 1987; Andre, Ward-Thompson and Barsony, 1993). At the earliest stage, a protostellar core derive its luminous energy by the infall kinetic energy of circumstellar matter. This phase is referred to as Class 0 phase (see Fig 1.1) (Andre, Ward-Thompson and Barsony, 1993). Class 0 sources are deeply embedded protostars accreting matter from the infalling circumstellar matter and displaying energetic mass ejections that are characterized by the occurrence of molecular bipolar outflows. This phase is also the most shortlived phase of the protostars (10^4 yrs; Andre, Ward-Thompson and Barsony (2000)). The energetic mass outflows observed during the Class 0 phase clears away the envelope in about 10^5 years after the start of the gravitational collapse (Class I Object of Lada (1987)). Subsequently, the young protostar becomes optically visible in about 10^6 years (Class II object of Lada (1987)). Young stars with masses less than $2 M_{\odot}$ are called T Tauri stars, while those between 2 and $8 M_{\odot}$ are called Herbig Ae/Be stars. During this Class II stage,

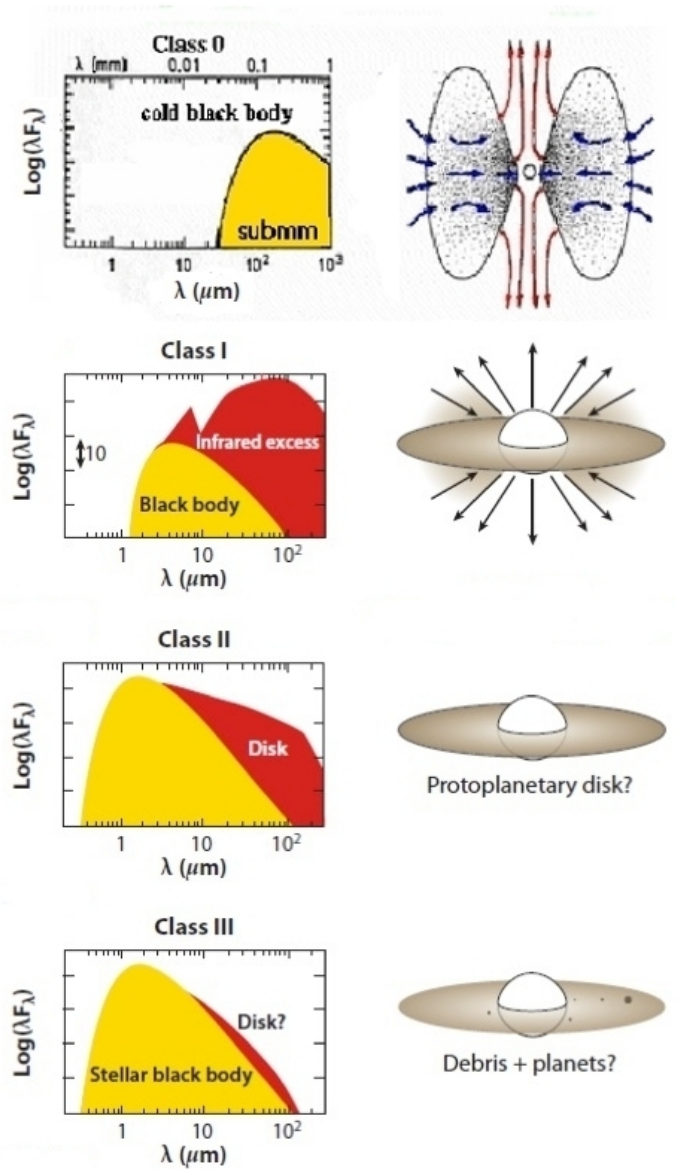


Figure 1.1: The spectral energy distribution for low-mass young stellar object during its pre-mainsequence evolution (left panel). Class 0 objects represent the earliest embedded phase in the star-formation process, while Class I objects are surrounded by a clear disk and an envelope. Class II objects (T-Tauri objects) are surrounded by accretion from the disk that decreases with age and the envelope dissipates. Class III objects dissipate their circumstellar material before reaching the zero-age main-sequence phase. The right panel shows the corresponding system geometry (Image credit: (Bachiller, 1996)).

stellar wind starts blowing and the accretion rate of the remnant envelope decreases. Finally, most of the gas and dust content disperses or coagulates into planetesimals in what is known as a debris disk surrounding the protostar (Class III objects of Lada (1987)) (see Fig 1.1). This classification is for low mass stars. It is possible that high mass stars go through these phases but at much shorter time scales. A very detailed description of stellar formation can be found in Stahler and Palla (2005).

1.1.1 Spectral Energy Distribution of Protostellar stages

The Spectral Energy Distribution (SED) is a powerful tool to study the evolutionary status of a protostar in star-forming regions. Infrared excess defined as the strong excess infrared (IR) flux in the SED due to the emission from circumstellar dust in young stellar objects may be used as an observational measure of the stellar youth or age of the star. The classification of the youth of protostars by Lada and Wilking (1984) and Lada (1987) was based on the slopes (i.e. spectral index) of their SED (see Fig 1.1). The spectral index defined in the range longward of $2 \mu\text{m}$ is given by

$$\alpha_\lambda = \frac{d \log(\lambda F_\lambda)}{d \log(\lambda)} \quad (1.1)$$

where λ is the wavelength and F_λ the observed flux. Objects for which $\alpha_\lambda > 0$ belong to Class I. As the IR excess decreases ($-1.5 < \alpha_\lambda < 0$), the object is said to be a Class II source. Class III ($\alpha_\lambda < -1.5$) indicates a star with no, or little, IR excess. Objects detected at far-IR and sub-millimeter wavelengths with no optical counterpart belong to the Class 0.

1.1.2 Eruptive young stars

Kenyon *et al.* (1990) suggested that the accretion may occur episodically during the main accretion stage, so that accreting stars intermittently become highly luminous and are called FUors and EXors, named after the prototypes FU Orionis and EX Lupi. Recent models by Dunham *et al.* (2010) also suggest

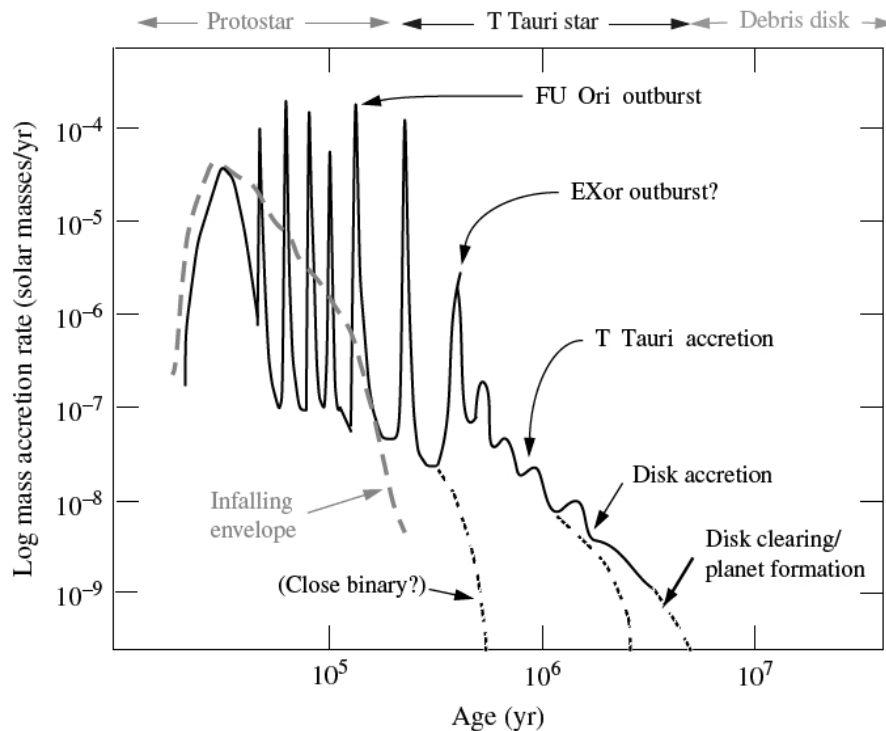


Figure 1.2: Estimated mass accretion rates during the early evolution of a solar-type star. The two main classes of eruptive young stars, namely, FU Ori and EX Lup (EXor) are indicated (Image credit: (Hartmann, 2009)).

episodic accretion as the best explanation for describing these eruptive phenomenon that cause these accreting stars to become highly luminous. Thus, material may be accreted at a much higher rate from the surrounding envelope, and 'stored' in the disk until the next outburst, which occur when the mass is transferred onto the young stars at rates of several orders of magnitude higher than usual (Hartmann, Heitsch and Ballesteros-Paredes, 2009). This might lead to disk instabilities and sudden enhanced accretion events (see Fig. 1.2).

Mass accretion of eruptive young stars during the Class II phase of the pre-main sequence star is seen to increase by more than four orders of magnitude and can occur on a time scale of months. The typical mass accretion rate observed in T Tauri stars varies between 10^{-7} to $10^{-12} M_{\odot} \text{ yr}^{-1}$ (Gullbring *et al.*, 1998). During the high state the accretion rate increases from 10^{-7} to $10^{-4} M_{\odot} \text{ yr}^{-1}$ (Hartmann and Kenyon, 1996). At the onset of these events

in FU Orionis and EX Lupi objects, the optical brightness can increase by 4 or more magnitudes. Statistical studies suggest that young low-mass stars experience several such outbursts during the early phase of stellar evolution (Hartmann and Kenyon, 1996). The outburst events may last for diverse periods of time. The longer flare-ups are called FUors (after FU Orionis) and typically last for decades in its outburst phase. The shorter flare-ups are called EXors (after EX Lupi), and typically last for few months to years (Stahler and Palla, 2005). Eruptive phases play a very important role in the early evolution of the stellar system. They affect the circumstellar environments, and consequently the formation of the planetary systems. The observational properties of the two classes of objects are described in the following subsection.

1.1.2.1 FUors

FUors drew attention by their unusual brightening by 4-6 mag at optical wave-

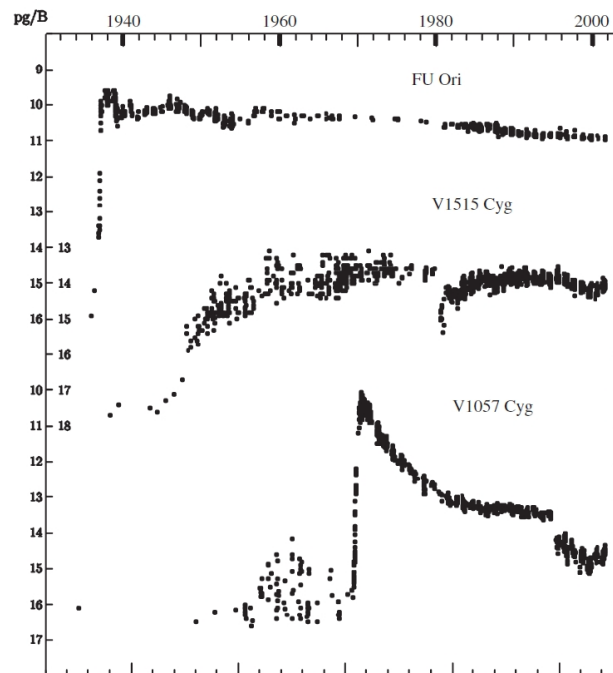


Figure 1.3: Light curves of the FUors: FU Ori, V1515 Cyg and V1057 Cyg. Recent photometry is in the B -band and historical data are by photographic photometry (Credit: Hartmann (2009)).

lengths. The prototype of this FU Orionis class brightened by 5 mag in 1936, compared to its previous brightness of ~ 16 mag in the B band (Herbig, 1977, 1989). Figure 1.3 represents the light curve of three FUors reproduced from Hartmann (2009). Among the three sources the amplitude of increase in brightness is similar, but the timescales of rising and fading vary. While FU Ori and V1057 Cyg reached their maximum brightness in less than a year, V1515 Cyg took almost a decade. FU Ori has been fading very slowly for ~ 80 yr, whereas V1057 Cyg faded quickly. The optical spectra of FUors resemble those of a fast rotating F-G type supergiant star, while the near-infrared (NIR) spectral characteristics indicate that of K-M supergiants (Hartmann and Kenyon, 1996). FUors also display strong absorption of Li I at 6707 \AA in their optical spectrum that are characteristic of young stars. The SED of these sources shows an IR excess at longer wavelengths.

1.1.2.2 EXors

Members of the EXor class show less dramatic flareups. Hence they are sometimes referred to as 'subfuors' (Herbig, 1989). The amplitudes of these outbursts are generally smaller, ranging between 1 - 5 mag at optical wavelengths. Figure 1.4 represents a typical light curve of VY Tau, an EXor candidate.

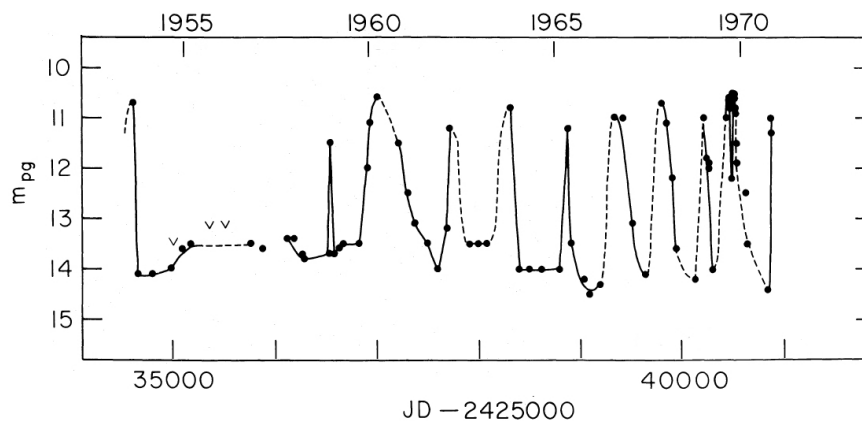


Figure 1.4: Photographic light curve of VY Tau showing EXor type of eruption (Credit: Herbig (1977)).

These repetitive eruptions last for a few months to years and are separated by intervals of quiescent periods ranging from a few months to years. Spectra of EXors resemble K- or early M-type dwarfs, in addition to their T Tauri-like emission lines (Sipos *et al.*, 2009).

1.1.3 Outburst mechanism

The physical mechanism behind the outbursts of EXor and FUor are considered to be the result of an enhanced accretion process (Hartmann and Kenyon, 1996; Audard *et al.*, 2014). Eruptive phenomena are generally associated with an enhancement of the mass accretion rate from the circumstellar disk. There is no consensus regarding the triggering mechanism of this enhanced accretion. The sudden dramatic increase of the accretion rate, is explained as the result of various types of instabilities in the disk. Possible mechanisms are (a) Gravitational instability (b) Magneto-rotational instability (c) Thermal instability (d) a combination of magneto-rotational and gravitational instabilities; and (e) Tidal forces from a binary companion.

Gravitational instability in the inner circumstellar disk may induce bursts of accretion (Vorobyov and Basu, 2006). This leads to the fragmentation of the material in the accretion disk. The fragments then move inwards and trigger the outburst. This model can account for highly variable values of accretion rates ranging from 10^{-8} to $10^{-4} M_{\odot} \text{ yr}^{-1}$. For this scenario, the disk has to be in the embedded phase (i.e. Class 0 & I), and a constant replenishment of material from the envelope to the star is necessary, and also the disks must fragment into dense concentration. However, it may be noted that most of the observed outburst belongs to Class II phase of evolution.

Balbus and Hawley (1991, 1998) and Balbus (2003) proposed a model based on the interaction of magnetic field and Keplerian rotation of a protoplanetary disk. The model assumes magnetic field lines threaded between the masses at neighboring annuli moving at different angular velocities in the disc. The magnetic field lines get stretched as the shear proceeds. The field lines will try to resist the shear by speeding up the outer annulus relative to the inner

annulus thereby transferring the angular momentum outwards. As the inner annulus loses angular momentum, the angular velocity increases while the outer annulus will tend to move outward, enhancing the stretching of the magnetic field. This phenomenon repeats and results in instability. Thus, however weak the disk magnetic field may be, as long as there is some ionized fraction in the disk threaded by magnetic field, an instability will grow in the disk. This type of instability is called **magnetorotational instability (MRI)**, or Balbus-Hawley instability.

A **thermal instability** is caused either by the presence of a planetary companion (Lodato and Clarke, 2004), or in the disk alone (Hartmann and Kenyon, 1996) in the absence of a planetary companion. This provides another possible triggering mechanism. According to the thermal instability model, the material from the envelope is still falling on to the young disk. The accretion rates from the disk onto the star, and from the envelope onto the disk do not match, with the envelope accretion on to the disk being considered to be higher. As a result matter piles up in the disk. In such a state, temperatures are low even in the regions very close to the star. At low temperatures turbulent motions in the disk and thus viscosity, responsible for angular momentum transport is low. Due to the slow angular momentum transport, accretion rates onto the star remain low, and mass piles up in the disk, close to its inner edge. Due to mass accumulation, the density and thus opacity in the disk grows, until the disk will be opaque enough to trap heat. As a result, the temperature increases rapidly. Opacity in the $\sim 3000 - 10000$ K temperature range varies steeply with temperature due to the ionization of hydrogen. In this temperature range, corresponding to a typical radial distance ~ 0.1 AU from the star, a small temperature fluctuation can switch on thermal instability resulting in the ionisation of the inner regions of the disk. The increased viscosity results in enhanced accretion. The thermal instability explanation for the onset of eruption can account for the observed high accretion rates. It can also account for both the rapid and the slow rise-time of the FUors, thereby making it, for a long time, the most widely accepted model.

A **combination of magneto-rotational and gravitational instabilities** was suggested by Armitage, Livio and Pringle (2001) as a modification to the thermal instability model. In this model gravitational instability drives accretion in the outer disk and material is accumulated at $\sim 1-2$ AU. This region slowly heats up until the temperature for thermal activation of the magneto-rotational instability (MRI) is reached. Then MRI becomes suddenly active and material starts moving in rapidly causing an outburst. This model is favored to the simple thermal instability model, because it makes accretion events possible even after the infall from the envelope has ceased. This model explains a number of observed features.

Bonnell and Bastien (1992) proposed that **tidal forces of the binary companion** perturb the circumstellar disk leading to an outburst. This hypothesis assumes that most of the eruptive objects are members of binary or multiple system. Most of the FUors are indeed found to be binary systems; but the binary tidal force mechanism may predict a periodic or quasi-periodic repetition of the outburst (cf. figures for FUori and EXor light curves).

1.2 Post-main-sequence evolution

In this section we describe briefly the evolution of low and intermediate mass stars ($0.8 - 8 M_{\odot}$) from the core hydrogen burning main-sequence phase to the Planetary Nebula phase with their cores ultimately going to the White Dwarf stage (Kwok, 1993; Iben, 1995; Lattanzio and Wood, 2003).

1.2.1 Red-Giant phase of evolution

When the hydrogen in the core of a main-sequence star is exhausted the core will start to collapse. This will heat up the layer of hydrogen just outside the helium core to temperatures high enough to start hydrogen fusion in a shell via the carbon-nitrogen-oxygen (CNO) process. This high temperature leads to high pressure just outside the core causing the hydrogen envelope to expand thereby increasing the luminosity of the star (Lattanzio and Wood,

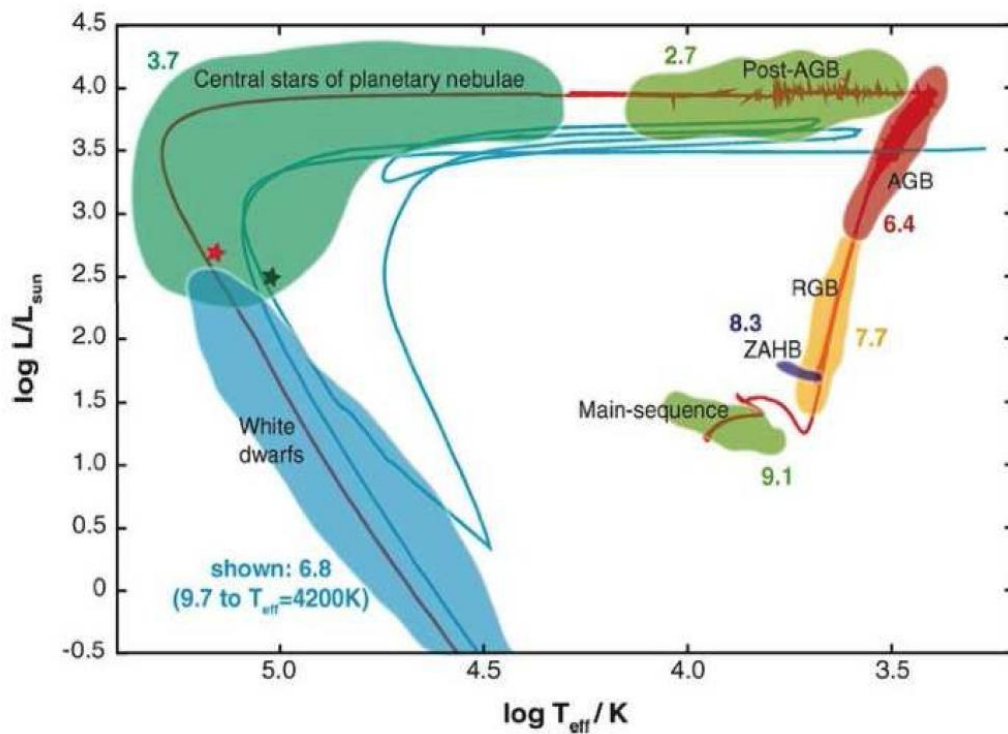


Figure 1.5: $L - T_{eff}$ (HR) diagram for a $2 M_{\odot}$ star. The red curve represents the evolutionary track from the main-sequence to white dwarf (WD) phase. The blue track shows the born-again evolution of a star with same mass due to a very late helium shell flash during the post-AGB (or WD) phase that transforms the star back into an AGB stage. The numbers besides each evolutionary phase show the logarithm of its approximate duration (Herwig, 2005)

2003; Herwig, 2005). In the mean time the outer layer of the star expands to larger radii ($< 100 R_{*}$, where R_{*} is stellar radii) and cools, marking the (*first*) *Red Giant branch* (RGB) phase of the star. During the RGB phase the outer layers of the star are convective and can bring the products of nucleosynthesis from the hydrogen burning shell to the outer layers of the envelope thereby enriching helium (^4He), nitrogen (^{14}N) and carbon (^{13}C) while depleting carbon (^{12}C) and oxygen (^{16}O) (Iben, 1967; Shadick, Falk and Mitalas, 1980; Gilroy and Brown, 1991). This process of transporting the products of nucleosynthesis from the interiors to the surface is known as "*dredge-up*", and the one that occurs during the RGB phase is called the first "*dredge-up*". The typical mass

loss rate at the tip of the red giant phase (the point of He ignition) is around 10^{-7} to $10^{-9} M_{\odot} \text{ yr}^{-1}$ (Origlia *et al.*, 2002). At the tip of RGB phase, when the central temperature has reached $\geq 10^8$ K, helium ignites in the core. For stars with initial mass approximately $1.8 M_{\odot}$, the core will become strongly electron-degenerate and ignite helium as a core helium flash (Herwig, 2005). The luminosity of the star then decreases and the star settles afterwards in quiescent helium core burning at the Zero Age Horizontal Branch (ZAHB) of the Hertzsprung-Russell (HR) diagram. More massive stars with masses about 1.8 to $8 M_{\odot}$, will ignite helium at a normal rate (without a flash) in the core and continue their evolution in the horizontal branch. Helium burning increases the mass fraction of ^{12}C and ^{16}O . The central helium burning and its eventual exhaustion give rise to blueward and redward parts of the loop (Lauterborn, Refsdal and Weigert, 1971) in the HR diagram (as shown in Fig 1.5 for a $2 M_{\odot}$ star).

1.2.2 Asymptotic Giant Branch (AGB) phase of evolution

The core of the low and intermediate mass stars contains carbon and oxygen after the exhaustion of helium burning during horizontal branch phase. Now helium and hydrogen fusion can continue alternatively in shells around the contracting carbon and oxygen core. The energy production during this phase is mostly due to the hydrogen burning shell. The carbon and oxygen core will continue to contract and for a star with a mass below $8 M_{\odot}$ the carbon will never ignite and an electron degenerate core will eventually be formed. The star expands and moves towards the early-AGB (EAGB), becoming a red-giant for the second time. During the AGB phase the star undergoes two significant phenomena; (a) pulsation with periods between 100 - 1000 days; (b) mass loss at the rates of $\sim 10^{-7}$ to $10^{-6} M_{\odot} \text{ yr}^{-1}$. The stars at this stage are called Mira variables named after its prototype Mira or *o Ceti*.

The expansion of the outer layers due to the helium shell burning ex-

tinguishes the hydrogen-burning shell in the intermediate-mass stars, which causes the convective envelope to move inward for a second time. This second dredge-up brings the products of hydrogen burning, mainly helium and nitrogen to the surface, but it does not occur in low mass stars since the hydrogen-burning shell is not extinguished.

Following the narrowing of the intershell helium layer, the hydrogen shell burning takes over until enough helium is produced. Eventually when the helium shell is sufficiently massive it ignites and drives the hydrogen burning shell outwards. This causes the hydrogen shell to cool, turn off and fall back after a time. When the burning in the helium shell diminishes, the hydrogen shell gets reignited and the entire process repeats. The helium-burning shell is known to be thermally unstable and it undergoes thermal pulses recurrently. This is the thermally-pulsating AGB (TP-AGB) phase, characterised by alternatively burning hydrogen and helium shells surrounding an electron-degenerate carbon-oxygen core. Schwarzschild and Härm (1967) suggest that thermal pulses may occur in both low- and intermediate mass stars with the release of a huge amount of energy. The period between pulses is a function of the mass of the star, ranging from 10^3 years for $5 M_{\odot}$ stars to 10^5 years for low-mass stars ($0.6 M_{\odot}$), with the pulse amplitude growing with each successive event (Iben, 1982; Stancliffe, Tout and Pols, 2004). The energy produced by the He shell burning cannot be transported by radiation alone, hence a intershell convective zone is developed below the hydrogen burning shell. The flash-driven convection zone is composed mostly of ^4He (about 75 %) and ^{12}C (about 22 %), and lasts for a few hundred years (Iben, 1976; Lattanzio, 1987; Boothroyd and Sackmann, 1988). When the helium shell burning ceases the intershell convection zone disappears. The star contracts and the H-burning shell is re-ignited and the star enters a interpulse phase. The intershell convection zone will bring the carbon that had been produced during helium burning into the envelope. The mixing of protons from the envelope with the ^{12}C rich intershell region during the interpulse phase produces ^{13}N which undergoes positive beta-decay to produce ^{13}C . During the next thermal

pulse the intershell convection zone engulfs ^{13}C , and neutrons are released via $^{13}\text{C}(\alpha, n)^{16}\text{O}$ reaction in the intershell convection zone (Kaeppeler *et al.*, 1990; Lattanzio and Forestini, 1999). Due to the increasing neutron density, slow-neutron capture or *s*-process produces iron group elements, which are brought to the surface by convection along with the helium burning products during the third dredge-up (TDUP) (Lattanzio and Wood, 2003). This is the process which creates carbon-rich stars. TDUP occurs in stars with masses of $1 M_{\odot}$ and above (Groenewegen and Marigo, 2003; Stancliffe, Izzard and Tout, 2005).

The occurrence of TDUP in intermediate mass stars with masses over $5 M_{\odot}$ produces a deep convective envelope that penetrates into the top of hydrogen shell where the temperature can be as high as 10^8 K. Penetration of the envelope results in nuclear burning at the bottom of convective envelope. The nuclear reaction converts the freshly dredged-up ^{12}C into ^{13}C and ^{14}N . This requires a temperature greater than 8×10^7 K (Iben, 1976) which was found to occur during TDUP (Iben, 1975). This process is known as hot bottom burning (HBB) and mostly occurs in intermediate mass stars ($M \geq 3 M_{\odot}$) via proton capture at the base of convective envelope and can dramatically alter the surface composition (Herwig, 2005).

1.2.3 Evolution of C/O during the AGB phase

When the star ascends along the AGB phase in the HR diagram it displays more O than C ($\text{C/O} < 1$) reflecting the original composition of the interstellar medium (ISM). However, repeated thermal pulses preferentially add C to the star's surface through TDUP. For this reason, AGB stars, originally O-rich, can turn into C-rich AGB stars ($\text{C/O} > 1$) after a few thermal pulses. This explains the observed sequence of evolution from being M-MS-S-SC-C star based on the increasing amounts of carbon in their atmospheres with successive thermal pulses (Lambert, 1991; Mowlavi, 1999; Habing and Olofsson, 2003). MS-stars have M spectral-types (a spectral classification with effective temperatures between 3850 to 2640) with C/O lower than one and smaller s-element overabundances ($[\text{s}/\text{Fe}] \sim 0.3$) in their surfaces, S-stars display C/O

ratio very close to one and higher s-element overabundances ($[s/Fe] > 0.5$), SC-stars are C-rich stars also strongly s-element enriched but with their C/O ratio still close to ~ 1 while C-stars are carbon-rich stars with C/O clearly larger than one. After TDUP event, the surface abundance of carbon increases until it exceeds the abundance of oxygen. The star has now turned from an oxygen-rich star into a carbon-rich star with abundance ratio of $C/O > 1$. The initial abundance of oxygen as well as carbon depends on the initial amount of elements heavier than hydrogen or helium (metallicity), metal-rich stars require more carbon to be mixed to the surface to change the C/O ratio to values larger than unity. Other than carbon and nitrogen, AGB stars are one of the main sources for the heavy elements in the universe, such as Zr, Tc, Y and La that are produced by the *s*-process (Arlandini *et al.*, 1999).

1.2.4 Circumstellar matter in AGB stars

The mass lost during the AGB phase generally leads to the formation of molecules and dust in the circumstellar environment (Millar, 2003). Dust nucleates when the atmosphere has been pushed far enough outward for the temperature to fall below 1500 K (Woitke, 2006). The formation of dust depends largely on the availability of atoms and molecules. The most abundant elements that form the building blocks of dust are C, H, O and N. However, the carbon monoxide (CO) molecule is very stable and already forms at high temperatures in the stellar atmosphere. This leads to a clear separation of the type of dust present around AGB stars. If oxygen is more than the available carbon, i.e. C/O ratio < 1 , all the C will be trapped in CO and only O will be available to form dust. In this case oxygen-rich dust (predominantly silicates) are formed. This is the initial situation for all M type stars. During the stellar evolution the C/O ratio will increase until carbon-rich stars are formed. In the dusty envelope of the C-stars, most of oxygen is trapped in CO and carbon is left to form carbon-rich dust such as silicon carbide (SiC), graphite and polycyclic aromatic hydrocarbons (PAHs). For objects where the C/O ratio is almost unity, the so-called S-stars, both the carbon and oxygen will be

highly depleted in the wind and other dust species like ferro silicon (FeSi) are expected to form (Smolders *et al.*, 2012). Thus, atomic abundances in stellar winds strongly determine the kind of dust that are formed.

The evolution of stars throughout the AGB phase is accompanied by an increasing mass-loss rate (\dot{M}), that varies from 10^{-7} to $10^{-5} M_{\odot} \text{ yr}^{-1}$ (Whitelock *et al.*, 1994). Mass loss in the EAGB phase is thought to be spherically symmetric. Mass loss from these low surface-gravity red giants requires a mechanism that allows matter to gain momentum and overcome the gravitational pull of the central star. Bowen (1988) showed that a combination of pulsations and the radiation pressure exerted on dust particles can drive a stellar wind from AGB stars. Large-amplitude pulsations levitate material to greater heights in the stellar atmosphere and reduce the temperatures enough to facilitate the condensation of dust grains a few stellar radii away from the stellar surface. As radiation pressure pushes these dust grains radially outward, they transfer momentum to the gas particles and basically drag them along. Momentum is transferred from the photons emitted by the star to the dust grains, through photon absorption and scattering and is subsequently redistributed to the more numerous gas particles by collisions with the dust grains (Wood, 1979; Bowen, 1988; Norris *et al.*, 2012). As the dust grains in the circumstellar matter absorb energetic radiation and re-emit at longer wavelengths the observed SED will contain the dust emission which contributes beyond the NIR wavelengths in addition to its photosphere contribution.

It is generally accepted that the mass loss of AGB stars is due to dust-driven winds (Lamers and Cassinelli, 1999). Although the mechanism to drive dust-driven wind is reasonably well understood, it remains a question as to which type of grain drives the wind. To be considered a good candidate, a dust species needs to (i) form close to the star where the temperatures are still high and (ii) have sufficient opacity to be accelerated by radiative pressure. Amorphous carbon grains in the atmospheres of C stars can account for the observed mass-loss rates (Winters *et al.*, 2000a). Interferometric observations show evidence for the existence of large dust grains of a few hundred nm in di-

ameter, less than one stellar radius above the stellar atmosphere (Norris *et al.*, 2012). Anandarao, Pottasch and Vaidya (1993) had established the correlation of circumstellar dust masses with the pulsation period of oxygen-rich Mira variables. This proximity to the atmosphere indicates that the dust species are transparent at optical wavelengths and hence resistant to sublimation by the intense radiation field. The IR spectra of cool M and S stars show the presence of an unidentified continuum opacity source (McDonald *et al.*, 2010).

The mass loss rate of AGB stars increases until the envelope gets so thin that the photosphere begins to contract and the star becomes a proto-planetary nebulae (PPNe). Reliable mass loss rates are obtained from the dust continuum emission and circumstellar molecular radio lines like hydroxyl (OH) and rotational lines of CO (Olofsson, 2003). Mass-loss during the AGB phase has been modeled based on both theoretical arguments (e.g., Bowen (1988); Fleischer, Gauger and Sedlmayr (1992); Bloeker (1995b); Arndt, Fleischer and Sedlmayr (1997); Venkata Raman and Anandarao (2008)) and semi-empirical calculations (e.g., Vassiliadis and Wood (1993)).

1.2.5 Post-AGB Evolution

Some AGB stars experiencing high mass-loss rate contain a large amount of dust rendering them completely obscured in the visible and NIR wavelength regions. The peak of the SED thus moves to mid-IR wavelengths. These stars are known as OH/IR stars, because they show strong OH maser emission in addition to the IR radiation. It is generally believed that M type stars eventually evolve into OH/IR stars (van der Veen and Habing, 1988), with the onset of a superwind phase, having mass loss rates of $\sim 10^{-4} M_{\odot} \text{ yr}^{-1}$ (Renzini, 1981). The outflow during the AGB stage, removes the outer parts of the star until the mass of the envelope is reduced to $\sim 10^{-2} M_{\odot}$ (Blöcker, 1999). Now the pulsations decrease in amplitude and the mass-loss may cease. Post-AGB (PAGB) evolutionary tracks cross the upper Cepheid instability strip leading to the possibility of pulsations in some objects. A distinct class of pulsating variables that resemble PAGB from their IRAS colors are called RV Tauri

stars (Jura, 1986; Wahlgren, 1993). These stars are defined by luminosity class I - II with spectral types ranging from mid-F to K type and show light curves with periods between 50 and 150 days. PAGB stars with the spectral types of F - G usually show photometric and spectroscopic variations on scales of the order of a month (Jura, 1986; Waelkens *et al.*, 1987; Oudmaijer, 1996). The overall characteristic of the photometric variability may be its irregularity. The variability may be attributed to the continued pulsation during the PAGB phase. The decrease or cessation of mass loss is normally considered to be the beginning of the short PAGB phase where the temperature of the central star quickly rises at roughly constant luminosity. During this phase the mass lost during the AGB phase slowly drifts away from the star ($v \sim 10$ km/sec), its (column) density drops and the central star becomes visible again. When the central star reaches temperatures of $\geq 30,000$ K and if the material lost during the AGB has not reached too large distances from the central star, the star can ionise this material to form a planetary nebula (PNe) (Kwok, 2000). Typical post-AGB stars are expected to have luminosities around $10^3 - 10^4 L_{\odot}$ (Bloeker, 1995a) where L_{\odot} is the solar luminosity.

Most PAGB candidates were detected and identified on the basis of their far-IR (IRAS) colors (Parthasarathy and Pottasch, 1986; Pottasch and Parthasarathy, 1988; Kwok, 1993; Anandarao, Pottasch and Vaidya, 1993). PAGB stars can be recognized from two distinct contributions that appear in their SED. First, the contribution from the expanding circumstellar envelope that leaves its mark in the mid-IR region. Second, the contribution from the central star that accounts for ultra-violet (UV) and optical wavelengths. This leads to double-peaked SED indicating detached envelopes around the star as distinguished from the single broad peak of AGB stars that have warmer dust.

1.2.6 IR spectra of Evolved Stars

AGB and PAGB stars are usually very faint at optical wavelengths. Hence they are mostly studied in the NIR and mid-IR wavelengths. Most of the molecular lines originate close to the star, where the temperature is relatively

high (Habing and Olofsson, 2003). Farther away from the star, in the cooler regions, the dust continuum along with the dust features may be detected. The excitation mechanisms of the rotational-vibrational spectra of CO observed in AGB stars at the NIR wavelengths, H₂ & PAH emissions observed in PAGB/PPNe stars at the mid-IR wavelengths are described here.

1.2.6.1 Rotational-vibrational spectra of CO

The CO molecule offers several advantages as a diagnostic probe of the structure of cool stellar atmospheres. It has a stable, closed-shell structure and a high dissociation energy of 11.2 eV. Hence, it is predicted to form in cool giant and supergiant atmospheres. Shock chemistry models predict that the CO abundance remains unaltered, even if the gas is shocked periodically by stellar pulsation (Duari, Cherchneff and Willacy, 1999). CO formed deep in the photosphere exists unchanged in abundance over large distances above the photosphere with the predicted lack of saturation in the rotational-vibrational lines. Hence CO should be a very useful probe for studying the extended atmospheres of AGB stars.

The total rotational-vibrational energy of a molecule experiencing rotation as well as vibration (stretching of bond lengths) is given by

$$\varepsilon_{total} = BJ(J + 1) + (v + \frac{1}{2})\bar{\omega}_e - x_e(v + \frac{1}{2})^2\bar{\omega}_e \quad (1.2)$$

where B , J , v , $\bar{\omega}_e$ are rotational constant, rotational quantum number, vibrational quantum number, equilibrium oscillation frequency respectively (see Banwell and McCash (1994)). The selection rule for the allowed transitions between these combined motions are $\Delta v = \pm 1, \pm 2$, etc and $\Delta J = \pm 1$. The transitions between the vibrational levels $\Delta v = \pm 1$ with $\Delta J = \pm 1$ is called the fundamental mode of transition. The vibrational transitions with $\Delta v = 2$ are called the first overtone bands while those with $\Delta v = 3$ are called the second overtone bands (see e.g., Emerson (1996); Tennyson (2005)). The NIR spectra of AGB stars mostly show the first and second overtone bands of CO in absorption. In contrast PAGB objects at these wavelengths mostly show

Brackett series lines in absorption.

1.2.6.2 Rotational spectra of H₂

Molecular hydrogen (H₂) is the most abundant molecular species in the universe (Shull and Beckwith, 1982; Dalgarno, 2000). H₂ is a homonuclear diatomic molecule and therefore does not have a permanent electric dipole moment or an allowed rotational-vibrational spectrum, thus making it a difficult species to observe directly. However, weak electric quadrupole transitions of H₂ can be observed. The selection rule for pure rotational spectra in the $v=0$ level is $\Delta J = \pm 2$, where v and J are vibrational and rotational quantum numbers respectively.

The small mass (1.673×10^{24} gm) and size (5.291×10^{-11} m) of the H₂ molecule gives it a low moment of inertia, thus leading to a large rotational constant of 85.25 K (expressed in Kelvin). As a result of this large value, the rotational levels are widely spaced. First few pure rotational lines of H₂ lines lie at the wavelengths 28.221, 17.035, 12.279, 9.665, 8.026 and 6.908 μm . For the pure rotational transition, $J = 2 \rightarrow 0$ at 28.221 μm the excitation temperature is 510 K. Similarly the excitation temperatures for the $J = 4 \rightarrow 2$ and $J = 7 \rightarrow 5$ transitions that occurs at 12.279 and 6.908 μm are 1200 and 2276 K respectively. However, if excited collisionally or by shock between the shell and the wind of the central hot source, they do not require such high temperatures and can be emitted at temperatures around 250 K (Parmar, Lacy and Achtermann, 1991). Burton, Hollenbach and Tielens (1992) have modeled the rotational line intensities of H₂ from photodissociation regions (PDR) and in shocks, that are emitted at temperatures around 100 - 300 K. These pure rotational lines of H₂ are observed in PPNe candidates having a hot central source (Herpin, Cernicharo and Heras, 2000).

1.2.6.3 Polycyclic Aromatic Hydrocarbons (PAHs)

The most common features observed at the mid-IR wavelengths in PAGB/PPNe are PAHs, C₂H₂, HCN, CH₄, C₃, SiC (dust), MgS (dust) (Cerrigone *et al.*,

2009; Manteiga *et al.*, 2011; Sloan *et al.*, 2014). These species contain the most common elements like H, C and N. The features located around 3.3, 6.2, 7.6, 7.9, 8.6, 11.2 and 12.7 μm observed in PNe, PAGB stars, HII regions, reflection nebulae around early-type stars and in some galaxies could not be identified with already known molecular emission bands and were therefore called as Unidentified Infrared Bands (UIR). Later it was realized that very small dust grains consisting of about 20 - 100 C-atoms, more typically large molecules, are the most likely candidates for the carriers of these bands (Leger and Puget, 1984; Allamandola, Tielens and Barker, 1985; Cohen *et al.*, 1986; Allamandola, Tielens and Barker, 1989).

The observed UIR wavelengths coincide with the typical resonances found in aromatic hydrocarbon molecules. These aromatic molecules may easily attain the temperature required to emit at such short wavelengths upon the absorption of a single UV photon ($\sim 2200 \text{ \AA}$). Therefore the carrier of the UIR bands is thought to be a family of connected aromatic species, or the so-called PAHs. PAHs are a family of molecules comprising of a group containing hundreds of organic material made up of two or more benzene rings. Naphthalene (C_{10}H_8), pyrene ($\text{C}_{16}\text{H}_{10}$), and coronene ($\text{C}_{24}\text{H}_{12}$) are simple examples of these structures. An exhaustive overview on PAHs in interstellar space is given by Omont (1986) & Tielens (2008). Table 1.1 lists the wavelengths with modes of excitation of PAH molecules (Tielens, 2005).

1.2.6.4 PAH formation

The main molecule from which PAHs are formed is acetylene and its radical derivatives (Millar and Williams, 1993; Tielens, 2005). The first step in PAH formation, which is the most difficult one, is the creation of the first aromatic ring. In additional reactions on the aromatic ring, it is believed that an addition of H-atoms and hydrocarbons, can lead to the formation of a PAH molecule. For H-poor environments there is a three-way route. After the formation of small, flexible, linear, C-chain radicals, monocyclic ring molecules are formed through the addition of C-atoms. The isomerization reactions on

Table 1.1: The mid-IR emission features with wavelength and mode identifications
Credit: Tielens (2005)

Bands(μm)	Mode(s)
Lines	
6.0	C-O stretch (?)
6.2	aromatic C-O stretching
6.9	aliphatic C-H bending
7.6	C-C stretching and C-H in-plane bending
7.8	C-C stretching and C-H in-plane bending
8.6	C-H in-plane bending
11.0	C-H out-of-plane bending, solo, cation
11.2	C-H out-of-plane bending, solo, neutral
12.7	C-H out-of plane bending, trio, cation (?)
13.6	C-H out-of-plane bending, quartet
14.2	C-H out-of-plane bending, quartet
16.4	in-plane and out-of-plane C-C-C bending modes in pendant ring (?)
Plateaus	
6-9	blend of many C-C stretch and C-H in-plane bend modes
11-14	blend of C-H out-of-plane bending modes
15-19	in-plane and out-of-plane C-C-C bending modes

the C-chain lead to planar carbon hexagon structures. The absence of hydrogen leads to dangling bonds. Incorporation of pentagons and curling reduces the dangling bonds, possibly creating fullerenes, better known as 'Bucky Balls' (Cataldo, Strazzulla and Iglesias-Groth, 2009; Ehrenfreund and Foing, 2010).

PAH processing and destruction can be caused by high energetic radiation with energies of 20 eV, or by strong shocks (Siebenmorgen and Krügel, 2010). However, only the smaller PAHs (up to 30 C-atoms) are completely destroyed.

Near the stellar photosphere the high densities and temperatures allow PAH to grow chemically.

1.2.6.5 PAH emission mechanism

PAHs are electronically excited into an upper electronic state upon the absorption of a single Far-UV (FUV) photon, raising the PAH's temperature as much as 1000 K. The energy is rapidly converted internally from the single excited vi-

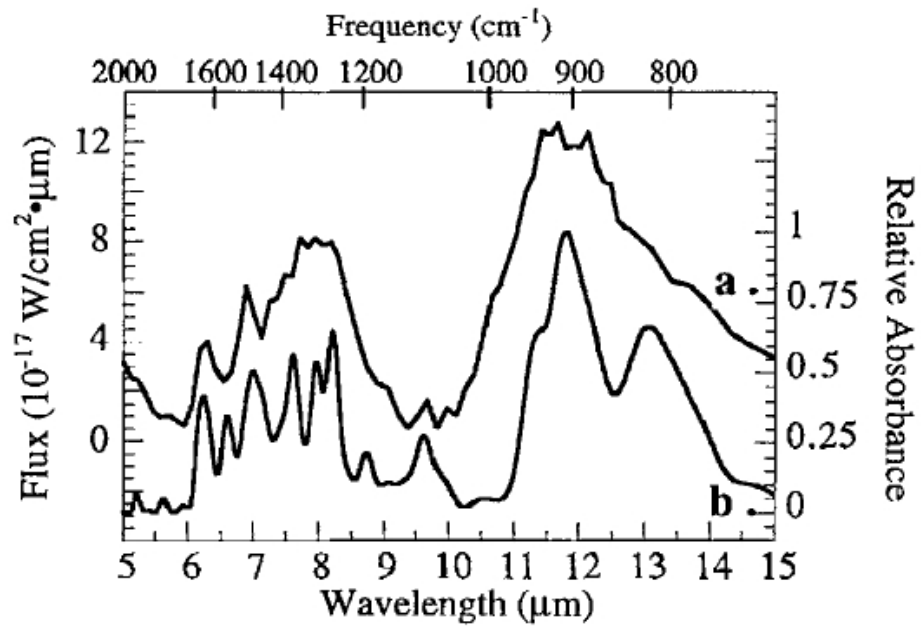


Figure 1.6: Comparison of the observed spectra of PPNe IRAS 22272+5435 (a) with the lab absorption spectra (b) produced from a mixture of neutral and ionised PAH (Allamandola, Hudgins and Sandford, 1999)

brational state into several excited vibrational states, bringing the PAH back into a lower electronic state (Allamandola, Tielens and Barker, 1989). The molecule cools down mainly by radiative cascade through IR emission in the C-C and C-H vibrational modes decreasing its temperature to ~ 10 K on a timescale of seconds (Bakes, Tielens and Bauschlicher, 2001; Tielens, 2008). The internal energy redistribution is a complex mechanism involving the coupling of different vibrational modes and can occur in several steps involving

different timescales.

Laboratory studies show that PAH ionizations do not affect the frequency of vibrational resonances very much (Tielens, 2005). But more striking is the effect on the relative intensity of the various modes. This effect is very clear in the 5 - 10 μm region, where the resonances are very weak in neutral PAHs and much stronger in charged PAHs. PAHs can both be positively and negatively charged. The charge is set by the balance between photoelectrically ejected electrons and the PAH electron recombination rate, and is thus determined by the ratio of the UV field and the electron density. Fig 1.6 shows a comparison of lab absorption spectra produced from a mixture of neutral and ionised PAH with the stellar spectra of the PPNe IRAS 22272+5435.

The stellar IR spectra often show narrower lines than those observed in laboratory spectra. This is due to fact that laboratory materials are more disordered. The precise position of a specific mode is dependent on the size, symmetry, structure, molecular heterogeneity of the PAH molecule and of the charge.

1.3 Organization of thesis

1.3.1 Chapter 1: Introduction

This Chapter gives an introduction to the circumstellar environments of eruptive low mass young stellar objects and evolved mass losing intermediate mass stars. The first part of the Chapter describes eruptive pre-main sequence stars and their outburst mechanism. The second part deals with the post-main sequence evolution of intermediate mass stars, the mass loss processes and the observed circumstellar dust features.

1.3.2 Chapter 2: Observations and Data analysis

This Chapter gives insights of the optical layout and detector characterisation of the first light NIR instrument Near Infrared Camera & Spectrograph

(NICS). It deals with the NIR observations and the data analysis techniques. The Infrared Spectrograph (IRS) on board *Spitzer* Space Telescope (SST) and Short wavelength Spectrometer (SWS) on board Infrared Space Observatory (ISO) that provided all the mid-IR data presented in this thesis are described. The data analysis techniques and the softwares used for the same are also described.

1.3.3 Chapter 3: Infrared study of V1647 Ori and five other eruptive young stellar objects

This Chapter presents the results of the NIR monitoring of V1647 Ori during its recent two outburst phases flanking the quiescent phase. It describes the spectroscopic variability in the NIR and mid-IR wavelengths. The results of the SED models during the outburst and quiescent phase are presented. The photometric and spectroscopic nature of V1647 Ori are compared with five other eruptive young stellar objects.

1.3.4 Chapter 4: Infrared photometric and spectroscopic study of Asymptotic Giant Branch stars

This Chapter deals with the NIR spectroscopic mass loss signatures during AGB phase on a sample of M, SR, S type stars. A correlation study of the observed NIR spectral signatures with the mass loss parameters and the implications are discussed. The circumstellar parameters derived from the SED models are compared between these three types.

1.3.5 Chapter 5: Infrared photometric and spectroscopic study of Post Asymptotic Giant Branch stars/Proto-Planetary Nebulae

Multi-epoch NIR spectroscopic observations on a sample of PAGB stars are presented to explore possible variability due to episodic mass loss. Mid-IR

spectra of a larger sample of PAGB/PPNe stars are also presented. These results combined with SED modeling of the sample sources are used to understand possible relationship between the strength of various spectroscopic features and the physical parameters of the sources. The Chapter presents a few PAGB/PPNe candidates making their transition to PNe. A rare detection of neutral fullerene (C_{60}) feature in the mid-IR spectra of a PAGB star is presented which is possibly only the second such detection in this class of objects.

1.3.6 Chapter 6: Summary and Future Work

This Chapter briefly describes the significant results obtained during the current research and the future direction of work.

Chapter 2

Observations and Data analysis

2.1 Introduction

NIR photometric and spectroscopic observations were carried out with the Physical Research Laboratory's (PRL) 1.2 m telescope using the NICS (Anandarao *et al.*, 2008) and Near-Infrared Camera and Multi-Object Spectrometer (NICMOS). Most of the mid-IR spectra were extracted by processing the data from the *Spitzer* archive. The data used were from IRS (Houck *et al.*, 2004) onboard SST (Werner *et al.*, 2004). The IR spectra obtained by SWS (de Graauw *et al.*, 1996) onboard ISO (Kessler *et al.*, 1996) were used for a few sources for which IRS *Spitzer* data were not available.

The SEDs for the selected sample of PAGB stars and PPNes were constructed using the available public archival data compiled from VIZIER, Two Micron All-Sky Survey (2MASS), AKARI (Ishihara *et al.*, 2010), *Spitzer* - InfraRed Array Camera (IRAC) (Fazio *et al.*, 2004), Infrared Astronomical Satellite (IRAS) (Bamberg and Zaun, 1985) and Midcourse Space Experiment (MSX) data archives (Egan, Price and Kraemer, 2003a). The SEDs thus obtained were modeled using the DUSTY software (Ivezic *et al.*, 1997).

This Chapter briefly describes the Mt. Abu Infrared Observatory, IR de-



Figure 2.1: Mt. Abu Infrared Observatory

teaching technique used and the parameters that determine the performance of the detector array. The details of the optics and the detector characteristics of the new focal plane instrument NICS are described. The instruments like IRS and SWS that are on board SST and ISO are outlined. The NIR observation procedures and the data analysis techniques are described.

2.2 Mt. Abu Infrared Observatory

Mt. Abu Infrared Observatory (MIRO) is geographically situated at Mt. Abu in the state of Rajasthan at $24^{\circ} 39' 10''$ N, $72^{\circ} 46' 47''$ E, at an altitude of 1680 m, adjacent to the Gurushikar peak of Aravalli mountain ranges. Figure 2.1 shows the outer view of MIRO. It consists of an equatorially mounted 1.2 m telescope mainly designed for NIR observations. The telescope was installed during December 1994 and has been operational since 2 decades. The site typically offers about 200 nights in a year for astronomical observations. Out of these 200 nights 70% are spectroscopic in nature. The typical seeing (measured as



Figure 2.2: Infrared telescope at MIRO

the full width at half maximum of a star image) is about 1.3 arcsecs in the months of October to March and about 1.7 arcsecs during the months of April to June. The site is very dry (precipitable water vapour ~ 2 mm) between October to May ($< 40\%$) and is hence excellent for NIR observations.

Optical observations are also possible since the surface accuracy for all the optical components had been optimized at 5000 \AA . The surface accuracy of the primary mirror is $\lambda/10$ (at the green line). The primary parabolic mirror has an aperture of 1.21 m with a focal ratio of $f/3$. The secondary hyperbolic mirror produces an effective focal ratio of $f/13$ at the Cassegrain focus. The Cassegrain focus is behind the primary at a distance of 0.38 m from the Cassegrain plate where the back-end instruments are mounted. Figure 2.2

shows the IR telescope operational at MIRO. The back-end instruments that are currently in operation at MIRO are

1. NICMOS Camera
2. NICS Camera
3. Imaging Fabry-Perot Spectrometer
4. Optical Polarimeter
5. PRL Advanced Radial-velocity All sky Search (PARAS)

Various science programs that are pursued using MIRO are described in Anandarao and Banerjee (2005). Part of the work presented in the thesis utilized the first two instruments mentioned above.

2.3 Detector principles

Detector arrays in the near- and mid-IR detect photons through photoconductivity. An incoming photon with energy greater than the bandgap energy is absorbed within the semiconductor material, exciting a bound electron into the conduction band. The remaining net positive charge behaves as a positively-charged particle, called 'a *hole*'. Thus an electron-hole pair is created, which can carry a measurable electric current (a photocurrent).

The cut-off wavelength (λ_c) of a detector with intrinsic absorption having a band gap energy (E_g) is given by

$$\lambda_c = \frac{hc}{E_g} = \frac{1.24}{E_g(eV)} \mu m \quad (2.1)$$

where h is a Planck's constant, c is the velocity of light. The E_g of the semiconductor materials varies with temperature. Band gap engineered alloys are used as materials for the detectors so that the band gap energies can be tuned, thereby changing its cutoff wavelength of operation. Popular semiconductor choices include indium gallium arsenide (InGaAs), which is sensitive up to 1.7 μm , indium antimonide (InSb) ($\lambda_c=5.4 \mu m$) and mercury cadmium telluride

(HgCdTe), whose composition can be tuned to give a desired cut-off wavelength above $2.4 \mu\text{m}$ (Joyce, 1992). Since a smaller band gap will enable detection at longer wavelengths, less energy is required to excite an electron across the gap, leading to larger thermally generated dark currents. This suggests that the lower functional temperature should be used so that thermal excitation of electrons can be minimized. The required passive cooling temperature for reducing the thermal electrons for low background detectors (Hoffman, Love and Rosbeck, 2004) is given by

$$T_{max} = \frac{200K}{\lambda_c(\mu m)} \quad (2.2)$$

For example, the required cooling temperatures for a cut off wavelength $\lambda_c = 2.5 \mu\text{m}$ is $\sim 80 \text{ K}$, a temperature that nearly corresponds to the boiling point of liquid nitrogen.

2.3.1 Mercury Cadmium Telluride (HgCdTe)

HgCdTe is often referred to as $\text{Hg}_{1-x}\text{Cd}_x\text{Te}$, where x is the mole fraction of cadmium. For $x = 0.45$, the cut-off wavelength is $2.3 \mu\text{m}$, while for $x = 0.24$, it is $9.19 \mu\text{m}$. The band gap energy is very sensitive to small fluctuations in x of around 0.24. For example, a change in x by 0.001 for $x \sim 0.24$ changes the cutoff wavelength $> 0.1 \mu\text{m}$. Because HgTe is a semi-metal and CdTe is a semiconductor, carefully tuned mix of these two compounds can create a semiconductor with a very small band gap, corresponding to a relatively longer cut-off wavelength.

Arrays of detectors are desirable for efficient direct imaging, but are necessarily much more complex to manufacture than single pixel detectors. The detectors are grown on a wafer of silicon with a matching grid of output contacts. Indium bumps are deposited on each grid for contact and the detector and amplifier grids are aligned, and pushed together by applying a large force. Such hybrid arrays are difficult to manufacture, as differential thermal expansion between the two layers can cause the array to break apart (Rieke, 2007). Partly as a result of this, such IR arrays are very expensive.

2.3.2 Detector performance

There are many parameters that determine the performance of a detector. The significant parameters are described below:

2.3.2.1 Dark current

Dark current is the small electric current that flows through the detector even when no photons are entering the device. The electron-hole pairs that are generated thermally within the semiconductor material are the main source of the dark current. To minimise this effect on the resulting signal, IR detectors are normally operated at low temperatures (see Eqn. 2.2).

2.3.2.2 Read noise

This is the component of the noise from a single pixel which is independent of the signal level. Read noise arises from the process by which the charge stored on the diode capacitor is converted to the final signal. If the readout procedure is optimised, the read noise is usually limited by electronic noise in the amplifier(s). The smallest signal which can be detected goes as the square of the read noise.

2.3.2.3 Readout time

Long readout times are usually needed to take out the effects of high frequency changes in bias voltages etc., and so the time taken to read out a pixel with the minimum read noise can be tens or hundreds of microseconds during which signal cannot be acquired (dead time).

2.3.2.4 Quantum efficiency

The Quantum efficiency (QE) of a detector is the fraction of incident photons (of appropriate wavelengths) that are detected. Modern direct-readout arrays typically have quantum efficiencies of well over 90 %. The quantum efficiency

and read noise of the detector decide the signal to noise ratio (S/N) of the observation of the faintest target (McLean, 2008). The S/N ratio is given by

$$\frac{S}{N} = \frac{N_S t \eta}{\sqrt{N_S t \eta + N_B t \eta + N_D t \eta + N_R^2}} \quad (2.3)$$

where η is the QE at the concerned wavelength; N_S is the total number of photons (signal) incident on the pixel in the exposure time (t); N_B is the total number of photons due to the sky background; N_D is the total number of dark current electrons; and N_R is the total number of electrons resulting from the readout noise.

2.3.2.5 Linearity

Linearity of the detector is a measure of how consistent the detector responds to its well depth (maximum number of electrons stored in a pixel before it is saturated). It also signifies a simple linear relation between the number of photons striking the detector and the charge collected during the exposure. The linearity is critical in obtaining the accurate intensity measurement.

2.3.2.6 Well capacity

The number of photoelectrons an individual pixel can contain before saturation is termed as well capacity. Charge exceeding the saturation level in a pixel of the IR array leads to a deviation from its linear response.

2.3.2.7 Array size

Large format arrays like H4RG-15 fabricated by Teledyne Imaging sensors (Beletic *et al.*, 2008) have potential usage in astronomy in conducting large area scientific survey of astronomical sources in astronomy.

2.3.3 Array Readouts

High speed time resolved astronomical observations demand arrays having very short dead times. Array readout schemes therefore play a crucial role in deciding the dead time of the array thereby using an appropriate or optimized

scheme in reading out the array quickly and more efficiently. There is usually no shutter in an IR camera to determine the exposure time. This is partially due to the requirement that the shutter be cold, and that it operates very rapidly to accommodate the short exposures demanded by the high backgrounds. IR arrays are continuously exposed to light, and the exposure time is controlled by a sequence of reset and read pulses. IR arrays employ non-destructive readout operation in which each pixel is read out separately without shifting the charge to the adjacent pixels.

There are four modes of reading the array:

1. Single Frame Mode
2. Correlated double-sampling mode (CDS)
3. Reset-read-read or Fowler sampling
4. Sampling up the ramp (SUTR)

In the single frame mode the entire array is reset pixel by pixel. During this mode only one sample frame is acquired after the reset-read cycle and hence is incapable of removing noise efficiently. In the correlated double-sampling mode, after the array is reset it is sampled once (pedestal level) and after passing through the desired integration time (signal level) it is sampled again. The resulting frame is the difference between the two reads. The Fowler sampling method employs multiple correlated frame reads of the detector. According to this scheme the entire array is reset pixel by pixel and then immediately the entire array is sampled non-destructively for N reads (pedestal level). After waiting for the required integration time it is again sampled non-destructively for N reads (signal level). The effective signal is the average of the difference between the individual reads in the pedestal and signal levels. The differencing process is usually accomplished in a front-end co-adder. By averaging N reads, the read-noise can be reduced by $\sim 1/\sqrt{N}$. The NICS employs this technique for its read out while the NICMOS uses a double-correlated sampling mode. In sampling up the ramp mode the array is reset row by row. After the initial

pedestal read many individual single reads are obtained during the given integration time. The effective signal acquired by a pixel over the integration time is given by the slope of a linear fit of the data samples during the multiple reads multiplied by the integration time.

Table 2.1: Detector characteristics of NICMOS

Array Format	256×256
Pixel size (μm)	40
Lower Cut-off λ (μm)	1.10
Upper Cut-off λ (μm)	2.30
Dark noise (e^-/s)	< 0.7
Read Noise (e^-)	53
Linear range	1000-10000 ADU
Bad pixels	~ 250
System Quantum efficiencies	
J band (%)	32.75
H band (%)	18.30
K band (%)	28.91

2.4 Near Infrared Camera and Multi-Object Spectrometer (NICMOS)

The NICMOS camera has been a major workhorse at MIRO for nearly 15 years. The instrument was designed and built by Infrared Labs Inc., USA. The array design is based on the NICMOS-3 concept that uses a 256×256 format of HgCdTe detector operating between 1.1 and 2.3 μm . The photometric mode offers two field of view (FOV) of $2' \times 2'$ and $4' \times 4'$. These options yield plate scales of $0.5''/\text{mm}$ and $1''/\text{mm}$ respectively, for the two FOV's. The

Table 2.2: Description of broad & narrow band filters in NICMOS

Band	Central Wavelength (μm)	Bandwidth (μm)	Lower cut-off (μm)	Upper cut-off (μm)	Transmission at peak Wavelength(%)
<i>J</i>	1.253	0.296	1.105	1.401	93.2
<i>H</i>	1.659	0.288	1.514	1.803	91.9
<i>K</i>	2.185	0.408	1.981	2.389	85.3
<i>K'</i>	2.120	0.360	1.940	2.300	> 80
Narrow-band filters					
[<i>FeII</i>]	1.645	0.0375	1.6262	1.6638	> 80
H ₂ 1-0S(1)	2.1175	0.0429	2.0961	2.1390	74.1
Narrow band 1	2.1352	0.0428	2.1138	2.1566	78.0
Br γ	2.164	0.0443	2.1427	2.1870	59.1
CO band	2.3726	0.1013	2.3220	2.4232	83.0
Narrow band 2	2.2169	0.0831	2.1754	2.2585	74.0

spectroscopic part of the instrument was designed to give a dispersion of about 9.5 Å per pixel in each of the *J*(1.253 μm), *H*(1.659 μm) and *K*(2.185 μm) bands, giving an over all resolving power of ~ 1000 . The optical layout of the instrument is described in Nanda Kumar (1999). The characteristic of the detector and the filters (both broad and narrow) are shown in Table 2.1 and 2.2.

2.5 Near Infrared Camera and Spectrograph (NICS)

The NICS camera is a recently commissioned HgCdTe (HAWAII-1) 1024 \times 1024 array imaging camera with both photometric and spectroscopic capabili-

ties as in NICMOS. In the photometric mode it delivers an angular resolution of $0.5''/\text{pixel}$ in an un-vignetted field of view of $\sim 8' \times 8'$. The spectral coverage is between $0.8 - 2.5 \mu\text{m}$. The dispersion of the spectrograph is designed so as to cover the combined bands of *IJ*, *JH* and *HK* (see Table 2.3 for filter definitions) on 1024 pixels.

2.5.1 Optical layout

In order to achieve the principal goal of the design of having seeing-limited angular resolution in an un-vignetted field of view of $\sim 8' \times 8'$ with $0.5''/\text{pixel}$, a focal reduction by a factor of 2 is required. The optical system design for these specifications are achieved using 9 singlet lenses. Of these 9 lenses, five are used for field definition (Lenses 1 and 2) and collimation (Lenses 3, 4 & 5). The remaining lenses are used for re-imaging on the Hawaii-1 array. The optics is arranged in an L-shaped configuration at the fold of which lies either a mirror for the photometric mode or a reflection grating for the spectroscopic mode of operation. The top panel in Fig 2.3 represents the collimating and re-imaging arms of NICS. Fig 2.4 shows the layout of the optics in the Y-Z plane. The operating temperature of the NICS is 77 K; and is achieved by liquid nitrogen. As the f/13 beam from the telescope enters the system through the window W, the Lenses 1 & 2, located before the Cassegrain focus (CAS FOCUS in Fig 2.4), serve as field lenses to image the virtual exit pupil of the telescope (located behind the secondary mirror) to a real pupil at a different location. At this point the focal ratio drops to f/10.5. The Lenses 3, 4 & 5 constitute the collimator that makes the diverging rays from the Cassegrain focus parallel. The beam then passes through two circular filter wheels containing interference filters before being incident on the flat fold mirror or grating located at the end of the collimating arm at 45° . The definitions of the filters are presented in Table 2.3. The imaging lenses L6 - L9 further decrease the focal ratio to f/6.5, the desired value.

The mirror/grating assembly is made from the same substrate that is polished for reflection on one side, for the imaging mode while the other side has

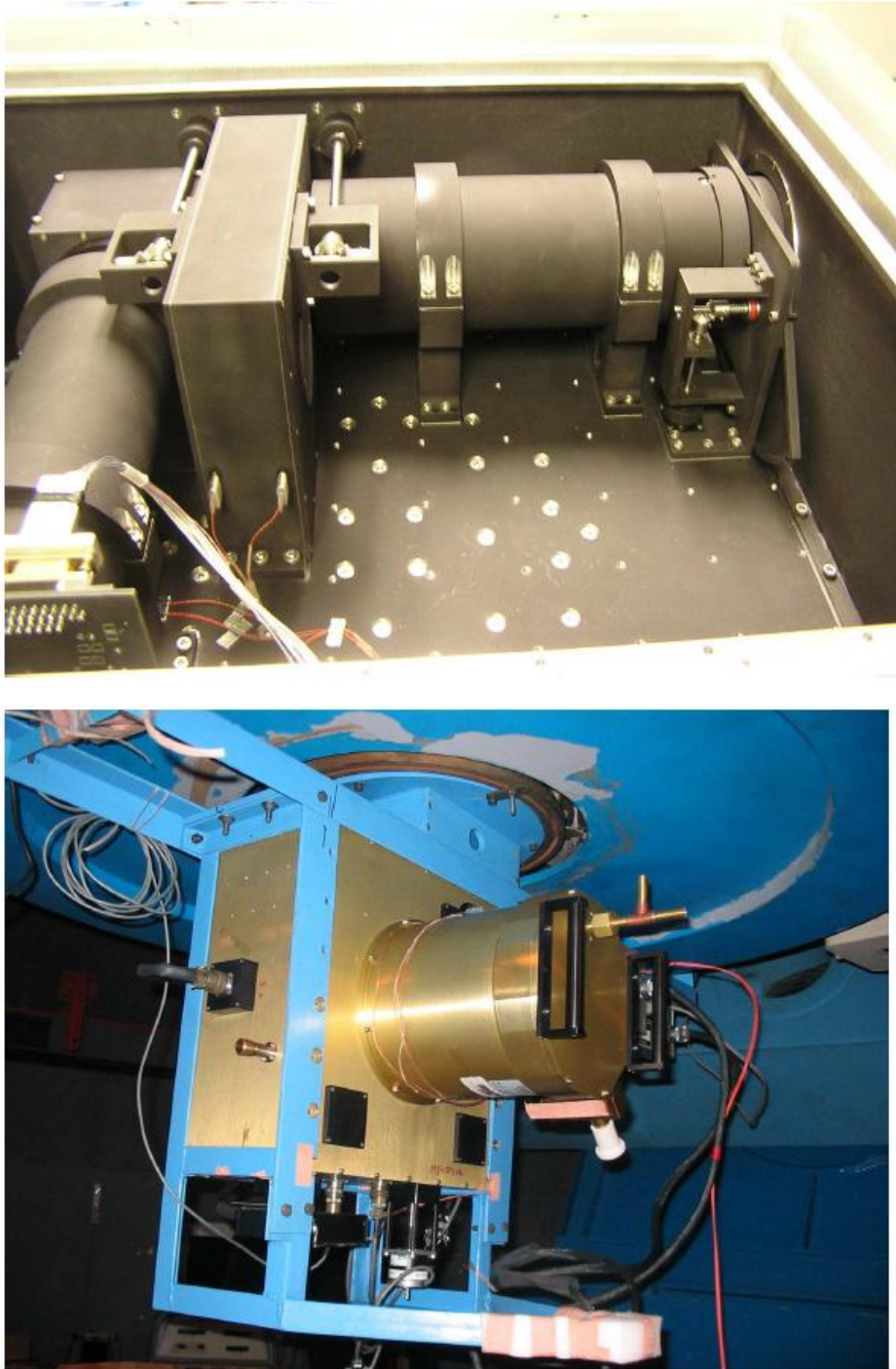


Figure 2.3: Inside view of the NICS dewar Top: the two perpendicular tubes show collimation and re-imaging arms. The HAWAII-1 detector is mounted at the end of the re-imaging tube to the bottom-left. Bottom: NICS mounted at the Cassegrain focus of the 1.2 m telescope at Mt Abu.

a reflection grating for the spectroscopic mode. After the rays pass through the collimator, a pupil mask is located, 25 mm before the mirror/grating, in order to block IR radiation from the spider holding the secondary mirror. The folded beam (at the mirror/grating) is then passed through the re-imaging arm of the optics at the end of which lies the HAWAII-1 array detector. All the lenses are anti-reflection-coated to maximize the throughput, in the entire wavelength range of 0.8 - 2.5 μm . In the optical design the angles of incidence between rays and the lens optical surfaces are constrained to be $< 30^\circ$ for the purpose of facilitating the design of anti-reflection coatings covering the full wavelength region over the full square field. The details of the optics are

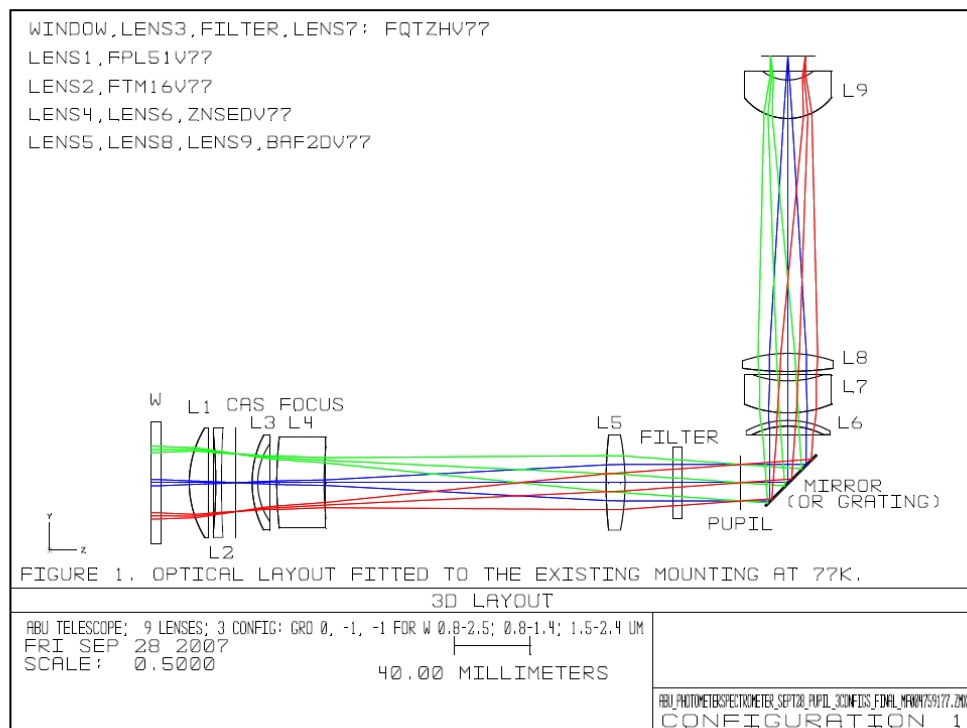


Figure 2.4: Optical layout of NICS. The lens materials are mentioned in the top left side. The system window is shown as W; position of the Cassegrain focus is indicated as CAS FOCUS (vertical line); L's represent lenses; and the horizontal line above L9 is the location of the HAWAII-1 array.

described in Anandarao *et al.* (2008).

Table 2.3: Description of filters in NICS

Band	Central Wavelength (μm)	Bandwidth (μm)	Lower cut-off (μm)	Upper cut-off (μm)	Transmission at peak Wavelength(%)
<i>Y</i>	1.021	0.118	0.9600	1.078	70
<i>J</i>	1.2449	0.181	1.1587	1.3400	85
<i>H</i>	1.6291	0.333	1.4687	1.8020	95
<i>K</i>	2.1979	0.389	2.0004	2.3895	97
<i>Ks</i>	2.1479	0.358	1.9666	2.3250	97
Narrow and combo-band filters					
H ₂ 1-0 S(1)	2.1231	0.0353	2.1053	2.1406	91
Br γ	2.1701	0.04	2.1505	2.1905	90
<i>IJ</i>	1.1675	0.595	0.8495	1.4445	97
<i>JH</i>	1.5166	0.7958	1.1166	1.9124	97
<i>HK</i>	1.9715	1.1754	1.3702	2.5456	98

2.5.2 Photometric mode

The photometric mode contains standard broadband filters: *Y* (0.97-1.07 μm), *J* (1.17-1.33 μm), *H* (1.49-1.78 μm), *K* (2.03-2.37 μm) and *Ks* (1.99-2.31 μm); and narrowband (NB) filters: H₂ 1-0 S(1) (2.121 μm) and Br γ (2.165 μm) arranged in filter wheels. The filters in the *J*, *H*, *K* and *Ks* bands follow the specifications of Tokunaga, Simons and Vacca (2002). The original platescale of the cassegrain is reduced by half to give 0.5''/pixel thus covering 8' \times 8' on the sky.

2.5.3 Spectroscopic Mode

The spectroscopic mode can be set up by rotating the fold mirror by 180° , bringing in a diffraction grating having 150 lines per mm, operating in the first order of diffraction. The combo filters *IJ*, *JH* and *HK* are used for the spectroscopic mode.

The grating equation is given by

$$d(\sin\alpha + \sin\beta) = m\lambda \quad (2.4)$$

where α and β are the angles of incidence and diffraction respectively and the inter groove distance d is 1/150 mm and m is the diffraction order ($m=+1$ in our case). To improve the efficiency, the grating was blazed at $2 \mu\text{m}$ with a blaze angle of $8^\circ 38'$ and an apex angle of 130° . Fig 2.5 represents the laboratory spectra of a mercury CFL using NICS in the *IJ*, *JH* and *HK* bands.

The reciprocal dispersion found by using spectra from a mercury lamp (Fig 2.5) is 7.70, 7.82 and $8.07 \text{ \AA}/\text{pixel}$ in *IJ*, *JH* and *HK* filters respectively. Thus the spectral coverage over the 1024 pixels of the entire detector is $\sim 0.80 \mu\text{m}$, enabling us to take spectra in two bands at a time.

There are two slits of widths 82 and $102 \mu\text{m}$ respectively, in the aperture/slit wheel sector. The slits placed at the $f/10.5$ focus are demagnified by a factor $(6.5/10.5)$ on the detector image plane. The wavelength dependent anamorphic demagnification in the direction of dispersion given by the factor $\cos(\alpha)/\cos(\beta)$ is 0.7 for NICS. Hence the total demagnification of the slit in $m = +1$ mode is 0.43. The $102 \mu\text{m}$ slit is therefore demagnified to $43 \mu\text{m}$ on the detector which is slightly more than 2 pixels (1 pixel = $18 \mu\text{m}$). The slit will be sharpest in the *K* band since the anamorphic demagnification has the largest value. Hence the $102 \mu\text{m}$ slit is used in the *K* band without appreciable loss of resolution while allowing a relatively larger amount of flux to be gathered. The resolving power of the spectrograph is ~ 1000 .

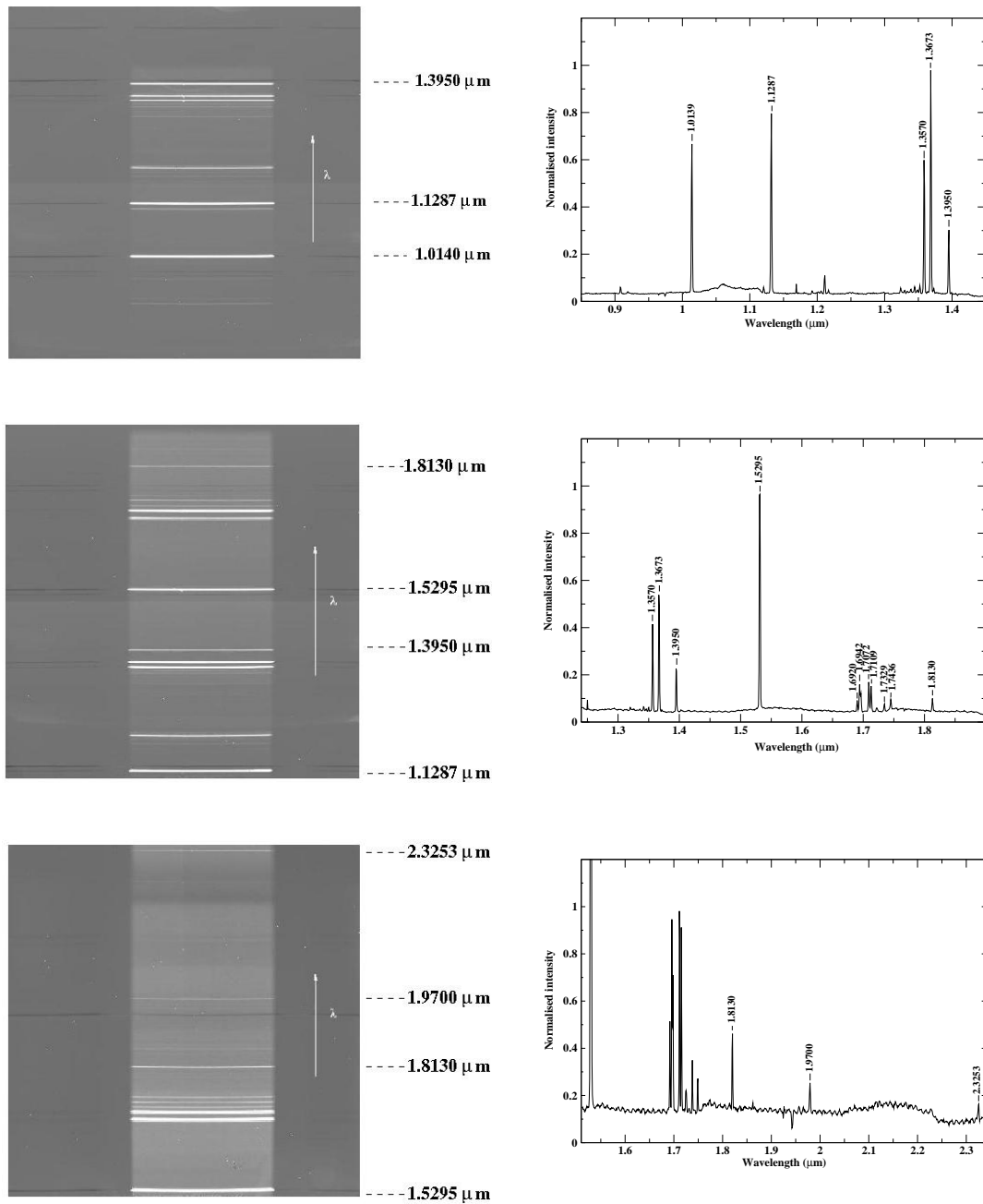


Figure 2.5: Spectral image (left side) & reduced spectra (right side) of Hg CFL spectra obtained in *IJ* (top panels), *JH* (middle panels) and *HK* (bottom panels) using NICS.

2.5.4 Detector Characteristics

This section describes the procedures followed for measuring the gain, read-out noise and linearity of the array.

2.5.4.1 Determination of Gain

The gain of the array is the ratio between the number of electrons recorded to the number of digital counts. The gain was measured by the following method in which two images were subtracted from one another at several illumination levels. For each intensity level, the following procedure was adopted.

Two images were obtained in succession at the same light level. The exposure was kept short (0.5 s) so that the dark counts are negligibly small. The mean signal level was measured in a chosen region of pixels on both the acquired images. The regions are chosen such that they are as small as 50×50 or 100×100 pixel² on both the images. The ratio of the mean signal levels of the regions is multiplied with one of the image so that the same signal level is maintained without affecting the noise structure. After subtracting these two images, the standard deviation over the already chosen region was determined. The level of illumination was varied while making the exposure time constant and the procedure was repeated. The slope determined from the photon transfer curve (PTC), which is a plot of the measured signal vs variance of the noise gives the gain of the detector. A different method of varying the exposure time with a constant illumination will also lead to the same result. Fig 2.6 represents the PTC curve of the HAWAII-1 array. The measured gain from the photon transfer curve was found to be $5 \text{ e}^-/\text{count}$.

2.5.4.2 Determination of read-out noise

The read-out noise was measured by subtracting two dark frames obtained at 0.5 s after removing the bad pixels. The resulting frame was found to have a mean count close to zero and a standard deviation (averaged over the entire frame of 1024×1024 pixels) of 6 to 7 counts per pixel. Since both the

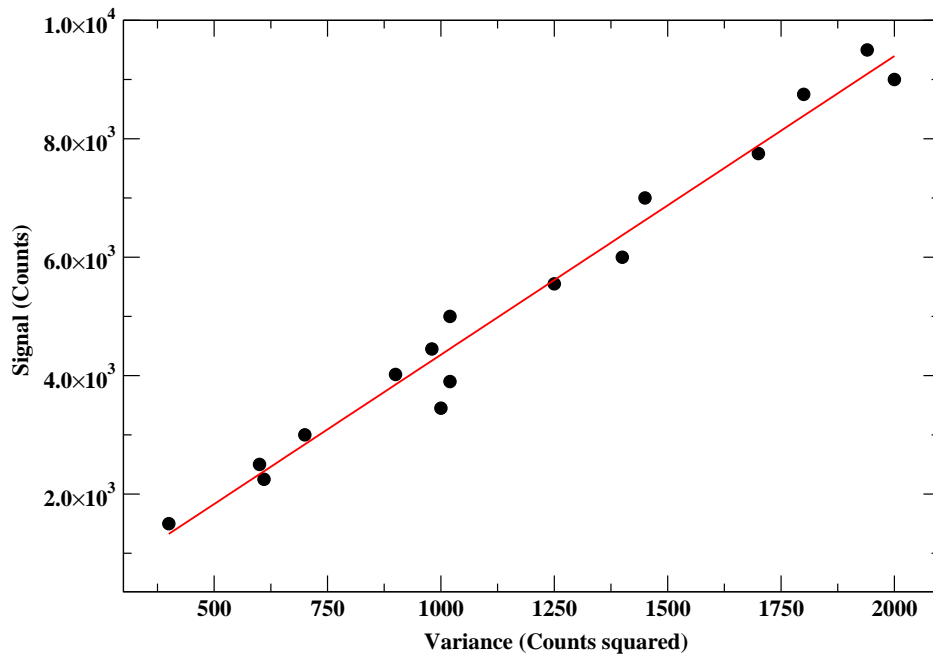


Figure 2.6: Photon transfer curve: The gain is equal to the slope which is measured to be close to $5 \text{ e}^-/\text{count}$

dark frames were taken using two reads (Em2 mode) having two readouts per frame, the observed standard deviation needs to be divided by $\sqrt{4}$. This gives an average readout noise of 3 to 3.5 counts. Since the gain is $5 \text{ e}^-/\text{count}$, the readout noise per pixel is approximately 15 to 18 electrons/pixel.

2.5.4.3 Linearity test

This test was conducted by illuminating a section of the telescope dome with a 100 W tungsten lamp and obtaining dome flats in the Ks filter at different integration times in integral values between 1 and 16 s. A set of 5 frames were obtained for each value of integration time. The median value of the counts of a particular frame was considered as a representative value of that frame. Fig 2.7 represents a plot of the median counts versus integration time. A linear fit shown as a red line reproduces the observed data between 2600 and 20000

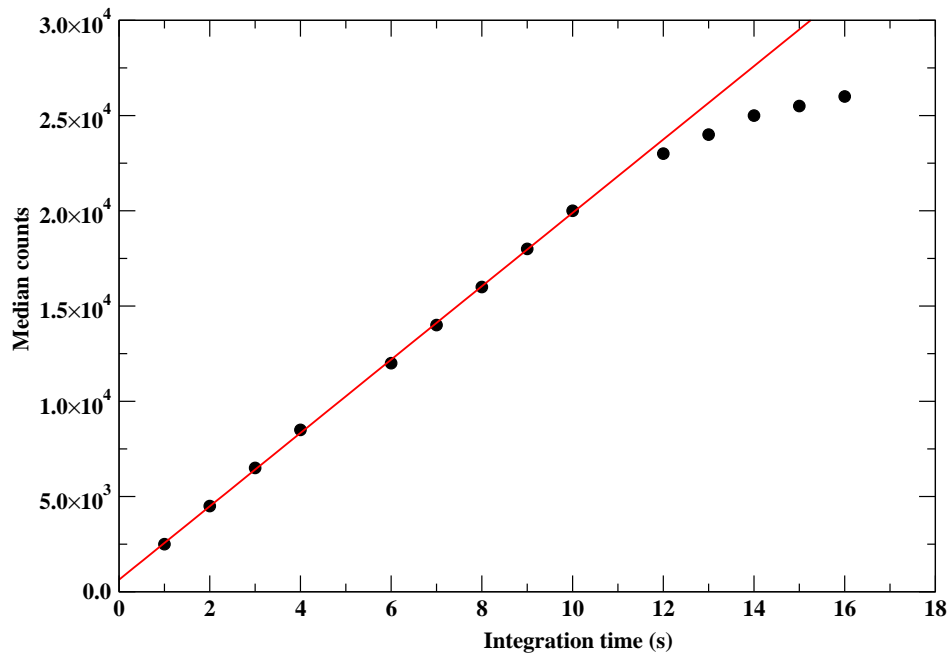


Figure 2.7: Response of the array to illumination. A linear response is seen up to approximately 20000 counts

counts. A deviation from linearity can be seen after 20000 counts.

The characteristics of the detector are summarised in Table 2.4.

2.6 Near-infrared Observations and data analysis

The large sky background due to the thermal continuum and OH line emission from the Earth's atmosphere contributes substantially at the NIR wavelengths. All these effects, which deteriorate the quality of observations, must be eliminated in order to obtain a proper image or spectrum of the source. Background subtraction thus remains an essential part of all IR observations. Dithered imaging is the most efficient method to take care of sky background issues with a minimum loss of observing time. By observing the same field

Table 2.4: Detector Characteristics of NICS

Array Format	1024 × 1024
Pixel size (μm)	18.5
Lower Cut-off λ (μm)	0.85
Upper Cut-off λ (μm)	2.50
QE @ 77 K, $2\mu\text{m}$	65
Dark current (e^-/s @ 77 K)	< 1.0
Read Noise (e^-)	15 - 18
Well Capacity (e^-)	1.3×10^5
Gain	5

on the sky with small offsets around a central position for each exposure, it is possible to measure the sky background variations. Care has been taken to ensure that these procedures have to be followed strictly while making both photometric and spectroscopic observations.

2.6.1 Photometric Observations

In all the observations included in this thesis, the images were obtained at six dithered positions in the *JHK* bands. The source was completely kept away from the field of view while acquiring the dithered frames. The nearest photometric standard star chosen from Hunt *et al.* (1998) was observed immediately after the source by following the same dithering procedures as done for the source. Several dark frames were obtained and median-combined to form a final dark frame for each exposure time. It is important to bear in mind that sky subtraction does not take care of the pixel to pixel QE variations. Therefore a flat field was applied after sky subtraction. Flat-field frames were acquired by observing the dome flat frames as described earlier. Since the telescope is focused to infinity, observing a dome flat illuminates the pixels uniformly and removes pixel to pixel QE variation. The data processing techniques are

described in section 2.6.3.

2.6.2 Spectroscopic Observations

Spectroscopic observations were made in the *JHK* bands by dithering the object to two spatial positions along the slit. The exposure times were kept constant during the two nod positions. The background subtraction (sky + dark) was accomplished by subtracting the images from each other. The atmospheric transmission is not uniform over the entire spectral region of 1-2.5 μm and varies with wavelength. To correct for this variation it is necessary to observe a standard star. Generally a spectral standard star of type AOV is chosen because the spectra of such a star shows a featureless continuum, except for the presence of prominent absorptions of HI which can be easily removed later.

2.6.3 NIR data reduction

The observed NIR data was analysed using Image Reduction and Analysis Facility (IRAF) developed at National Optical Astronomy Observatories (NOAO), USA.

2.6.3.1 Photometric data reduction

Photometry refers to measurement of flux over broad wavelength band of radiation. The obtained data were reduced to derive the *JHK* magnitudes using IRAF. The aperture photometry task was used for sources that were isolated i.e. without any close neighbours. The Point Spread Function (PSF) photometry task was used for crowded fields.

An average frame was generated from each set of images observed at the source and dithered positions. This process improves the S/N ratio in the average frame. Various sets of dithered sky frames were median combined so that the final sky frame was devoid of field stars. The sky background was removed by subtracting the averaged source frame from the median combined

sky frame. Similarly, the multiple images of dome flats and dark frames were also median combined. The final background subtracted image was obtained by

$$FinalFrame = \frac{SourceFrame - SkyFrame}{FlatFrame - DarkFrame} \quad (2.5)$$

The same method of background subtraction was performed for the standard star. These frames were used to determine the instrumental magnitude of the source and standard star. Aperture photometry was performed using the available tasks in the IRAF APPHOT package. The DAOPHOT package in IRAF was used for locating objects, fitting point spread functions, subtracting stars and performing photometry.

2.6.3.2 Spectroscopic data reduction

The spectra were extracted using the APEXTRACT package in IRAF. The sky background was removed by subtracting the frames observed with star shifted along the slit. The APALL task was used to extract one dimensional spectra from the background subtracted images. The calibration of the *JHK* spectra were done using the OH sky emission lines that register along with the stellar spectra. The Paschen and Brackett series lines were manually removed from the spectra of the standard star and the resulting spectra were ratioed with the source spectra to remove telluric absorption features. The ratioed spectra were then multiplied by a blackbody spectrum at the effective temperature, corresponding to the standard star, to obtain the final calibrated spectra.

2.7 Infrared Space Observatory

The ISO was launched on 17 November 1995 into a highly elliptical geocentric orbit by European Space Agency (ESA). The ISO telescope consists of a 60 cm diameter primary mirror, cooled to 1.7 K. The ISO satellite contains four instruments in which two are for photometry from 2.5 to 240 μm and the

other two are for spectroscopy from 2.5 to 196.8 μm . The four scientific instruments on board ISO are the Infrared Camera (ISOCAM), Photo-polarimeter (ISOPHOT), Short Wave Spectrometer (SWS) and the Long Wave Spectrometer (LWS). The ISOCAM and ISOPHOT are high-resolution cameras covering the range 2.5 to 17 and 2.4 to 240 μm , respectively. The SWS operates between the wavelengths 2.38 and 45.2 μm with two nearly independent grating spectrometers having a spectral resolution ranging from 1000 to 2000 (de Graauw *et al.*, 1996). The LWS provides a wavelength coverage in the range 47-196 μm . It uses a grating in tandem with a Fabry-Perot interferometer to make medium ($\lambda/\Delta\lambda \sim 200$) and high ($\lambda/\Delta\lambda \sim 10000$) resolution spectroscopic observations (Clegg *et al.*, 1996).

2.7.1 ISO SWS data reduction

The three types of data products provided by ISO are Raw data products, Basic Science data products and Fully Auto-processed Science data products. Raw Data products are essentially unpacked telemetry in which no data reduction has taken place. Basic Science data products have been processed further to an intermediate level (with the use of calibration files where necessary), often containing physical units. The fully auto-processed science data products data contain a set of coherent data that are produced by an automatic pipeline that produces results very close to those obtained otherwise from a step by step analysis using Basic Science data products. There are also Highly Processed Data Products (HPDP) that are the result of further processing beyond the pipeline and/or using new, refined algorithms. The data presented in this thesis use Fully Auto-processed Science data products and Highly Processed Data Products (HPDP) by Sloan *et al.* (2003).

Fully Auto-processed Science data products were reduced using ISO Spectral Analysis Package (ISAP), whose primary function was to simplify the process of visualizing, subsetting, shifting, rebinning, masking, combining scans with weighted means or medians, filtering, and smoothing the Auto Analysis Results (AAR).

2.8 *Spitzer* Space Observatory

The SST, was launched on August 25, 2003 in a Earth-trailing solar orbit. The *Spitzer* telescope consists of a 85 cm diameter primary mirror cooled and maintained at 5.5 K. The three IR scientific instruments, the IRAC, the IRS and the Multiband Infrared Photometer for *Spitzer* (MIPS) share a common focal plane. IRAC is a four-channel camera that obtains simultaneous broadband images at 3.6, 4.5, 5.8, and 8.0 μm . Channels 1 (3.6 μm) and 2 (4.5 μm) use InSb detector arrays that operate at a temperature of 15 K, and channels 3 (5.8 μm) and 4 (8.0 μm) use Si:As detectors that operate at 6 K. Both the array types are 256×256 pixels in size and have the physical pixel size of 30 μm . MIPS provides photometry in the three wavelength bands centered near 24, 70 and 160 μm .

IRS has four separate modules, known by their wavelength coverage and resolution as Short-Low (SL), Short-High (SH), Long-Low (LL) and Long-High (LH). It operates in the wavelength range between 5.3 to 38 μm with spectral resolving power, $R = \lambda/\Delta\lambda \approx$ ranging from 60 to 120 for SL and LL modules. The SH and LH modules operate in the wavelength region of 9.89 to 37.14 with a spectral resolving power of 600. The details of the spectrograph are described in Houck *et al.* (2004).

2.8.1 *Spitzer* archival data and analysis

The IRS has two modes of operation, the spectral "staring" and "mapping" modes. In the staring mode, science targets were placed on one or more of the IRS slits for a specified integration time. The spectral mapping mode allowed an observer to configure a grid of map positions around a central target position and obtain spectra at each position. All the observations presented in thesis are in the "staring" mode.

The IRS data products are organised into three categories: Raw Data, Basic Calibrated Data (BCD), Post-BCD (PBCD). The Raw data consist of the raw detector sample images, with some descriptive information in the FITS file

header. The BCD files were the fundamental basis for science analysis, with the primary product being a two-dimensional slope image of each Data collection event (DCE) in units of electrons $\text{s}^{-1} \text{ pixel}^{-1}$, accompanied by a header containing the essential programmatic information and the processing, calibration, and pointing history. Additional BCD data files include uncertainty images that accompany each slope image. The BCD also include co-added image data for those observations with more than one ramp at a sky location. The BCD (also called Level 1) files were used for the data analysis of SL and LL spectra. The primary products that were formed by combining individual BCDs are called PBCD (Level 2) data. PBCD data were used for SH and LH spectra.

Spectroscopic Modeling Analysis and Reduction Tool (SMART) was used to reduce and analyze IRS data from the *Spitzer* data archive. SMART was designed to operate on the BCD delivered by the *Spitzer* Science Centre (SSC). SMART was used to extract spectra for sources having low resolution observations. The extraction routines include column extraction of a point source scaled to the instrumental PSF, fixed-aperture extraction for extended sources and a weighted Gaussian for point sources.

The *Spitzer* IRS Custom Extraction (SPICE) software is a JAVA-based tool used to extract spectra from the PBCD data sets. SPICE was used to extract spectra for sources having high resolution observations. SPICE offers two extraction algorithms: "regular" and "optimal". The regular algorithm works well for bright point sources while the optimal extraction algorithm is especially suited for faint point sources as it weights the extraction by the instrumental PSF and S/N ratio of each pixel.

Chapter 3

Infrared study of V1647

Ori and five other eruptive young stellar objects

3.1 Introduction

V1647 Ori is a young eruptive variable star known to be the illuminating source of McNeil's object, a reflecting nebula discovered by the amateur astronomer J.W. McNeil on January 23, 2004 (McNeil, Reipurth and Meech, 2004). This offered a rare opportunity to study phenomena accompanying the eruption of a low-mass pre-mainsequence star. The star brightened by ~ 4.5 mag in the I_c band in a period of 3 months (Briceño *et al.*, 2004), until it reached a peak brightness in early 2004. In February 2004, 4 months after the onset of the outburst (during November 2003), the rise of the brightness stopped and the magnitude remained (relatively) constant. The object stayed in the high state for about 2 years, then started a rapid fading in October 2005 (Kospal *et al.*, 2005). Already during 1966 - 67, it may be noted that V1647 Ori exhibited a similar eruption (Aspin *et al.*, 2006). The outbursting star V1647 Ori is located in the vicinity of the T Tauri star LkH α 301 and Herbig-

Haro object HH22. These outbursts are thought to be a consequence of a sudden and steep increase of the mass accretion rate onto the central low-mass pre-mainsequence star (Hartmann and Kenyon, 1996). The optical and NIR spectra of V1647 Ori are characterized by various emission lines with the continuum showing a positive slope, thus depicting a red energy distribution. Following the discovery of the outburst by McNeil, Reipurth and Meech (2004), the brightness evolution at the NIR wavelengths was monitored by Reipurth and Aspin (2004a); McGehee *et al.* (2004) and Ojha *et al.* (2005, 2006). The optical/NIR spectrum, and its changes were studied by Vacca, Cushing and Simon (2004); Walter *et al.* (2004); Andrews, Rothberg and Simon (2004); Rettig *et al.* (2005); Ojha *et al.* (2006) and Gibb *et al.* (2006). Based on the observed spectral signatures they classified it to be an EXor class of eruptive variable. The X-ray emissions from the star during the outburst were studied by Kastner *et al.* (2004); Grosso *et al.* (2005) and Kastner *et al.* (2006). The physical processes causing the outburst and their influence on the structure of the circumstellar matter were studied by Muzerolle *et al.* (2005) and Rettig *et al.* (2005). All these studies revealed V1647 Ori to be a deeply embedded low-mass pre-mainsequence object surrounded by a disk and envelope. They also indicate the increased disk accretion to be the cause of the outburst which is accompanied by strong stellar wind.

However, rather unexpectedly, in 2008, V1647 Ori underwent a second outburst phase by increasing the optical brightness by ~ 5 mags (Kun, 2008) and NIR brightness by ~ 3 mags (Venkat and Anandarao, 2008; Aspin *et al.*, 2009). Observations taken during the second (2008) and on-going outburst showed nearly identical morphological features and photometric brightness similar to the earlier event at the optical and NIR wavelengths. The NIR spectra during the more recent (2008) outburst possess Br γ in emission along with a very weak CO overtone bandhead absorption in contrast to the strong bandhead emission seen soon after the 2003 event (Aspin *et al.*, 2009). Also, water vapor absorption bands were observed to be much stronger than the previous outburst. Teets *et al.* (2011) found that V1647 Ori was very active during

September 2008 to April 2009 with the X-ray flux varying between 2 and 8×10^{30} ergs s⁻¹ on a short time scale of 8 months. Also during 2002 to 2009, Teets *et al.* (2011) found that the X-ray flux from V1647 Ori was correlated with its optical and NIR outbursts that are driven by the enhanced disk accretion. Reipurth and Aspin (2004a) described the variations in the NIR colours of V1647 Ori along the reddening path as the combined effect of its intrinsic brightening and the clearing away of the circumstellar matter along the line of sight. Using high resolution NIR spectroscopy, Brittain *et al.* (2010) showed that the accretion rates derived from Br γ emission were similar during the two outbursts and a factor of ~ 16 higher than the smallest accretion rate during the quiescent phase. While the duration of its outburst during the 2004 outburst which lasted for 18 months was similar to EXors, the object's spectral characteristics seemed to be so different from EXors that it may as well be a new class in itself (Kun, 2008). Thus, the current (ongoing) outburst is basically different from the earlier one and merits further investigations. Clearly, therefore, continued monitoring of the object is necessary to detect possible changes in its behavior. Here we present the results from a continuous monitoring of the object during the period 2004 to 2012 including the previous outburst during January, 2004 and October, 2005 and the on-going outburst since August, 2008 flanking the brief period of quiescence between February, 2006 to July, 2008. In order to investigate the similarities in the photometric and spectroscopic properties of V1647 Ori with other known young stellar eruptive variables, we have additionally observed another set of five eruptive young stellar sources.

3.2 Observations and data reduction

NIR photometric and spectroscopic observations were made using the 1.2 m telescope at Mt.Abu, operated by PRL. Mid-IR spectroscopic data were obtained from the *Spitzer* public data archive.

3.2.1 Near-infrared Photometric & Spectroscopic Observations

NIR photometric observations of V1647 Ori were made in the *JHK* photometric bands using the NICMOS and the NICS, mounted at the Cassegrain focus of the PRL's 1.2 m IR telescope situated at Mt.Abu. The data consist of more than 40 sets of photometric observations during the period 2004 - 2012, a majority of which were made during the period 2008 - 2012. Single frame integration times used were 40 - 60 s/20 - 30 s for *J*, 20 - 40 s/10-20 s for *H* and 2 s/10 - 15 s for *K* band with the NICMOS/NICS cameras. Several such frames were taken, amounting to total integration times of 120 - 720 s for NICMOS and 120 - 400 s for NICS. A sufficient number of dithered frames were also obtained for effective background subtraction and flat fielding. The seeing during the observations was typically 1.7'' - 2.5''. Photometric flux calibration was done by observing a standard star in the AS 13 region (Hunt *et al.*, 1998). The magnitudes of extended sources such as HH22 were also estimated using a larger sampling aperture (usually four times the FWHM of a star image). The integrated magnitude of the nebula surrounding V1647 Ori was estimated from the images after the star was subtracted using a 40'' aperture.

Spectroscopic observations at a spectral resolving power of ~ 1000 were made in the *K* and *JHK* bands using NICMOS and NICS arrays respectively. The spectroscopic standard star SAO 94426 of A0V type was observed at a similar airmass as the programme star V1647 Ori to remove the telluric absorptions. The integration time for the programme and standard stars are 60 and 25 s per frame respectively. The star was dithered at two positions along the slit. Four frames of the same integration time were acquired at each position of the star along the slit.

Photometric and spectroscopic data acquisition and data reduction procedures using IRAF have been described in Chapter 2. The strength of the spectral features are measured in terms of its equivalent width (EW), defined as the width (in wavelength units) of a rectangular strip of spectrum having

the same area as the spectral line.

3.2.2 *Spitzer* archival Spectroscopic data

Mid-IR spectra were obtained by reducing the data from the *Spitzer* public data archive. The BCD data products from the IRS on board *Spitzer* Space Telescope were reduced using SMART. Multi-epoch spectroscopic data of V1647 Ori during October 21, 2004 and March 11 & 24, 2005 within a span of six months during the 2004 outburst were obtained from the data archive. These data sets during October 21, 2004 and March 24, 2005 contained observations in the SL, SH and LH channels while on March 11, 2005 contained only SL and LL channels (see Chapter 2 for the definitions of these channels).

3.3 Results and Discussion

3.3.1 Near Infra-red photometry

The Table A.1 in Appendix A gives the *JHK* magnitudes and colors of V1647 Ori for all the dates of our observations. The photometric errors are typically between 0.02 to 0.05 magnitudes. For the on-going 2008 outburst period (observations from November 2008 till November 2012), the average magnitudes with standard deviation (σ) for 29 data sets are: 10.85 (0.17); 9.02 (0.18); 7.60 (0.24) for the *J*, *H*, and *K* bands respectively. Occasional deviations of more than 3σ due to variability of object were noticed in all the three bands. For the 2004 outburst period (observations from March 2004 till December 2004) the averages for 7 data sets are: 11.01 (0.16); 9.06 (0.17); 7.73 (0.15) for the *J*, *H*, and *K* bands respectively; the deviations were within 2σ . For the quiescent phase during 2006-2007 (observations from December 2005 till December 2006), the averages for 8 data sets are : 14.2 (0.18); 11.61 (0.14); 9.89 (0.18) for the *J*, *H*, and *K* bands respectively; the occasional deviations seen were within 2σ . Thus, the on-going outburst shows higher amplitude fluctuations in brightness especially in *K* band (more than 0.5 mag) than the 2004 - 2005

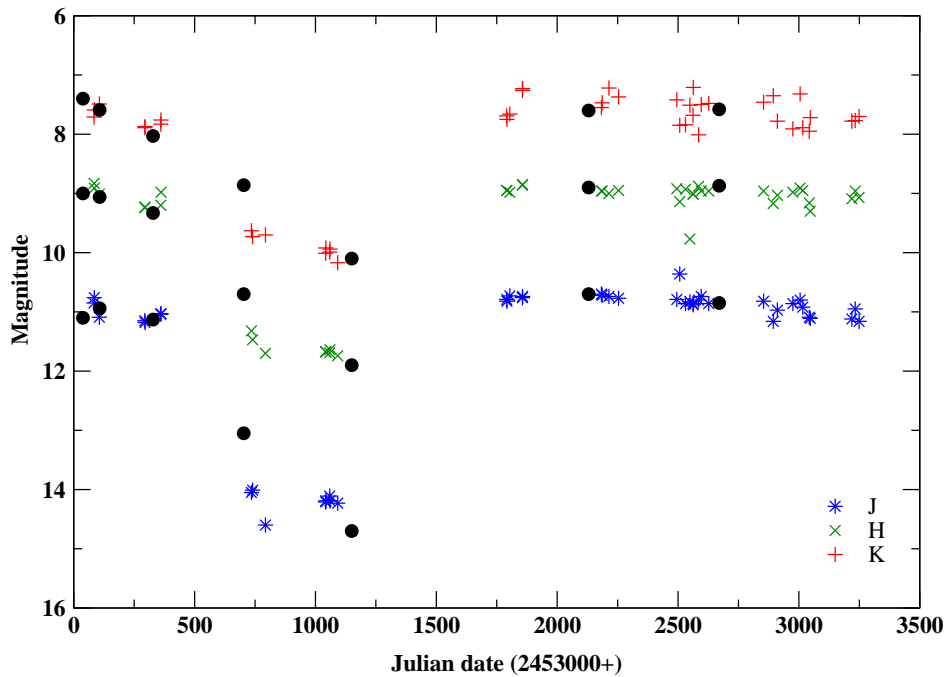


Figure 3.1: V1647 Ori: Light Curves in the J , H , K bands from Mt Abu observations during 2004-2012 covering the two outbursts with the ~ 2 yr quiescence in between. The blue asterisks represent the J band, green crosses represent the H band and red pluses represent the K band. Observations made elsewhere are shown in black filled circles (see text for references).

outburst. The light curves in the J , H and K bands are shown in Fig 3.1 covering the period between 2004 - 2012. For comparison, a few data points from other published work are also shown (from McGehee *et al.* (2004); Ojha *et al.* (2006); Acosta-Pulido *et al.* (2007); Aspin (2011)). It may be mentioned here that Acosta-Pulido *et al.* (2007) reported a 56 day periodic component in their optical light curves in the visible bands. Our JHK data do not show this component.

Trend of decline of outburst phase since early 2012:

In comparison with its behavior till 2011 (e.g., Venkat and Anandarao

(2011)), the object seems to show a steady decline in the brightness beginning from February to March 2012 (cf. Semkov and Peneva (2012) & Ninan *et al.* (2013)) with an approximate rate of 0.16, 0.06, 0.18 mag per year in the *JHK* bands respectively (see Fig 3.1). It is necessary to confirm this declining trend

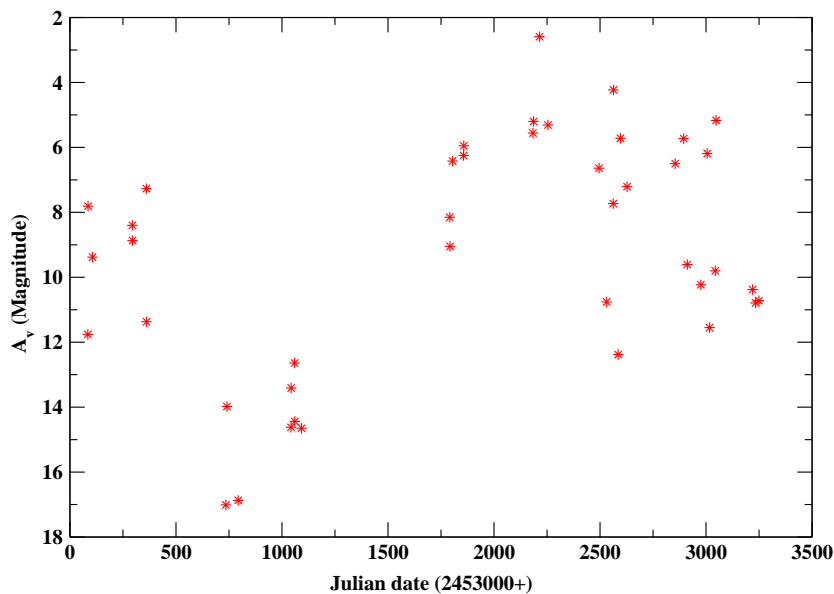


Figure 3.2: V1647 Ori: Time variation of A_V from Mt Abu observations during 2004-2012 comprising of two outbursts flanking the quiescent epoch (of larger extinction).

by continued monitoring. The slow decline compared to the one noticed after the 2004 outburst is reminiscent of a typical FUors light curve. However, it is premature to conclude that it is a FUor, as there have been spectroscopic indications to the contrary. In fact it could be a class in itself which shows both FUor and EXor characteristic features (see Kun (2008)).

We have computed the visual extinction A_V from the colors $[J - H]$ and $[H - K]$ for both the epochs, using an empirical formula derived from Meyer, Calvet and Hillenbrand (1997) and the extinction model of Bessell and Brett

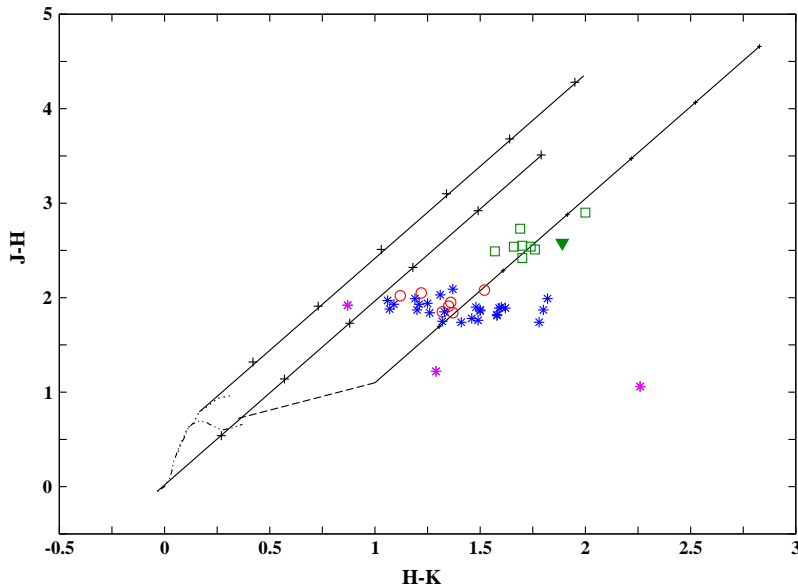


Figure 3.3: V1647 Ori: Color-color diagram from Mt Abu observations. The 2MASS value is marked as inverted green triangle (corresponding to October 7, 1998). The blue asterisks correspond to the on-going outburst period 2008 - 2012; while the red circles correspond to the outburst period of 2004 - 2005. The green squares are for the quiescent epoch of 2006 - 2007. The three "stray" magenta asterisks, two appearing around $J - H \sim 1.0$ and the one appearing around $H - K \sim 0.8$ correspond to extremities in photometric magnitudes observed in our monitoring. See text for discussion. The dot-dashed curve represents the unreddened main-sequence stars; the dotted curve shows the unreddened giant stars. The black slanting parallel lines indicate the extinction vectors for $A_V = 30$ mag (Bessell and Brett (1988) extinction law was adopted). The pluses along the extinction vector correspond to an extinction interval of $A_V = 5$ mag. The T Tauri stars fall on the black dashed straight line, adopted from Meyer, Calvet and Hillenbrand (1997).

(1988)

$$A_V = 13.83 \times [J - H] - 8.02 \times [H - K] - 7.19 \quad (3.1)$$

The computed A_V values are listed in Table A.1. For comparison, the A_V corresponding to 2MASS epoch (quiescent on October 7, 1998) is 13.3. The

time evolution of A_V is shown in Fig 3.2. We find that there is ~ 6 mag difference in A_V between the two phases, with the outburst phase having a lower extinction. This can be attributed to the excess mass accreted by the envelope (from the environment) during the quiescent phase in comparison with the outburst phase during which the disk accretion (from the envelope) is expected to dominate (e.g. Aspin, Beck and Reipurth (2008) and Aspin (2011)). During the on-going outburst post-2008, the extinction varies quite significantly in comparison to the 2004 outburst. A JHK color-color diagram constructed from Mt Abu data during 2004-2012 is shown in Fig 3.3. The A_V values computed using Eqn. 3.1 are in reasonable agreement (within 1 - 2 mag) with those obtained by de-reddening the JHK colors to the T Tauri locus in the color-color diagram.

The color-color diagram demonstrates the variable nature of the source in the on-going 2008 outburst phase in comparison with the 2004 outburst. The region occupied by the latest outburst (asterisks in Fig 3.3) extends horizontally (i.e., with $[J - H] \sim 1.7 - 2.0$) beyond the T Tauri region; quite in contrast with the 2004 outburst phase (open circles). This tendency during the on-going outburst indicates the presence of cold dust in the envelope/disk of the star compared to the 2004 outburst. Also, we found at least two occasions (in November 7, 2010 & December 19, 2010) during which the colors showed extreme values - as indicated by the magenta asterisks in Fig 3.3 at around $[J - H] \sim 1.0-1.2$, with $[H - K]$ at 1.3 and 2.3. On another occasion (January 24, 2011) the colors indicate a position to the left of the T Tauri region. The A_V could not be calculated for these cases falling well beyond the T Tauri regime (shown as dashes in Table A.1). We suspect that such extreme fluctuations may be of short duration (a few days) and may be attributed to circumstellar dust temperature variation.

3.3.2 Spectroscopic Variations

Figs 3.4 and 3.5 show the multi-epoch NIR spectra of V1647 Ori showing its variable nature during the recent (2008) outburst. Spectral variability in the

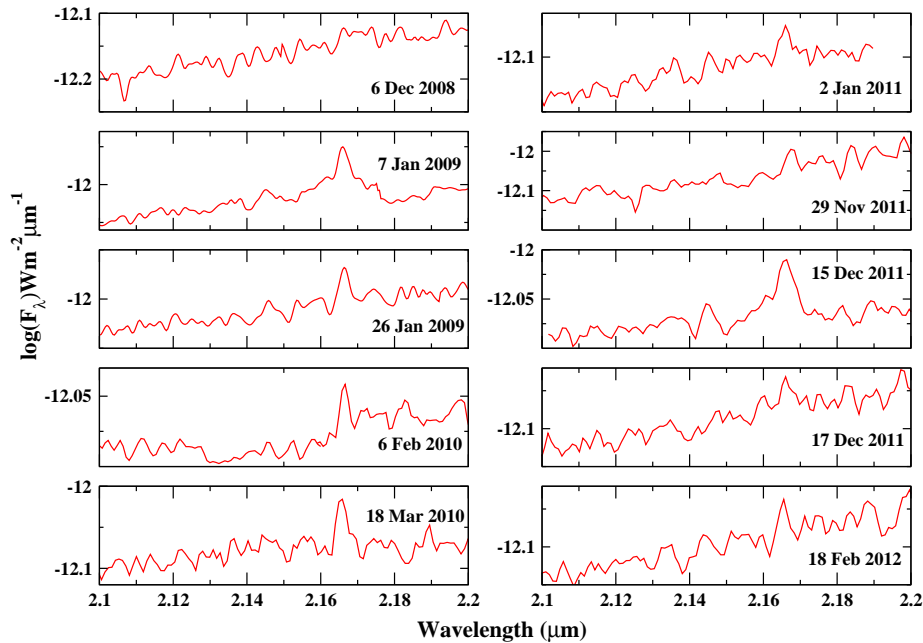


Figure 3.4: V1647 Ori: Br γ line (at $2.16 \mu\text{m}$) in the K band observed using NICMOS on a few occasions at Mt Abu. Variability is evident.

Br γ line due to variable disk accretion rates is shown in Fig 3.4. The Br γ line shows a fluctuating trend that does not seem to be associated with photometric fluctuations (cf. H α line reported by Walter *et al.* (2004) and Aspin and Reipurth (2009)). Fig 3.5 represents the spectra of V1647 Ori obtained during March 20, 2014 and December 5, 2014 using NICS nearly two years after the last observation in Fig 3.4. The NIR spectra observed on December 5, 2014 show the onset of CO emissions in its first and second overtone bands. This may be due to increase in the disk surface temperature triggered by the irradiation from the central star (Calvet, Hartmann and Kenyon, 1991). It may be noted that the width at zero-intensity and the ratio of peak to continuum intensity in Mt. Abu profiles are in reasonable agreement with those of Brittain *et al.* (2010) for the year 2009, in spite of the large differences in the resolving power employed and S/N values between the two observations. The

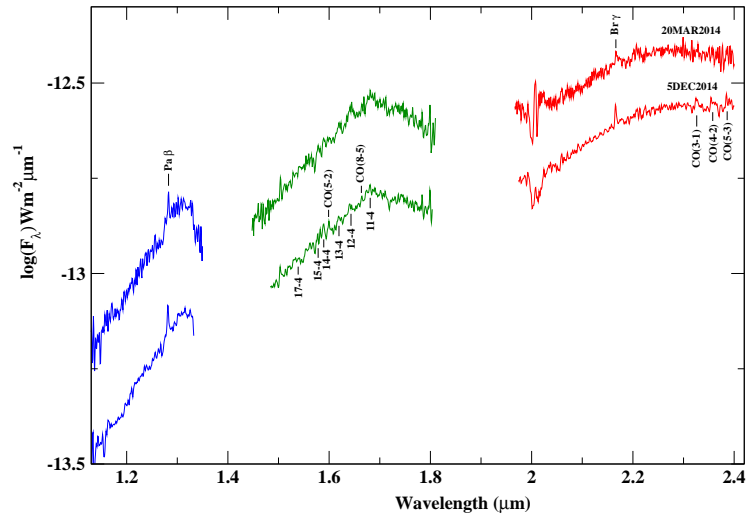


Figure 3.5: NICS spectra of V1647 Ori observed during March 20, 2014 & December 5, 2014. The variability in the Br γ line is clearly evident.

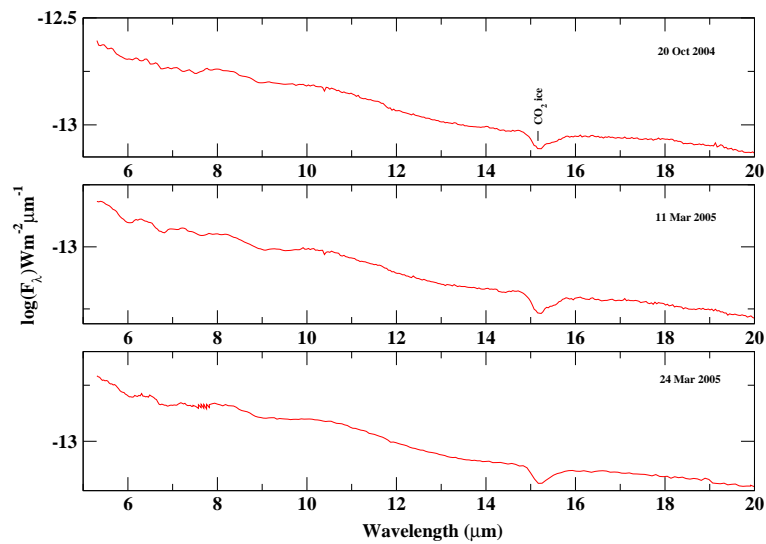


Figure 3.6: Multi epoch *Spitzer* spectra of V1647 Ori. The silicate emission at 10 μm and absorption at 15.2 μm due to CO_2 ice are clearly evident.

accretion luminosities and disk accretion rates derived from the dereddened Br γ line fluxes from our spectra (following the procedure described by Muzerolle, Hartmann and Calvet (1998)) range from 20 - 60 L_{\odot} and 1.0×10^{-6} to 3.0×10^{-6} $M_{\odot} \text{ yr}^{-1}$ respectively which are comparable with those reported by Brittain *et al.* (2010).

Figure 3.6 represents the multi-epoch mid-IR spectra of V1647 Ori observed during the 2004 outburst. Using these spectra Quanz *et al.* (2007) had reported 10 μm silicate emission from the surface layers of the accretion disk with variability in the overall flux levels. However, they did not notice any change in the overall shape of the spectral features during this period. Based on the observed absorption profile at 15.2 μm due to CO_2 ice they concluded its origin to be from cold foreground material that cause huge extinction along the line of sight, rather than by ice processing due to heating effects in the circumstellar disk/envelope. The EW of the 15.2 μm absorption feature was found to change within the period of ~ 6 months between the *Spitzer* IRS observations. If the absorption feature is indeed due to the foreground material then the variation in the EW is not expected during this period. Also the high resolution IRS *Spitzer* spectra observed on October 20, 2004 & March 11, 2005 showed double peaked sub-structure in the 15.2 μm profile that may be caused by the crystallization and effective segregation of the CO_2 and H_2O ice. This suggest the possibility of V1647 Ori being located within an icy envelope thus depicting its highly embedded nature. Aspin, Beck and Reipurth (2008) reported silicate absorption in V1647 Ori during the 2006 quiescent phase. This implies significant dust evolution over the period between 2004 to 2007.

3.3.3 Variations in HH22 and the nebula around V1647 Ori

The deep [SII] imaging of Herbig-Haro (HH) objects by Eisloffel and Mundt (1997) reveal V1647Ori and parts of the nebula in the vicinity of the Herbig-Haro objects HH22 and HH23. Fig 3.7 shows a *JHK* color composite image of

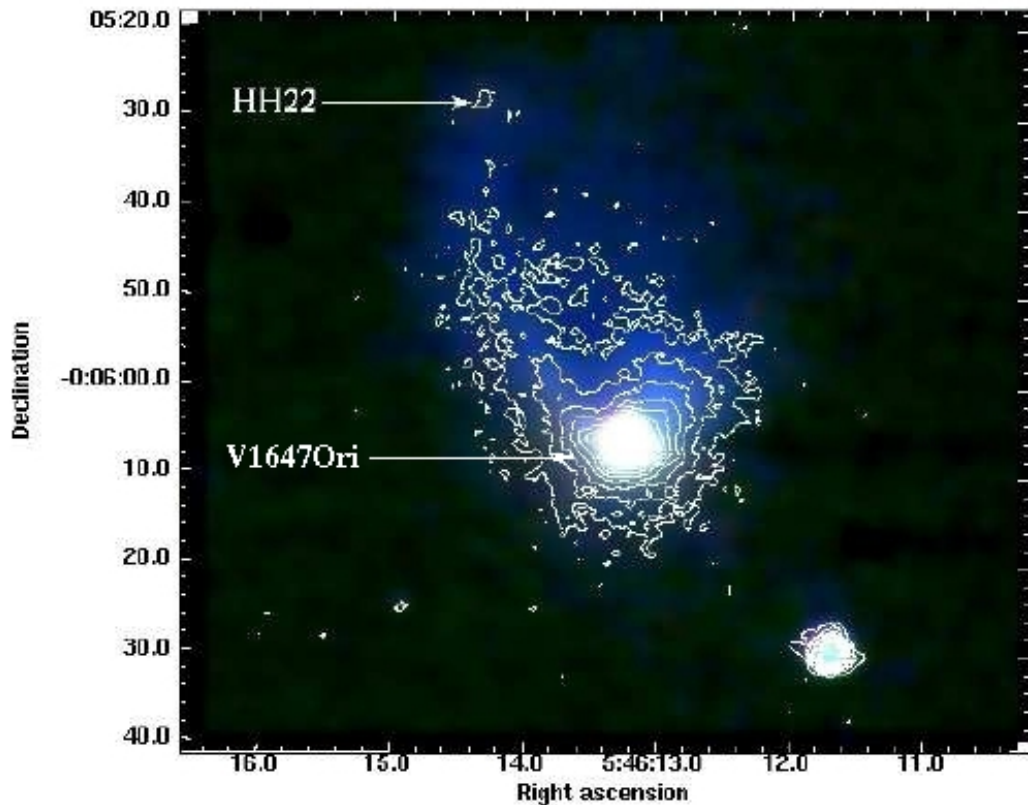


Figure 3.7: Color composite image of V1647 Ori and the surrounding McNeil's nebula in the J (blue), H (green) and K (red) bands taken at Mt Abu using NICS on February 4, 2011; HH22 is seen at nearly the north of V1647 Ori. The H Band contours (in white) are shown superposed on the image: the outermost contour is $20 \text{ mag arcsec}^{-2}$ with each contour brightening by $2 \text{ mag arcsec}^{-2}$ inwards.

V1647 Ori and its associated nebula taken from Mt Abu on February 4, 2011 using the NICS. Superposed on the image are the contours of iso-magnitudes in H band. The curved tail at the top left part of the nebular object is usually attributed to the on-going accretion (cf. Reipurth and Aspin (2004a)). HH22 (knot A in Eisloffel and Mundt (1997)) seen nearly to the north of V1647 Ori (see Fig 3.7), is a Herbig-Haro type object (for its mid-IR counterpart, see Muzerolle *et al.* (2005)). It happens to be present very close to V1647 Ori ($30''$ of separation at an assumed distance of 0.40 kpc) and its originating source is not yet identified. It could possibly be a reflection nebulosity powered by V1647 Ori (see, Briceño *et al.* (2004) and Aspin, Beck and Reipurth (2008)).

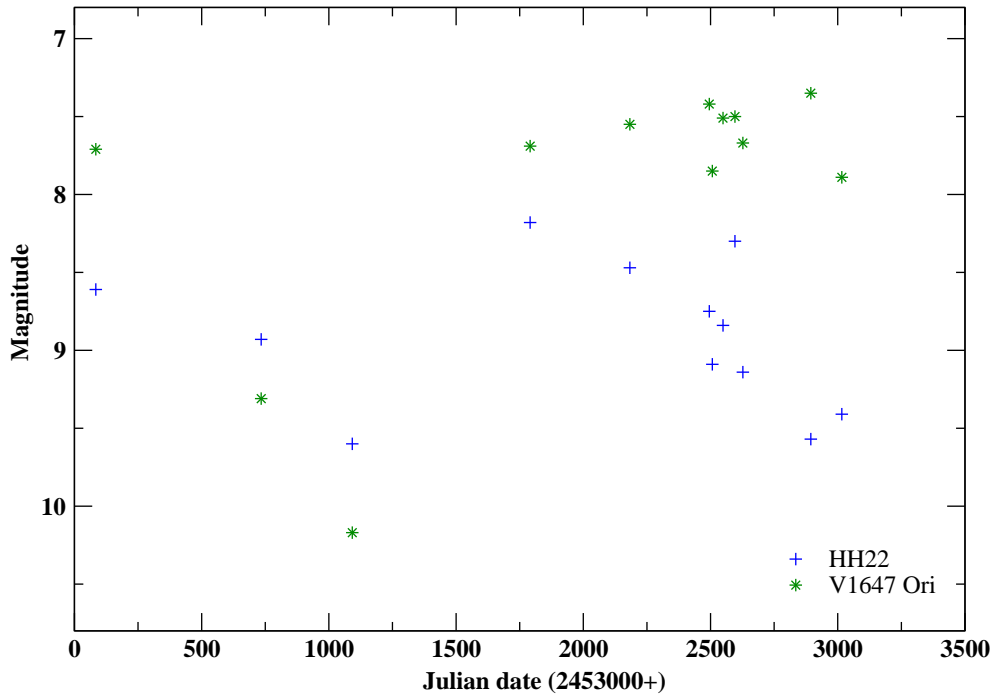


Figure 3.8: Time variations of V1647 Ori in the K band seen against those in HH22. The green asterisks correspond to V1647 Ori and blue pluses represent HH22. For HH22 the magnitudes are made brighter by subtracting 5 to facilitate a closer comparison.

It may be expected therefore that the outburst from V1647 Ori could cause the nebulosity to show a corresponding brightening. The light travel time from the young stellar object (YSO) to HH22 is ~ 70 days. We therefore analyzed the images in JHK bands obtained from Mt Abu to see if HH22 shows any variability in its brightness. Fig 3.8 shows integrated K magnitude of HH22 with time along with V1647 Ori magnitudes. The plot indicates a possible correspondence of HH22 (knot A) with the outburst activity; as well as indication of trigger from even short term fluctuations from V1647 Ori. We also noticed fluctuations in the brightness of the nebula around V1647 Ori which typically follow those of V1647 Ori itself. Similar fluctuations were also

noticed in the J and H bands.

3.3.4 Modeling of Spectral Energy Distribution

Modeling of SEDs provides important inputs on various physical parameters of the source. For this purpose, three sets of photometric data on V1647 Ori were considered: during (i) the outburst phase 2004 - 2005; (ii) the quiescent phase 2006 - 2007 and (iii) the second (on-going) outburst phase 2008 - 2012. For each of these three phases the mean values of Mt Abu JHK magnitudes were considered. To the JHK data we added the visible, mid-IR, far-IR and mm-wave data during the quiescent and outburst epochs taken from Andrews, Rothberg and Simon (2004) and Aspin, Beck and Reipurth (2008). The SEDs given in Aspin, Beck and Reipurth (2008) for the outburst and quiescent phases show that the fluxes of the pre-mainsequence star in sub-mm and mm regions did not change more than 10% between the two phases. It is in the visible and IR that a substantial change had taken place. The NIR region occurs right at the position of turn-over in the SED and hence is quite important. It was assumed that the small photometric variations if present, in the mid-IR and far-IR, are not significant in each phase.

We used an on-line modeling tool developed by Robitaille *et al.* (2007). Using this tool, several authors have successfully modeled T Tauri stars and massive protostars with masses up to $25 M_{\odot}$ (e.g., Kumar Dewangan and Anandarao (2010)). The SED modeling tool consists of a central pre-mainsequence source associated with rotationally flattened envelope, different combinations of axisymmetric flared accretion disk, with bipolar cavities all under radiative equilibrium. The input parameters include, apart from a minimum of three data points in SED and their corresponding errors, a range of distances to the object and the visual extinction. The output parameters fall into three categories: the central source parameters (stellar mass, radius, and temperature), the infalling envelope parameters (the envelope mass accretion rate, outer radius, inner radius, cavity opening angle and cavity density) and disk parameters (disk mass, accretion rate, outer radius, inner radius, flaring power,

and scale height). The stellar masses M_* are varied between 0.1 and 50 M_\odot . The on-line tool selects the best-fit solutions from 20,000 models (each with 10 different angles of inclination for the accretion disk, making a total of 200,000 models).

The tool finds the best fit model along with a group of models that are interpolated to different apertures at different wavelengths depending upon the beam sizes. In order to minimize the degeneracy of solutions, only those solutions that satisfy the criterion

$$\chi^2 - \chi_{best}^2 < 3 \quad (3.2)$$

are chosen with χ^2 considered per data point (see Robitaille *et al.* (2006)). Further, in order to avoid ‘over-interpretation’ of SEDs, we provided a small range of visual extinction values (from the *JHK* photometry) for each phase, to account for the inherent uncertainties in their determination. In the present case, a distance of 0.40 kpc is adopted (from Anthony-Twarog (1982)). The best fit models are displayed in Fig 3.9 along with the observed data (open circles) for the quiescent phase of 2006 - 2007 and the on-going outburst phase of 2008 - 2012 (filled green circles).

Table 3.1 lists the mean values and standard deviations of physical parameters derived from the models for the two epochs. The model parameters for the outburst phase 2004 - 2005 match quite well with those of the on-going outburst phase of 2008 - 2012. In the quiescent phase one can notice the stellar parameters similar to those of a T Tauri star. But for the outburst phase the derived physical parameters mimic more of an intermediate mass star rather than a low mass pre-mainsequence star. In the outburst phase the disk mass and accretion rate are enhanced substantially when compared to the quiescent phase. The envelope accretion rate decreases by more than an order of magnitude in the outburst phase compared to the quiescence while the envelope mass decreases by several orders of magnitude. This may be due to the enhanced luminosity in the outburst phase which could prevent mass accretion from the envelope. In the quiescent phase, the envelope emission dominates

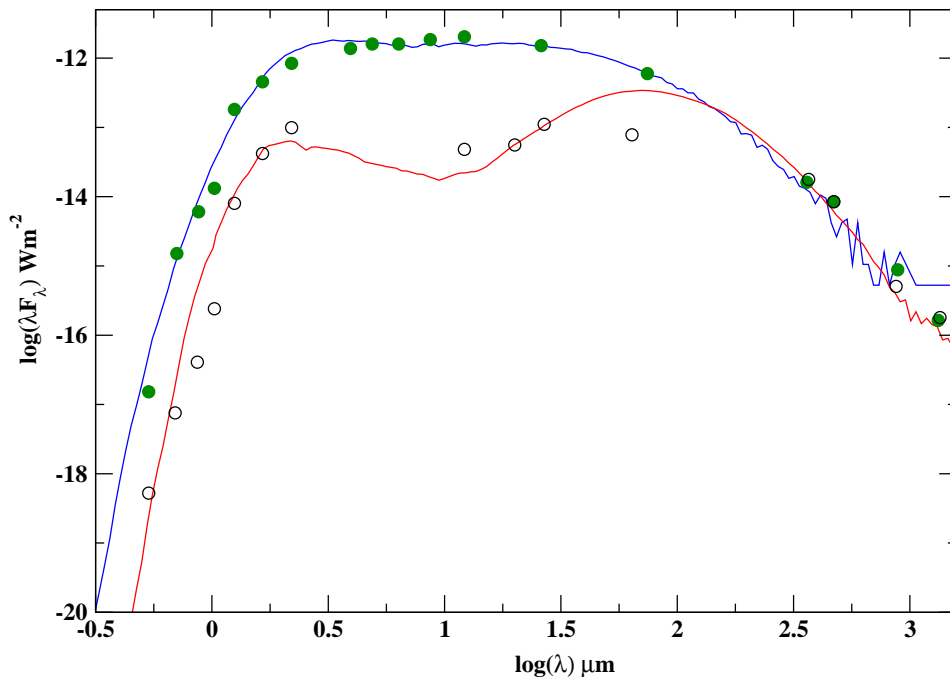


Figure 3.9: SED models for V1647 Ori during its quiescent phase (2006 - 2007) and outburst phase (2008 - 2012). The black open and green filled circles represent data points of the quiescent & outburst phase respectively. The red and blue curves represent the best fit model for the quiescent & outburst phases respectively. (see text for details).

in the mid-IR and longer wavelength region; while in the outburst phase the disk emission contributes substantially in the region beyond $1 \mu\text{m}$.

It may be noted that the disk accretion rate for the outburst phase given in Table 3.1 matches well with those reported by Briceño *et al.* (2004); Brittain *et al.* (2010) and Aspin (2011). However, the disk accretion rates in the quiescent phase derived from Br γ /Pa β emission lines by Aspin, Beck and Reipurth (2008) are much higher than the model-derived value reported here. While this could be due to uncertainties in the SED model or emission line method, the important point to be noted is that the disk accretion rate dur-

Table 3.1: Model Parameters for V1647 Ori in its quiescent (2006 - 2007) and outburst (2008 - 2012) phases

Physical Parameter	Quiescent Phase	Outburst Phase
Stellar Age (yr)	$4.8 \pm 2.5 \times 10^4$	$6.3 \pm 3.1 \times 10^5$
Star Mass (M_{\odot})	0.34 ± 0.15	4.44 ± 0.34
Star Temperature (T (K))	3360 ± 170	7560 ± 1590
Star Radius (R_{\odot})	4.01 ± 0.12	7.08 ± 2.28
Total Luminosity (L_{\odot})	1.85 ± 0.24	156.5 ± 28.0
Envelope Mass (M_{\odot})	1.51 ± 0.02	$1.40 \pm 3.79 \times 10^{-4}$
Envelope Accretion Rate ($M_{\odot} \text{ yr}^{-1}$)	$5.3 \pm 0.1 \times 10^{-5}$	$3.7 \pm 0.0 \times 10^{-6}$
Disk Mass (M_{\odot})	$6.8 \pm 8.00 \times 10^{-5}$	$6.9 \pm 1.8 \times 10^{-2}$
Disk Accretion Rate ($M_{\odot} \text{ yr}^{-1}$)	$5.5 \pm 3.3 \times 10^{-9}$	$2.2 \pm 1.6 \times 10^{-7}$

ing the outburst phase is much larger than that in the quiescent period. The total luminosity obtained here (which includes the contributions from the star and its disk and envelope) matches well with those derived by Ábrahám *et al.* (2004) and Aspin, Beck and Reipurth (2008) from the SEDs of the pre-outburst phase. The total outburst luminosity during the 2004 outburst as derived by Briceño *et al.* (2004) from the SED is $219 L_{\odot}$, which agrees well with that obtained from our model for the current on-going outburst. Earlier, using a simpler model, Muzerolle *et al.* (2005) interpreted the *Spitzer* IRAC/MIPS (photometric bands between 3.5-70 μm) data for the pre- and post-outburst phases. Their results are qualitatively similar to ours.

3.4 Infrared investigations of other eruptive young stellar objects

In this section we present the NIR and mid-IR spectra of the FU Ori sources IRAS 05426+0903 (FU Ori itself), IRAS 07013-1128, V1515 Cyg, V1057 Cyg and V1331 Cyg. We try to investigate similarities in the photometric and

spectroscopic properties of V1647 Ori with these objects.

3.4.1 IRAS 05426+0903 (FU Orionis)

IRAS 05426+0903 (also called FU Ori) is located at a distance of 600 pc. The outburst in 1936 raised the brightness by 6 magnitudes in B over the period of 3 months and still remains in its on-going outburst phase. Based on the NIR long-baseline interferometric observations, Malbet *et al.* (2005) and Quanz *et al.* (2006) suggest FU Ori as a binary system with a separation of 217 AU. It has no associated optical jet or molecular outflow (Evans *et al.*, 1994). The light curve shows a fading by ~ 1 mag, at a rate of 14 mmag yr⁻¹ since 1936 (Kenyon *et al.*, 2000). FU Ori shows a relatively blue SED (Hartmann and Kenyon, 1996; Green *et al.*, 2006; Quanz *et al.*, 2007), with emission from silicate dust as shown by *Spitzer* spectra (see Fig 3.10). It is believed that outer flared disk accounts for the 10 and 18 μm silicate emission features. Models of the FU Ori system (with a central stellar mass of $0.3 M_{\odot}$) suggest that the current accretion rate remains very high ($10^{-4} M_{\odot} \text{ yr}^{-1}$) and it is the northern component in a close ($0.5''$) binary system (Reipurth and Aspin, 2004b; Wang *et al.*, 2004) that is responsible for the outburst. The NIR spectra observed on March 2, 2014 shows Brackett series lines and the first and second overtone bands of CO in absorption (see Fig 3.10). The CO absorption bands are believed to be originating from the cooler regions of the active circumstellar disks (Calvet, Hartmann and Kenyon, 1991). Reipurth and Aspin (1997) suggested that high disk accretion rates cause strong CO bands in absorption. Malbet *et al.* (2005) derived a disk accretion rate of $6.5 \times 10^{-5} M_{\odot} \text{ yr}^{-1}$ from the NIR interferometric data.

3.4.2 IRAS 07013-1128 (Z CMa)

IRAS 07013-1128 (also called Z CMa) is a close binary located at a distance of 1050 pc with $V = 9.5$ (Hillenbrand *et al.*, 1992). The binary consists of two young stars Z CMa NW and Z CMa SE located at a separation of $0.1''$

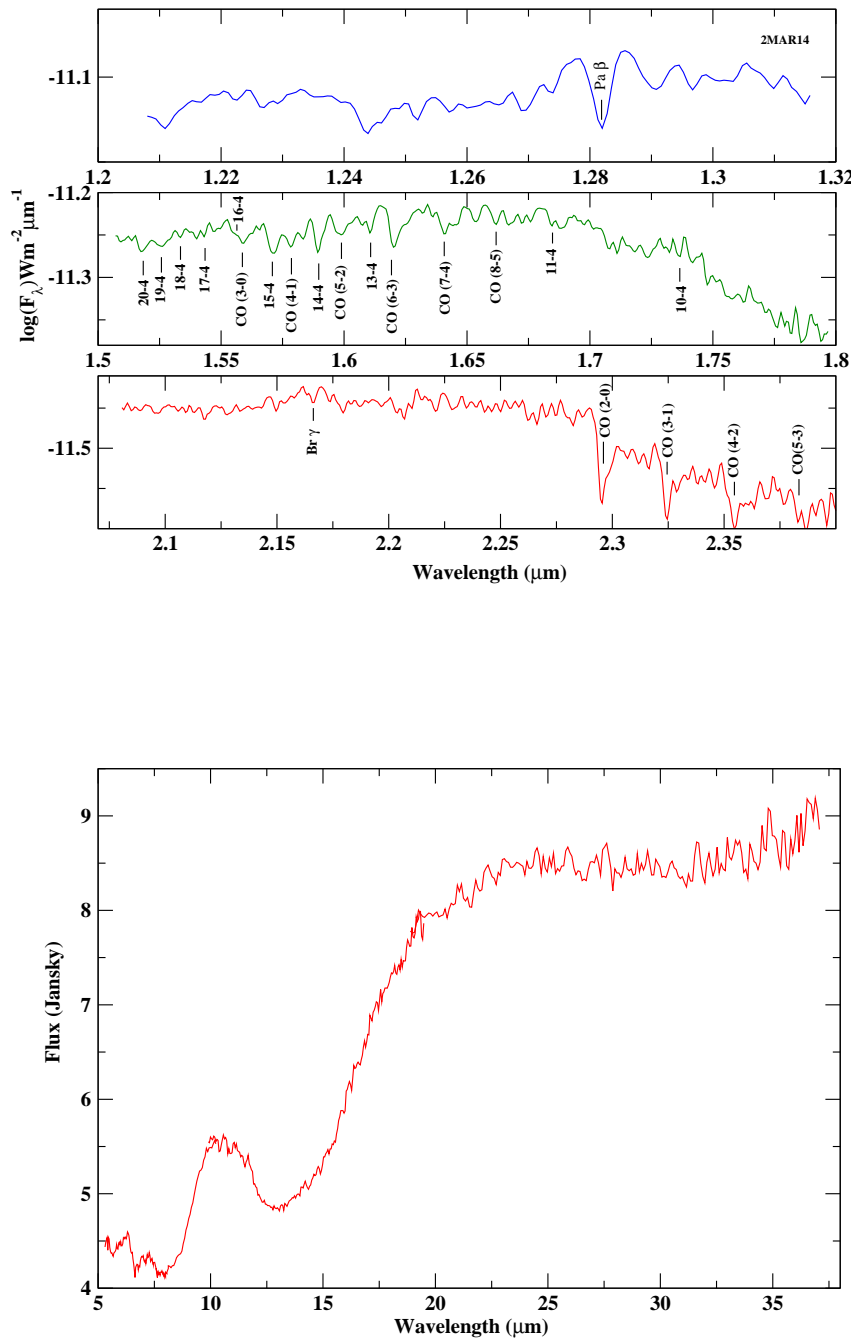


Figure 3.10: NIR JHK spectra of IRAS 05426+0903 (FU Ori) observed on March 2, 2014 using NICS (top panel) and *Spitzer* mid-IR spectra (bottom panel)

(Koresko *et al.*, 1991; Haas *et al.*, 1993). Z CMa NW is a Herbig Be star with a mass of $12 M_{\odot}$ and a spectral type of B8 (van den Ancker *et al.*, 2004). The other companion Z CMa SE has been classified as a FU Orionis object with a spectral type of F5 (Hartmann *et al.*, 1989). Both the components are surrounded by active accretion disk. Extended nebulosity was detected around Z CMa in the millimeter by Henning *et al.* (1998) and NIR by Testi, Palla and Natta (1998). Whelan *et al.* (2010) showed the presence of a 3.6 parsec-sized jet associated with this object. Z CMa has shown outburst events with brightness variations between 1 - 2 visual magnitudes during 1987, 2000, 2004 and 2008 (van den Ancker *et al.*, 2004; Grankin and Artemenko, 2009) that are typical of EXor variables. Based on the spectropolarimetric observations, Szeifert *et al.* (2010) suggested the outburst during 2008 is associated with the Z CMa NW component. van den Ancker *et al.* (2004) derived a mass accretion rate of $3 \times 10^{-5} M_{\odot} \text{ yr}^{-1}$ from the SED models. Fig 3.11 shows the Mt. Abu NIR spectra taken during two dates, January 19, 2013 and March 19, 2014. The spectra on March 19, 2014 showed Brackett series lines and faint emissions in the CO overtone bands while similar features may also be seen on 19 January 2013. The NIR CO emissions may be due to the increase in the disk temperature by the irradiation of the central star winds (Calvet, Hartmann and Kenyon, 1991). Martin (1997) suggested that the CO emissions may be also due to the gas free-falling from the accretion disc through the accretion funnels on to the central star through its strong magnetic fields. The Mt. Abu Pa β profile showed a blue shifted P Cyni profile which is believed to trace the accretion of materials onto the central star. The emission lines observed in the NIR may be due to an irradiated circumstellar disk by the stellar winds from the central source. The *Spitzer* mid-IR spectra of Z CMa show (Fig 3.11) strong silicate absorption and an increase in the continuum flux towards the longer wavelengths due to the emission from cold dust.

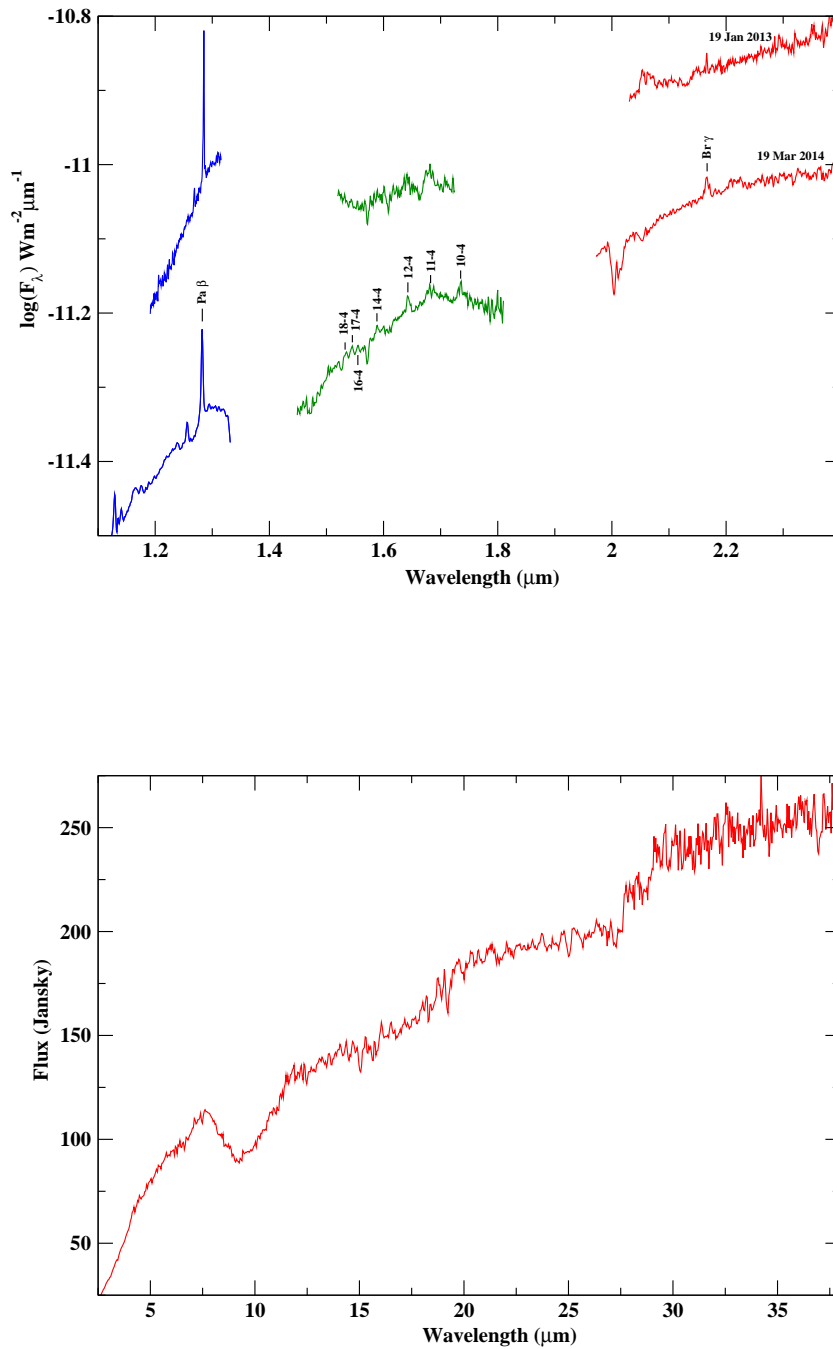


Figure 3.11: NIR *JHK* spectra of IRAS 07013-1128 (Z CMa) observed on January 19, 2013 & March 19, 2014 using NICMOS and NICS (top panel) and *Spitzer* mid-IR spectra (bottom panel)

3.4.3 V1515 Cyg

V1515 Cyg is a FU Orionis star (Kenyon, Hartmann and Kolotilov, 1991) located at a distance of 1000 pc (Racine, 1968). The brightness gradually rose during 1940s and 50s and continues to remain in the outburst stage since then (Herbig, 1977). Evans *et al.* (1994) suggested the presence of molecular outflow associated with this object. The region around V1515 Cyg shows arc-like reflection nebular structure (Kóspál, 2011). The SED of V1515 Cyg shows a double-peaked SED with disk accretion rates of $1.0 \times 10^{-5} M_{\odot} \text{ yr}^{-1}$ (Lodato and Bertin, 2001). It is not known to harbor a close binary companion (Audard *et al.*, 2014). Fig 3.12 represents the observed spectra on March 19, 2012 using the NICS. The NIR spectra show Brackett series lines and CO overtone bands in absorption. The NIR spectral signatures signify their circumstellar disk origin. The mid-IR spectra (Fig 3.12) show silicate emission and a redward increase in the continuum emission due to cold dust.

3.4.4 V1057 Cyg

V1057 Cyg (also called as LkH α 190) is a FU Orionis star, with a spectral type F7/G3I/IIf (Welin, 1976; Herbig, Petrov and Duemmler, 2003) located in the NGC 7000 (North America Nebula) at a distance of 550 pc (Straizys *et al.*, 1989). It underwent an outburst in 1969 with an increase in its brightness by ~ 6 mag in less than a year (Welin, 1971). It started moving towards its quiescent phase by gradually declining in its brightness. Evans *et al.* (1994) suggest molecular outflow associated with the source. The pre-outburst optical spectrum was consistent with a T Tauri star (Herbig, 1977). Popham *et al.* (1996) derived a disk accretion rate of $1.0 \times 10^{-4} M_{\odot} \text{ yr}^{-1}$ from their SED model. Mt. Abu NIR spectra observed on March 28, 2014 showed Brackett series lines and CO bands in absorption (not shown here). The IR spectrum is quite similar to that of V1515 Cyg. The presence of a close binary companion for V1057 is not yet known (Audard *et al.*, 2014). Fig 3.13 displays a weak silicate emission in the *Spitzer* mid-IR spectra since the object is moving

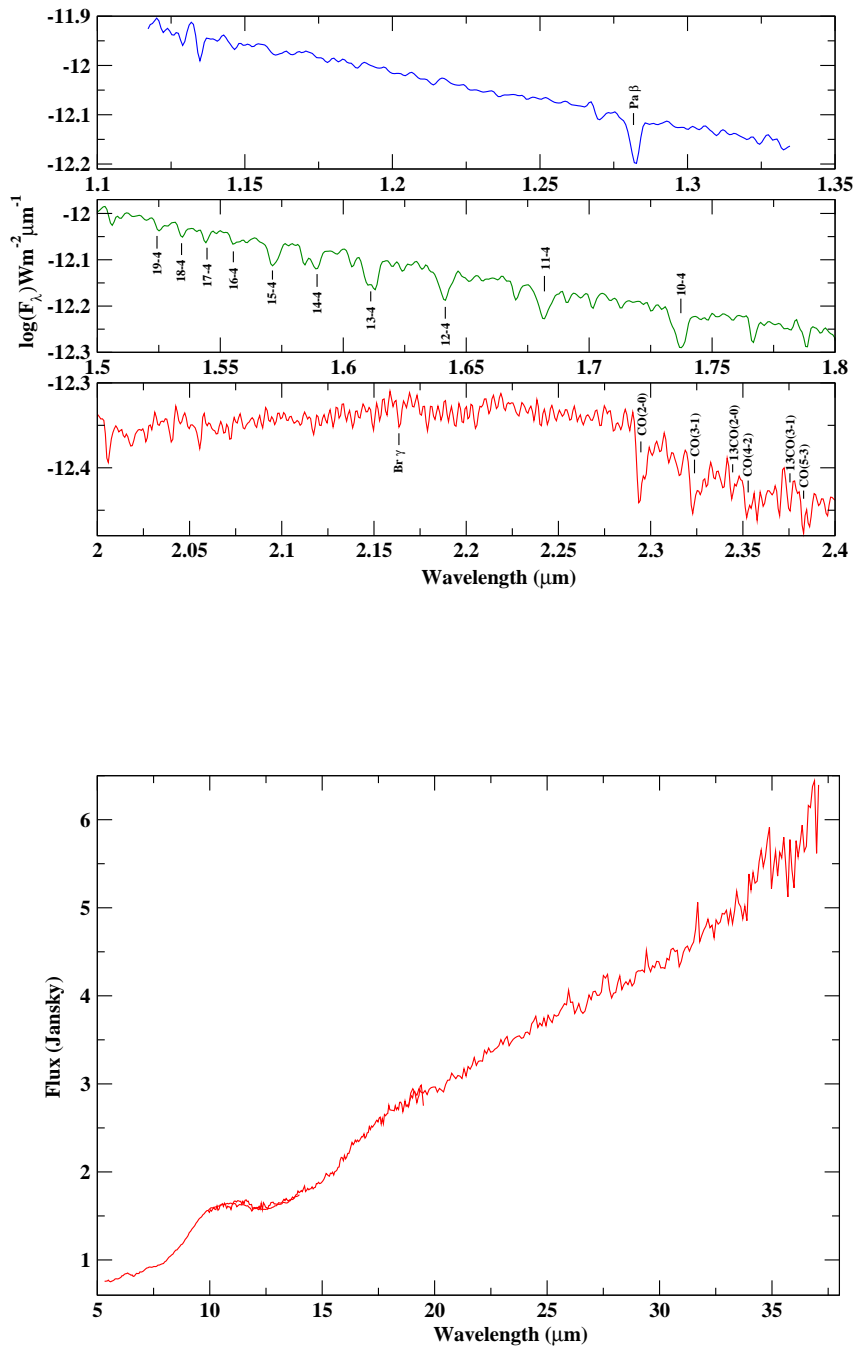


Figure 3.12: NIR *JHK* spectra of V1515 Cyg observed on March 19, 2014 using NICS (top panel) and *Spitzer* mid-IR spectra (bottom panel)

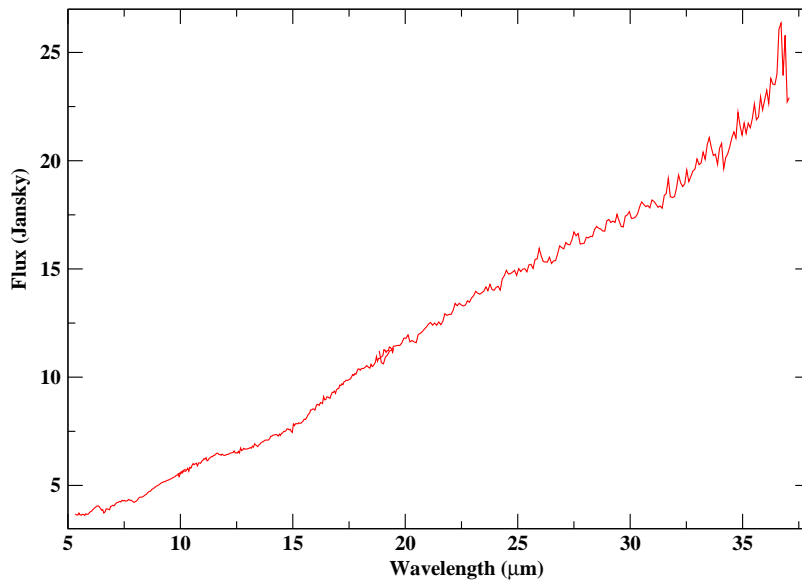


Figure 3.13: *Spitzer* mid-IR spectra V1057 Cyg

towards its quiescent phase due to the sublimation of dust. The steady increase in the continuum flux at longer wavelengths shows the presence of sublimated cold dust emission.

3.4.5 V1331 Cyg

V1331 Cyg, also called as LkH α 120, is a FU Ori candidate. It is also considered as a T Tauri star at the pre-FUor stage by Petrov *et al.* (2014). It is located in the L988 complex at a distance of 550 pc with a spectral type between A8-G5 that falls between those of Herbig Ae stars and typical T Tauri stars (Hamann and Persson, 1992). Biscaya *et al.* (1997) used NIR spectroscopy to suggest the presence of an active circumstellar accretion disk by observing the variability in the first overtone of CO. It exhibits spectral characteristics very similar to the pre-outburst optical spectrum of V1057 Cyg. Eventhough it shares several properties with FUors, its nature is still uncertain (Sandell and Weintraub, 2001). The American Association of Variable

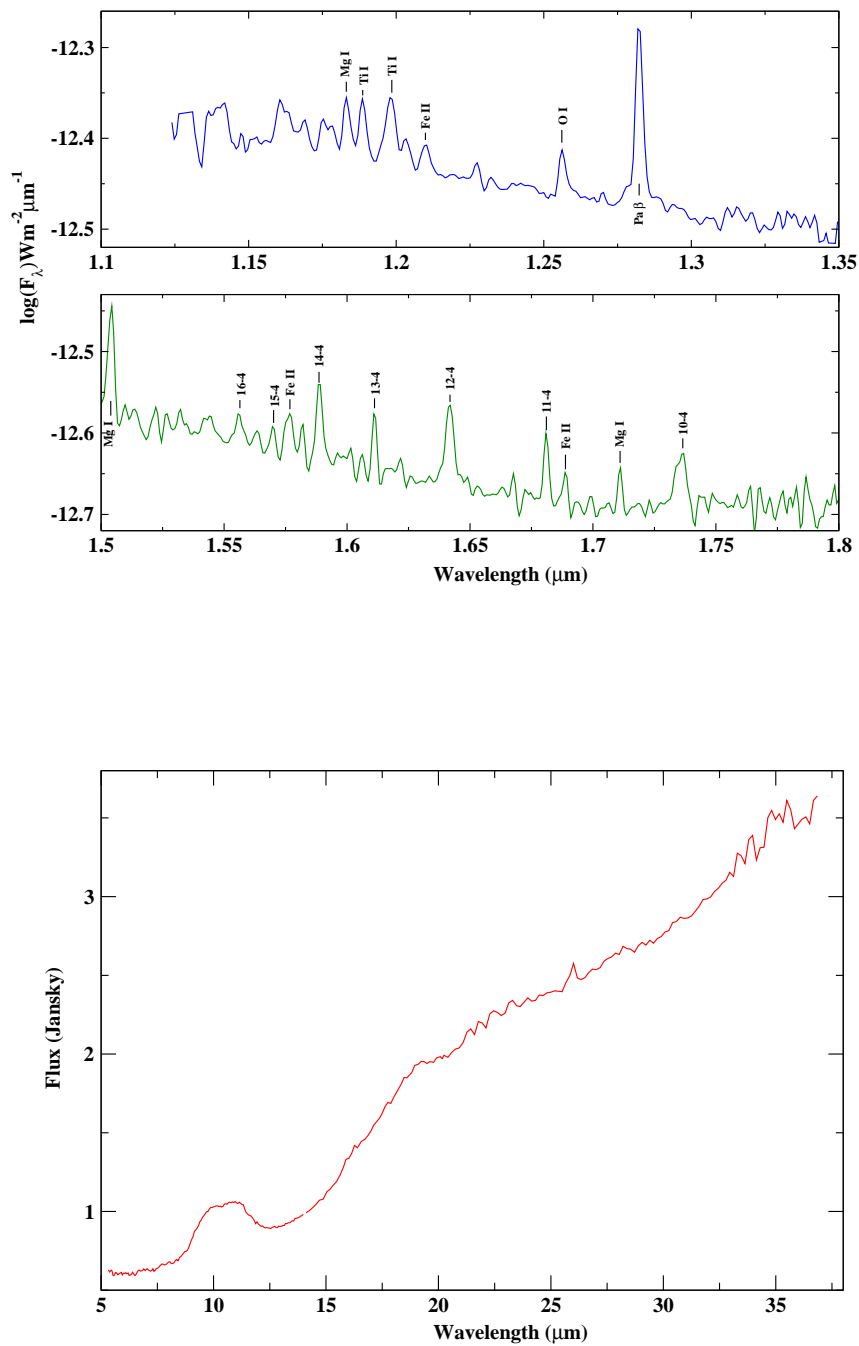


Figure 3.14: NIR *JH* spectra of V1331 Cyg (LkH α 120) observed on April 23, 2014 using NICS (top panel) and *Spitzer* mid-IR spectra (bottom panel)

Star Observers (AAVSO) light curve does not show significant variability over the past decade in the B and V bands. However, the Fourier analysis of the light curve shows a periodicity of 36.2 days (Van Genderen, 1999). The star also drives a bipolar optical jet that extends at least $180''$ from it (Mundt and Eislöffel, 1998). Najita *et al.* (2009) observed water and first overtone band of CO emissions in the K band that probe the hot (> 1500 K) circumstellar disk. Petrov *et al.* (2014) derived a mass accretion rate of $2 \times 10^{-6} M_{\odot} \text{ yr}^{-1}$ and wind mass loss rate of $(6-11) \times 10^{-8} M_{\odot} \text{ yr}^{-1}$. Weintraub, Sandell and Duncan (1991) suggested an edge-on circumstellar disk based on submillimeter data. Millimeter observations by Henning *et al.* (1998) did not resolve dust around this object, unlike for several other FUors. The Mt. Abu NIR JH spectra shown in Fig 3.14 revealed prominent Brackett series lines, Ti I, Mg I and Fe II lines in emission. The Ti I, Mg I and Fe II lines may be excited due to the shocks created by the winds from the central source. Fig 3.14 shows *Spitzer* mid-IR spectra with the $10 \mu\text{m}$ silicate feature seen in emission.

3.4.6 Discussion

Various models of FUors are used in the literature to explain the observed NIR and mid-IR properties during the outburst and quiescent phases. Most accretion disk models assume that apart from the circumstellar disk, whose inner radius is of the order of a few AU, there is an infalling remnant envelope also (Kenyon, Hartmann and Kolotilov, 1991). The eruptions are commonly explained as a consequence of dramatically enhanced accretion from the circumstellar disk on to the central star. The emissions from the hot, optically thick accretion disk are responsible for the elevated brightness in the star's light curve (Hartmann and Kenyon, 1985). In the steady disk accretion model, high accretion rates are needed to induce a temperature gradient with a hot mid-plane and cooler exterior to produce the observed absorption features in FUors (Kenyon, Hartmann and Hewett, 1988). These self-heated viscous accretion discs (active disc) outshine the stellar light from the central star and reproduces the properties of the FUor outburst (Hartmann and Kenyon, 1985; Bell

et al., 1995). Yet, active disc models fail to explain the mid- and far-IR excess as well as weak silicate emissions at 10 μm . Calvet, Hartmann and Kenyon (1991) found that an irradiated accretion disk model with accretion rate of $1.6 \times 10^{-4} M_{\odot} \text{ yr}^{-1}$ reproduced the CO and silicate emission features of FUors. They suggested that as the stellar effective temperature increases for a given mass accretion rate, the disk surface temperature increases and the CO bands turn into emission. On the other hand, as the mass accretion rate increases, the intrinsic viscous temperature increases and the effect of irradiation becomes less important and CO turns into absorption.

Lachaume, Malbet and Monin (2003) developed a two-layer disc model, in which the irradiation by a central star and viscous heating are taken in to account, for explaining the spectral properties of the FUors. Observations at NIR wavelengths probe the gaseous inner disk of circumstellar material located at a distance ≤ 1 AU. The recombination lines of hydrogen observed in absorption in the NIR spectra of IRAS 05426+0902, V1515 Cyg and V1507 Cyg are possibly due the viscous heating at the disk interiors resulting in a temperature gradient that decreases vertically outwards. The light curves of these objects also suggest their elevated photometric state of outburst. The origin of HI series lines in emission is related to the accretion processes (Acosta-Pulido *et al.*, 2007). If the envelope accretion rate is not high enough to replenish the accreted material, shorter and smaller amplitude outburst like EXors occur. Also if the disk accretion rate is not high enough to invert the temperature gradient in the disks interior, the final spectrum will be dominated by emission features that are produced in the disk wind and/or in the magnetospheric accretion columns (Fedele *et al.*, 2007). The spectral signatures of hydrogen recombination lines from IRAS 07013-1128 and V1331 Cyg suggest such a scenario. Also, the irradiated accretion disk model can explain these observed properties.

Spitzer mid-IR observations probe the cool dusty component of the circumstellar material in the accretion disks or in the envelopes of these objects. All the six objects (including V1647 Ori) in our sample with the exception of Z

CMa showed silicate in emission at $10\mu\text{m}$. The mid-IR properties of the FUors can be explained with an accretion disk surrounded by optically thick infalling envelope of gas and dust (Kenyon and Hartmann, 1991). The silicate emission features are due to the heated surface layers of the disk from the irradiation of the central star which results in a higher surface temperature than its interior (Calvet *et al.*, 1992). The silicate absorption may be due to the absorption of disk emission by the surrounding optically thick circumstellar envelope. Such objects are considered to be younger than those with silicate emission. Among these samples, V1331 Cyg showed spectral signatures similar to those of V1647 Ori. The NIR and silicate emission features in V1331 Cyg are similar to those observed in V1647 Ori. However, the $15.2\mu\text{m}$ CO_2 ice feature observed in V1647 Ori is absent in the mid-IR spectra of V1331 Cyg. IRAS 05426+0903 (FU ori) exhibits 10 and $18\mu\text{m}$ silicate emission features that may be due to irradiated disk heating and an increasing mid-IR flux due to the flared disk geometry. The IRS spectra of V1515 Cyg & V1057 Cyg show less intense $10\mu\text{m}$ silicate feature. These differences are probably due to the difference in the optical thickness of the system (disk + envelope) at $10\mu\text{m}$. Also, out of the five FUor candidates observed for comparison with V1647 Ori, three sources have a close binary companion close to the central source. Hence, the initiation of the disk instability by tidal forces from a close binary companion cannot be ruled out in these sources. The mid-IR interferometric observations of V1647 Ori at VLTI suggest the absence of a close companion and the possibility of a moderately flared circumstellar disk (Ábrahám *et al.*, 2006), thus, suggesting it to be a new class of objects with properties similar to both the FUors and EXors.

3.5 Conclusions

The important conclusions of this work are:

1. Long term monitoring of V1647 Ori in the *JHK* bands from Mt. Abu, India shows that the object had been undergoing episodes of mass accre-

tion variation as indicated by small but significant variations in its *JHK* fluxes. This conclusion is also supported by its NIR spectral variations;

2. Starting from early 2012, the object seems to show a slow fading out with a rate of ~ 0.06 - 0.18 mag per year. This may indicate that V1647 Ori is an intermediate type object falling between FUors and EXors, having characteristic features of both the proto-types;
3. *JHK* color-color diagram for V1647 Ori indicates several occasions in the current, on-going outburst in which the star displays positions beyond the T Tauri region indicating the presence of colder dust compared to its 2004 outburst phase;
4. V1647 Ori displayed silicate emission and CO₂ ice absorption indicating the presence of an icy envelope;
5. The Herbig-Haro object HH22, with a yet unidentified energizing YSO situated at about 30 arcsec from V1647 Ori, seems to show light fluctuations corresponding to those of the latter, thereby confirming that it is a reflection nebulosity triggered by the YSO;
6. Mt. Abu NIR spectra of IRAS 05426+0903 (FU Ori), V1515 Cyg, V1057 Cyg showed hydrogen recombination lines in absorption, whereas IRAS 07013-1128 (Z CMa) and V1331 Cyg showed the lines in emission. Mid-IR spectra of all the FU Ori candidates showed silicate emission except for Z CMa. The sources displaying hydrogen series lines in absorption at the NIR wavelengths have high disk accretion rates, thus resulting in active discs due to viscous heating at the centre of the disk with temperatures decreasing radially outwards. The hydrogen series lines in emission are believed to be caused by irradiated heating of the disk surface by stellar wind from the central source.

Chapter 4

Infrared photometric and spectroscopic study of Asymptotic Giant Branch stars

4.1 Introduction

It is known that AGB stars, also referred to as Mira variables, are cool stars ($T_{eff} \sim 2000 - 2500$ K, spectral type M) with carbon/oxygen cores surrounded by He and H burning shells and having very extended, low density photospheres. Most AGB stars lose their mass at a moderate rate of $10^{-7} - 10^{-6} M_{\odot} \text{ yr}^{-1}$, and thus, have optically thick dust shells. The gas in the shells is molecular to a large extent. Dust grains are formed at distances much farther from the star than the site where molecules are formed. The molecular and dust properties are a strong function of C/O ratio. The dust grains in the envelopes absorb stellar radiation and re-emit it at the IR wavelengths. These IR dust emissions contribute as an excess to the stellar SED. Based on the regularity of the light curve and its amplitude, different variability types on the AGB are

distinguished. Variables that do not have a prominent period of light change and with rather small amplitudes are called as Semiregular variables (SR or SRV). These stars exhibit light variations with amplitudes in the V -band ≤ 2.5 magnitude. SR variables are placed on the early AGB, while Mira variables are more evolved and populate the thermally pulsing AGB (Lebzelter and Hron, 1999). SRVs and Miras make up a large part of the so-called long period variables (LPVs). As mentioned in Chapter 1, it is believed that Miras eventually evolve into OH/IR stars (van der Veen and Habing, 1988), with the onset of a superwind phase (Renzini, 1981). Another sub-class of AGB stars called S type are intermediate between the M (oxygen-rich) and C (carbon-rich) classes but distinguish themselves with the appearance of ZrO absorption bands (Keenan, 1954).

The circumstellar shells of AGB stars may retain the fossil record of the mass loss processes by which they formed. Changes in mass loss rate are imprinted in the shell as density variations. Through this mass-loss process, AGB stars shed their entire mantle, and the naked carbon/oxygen core remains behind. Once the mass-loss stops, the dust shell still moves outward, and the optical depth towards the core decreases. Hydrodynamical models show that the structure of the atmosphere of pulsating stars is dependent on the pulsation driven shocks and formation of dust grains on the circumstellar envelope. The SED of AGB stars peaks in the NIR, enabling the study of circumstellar molecular features.

The physical mechanisms that are responsible for driving mass loss are not yet fully understood, inspite of the considerable progress in the hydrodynamic calculations for pulsating AGB stars (Loidl *et al.*, 1999; Winters *et al.*, 2000b). To understand the mass loss process, it is important to compare the predictions of the hydrodynamic models with the observable properties of these stars to assess the validity of the models. NIR spectroscopy is one of the recognized tools to study the mass-loss processes (Kleinmann and Hall, 1986; Lançon and Wood, 2000; Bieging, Rieke and Rieke, 2002). The SEDs of AGB stars peak in the NIR that contain several important diagnostic lines (e.g. TiO, H₂O and

CO) that can be used as signatures to probe the atmospheres of these stars (Hinkle, Hall and Ridgway, 1982). We seek correlations between the equivalent widths of some spectral signatures and infra-red colors that may be indicative of mass-loss.

4.2 The Sample Stars

The programme stars were selected from published literature or catalogues (Fouque *et al.*, 1992; Kerschbaum and Hron, 1994; Chen, Gao and Jorissen, 1995; Wang and Chen, 2002). Our sample contains about 62 stars with the selection based on the observability at Mt. Abu during the period November - May and *JHK* band magnitudes brighter than 8 - 9. Among these stars, 30 are M type; 17 S type; 15 SR type. The greater bias towards M types in the sample is due to the fact that they are brighter in *K* band than the others. Tables B.1 - B.3 list all the stars in the three categories along with their [*H* - *K*] and [*K* - 12] colors computed from the 2MASS and IRAS photometric archival data. The phases (ϕ) of the variable stars of M and SR types, corresponding to the dates of our observations, are also listed in the tables (epochs taken from Kholopov (1987)). The spectral types are taken from the Set of Identifications, Measurements, and Bibliography for Astronomical Data (SIMBAD) data base.

4.3 Near-Infrared Observations and analysis

NIR spectroscopic observations were made in the *H* and *K* bands on the selected stars, using the NICMOS at the Cassegrain focus of the 1.2 m telescope at Mt. Abu, India. The observations were made at a spectral resolution of ~ 1000 . Spectrophotometric standard stars of A0V type were also observed for each programme star at a similar air mass to remove telluric absorptions. For sky background subtraction, two traces were taken for each star at two spatially separated positions along the slit. Typical overall integration times varied between 0.6 to 160 s for the brightest and faintest stars in our sam-

ple (in each of the two bands). The atmospheric OH telluric lines were used to calibrate the wavelength. The HI absorption lines from the standard star spectra were removed by interpolation. The resulting spectra of the standard star were used for the removal of telluric lines from the program star by ratiointing. The ratioed spectra were then multiplied by a blackbody spectrum at the effective temperature corresponding to the standard star to obtain the final spectra. Data processing, using the IRAF software, was done using standard spectroscopic task (e.g., APALL). The NIR EWs were measured using the SPLOT task in IRAF. The errors in the EWs are mainly due to the S/N ratio of the lines. Typically, the S/N ratios at the strongest and the weakest spectral features varied between 100 and 3 respectively. To that extent the errors are estimated to be about 3 Å, mostly applicable to the low S/N (~ 3) line detections, such as the metallic lines; but for the CO bands the S/N ratio is high (in many cases ≥ 5) and hence the errors in EW are ≤ 1 Å for these lines.

4.4 Results and Discussion

In general, the CO vibration-rotation lines of first and second overtone bands (see Chapter 1 for details) were seen in all the sample stars of M, S and SR type.

CO molecules that are believed to form deep in the photosphere of these stars owing to its high dissociation energy remain unchanged in its abundance even over large distances above the photosphere with values close to the chemical thermodynamic equilibrium (TE), suggest its significance to probe the entire extended atmosphere. In addition, all the AGB stars in our sample, display the photospheric absorption lines of the Na I doublet at 2.21 μm , the Ca I triplet at ~ 2.26 μm , as well as the Mg I line at 1.708 μm . Figures 4.1, 4.2 and 4.3 show some typical spectra for M, SR and S type stars considered here. Tables B.1, B.2, B.3 in Appendix B list the EWs (in Å, positive for absorption and negative for emission) of the CO(3-0, 4-1) second overtone bands in the *H* band and CO(2-0, 3-1) first overtone bands in the *K* band, for the program

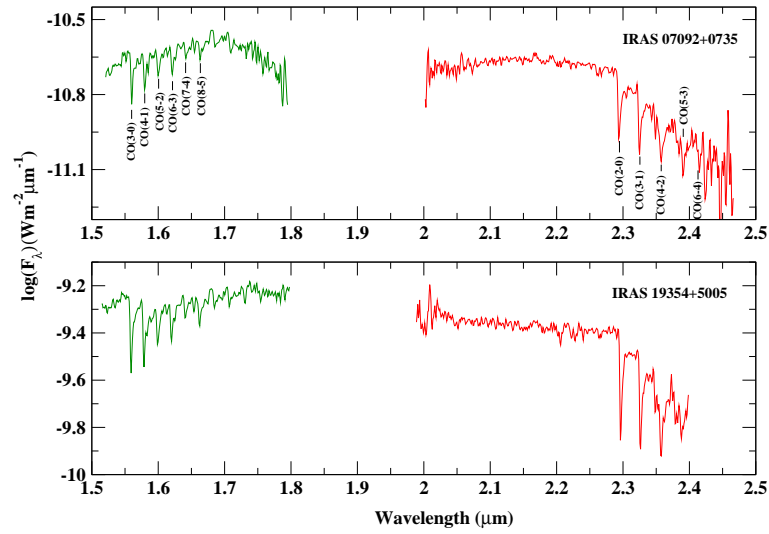


Figure 4.1: Mt Abu *HK* spectra of the M type stars IRAS 07092+0735 (top) and IRAS 19354+5005 (bottom)

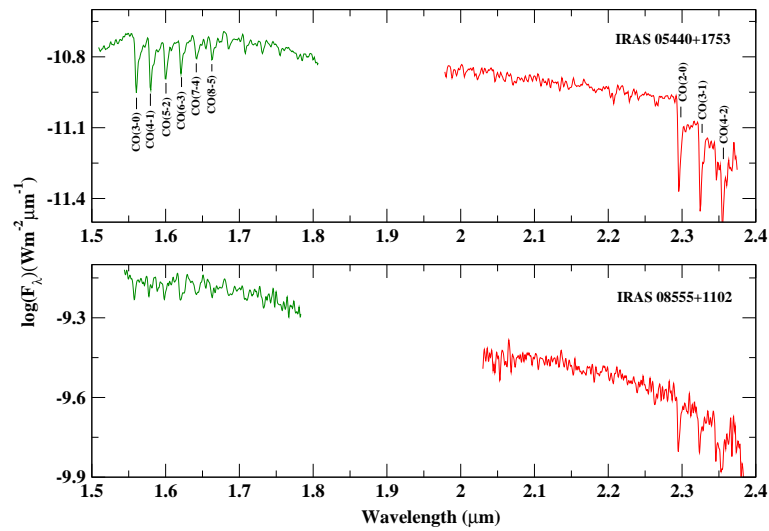


Figure 4.2: Mt Abu *HK* spectra of the SR type stars IRAS 05440+1753 (top) and IRAS 08555+1102 (bottom)

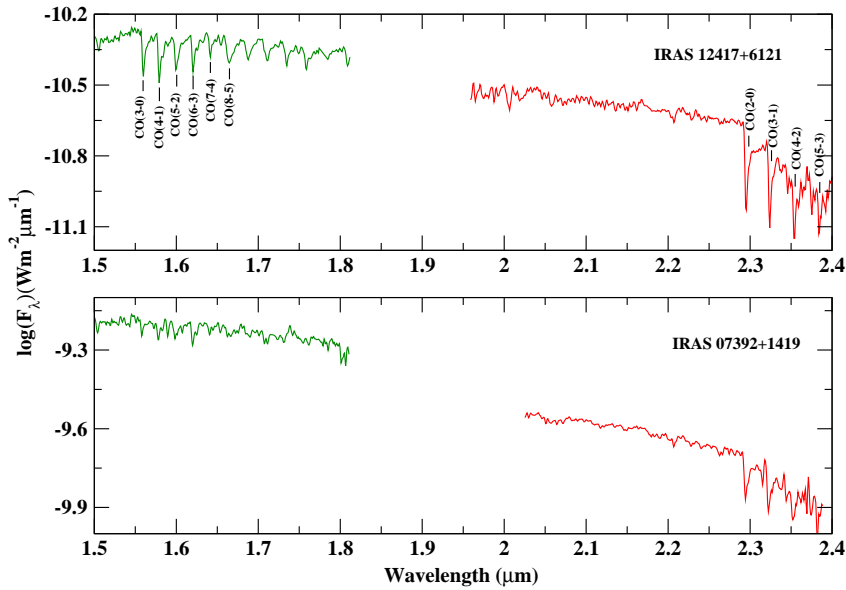


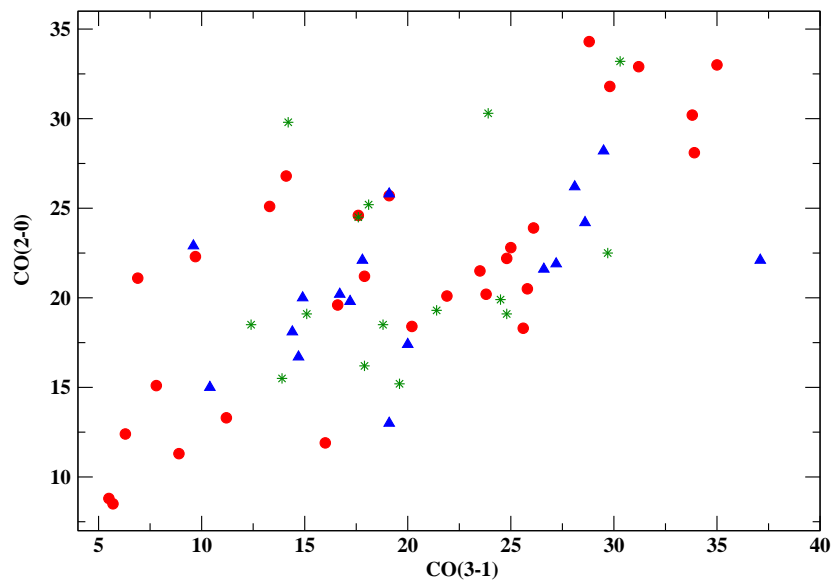
Figure 4.3: Mt Abu *HK* spectra of the S type stars IRAS 12417+6121 (top) and IRAS 07392+1419 (bottom)

stars of each category.

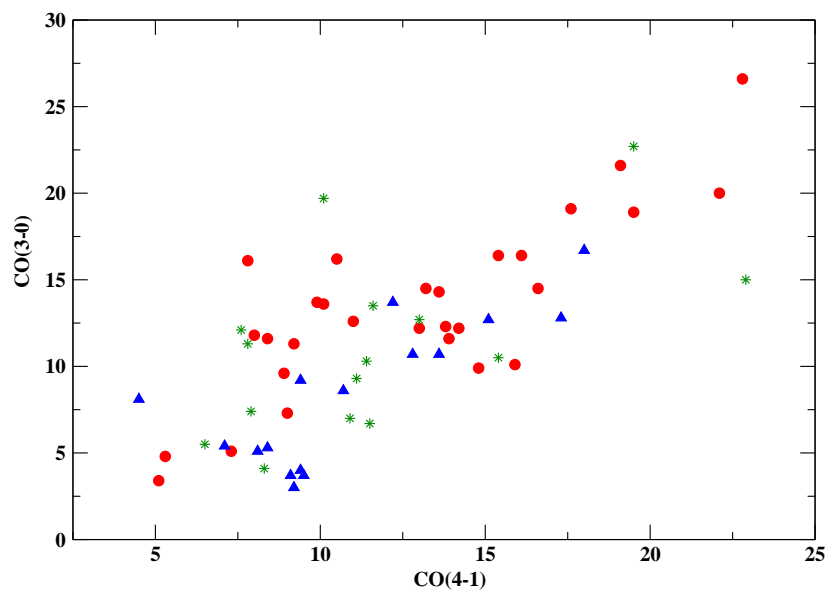
4.4.1 Correlations and their implications:

A positive correlation between the line strength of CO(2-0) & CO(3-1) and CO(3-0) & CO(4-1) is expected if the population of these levels are excited under equilibrium conditions. The top panel of Fig 4.4 demonstrates this trend between CO(2-0) & CO(3-1), while the bottom panel indicates a correlation between CO(3-0) and CO(4-1) bands.

Earlier, Biegging, Rieke and Rieke (2002) had looked for correlations between the spectral signatures observed in AGB stars (Kleinmann and Hall, 1986; Lançon and Wood, 2000) with the stellar properties like IR colors and mass loss rates. In our sample, we tried to establish a correlation between the intensities of first and second overtone bands of CO with their stellar parameters. Figure 4.5 shows the correlation of CO(3-0) and CO(2-0) with the



(a)



(b)

Figure 4.4: Plot of (a) EWs (in \AA) of the CO(2-0) versus CO(3-1) (b) EWs (in \AA) of the CO(3-0) versus CO(4-1). The M, SR, S type stars are represented by red closed circles, green asterisks and filled blue triangles

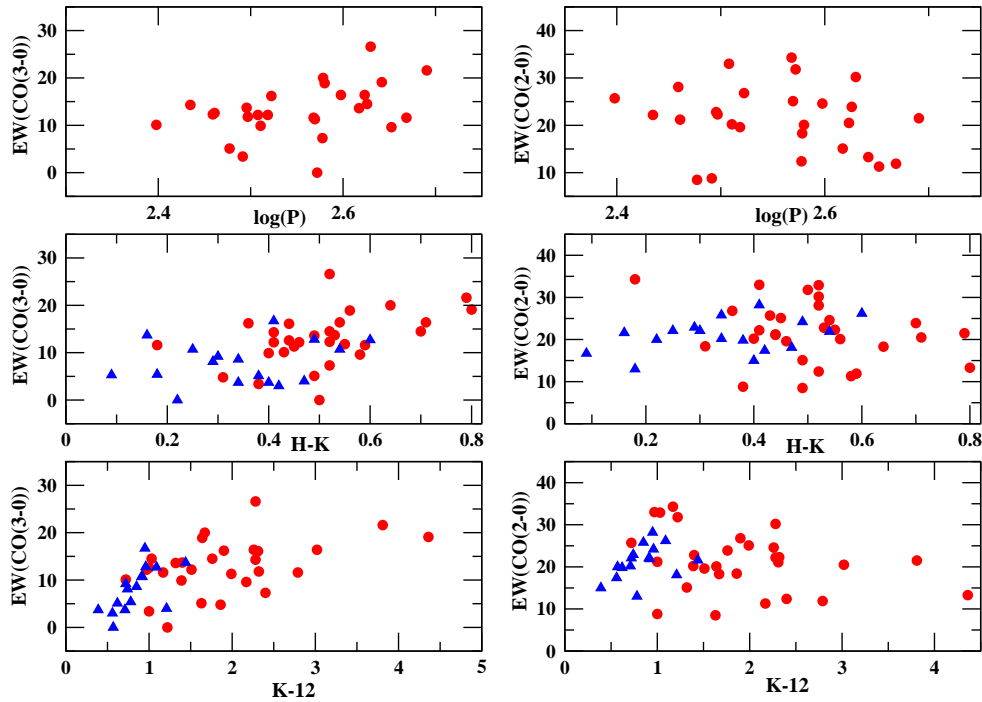


Figure 4.5: Plots of EWs (in \AA) of the CO(3-0) and CO(2-0) bands with the period for M type stars (top panel); with $[H - K]$ color (middle panel) ; and $[K - 12]$ in bottom panel. M star are shown in filled red circles and S type stars are shown in filled blue triangles

period for M type stars and also with the mass loss indicators like $[H - K]$ & $[K - 12]$ colors for M and S type stars. For M stars, one can see a positive correlation in the CO ($\Delta v = 3$) vs $\log P$; whereas, the CO($\Delta v = 2$) vs $\log P$ plot shows a negative correlation (see Fig. 4.5). The first overtone bands of CO ($\Delta v = 2$) in the K band arise at a temperature of $T \sim 800$ K, partly in the photosphere and partly in the circumstellar envelopes; while the second overtone bands ($\Delta v = 3$) in the H band arises at a temperature of $T \sim 3000$ - 4000 K entirely in the photospheric layers (e.g., Hinkle, Hall and Ridgway (1982); Emerson (1996)). As a result, the pulsational effects may be more

pronounced in the $\Delta v = 3$ bands than in the $\Delta v = 2$ bands; while the latter would reflect the circumstellar matter properties better. Thus we expect a better correlation between EW of $\Delta v = 3$ bands with pulsation period P than the $\Delta v = 2$ bands. Also, as the star expands the mass loss increases but the circumstellar envelope becomes tenuous while the column densities of CO where the CO(2-0) band is excited decreases; hence the EW of CO(2-0) band may show a decreasing trend. Since CO(3-0) originates entirely from the photosphere, as the star expands the column densities of CO may still remain high; hence a positive correlation is obtained.

The phases of these variable stars are not necessarily the same between our observations and 2MASS or IRAS data (see Tables B.1 & B.3 for phases during our observations). These stars show variability as their surface expands and contracts, hence their colors may be different at various phases. Hence as the phases are different during these observations, the correlation of CO(2-0) with $[H - K]$ show scatter. Lançon and Wood (2000) & Loidl, Lançon and Jørgensen (2001) argued that in the case of carbon-rich AGB stars, the CO lines arise deeper inside their atmospheres (close to their photospheres) and hence may not respond as much to dynamical effects such as pulsations, as those lines that arise in the outer atmospheres. In our sample of M stars, a large number of them are oxygen-rich and hence the pulsation effects may be significant. The trend of correlation for CO(3-0) band with the IR color $[K - 12]$ for S type stars is quite clear. For SR stars, we did not find any such trend. In order to quantify the degree of correlation between two parameters, we have used the Spearman's rank correlation method that does not a priori assume any functional relationship between them (e.g., Loidl, Lançon and Jørgensen (2001)). We find that for M type stars, for the CO(3-0) vs $[H - K]$, the rank correlation coefficient ρ is 0.50 with its significance s of 0.008 (a chance occurrence of 8 in 1000); while for S stars, for CO(3-0) vs $[K - 12]$ ρ is 0.74 with s of 0.003. These are moderately significant correlations as may also be visually seen from the plots. In comparison, the coefficients and their significances are quite poor for the CO(2-0) plots in Fig 4.5. Usually the mass

loss is correlated well with the pulsation period; as also by the color indices $[H - K]$ and $[K - 12]$ (Whitelock *et al.*, 1994). While the trends in Fig 4.5 are certainly beyond the errors in EW, we find that the scatter is rather significant in the correlation plot between the CO(3-0) band EWs and $[H - K]$ and other mass loss indicators (Fig 4.5) such as $\log P$ and $[K - 12]$, although it is much less in comparison to the plots for CO(2-0) band.

4.4.2 Modeling of Infrared Spectral Energy Distribution:

The IR SEDs of the sample stars, constructed from archival data in the visible, near and far-IR regions were modeled using the DUSTY code (Ivezic, Nenkova and Elitzur, 1999) to investigate basic differences in the photospheric and circumstellar parameters among the various types of AGB stars. DUSTY assumes that the external radiation comes from a point source at the center of a density distribution. Dusty contains data for the optical properties of six common grain types: 'Warm' and 'cold' silicates, astronomical silicate and graphite grains, amorphous carbon and SiC. We adopted a grain size distribution that follows the MRN power law (Mathis, Rumpl and Nordsieck, 1977) $n(a) \propto a^{-q}$, where a is grain radius with $a_{min} = 0.005$, $a_{max} = 0.250 \mu\text{m}$ and $q = 3.5$. The SED model assumes the envelope expansion driven by radiation pressure on the dust grains. This code incorporates full dynamical calculation for radiatively driven winds in AGB stars. DUSTY computes the wind structure by solving the hydrodynamics equations, including dust drift and the star's gravitational attraction, as a set coupled to radiative transfer. For the above set of parameters DUSTY generates models with different optical depths that may be specified.

The photometric data on all the programme objects were compiled mainly from the 2MASS and IRAS archives. In a few cases we obtained data from DENIS and MSX archives as well. We have modeled the SEDs of all the programme stars except those that have upper-limits (quality = 1) in IRAS

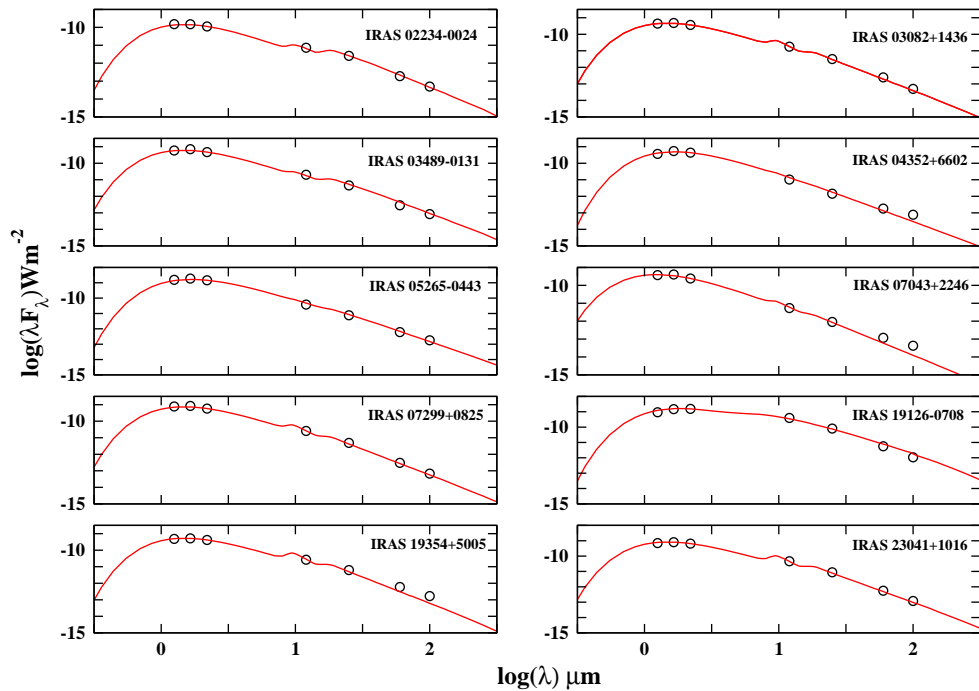


Figure 4.6: Model SEDs (red lines) of some M type stars compared with observed data from literature (closed circles). See text for model parameters and explanation.

data in more than one band. We assumed silicate dust for M, S and SR types. We fix stellar parameters like the photometric temperature (based on the visible and the NIR data), inner dust shell temperature, type of dust and size distribution (MRN assumed) and opacity at $0.5 \mu\text{m}$ (usually taken value between 0.1 and 1.0). We have used the density distribution, relevant for modeling the radiatively driven winds in AGB stars, as incorporated in to DUSTY by its authors. There would be a 10-20 % uncertainty in all the model output parameters. We have generated nearly 150 models using several combinations of the grain composition and opacity. We then take the fluxes computed by the code and normalize it with the observed $2 \mu\text{m}$ flux from each object and construct the model SEDs. A χ^2 test is performed to select the best fit model.

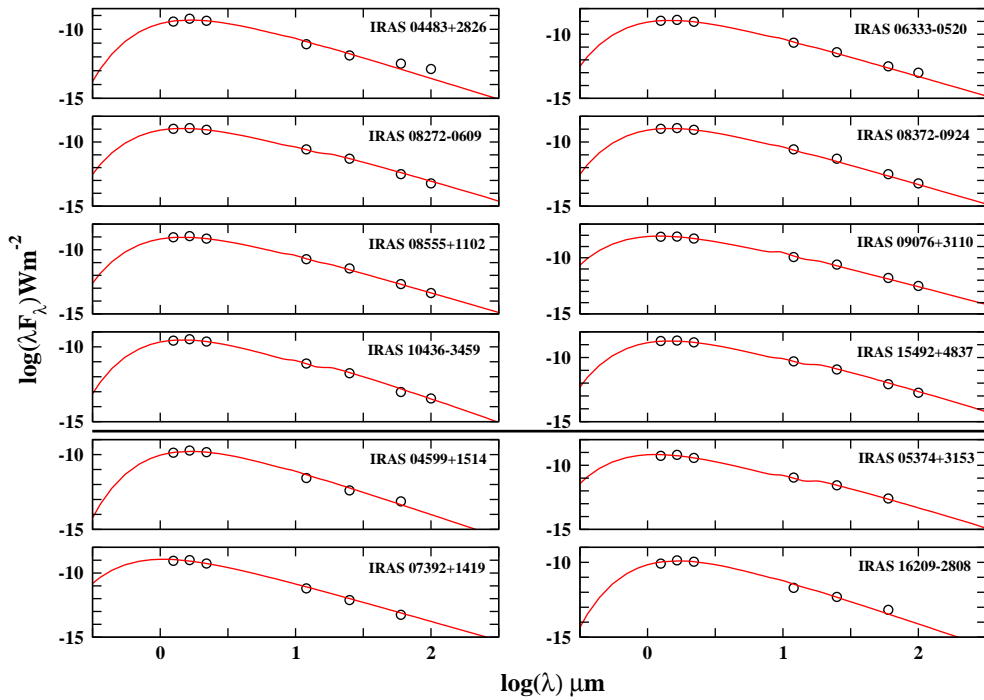


Figure 4.7: Model SEDs (red lines) of some SR type (in the top 8 panels) and S type stars (in the bottom 4 panels below the horizontal line) compared with observed data from literature (closed circles). See text for model parameters and explanation.

In general, the model shows that the M types have lower effective temperatures than the S and SR types. M types show higher opacities by a factor of 2, than the S and SR types; S type being lowest. However, the inner dust shell temperature for all the types were found to be in the range 450-700 K. The dust parameters that we obtained are in good agreement with those in the published literature for some objects. A few examples of SEDs of M, S, and SR and their model fits are shown in Figs 4.6 & 4.7. All the program stars show a monotonous decrease in the flux beyond the IR wavelengths. The AGB candidates show the absence of detached shells due to its on going mass loss where the sources have not yet reached the superwind phase. Also one can see the origin of 10 μm silicate emission in the M type, while it is absent for SR

type thus signifying their advanced stage of evolution in the AGB phase.

The DUSTY models of AGB stars estimates mass loss rate also but with larger uncertainty of 30%. The mass loss rates ($dM_{gas}/dt = \dot{M}$ in $M_{\odot} \text{ yr}^{-1}$) thus obtained are listed in Tables B.1 - B.3 for all the types; the sign † shows stars for which the rates are independently available from CO rotational line observations by several authors, namely, Loup *et al.* (1993a); Sahai and Liechti (1995); Groenewegen and de Jong (1998); Jorissen and Knapp (1998); Winters *et al.* (2000a); Ramstedt *et al.* (2006) for M, S and SR stars. Our model mass loss rates are in reasonably good agreement with those determined from CO rotational lines, for all cases. From Tables B.1, B.2 and B.3 one may see a clear trend of increase of mass loss rate with increase of the color $[K - 12]$ (e.g., Bieging, Rieke and Rieke (2002)). Basically most of our sample M type stars are in the ascending phase of their AGB stage and hence the mass loss rate increases with the $[K - 12]$ index (see Whitelock *et al.* (1994) & Habing (1996)). The variation of mass loss rate with $[K - 12]$ among the AGB and PAGB candidates is discussed in the next chapter.

4.5 Conclusions

1. The Mt Abu H and K band spectra of AGB stars showed CO first and second overtone bands in absorption. Hydrogen Brackett series lines were not detected in none of the three types.
2. The EWs of CO (3-0) show a positive trend of correlation with $[H - K]$ and $[K - 12]$ in M and S type stars. The EWs of CO(3-1) and CO(4-1) show a positive correlation with CO(2-0) and CO(3-0) respectively thus signifying the population of the levels under thermodynamic equilibrium.
3. The EWs of CO(3-0) shows a positive correlation with the period of M type stars whereas a negative correlation with CO(2-0), thus reflecting a more pronounced effect of pulsation from the second overtone band.
4. Modeling of the SEDs of the sample stars revealed higher opacities for

M type stars by a factor of 2 than S and SR types. The inner dust shell temperature for all the types were found to be in the range 450-700 K.

5. Model mass loss rates for M type stars show an increasing trend with the color $[K - 12]$.

Chapter 5

Infrared photometric and spectroscopic study of Post Asymptotic Giant Branch stars/Proto-Planetary Nebulae

5.1 Introduction

During the PAGB phase the effective temperature of the central star increases from K to B ($T_{eff} \sim 3500 - 10,000$ K) type, while its luminosity remains largely constant ($10^3 - 10^4 L_{\odot}$). The PAGB duration is a function of the initial mass and ranges from ~ 30 years for intermediate mass stars (i.e. close to $8 M_{\odot}$), to 10^4 years for low mass stars (Bloeker, 1995a). The circumstellar envelopes of carbon-rich objects display emission from molecules such as HCN or CN and PAHs (Wallerstein and Knapp, 1998). A strong emission at $21 \mu\text{m}$ due to TiC or SiC is also observed in C-rich PAGB stars (von Helden

et al., 2000; Speck and Hofmeister, 2004). Some PAGB stars show a mixed chemistry with signatures from carbon-rich PAHs and oxygen-rich crystalline silicates in their IR spectra. The formation history of these object is not well understood. Waters *et al.* (1998) and Molster *et al.* (1999) proposed that the PAHs are formed during a later mass-loss phase after the star becomes carbon-rich, while the gas stored in a circumbinary disk retain the earlier oxygen-rich chemistry. In these types of objects, the emission lines most often observed are the rotational transitions of CO, which trace the locations of cool gas (Loup *et al.*, 1993b). Oxygen-rich objects are also detected in the 18 cm OH maser (Lewis, 1989; te Lintel Hekkert, Chapman and Zijlstra, 1992) and exhibit the silicate features at 10 and 18 μm . The (sub)mm wavelength regime provides many transitional wavelengths of oxygen-rich molecules such as SO₂, SiO etc (Omont *et al.*, 1993b). The chemical reaction time scale of the PAGB/PPNe phases are constrained by their short evolutionary time scale ($< 10^3$ years) (Kwok, 2004). Hence, the detection of these carbonaceous compounds in the C-rich circumstellar envelopes suggests that they form in a short period of time.

A large number of PAGB stars were identified using the IRAS ([12]-[25],[25]-[60]) colour-colour diagram. Ground-based follow-up programmes were conducted for these sources to distinguish between late-type AGB stars, supergiants or early-type PNe (Kwok, Boreiko and Hrivnak, 1987; Hrivnak, Kwok and Volk, 1989; Oudmaijer *et al.*, 1992; Garcia-Lario *et al.*, 1997; Suárez *et al.*, 2006). A more refined evolutionary catalog was given by Szczerba *et al.* (2007).

The transition objects from the PAGB to the PNe stage show manifestation of pulsations showing variability in the hydrogen series lines and CO overtone bands. These objects display irregular photometric variability with amplitudes varying between 0.1 and 0.3 mag. The episodic PAGB mass loss has a direct effect on the life time of the PAGB phase and hence monitoring of these sources is very essential to understand its variability. The circumstellar environment around these sources evolves as the central star proceeds towards the PNe phase. It is still not very clear if the dust composition in the envelopes of

PAGB/PPNe is predominantly carbonaceous or not (Cerrigone *et al.*, 2009; Zhang, Kwok and Hrivnak, 2010). Hence studying the observed PAH, silicate, 21 and 30 μm features and their relation with the evolution of the central source helps in a better understanding of the minerology.

In this Chapter we present our investigation of an unprecedented large sample of PAGB/PPNe candidates. Our study includes NIR and mid-IR spectra as well as SED modeling.

5.2 The Sample Stars

The PPNe and PAGB stars for the present study were selected from Stasińska *et al.* (2006) and Szczerba *et al.* (2007). A sample of 14 PAGB stars was used for the variability studies at the NIR wavelengths. Mid-IR investigations were done on a sample of 50 PPNe and about 21 PAGB stars. Spectral types for most of the PPNe candidates were taken from SIMBAD and for those objects without SIMBAD classification, we have used the spectral classification by the optical survey of Suárez *et al.* (2006). Some of the objects in the selected PPNe and PAGB star samples are identified as "transition objects" by Suárez *et al.* (2006). It may be noted that there exist small (and in some cases, large) differences in spectral types of some of the common objects between SIMBAD and Suárez *et al.* (2006).

The classification based on the IRAS [25-60] vs [12-25] colours (van der Veen and Habing, 1988) for all the PAGB/PPNe objects in our sample that are used for the mid-IR study showed an advanced stage of evolution with cooler circumstellar shells than their AGB counterparts (see Fig 5.1). The green circles in Fig. 5.1 represent the AGB stars (from Chapter 4) with warm circumstellar envelopes. The blue triangles and red asterisks represent the PAGB and PPNe sources in our sample. The warm circumstellar matter in the AGB stars may be due to the presence of the expanding envelopes at a smaller radii from the central source than in the case of PAGB/PPNe. In PAGB/PPNe the shells are detached from the central star and drifted far off,

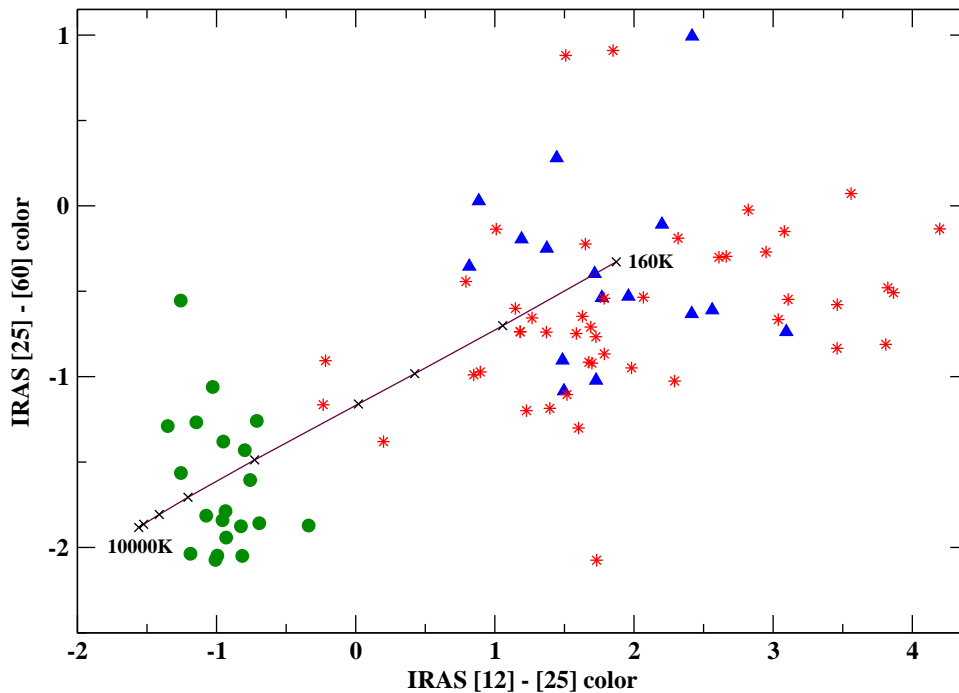


Figure 5.1: IRAS color-color diagram for the stars in our sample. PAGB (blue triangles) & PPNe (red asterisks) occupy positions that have very cool circumstellar shells. The AGB stars (filled green circles) from the previous chapter are also shown for comparison. The crosses along the maroon line represent the black-body temperatures of 10,000, 5000, 2000, 1000, 500, 300, 250, 200 and 160 K

hence their lower temperatures which depict the advanced stage in evolution.

5.3 NIR Observations of a sample of PAGB stars

NIR spectrophotometric observations on a sample of PAGB/PPNe objects were made using NICMOS/NICS at the cassegrain focus of the PRL's 1.2 m telescope facility situated at Mt. Abu.

5.3.1 Data reduction:

NIR spectroscopic observations were made in the JHK bands. Sky subtraction, wavelength and photometric calibrations were performed using the same techniques as described in the earlier Chapter(s).

EWs were computed for all the spectral features detected in our sample stars. The errors in the EWs were estimated to be about 3 \AA for 3σ line detection and $\leq 1 \text{ \AA}$ for detection greater than 5σ .

5.3.2 Spectral variations in some PAGB objects

Repeated spectroscopic observations were made on a few selected stars as listed in Table C.1. The spectral classification (see Table C.1) of these sources was made by Szczerba *et al.* (2007), He *et al.* (2014) and Yoon *et al.* (2014). Table C.1 list the EWs (in \AA , positive for absorption and negative for emission) for the Paschen β , Brackett γ and sum of the Brackett series lines observed in H band. In addition it also gives the EW of the sum of first and second overtone bands in the K and H bands for the stars in our sample. The obtained spectra are compared for sources that had earlier observations from Hrivnak, Kwok and Geballe (1994), Oudmaijer *et al.* (1995) and Kelly and Hrivnak (2005) to identify possible spectral variability. The nature of sources that showed considerable variability are described.

IRAS 10158-2844:

The PAGB star IRAS 10158-2844 (spectral class B9.5Ib-II) was observed on March 18, 2010, February 18, 2012, March 19, 2012, March 30, 2012 and January 19, 2013. The NIR spectra observed between February 18, 2012 and March 30, 2012 showed variability in the Paschen β and first overtone bands of CO. The faint CO first overtone band emission observed on February 18, 2012 became featureless during our observation on March 30, 2012. Also the Paschen β line which was absent during February 18, 2012, reappeared in absorption during March 30, 2012 in a time span of 42 days. The observed

short-term variability may be attributed to episodic nature of PAGB mass-loss. The K band spectra observed during March 18, 2010 was almost featureless, apart from a weak $\text{Br}\gamma$ absorption. The line profiles of the Paschen β and Brackett series show an inverse P-Cygni profile during January 19, 2013. The absorption profile is partially filled with emission, leading to complex structured profiles that can be interpreted as an indication of PAGB mass-loss (Sánchez Contreras *et al.*, 2008).

IRAS 12538-2611:

IRAS 12538-2611 (spectral type F3Ia) is located at a high Galactic latitude ($l=304.3$, $b=36.4$) with a pulsation period of 44 to 68 days (Arellano Ferro, 1981). It has been classified as a semi-regular pulsating star by SIMBAD

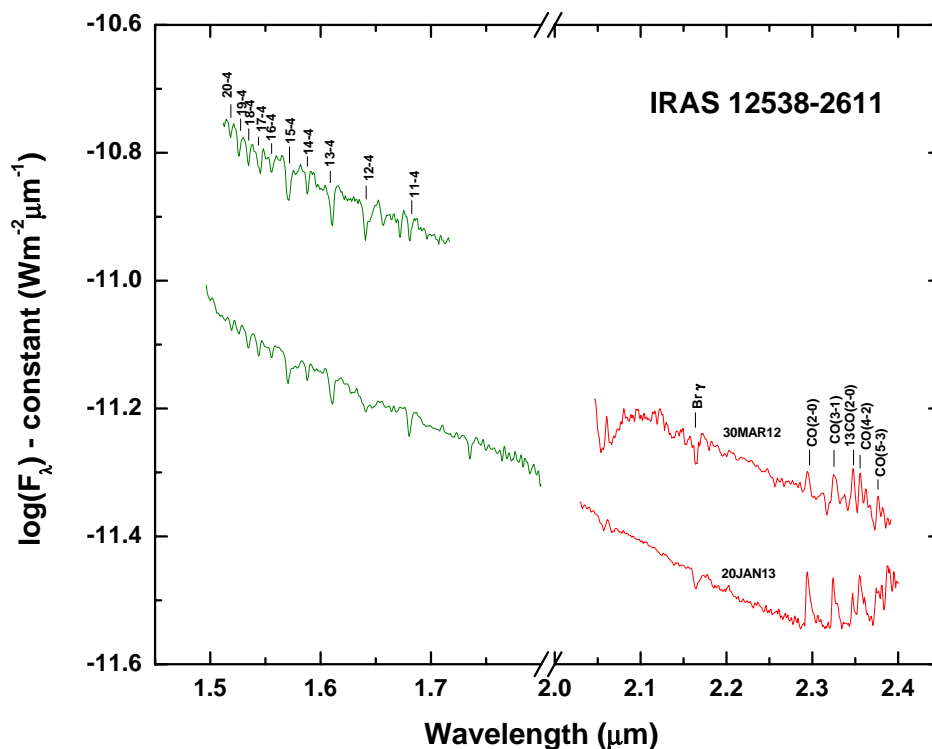


Figure 5.2: NIR H - and K -band spectra of IRAS 12538-2611 observed on March 30, 2012 and January 20, 2013

and as a Cepheid-like supergiant by Arellano Ferro (1981). Luck, Lambert and Bond (1983) has suggested this object as a possible PAGB star based on their spectroscopic studies at optical wavelengths. Giridhar, Ferro and Parrao (1997) found the abundance pattern similar to oxygen-rich PAGB stars. The NIR spectra show Brackett series lines in absorption and CO first overtone bands in emission. Earlier Gorlova *et al.* (2006) had obtained similar features for yellow hypergiant ρ Cas and explained their results by considering the CO emission arising from regions in the near vicinity of the photosphere that are surrounded by a layer of cool gas. The CO emissions arising from the photospheric pulsations are least influenced by the surrounding cool gas. The HI absorption profiles are believed to be caused by these cool layers of gas. Such a scenario can be used to explain the observed NIR features from IRAS 12538-2611. Figure 5.2 represents the NIR spectra observed on March 30, 2012 & January 20, 2013 displaying variability in the first overtone bands of CO. The CO band intensity increased between the two epochs of observations separated by 10 months. The second overtone band of CO displays faint emission.

IRAS 17423-1755:

The PAGB star IRAS 17423-1755 displays bipolar morphology with a spectral classification of Be (Manteiga *et al.*, 2011). The NIR spectra showed emissions in the Brackett series and first and second overtone bands of CO. We made repeated observations on May 29, 2003, May 13, 2007 and April 28, 2012. The EWs of the observed features are listed in Table C.1. Traditionally the hydrogen recombination lines observed in emission lie between the two limits, Case A and Case B. Case A assumes an optically thin limit where hydrogen emission from all energy levels (Lyman, Balmer, etc) can escape the nebula unabsorbed. Case B situation assumes an optically thick case where all transitions more energetic than $\text{Ly}\alpha$ are absorbed and re-radiated at longer wavelengths. The line ratios reveal information on the ionizing continuum, gas temperature etc. The line ratios of Brackett series lines deviated from Case B during the observation on May 29, 2003 and May 13, 2007. These

observations indicate the changes in electron density or opacity. This star also showed CO first overtone bands in emission. Gauba *et al.* (2003) found emission lines in the optical spectra of IRAS 17423-1755 and hence termed it as transition objects. Our NIR spectra observed on April 28, 2012 showed first and second overtone bands of CO and Brackett series lines in emission. Earlier García-Hernández *et al.* (2002) had observed this source in the *K* band and our results are consistent with their result. The presence of regions of hot and dense equatorial winds is clearly evident from the NIR spectra that show strong emissions in the CO overtone bands and Brackett series.

IRAS 17436+5003:

This object has been classified as a semi-regular pulsating star with a spectral type of F3Ib by SIMBAD. However Sahai *et al.* (2007) and He *et al.* (2014) classified it as a high-latitude PAGB star and proto-planetary nebulae respectively. Our observations of IRAS 17436+5003 on March 18, 2010 showed the absence of the first overtone bands of CO, whereas Hrivnak, Kwok and Geballe (1994) observed faint CO emission. Our observations, made about 16 years later, show clear indication of variability of CO in the star which might have occurred during the intervening period. In this case, the variation was found only in CO bands while the HI lines did not change.

IRAS 18237-0715:

IRAS 18237-0715 (spectral type B5-B9) has been classified as a Be star by SIMBAD and Szczerba *et al.* (2007). Gauba *et al.* (2003) classified it as a hot-PAGB star. It shows strong hydrogen series lines in emission. Repeated spectroscopic observations were made on May 28, 2004, November 3, 2006 and May 14, 2007. The EWs of the observed features are listed in Table C.1. The object showed variability in the HI Brackett series lines between these observations. The Brackett line ratios matched well with the Case B assumption on May 28, 2004 and November 3, 2006; while on May 14, 2007 the ratios deviated from Case B. Earlier in a detailed study Miroshnichenko *et al.* (2005) found

spectral line variations in this object. Miroshnichenko *et al.* (2005) suggested the nature of the object to be a luminous blue variable. Gauba *et al.* (2003) found emission lines in the optical spectra and classified it as transition object. Our IR spectra of this object closely resemble those of Miroshnichenko *et al.* (2005) which was obtained at a spectral resolving power of 1200.

IRAS 19399+2312:

On the basis of the IRAS colors, Gauba *et al.* (2003) suggested that IRAS 19399+2312 (also known as V450 Vul) as a hot PAGB star, possibly in transition to become a PPNe. It was classified as a B1III star by Parthasarathy, Vijapurkar and Drilling (2000) but as B1IIIe by Kohoutek and Wehmeyer (1999). Greaves (2003) argued that being a possible member of the cluster NGC 6823, this star is unlikely to be a PAGB transition object but could be a spectroscopic type Be star. We made *JHK* band spectrometry at Mt Abu Observatory on this object on five occasions during November 1, 2005, May 15, 2007, June 6, 2007, April 24, 2008 and December 1, 2010. The EWs of the observed spectral features are listed in Table C.1. Figure 5.3 represents the observed NIR spectra.

The spectra of November 1, 2005 showed some what shallow absorption in HI Paschen β and Brackett series lines. The later spectra (on June 6, 2007) however showed very prominent emissions in the HI lines, as well as a few permitted lines in HeI and even the forbidden line in [FeII] ($1.60 \mu\text{m}$) though at relatively lower S/N (see Fig 5.3). We also notice at a rather low S/N but still discernable CO ($\Delta v=3$) bands in absorption. The appearance of the CO absorption bands is not usual in Be stars, as also the forbidden lines of metals ([FeII]). In view of the appearance of forbidden lines (which was not reported earlier), and faint but significant CO bands, we believe that this object may as well be a transition object. The emission lines reverted back to their earlier absorption profile during December 1, 2010. To the best of our knowledge, these are the first observations that show spectral variability in this object. From the ratios of the Brackett series lines, which deviate from the Case B as-

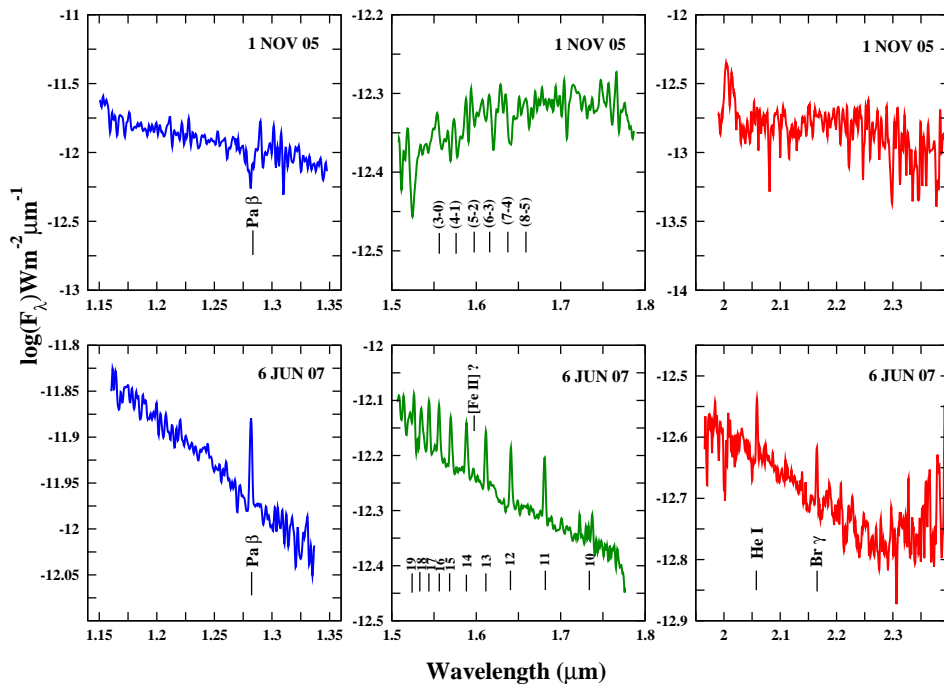


Figure 5.3: NIR J -, H - and K -band spectra of the PAGB star IRAS 19399+2312 observed on two dates

sumption (see for example, Lynch *et al.* (2000)), we infer variations in electron density or opacity in the atmosphere of this object between May 15, 2007 and June 5/6, 2007.

IRAS 20004+2955:

This object has been classified as a pulsating variable star (spectral type G7Ia) by SIMBAD; but as a post-AGB star by He *et al.* (2014). The star observed on November 2, 2012 displayed Brackett HI series lines in absorption in the H and K bands. The first overtone bands of CO and the Na lines are seen in emission. Hrivnak, Kwok and Geballe (1994) showed strong absorption in these bands. The possible mechanism for the CO first overtone band emission with Brackett series lines in absorption may be similar to the scenario that

explains the spectra of IRAS 12538-2611.

IRAS 22272+5435:

The spectra of this object of spectral type G5Ia show signatures that are probably indicative of its advanced stage of evolution in the PAGB phase. It

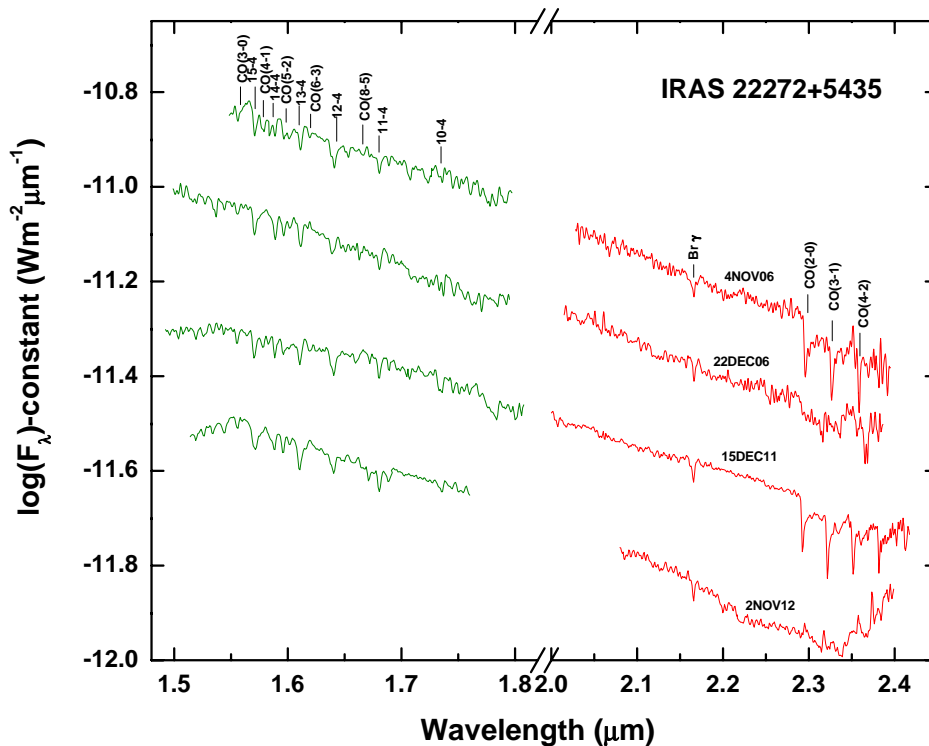


Figure 5.4: Mt. Abu multi-epoch *H*- and *K*-band spectra of the PAGB star IRAS 22272+5435

was shown by Hrivnak, Kwok and Geballe (1994) that the object had undergone episodes of mass loss evident from the month-scale variability in its spectra. They also suggested that it changed from CO emission to absorption in a period of three months. Fig 5.4 shows the spectra on 4 occasions and it is clear that the CO first overtone bands in the *K* band seen on November 4, 2006 were absent on December 22, 2006 and re-appears in emission during November 2, 2012. But the Brackett HI absorption lines were seen in both *H*

and K band spectra on all occasions. Interestingly the H band second overtone bands of CO were still present in the spectra on December 22, 2006. This shows that the mass loss reached the outer regions of the atmosphere where the temperature is about a few hundreds of degrees K. The pulsations must be responsible for heating the matter in these regions resulting in the excitation of these lines and filling the absorption seen earlier.

The K band spectra obtained on November 2, 2012 show the first overtone bands of CO in emission. The CO second overtone emissions are not detected. The CO emissions may be due to heating of the circumstellar material by the stellar wind that is generated during the pulsation resulting in episodic mass loss from the central source.

IRAS 22327-1731:

This object (spectral type A0III) has been classified as a PAGB/PPNe by SIMBAD. The NIR spectra during the 2006 observation showed Paschen β , Brackett series lines and CO overtone bands in absorption. Repeated observations during December 16, 2011 showed very broad HI Brackett series lines in absorption with faint emission in the first overtone band of CO. The CO first overtone band and the Brackett series lines are not detected in the earlier observations of Oudmaijer *et al.* (1995), thus these lines show variability.

5.3.3 Discussion

From the Table C.1, it is clear that the Brackett series lines of HI were found mostly among the PAGB/PPNe stars where a hotter central source is believed to be present. Some PAGB stars in our sample (IRAS 06556+1623, 17423-1755, 18237-0715 and 19399+2312) showed HI Brackett series line in emission and an indication of fainter emission in CO. This could be due to the fact that as the central star evolves, its temperature increases and heats up the circumstellar material making the CO bands progressively weaker until they finally disappear. Around this time the HI recombination lines start becoming prominent in emission. The evolution of the central source and its relation to

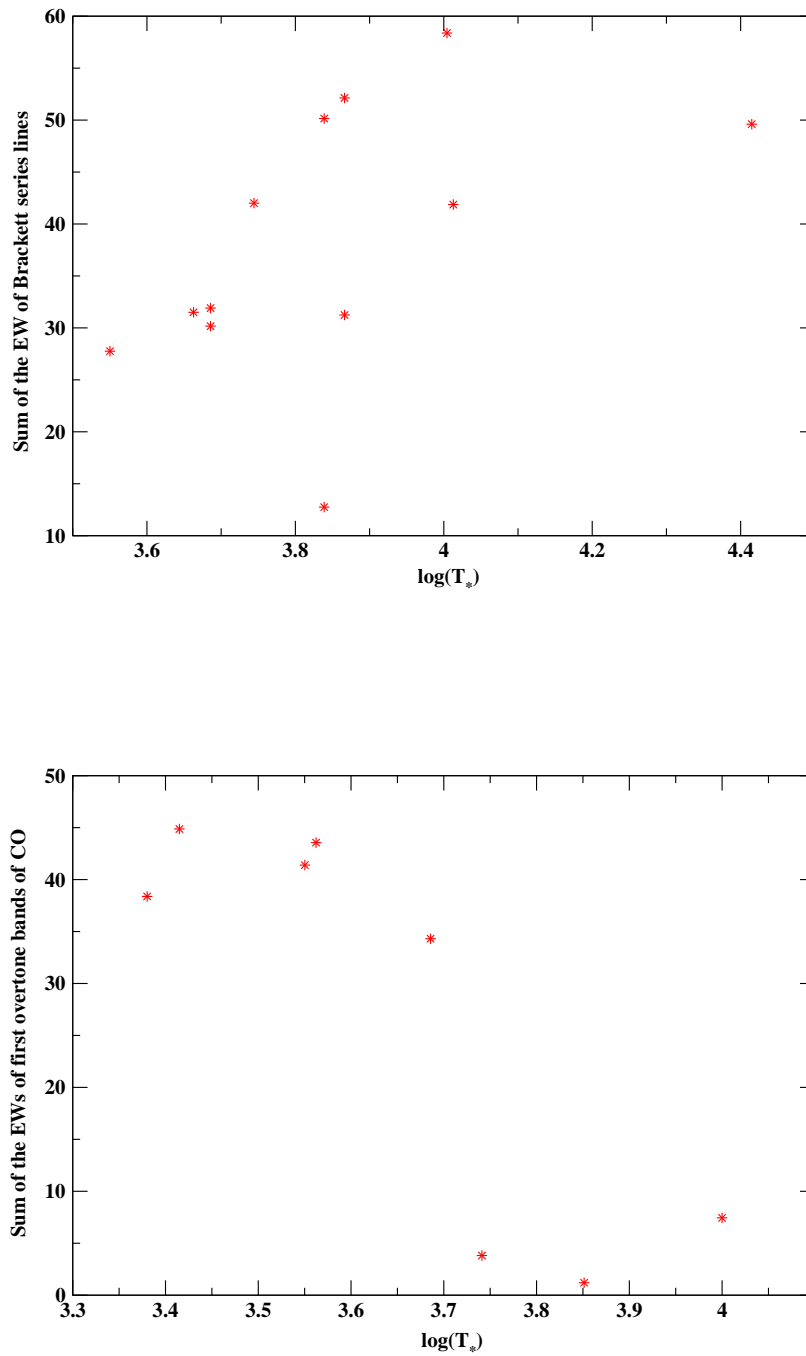


Figure 5.5: Plot of the sum of Brackett series lines (top panel) and sum of the first overtone bands of CO (bottom panel) with the effective temperature of the star

the observed Brackett series lines and CO overtone bands for the PAGB/PPNe candidates in our sample are discussed below.

5.3.3.1 Evolutionary trends in the NIR spectra

The strengths of the Brackett lines are sensitive to photospheric temperature and degree of ionisation. Fig 5.5 (top panel) shows a positive correlation between the effective temperature of stars (obtained from the spectral types) and the sum of the EWs of the HI Brackett series lines. For stars with repeated observations an average value of the EW was considered. The plot shows that the EW of Brackett series lines reaches a maximum as the stellar temperature approaches 10,000 K, a behavior similar to stars with spectral type A0. Fig 5.5 (bottom panel) shows the sum of the first overtone bands of CO plotted with the photospheric temperature with T_* . The plot shows a decreasing tendency for CO bands with T_* . Thi, Bik and Waters (2005) suggested that CO molecule start to get dissociated at temperatures greater than 3000 K. Thus, the decreasing trend in the first overtone bands of CO beyond the photospheric temperature of 3000 K corroborates this result. Cooler PAGB/PPNe stars show variability in CO first overtone bands and hotter stars showed variability in HI lines. In both cases variability may be associated with episodic mass loss.

5.4 *Spitzer* spectra of PAGB/PPNe objects

Mid-IR spectra of stars in our sample were mostly obtained from the public data archives of the *Spitzer*. The data from the ISO archive were used for a few sources in our list where *Spitzer* data were not available. The archival spectroscopic data in the mid-IR region of 5 - 38 μm were used in the present study for a sample of 50 PPNe and 21 PAGB candidates. The details of the *Spitzer* and ISO instruments and the data analysis procedures are described in Chapter 2. The present analysis of the mid-IR spectra for the sample of PAGB/PPNe objects indicated a broad classification based on the identified

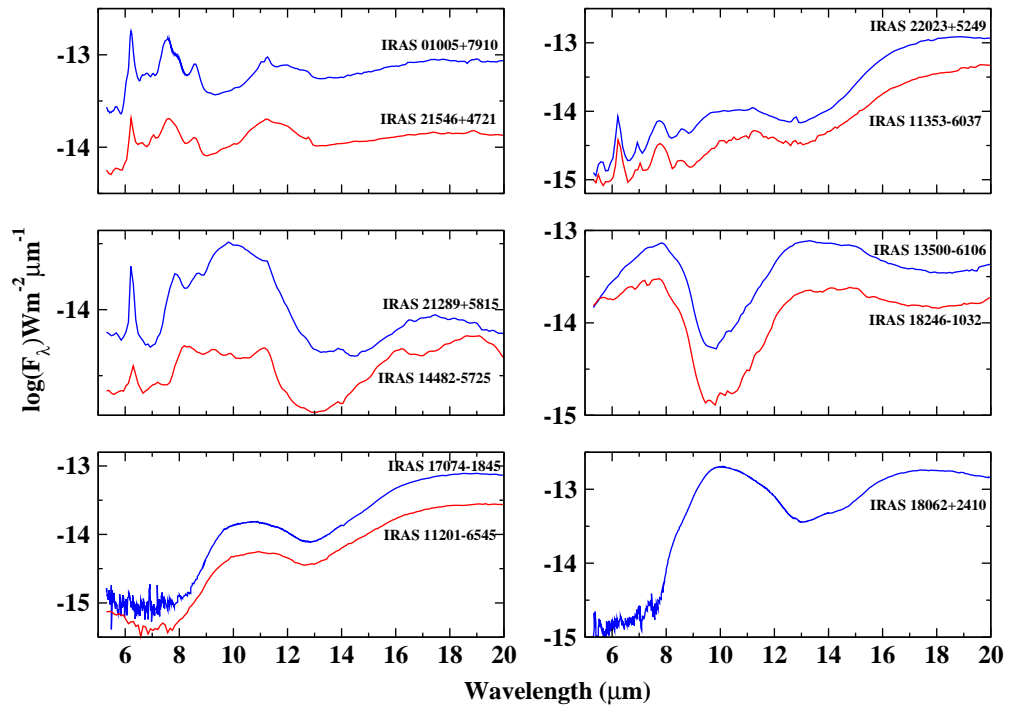


Figure 5.6: Typical *Spitzer* IRS spectra of the PPNe (blue) & PAGB (red) stars showing strong PAH features (top left), weak or blended PAH features (top right), PAH + silicate dust emission features (middle left), silicate absorption (middle right), prominent broad bump around $11 \mu\text{m}$ (bottom left) and silicate emission (bottom right)

spectral features as those having (i) strong PAH features (ii) weak or blended PAH features (iii) PAH + silicate dust in emission (iv) silicate absorption (v) prominent broad bump around $11 \mu\text{m}$ (vi) silicate emission and (vii) nearly featureless spectra. Figure 5.6 gives typical spectra of the PAGB & PPNe candidates depicting the above classifications.

In general, about 34% of the PPNe sample considered here showed strong or weak/blended PAH features, 20% of sources showed $11 \mu\text{m}$ feature, 30% of sources are featureless, 6% of sources showed silicate absorption and 10% showed silicate emission. In comparison, about 35% of the PAGB stars consid-

ered here showed strong or weak/blended PAH features, 15% of sources showed 11 μm feature and 50% of sources showed featureless spectra. It may be conjectured that the objects showing featureless spectra may be relatively young compared to the other sources (Waelkens and Waters, 2003). The equivalent widths of the mid-IR spectral features were determined using SMART. The errors are estimated to be 0.001 μm for a high S/N (≥ 5) and 0.01 μm for low S/N (≥ 3) line/band. Tables C.2, C.3 list the EWs of the PAH features for PPNe and PAGB candidates respectively.

5.5 Modelling of SEDs

The photometric data required for constructing the SEDs were obtained from several archives covering the entire visible to far-IR region. The visible *UBVRI* photometry was obtained from VIZIER data archives; the NIR *JHK* bands from the 2MASS archive (Skrutskie *et al.*, 2006); mid-IR from MSX (Egan *et al.*, 2003b) and IRAC-SPITZER (Benjamin *et al.*, 2003) and the mid-IR bands from AKARI (Ishihara *et al.*, 2010) and IRAS (Helou and Walker, 1988) archives. The SEDs of the sample stars were modeled using the software DUSTY (Ivezic, Nenkova and Elitzur, 1999). The input parameters for each object consist of stellar photospheric temperature (T_*), temperature of the inner region of the dust shell (T_d), composition of the dust grains and the optical depth at 0.55 μm ($\tau_{0.55}$). For all the sources modelled, a modified MRN (Mathis, Rumpl and Nordsieck, 1977) dust size distribution was assumed with an exponent of 3.5 having minimum and maximum dust grain sizes of 0.005 and 0.25 μm respectively. A radiatively driven wind model was chosen in which the envelope expansion is owing to the radiation pressure on dust grain particles (see Ivezic and Elitzur (1997)). The code solves the radiative transfer problem for a source embedded in a spherically symmetric dusty envelope. The important output parameters of the code are the total flux versus wavelength, the inner shell radius r_1 , the ratio of inner shell radius and the radius of central source r_1/r_c . The model also gives an estimate of mass loss rates

($dM_{gas}/dt=\dot{M}$) for envelope expansion that are driven by radiatively driven winds.

The model fluxes at each wavelength for which observed flux is available, were computed by normalising with the flux at either 2 μm (K band) or at 9 μm band (of MSX or AKARI or IRAC) depending upon the distribution of data points in the IR range. For those objects whose spectral types are identified, T_* was taken from Lang (1999) and Cox (2000). For all the other objects whose spectral types are not available, we have estimated T_* from model best fits. A criterion for the best fit was chosen as, $\chi^2 = \sum_i [(F_{O_i} - F_{M_i})^2 / F_{M_i}] \leq 10^{-12}$, where \sum_i indicates summing over all the data points ($i = 1$ to n , n being the number of data points for a particular source) and F_{O_i} and F_{M_i} are the observed and model fluxes at i^{th} data point respectively. For most of the sources in our sample this limit had resulted in reasonably good fits (visually), except for a few sources. It may be noted that the spectral class differences in some of the objects that are common in SIMBAD and Suárez *et al.* (2006) did not alter the model derived parameters by more than 10%.

For the purpose of modeling, we have divided our sample stars (PPNe/PAGB) into two categories: (i) those showing no PAH feature at all and (ii) those that show clearly the PAH features in the region of 6-15 μm . The first category was modeled using a single shell to represent the circumstellar matter. Tables C.4 & C.5 show the list of such PPNe & PAGB sources respectively along with model-derived photospheric and circumstellar shell parameters, namely, T_* , T_d , \dot{M} , $\tau_{0.55}$, r_1 , r_1/r_c and the grain composition (Gr is for graphite and AmC for amorphous carbon and Sil for silicate grains with the portion in 1 given in parentheses). It is clear from the two tables that the grain composition for all the sample stars contain carbonaceous dust (either graphite or amorphous carbon or a combination of the two); except for about 14 PPNe & 3 PAGB objects for which silicate grains constitute their dust envelopes. There is a preponderance of graphite grains in the dust composition in PAGB stars (about 95% of cases), while in the case of PPNe there seems to be a diminishing of this trend with graphite dominating in about 84% of the

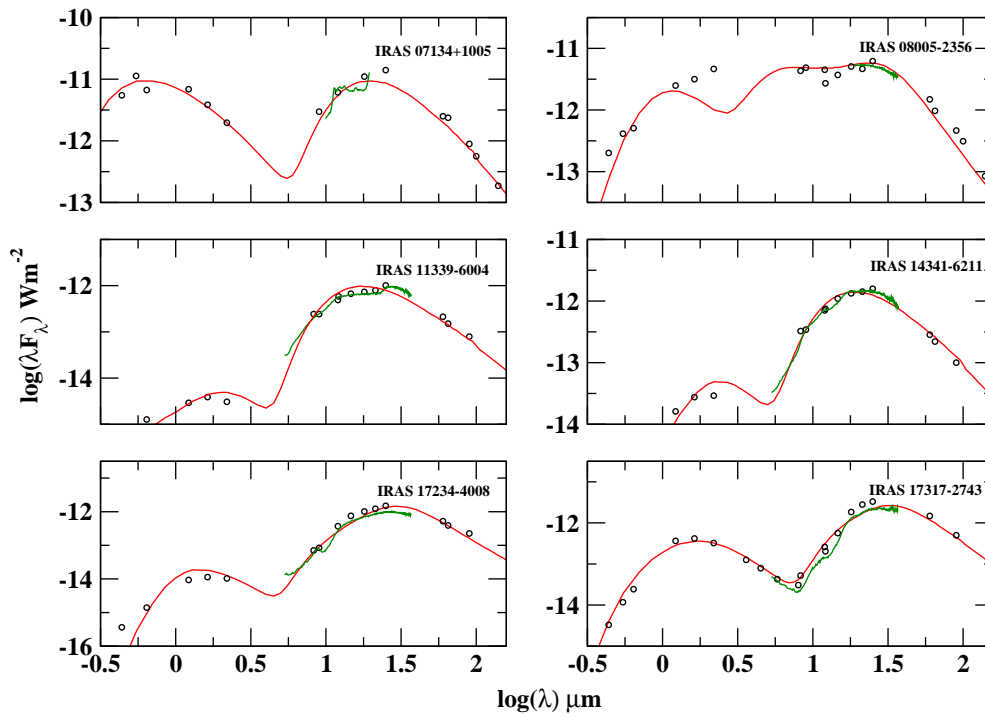


Figure 5.7: Model SEDs with single shell using DUSTY (red line) for a few PPNe compared with observed data from literature (open circles). The *Spitzer* IRS spectra are shown in green for comparison

cases. The result from our SED modeling showing most of the sample stars (both PPNe and PAGB stars) to have predominantly carbonaceous circumstellar dust does not fall in line with the finding of Cerrigone *et al.* (2009), whose sample showed a mere 25% having carbon rich envelopes. Figures 5.7 & 5.8 show typical model fits for the PPNe and PAGB objects in our sample. The *Spitzer* IRS spectra are overplotted in green for comparison.

For those sources for which the *Spitzer* IRS spectra showed strong PAH emissions (26 in number), we have used two spherical shells (instead of one used before) for the SED modeling using DUSTY. The first shell contains neutral or ionised PAH while the second, outer shell contains any of the common dust grains (amorphous carbon/silicate/graphite). So it is assumed that PAH and

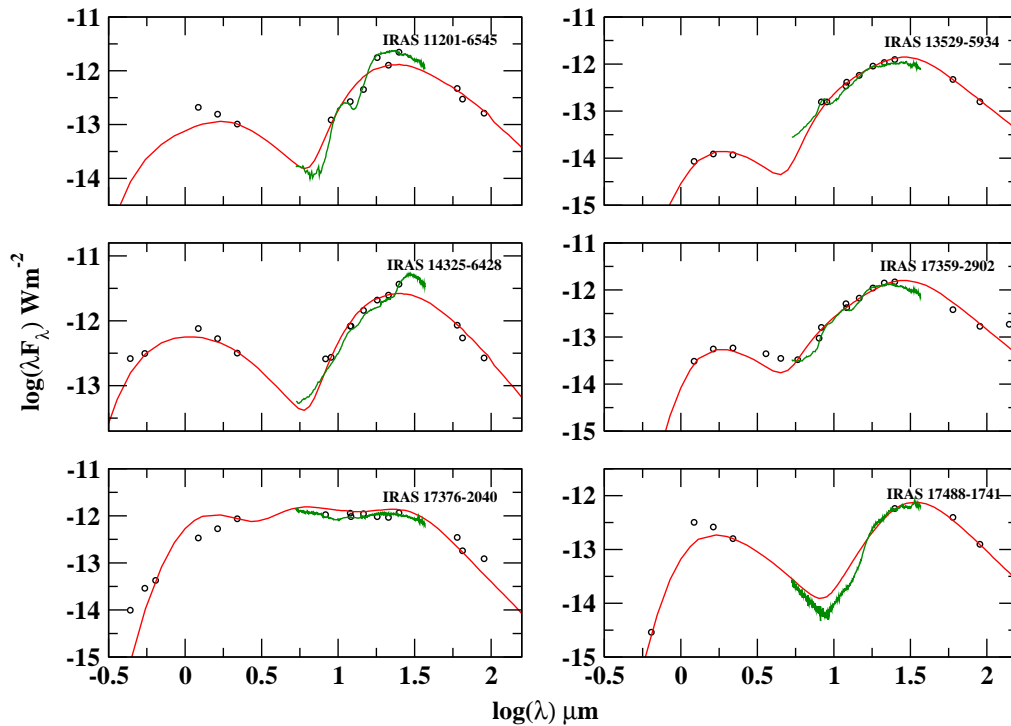


Figure 5.8: Model SEDs with single shell using DUSTY (red line) for a few PAGB compared with observed data from literature (open circles). The *Spitzer* IRS spectra are shown in green for comparison

dust exist in two separate shells and are not mixed. The density distribution falling off as r^{-2} was used for both the dust shells. Tables C.6 & C.7 show the list of these PPNe & PAGB sources respectively along with the derived photospheric and circumstellar shell parameters, T_* , T_d , ionised state of PAH in the first sphere, as inferred from the ratio of $6.2/7.6 \mu\text{m}$ and $11.2 \mu\text{m}$ features (see section 5.6.1), r_1 , r_1/r_c for both the shells and the grain composition in the shell 2. Figure 5.9 shows typical model fits for six PPNe sources with PAH emissions observed from *Spitzer* IRS spectra. The *Spitzer* IRS spectra are shown in green for comparison.

The SED modelling reveals a few interesting physically viable relationship

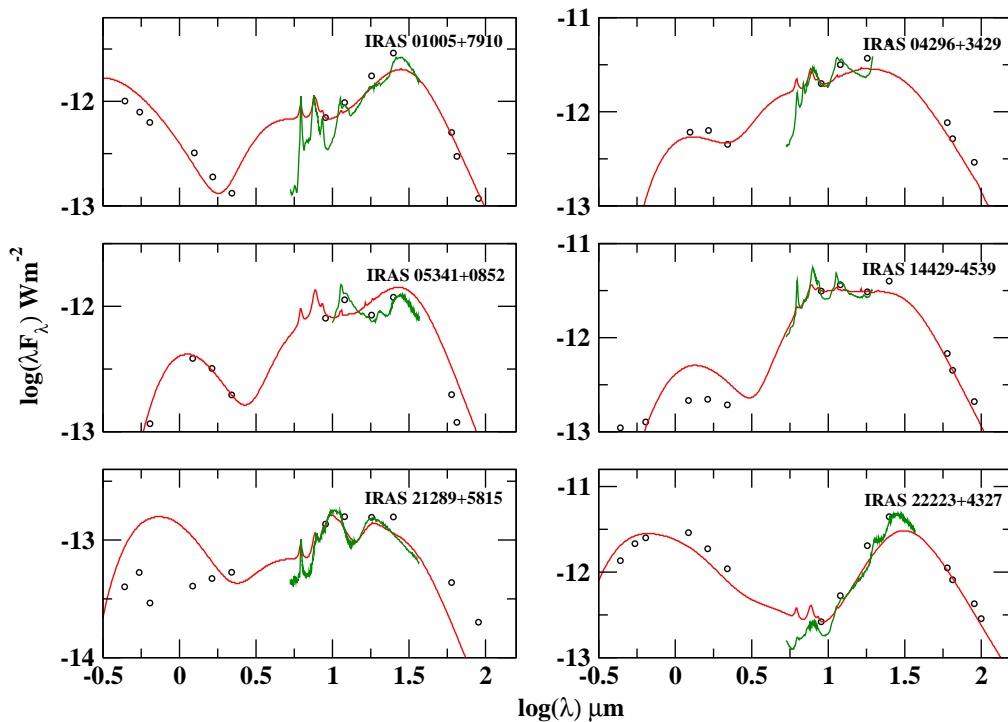


Figure 5.9: Model SEDs with two spherical shells using DUSTY (red line) for a few PPNe that showed strong PAH emissions compared with observed data from literature (open circles). The *Spitzer* IRS spectra are shown in green for comparison

between various derived parameters. Fig 5.10 shows the plot between inner dust temperature and the inner radius of the dust shell for all the programme stars. In the case of objects modeled with two shells, the inner radii of both the PAH and dust shells are shown. The plot shows that as the dust temperature increases the radius of the inner shell decreases. This implies that as the dust get cooler it is located farther from the star. It may be inferred from Figure 5.10 that the radius of the inner dust shell corresponding to the typical condensation temperature for (silicate) dust grains, $T_c \sim 1600$ K turns out to be $\sim 3.5 \times 10^{12}$ m. It indicates that the dust formation distance from the stellar photosphere is typically a few stellar radii. It was argued by Woitke,

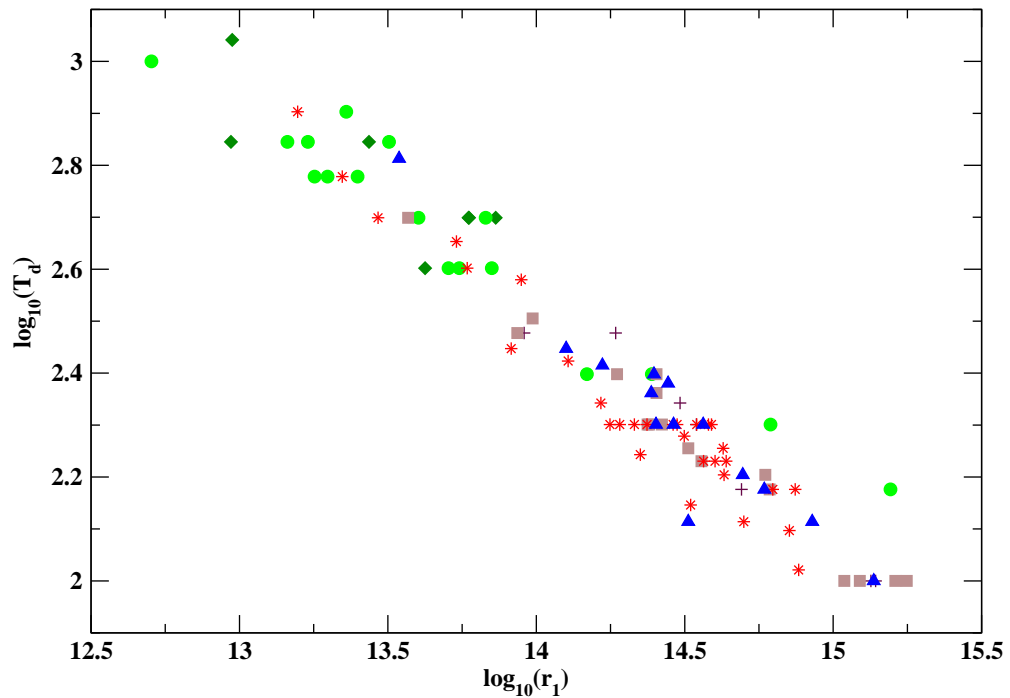


Figure 5.10: Plot of dust temperature T_d versus the inner dust shell radius r_1 (in m) for PPNe (red asterisks) and PAGB stars (blue triangles) obtained from DUSTY SED models with single shell irradiated by radiatively driven winds. The green filled circles and brown squares represent the sphere 1 (PAH) and sphere 2 for PPNe's that showed PAH feature. The dark green diamonds and maroon pluses represent the sphere 1 (PAH) and sphere 2 for PAGB's that showed PAH feature

Goeres and Sedlmayr (1996); Sedlmayr and Winters (2000) that for pulsationally driven mass loss to be most efficient, the dust formation should occur at a few stellar radii (R_*). Fig 5.11 shows the plot of the ratio r_1/r_c as a function of T_* . The plot indicates that the ratio r_1/r_c increases with T_* . As the photospheric temperature increases the star emits copious amount of UV photons that destroy the dust and hence dust can survive only at distances far from the star. This explains the positive correlation between the two parameters, and is in line with the above minimum distance of dust formation argument.

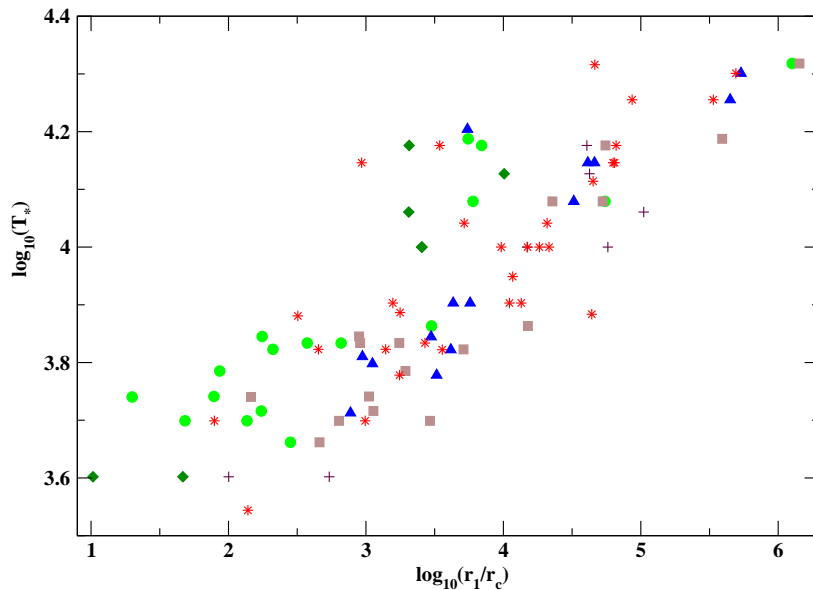


Figure 5.11: Plot of central source temperature T_* versus the ratio of inner dust shell radius r_1 and the central source radius r_c for PPNe (red asterisks) and PAGB stars (blue triangles) obtained from DUSTY SED models with single shell irradiated by radiatively driven winds. The green filled circles and brown squares represent the sphere 1 (PAH) and sphere 2 for PPNe's that showed PAH feature. The dark green diamonds and maroon pluses represent the sphere 1 (PAH) and sphere 2 for PAGB's that showed PAH feature

5.6 Variation of mid-IR spectral features with the evolution (T_*)

In this section we investigate the variation of mid-IR spectral features with evolution of PAGB/PPNe stars. Since, the stellar effective temperature T_* of PAGB stars and PPNe is an indicator of their evolution, we examine the trends in the features with T_* . The SED model-derived T_* is used to represent the evolution.

5.6.1 PAH modes:

Firstly, we investigate various modes of PAH (see Table 1.1 in Chapter 1). Interesting correlations were obtained between the strengths of the PAH spectral features with the physical & circumstellar parameters of the PAGB/PPNe candidates. It may be noted that through out the Chapter we have used the EW as the measure of the strength of the PAH feature instead of the feature intensity used by other authors (e.g. Cerrigone *et al.* (2009); Zhang, Kwok and Hrivnak (2010)). We have found that the usage of EW yielded mainly the same results as that obtained using the intensity of spectral features.

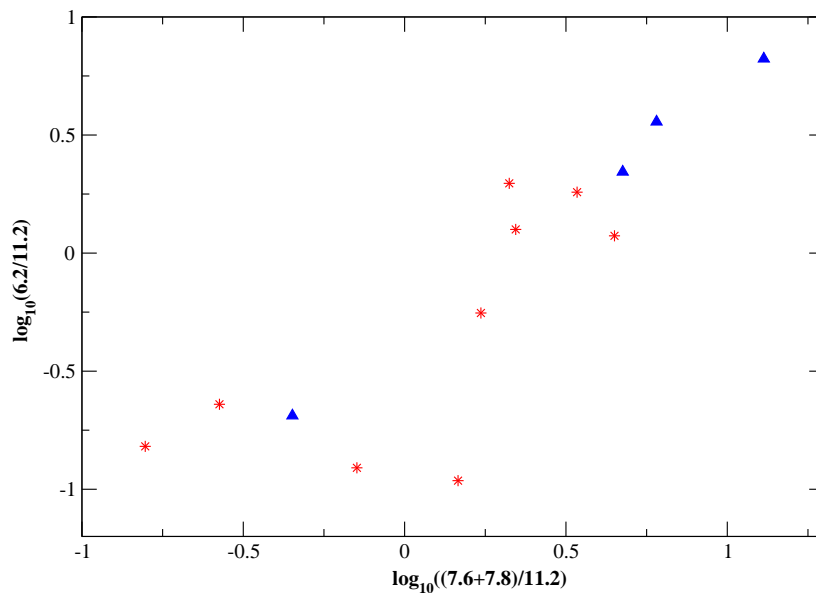


Figure 5.12: Plot of the PAH mode ratio $\log(\text{EW}(6.2)/\text{EW}(11.2))$ vs $\log(\text{EW}(7.6+7.8)/\text{EW}(11.2))$ for PPNe (red asterisks) and PAGB stars (blue triangles).

Ionized PAHs emit more strongly in the 6.2 and 7.7 μm bands while the 11.2 μm band is stronger in neutral PAHs; therefore the ratio of the 6.2 or 7.7 μm PAH over 11.2 μm feature can be used as a measure of the ionization fraction of the PAHs. Cerrigone *et al.* (2009) found an interesting correlation

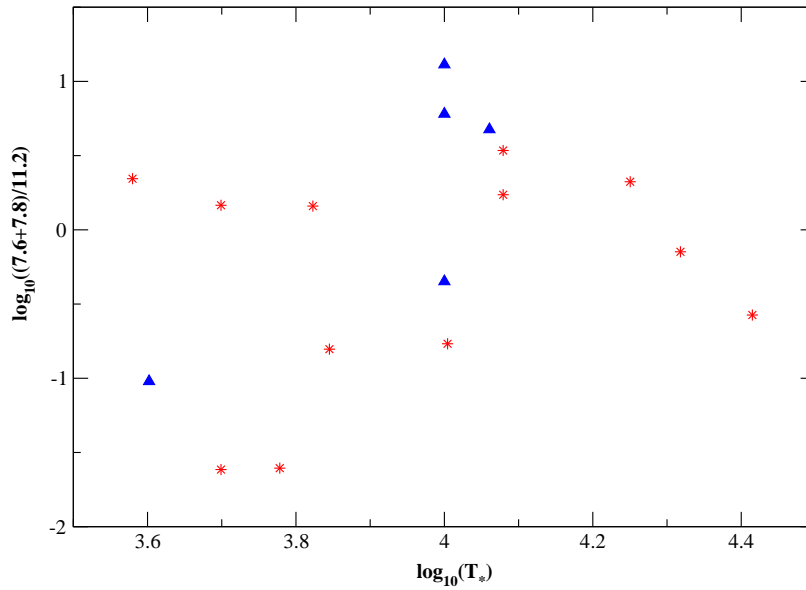


Figure 5.13: Plot of the PAH mode ratio $\log(\text{EW}(7.6+7.8)/\text{EW}(11.2))$ versus effective temperature T_* for PPNe (red asterisks) and PAGB stars (blue triangles).

between $I(6.2)/I(11.2)$ and $I(7.7)/I(11.2)$. Fig 5.12 shows a similar plot of $\log(\text{EW}(6.2)/\text{EW}(11.2))$ vs $\log(\text{EW}(7.6+7.8)/\text{EW}(11.2))$. One may notice an increasing trend as also found by Cerrigone *et al.* (2009). The clear correlation is due to the dependence of these ratios on the ionization fraction (Galliano *et al.*, 2008).

Fig 5.13 shows the plot of the PAH features of $\log(\text{EW}(7.6+7.8)/\text{EW}(11.2))$ versus T_* . It can be concluded from this plot that stars that show ratio $(7.6/11.2) > 1$ have ionised PAH in their circumstellar matter. The PAH bands in the numerator represent the C-C stretching and C-H in-plane bending modes and those in the denominator represent the solo C-H out-of-plane bending modes. One can notice, in the Fig 5.13, a tendency of increasing ratio with T_* , up to a value of 10^4 K indicating the dominance of C-C stretching and C-H in-plane bending modes as the objects evolve. But beyond this value, when the UV photon flux starts becoming significant, the solo C-H out-of-plane bending

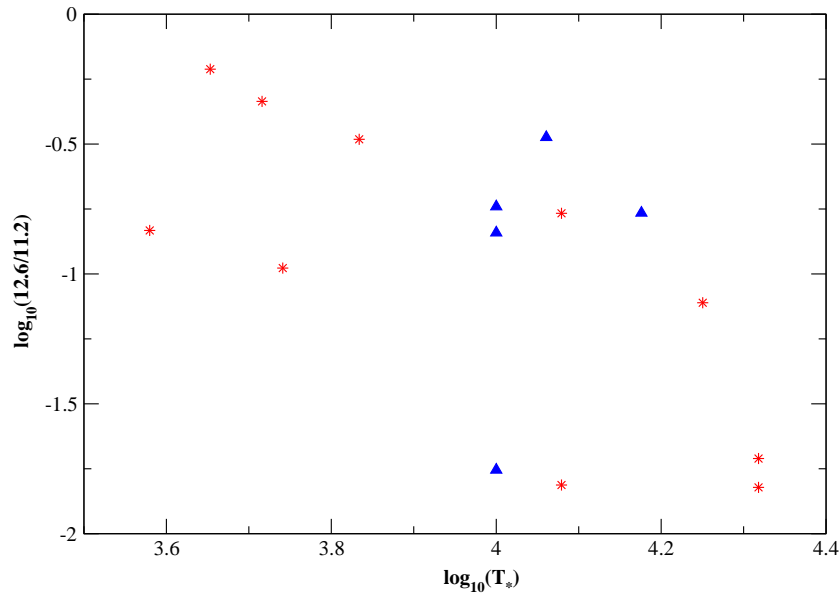


Figure 5.14: Plot of the PAH mode ratio $\log(\text{EW}(12.6)/\text{EW}(11.2))$ versus effective temperature T_* for PPNe (red asterisks) and PAGB stars (blue triangles).

modes dominate as seen from the declining trend of the ratio.

Zhang, Kwok and Hrivnak (2010), in their study of a few PPNe candidates indicated that the ratio of the PAH features of the fluxes $(12.0+12.6+13.5)/11.2$ showed a decreasing trend with the central star temperature indicating that the solo C-H modes at $11.2 \mu\text{m}$ become more and more predominant over the duo- or trio- and quarto- modes around $12-13 \mu\text{m}$. This is suggestive of the possibility that the solo C-H out-of-plane bending modes get stronger as the star evolves to PNe (Kwok, 2004). Fig 5.14 shows the scatter plot of the ratio of $\log(\text{EW}(12.6)/\text{EW}(11.2))$ with T_* . In general, our results show that for nearly all the sources that showed PAH bands, the above ratio is less than 1 suggesting that the solo-modes dominate over the other modes. The ratio also shows a decreasing trend with T_* , in agreement with Zhang, Kwok and Hrivnak (2010). It appears therefore that the PAH ratios for PPNe/PAGB show a changing trend with evolution.

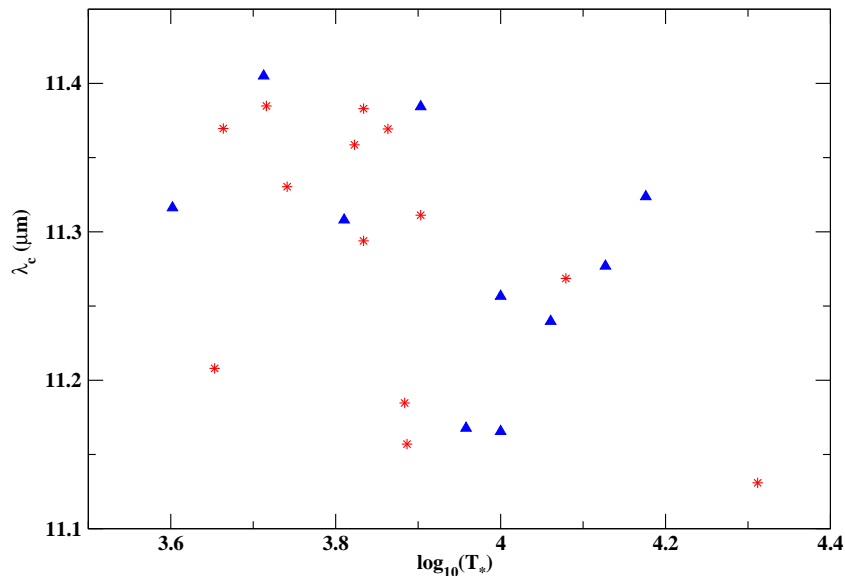


Figure 5.15: Plot of the peak wavelength of the PAH feature at $11.2 \mu\text{m}$ versus the photospheric temperature T_* for PPNe (red asterisks) and PAGB stars (blue triangles).

Sloan *et al.* (2007) showed that the peak wavelength of the $11.2 \mu\text{m}$ feature changes with T_* for a small sample of carbon stars. We verified this result with our sample. Fig 5.15 shows the plot of the peak wavelength of $11.2 \mu\text{m}$ with T_* . One can notice largely a shift towards the shorter wavelengths with increasing T_* up to a value of 10^4 K , beyond which there is a increasing trend.

5.6.2 H₂ rotational lines:

The IRS-*Spitzer* spectra of a few sources in our sample showed the purely rotational lines of H₂ in the ground vibrational level ($v = 0$) (see Chapter 1 for details). Table C.8 lists the EWs of the observed rotational lines of H₂ determined using SMART. Fig 5.16 shows the EW of the rotational lines S(5) (i.e. $J=7 \rightarrow 5$, see Chapter 1 for details) at $6.908 \mu\text{m}$ as a function of stellar photospheric and dust temperatures (blue asterisks for PPNe and red

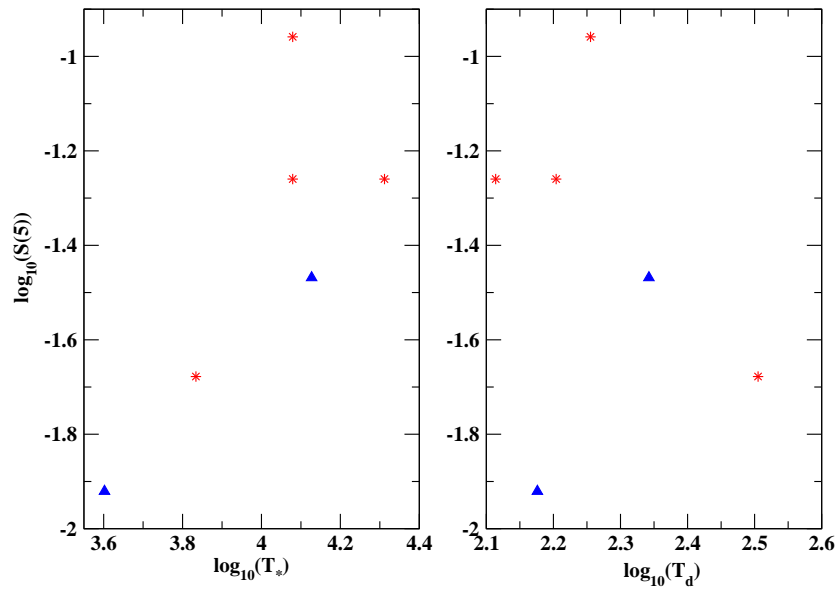


Figure 5.16: Plot of EW of the rotational lines S(5) of H_2 versus the photospheric temperature T_* (left) and dust temperature T_d (right) for PPNe (red asterisks) and PAGB stars (blue triangles).

triangles for PAGB stars). The EW of the molecular line at $6.9 \mu\text{m}$ seems to show a positive correlation with T_* and a negative correlation with T_d . This is understandable because, as the T_* is increasing, the dust can form further off from the star where H_2 is being excited (rotational lines). The range of T_d for which H_2 S(5) is identified for our sample stars is $\sim 125 - 320$ K. It may be noted that the thermal excitation temperature of the rotational lines of H_2 is $500 - 800$ K in photo-dissociation region and shocks. However, if excited collisionally they do not require such high-temperature and can be emitted at 200 K (Glass, 1999), which appears to be the case here.

5.6.3 Trends in the mass-loss rates

The mass loss rates obtained from the model for our sample of post-AGB stars showed expected trends with the other model-derived parameters. Fig 5.17

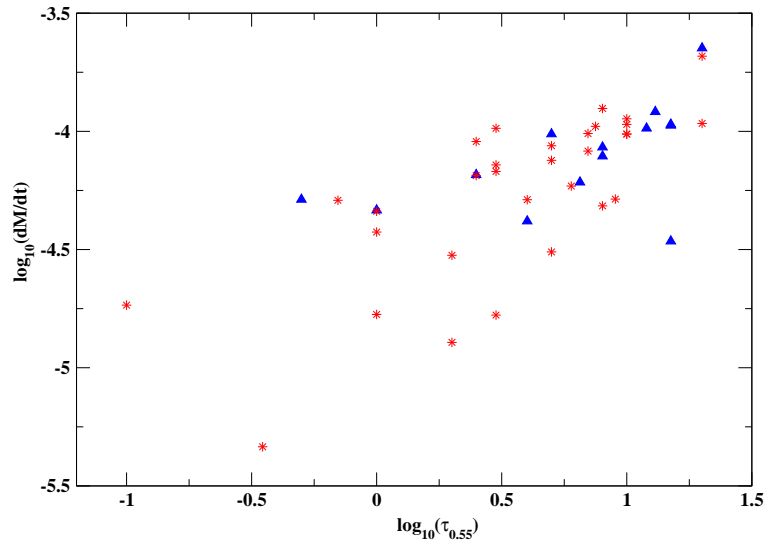


Figure 5.17: Plot of gas mass loss rate dM_{gas}/dt versus the optical depth at $0.55\mu m$ $\tau_{0.55}$ for PPNe (red asterisks) and PAGB stars (blue triangles).

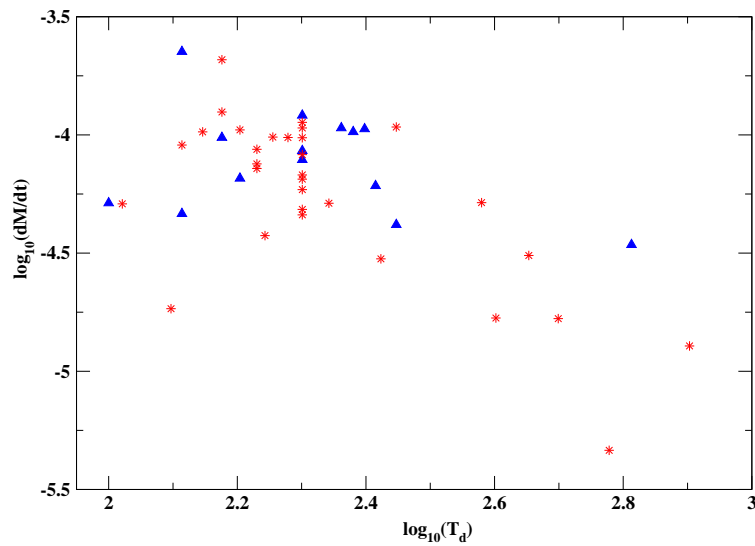


Figure 5.18: Plot of gas mass loss rate dM_{gas}/dt versus the dust temperature T_d for PPNe (red asterisks) and PAGB stars (blue triangles)

shows increasing mass loss rate with increasing optical depth at $0.55 \mu\text{m}$. From the figure it may be inferred that for a majority of the objects the dust shells are optically thick ($\tau_{0.55} \geq 1.0$).

During the mass loss process, the dust shell remains optically thin initially, allowing the radiation from the central star to escape out. But as the mass loss increases, the optical depth increases leading to the formation of more dust that completely blocks the radiation escaping the central star. These are

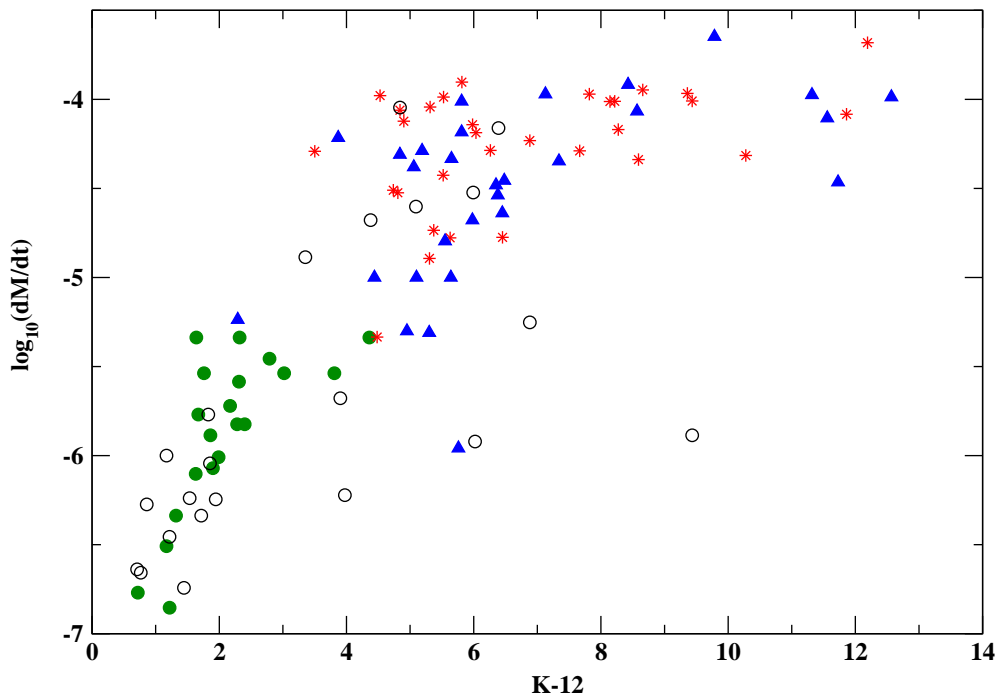


Figure 5.19: Plot of the mass loss rate obtained from DUSTY with the mass loss index $[K - 12]$ for AGB (green circles), PPNe (red asterisks) and PAGB stars (blue triangles). The mass loss rates derived from the observed rotational transitions of CO at mm wavelengths for some of the AGB, PAGB and PPNe stars in our sample (black open circles) are also shown for comparison.

physically expected results and hence the plots not only serve as a validation of circumstellar dust shell properties, but also gives confidence on the accuracy

of the derived model parameters. Fig 5.18 shows the tendency of decreasing mass loss rate with increasing inner dust temperature in line with the above arguments. Fig. 5.19 shows the plot of the mass loss rates with mass loss index $[K - 12]$ for PAGB/PPNe stars obtained from the modeling along with those for AGB stars of the previous chapter. The plot indicates the clear distinction between the three groups and in general leads to a positive correlation. It also indicates that the mass loss does not cease completely towards the end of the AGB phase. The PAGB mass loss rate was found to be much higher than the AGB mass loss rate. The mass loss rates obtained from the SED model for PAGB stars (this Chapter) and AGB stars (previous Chapter) are in reasonably (see Fig. 5.19) good agreement with those determined from the observed CO rotational line profiles by several authors, namely Loup *et al.* (1993a), Sahai and Liechti (1995), Groenewegen and de Jong (1998), Jorissen and Knapp (1998), Winters *et al.* (2000a) and Ramstedt *et al.* (2006) for M, S and SR stars; and Woodsworth, Kwok and Chan (1990), Likkell *et al.* (1991), Omont *et al.* (1993a), Hrivnak and Kwok (1999), Bujarrabal *et al.* (2001), Hoogzaad *et al.* (2002) and Hrivnak and Bieging (2005) for PAGB/PPNe stars (stars marked with † in Tables C.2 & C.3).

5.6.4 Unidentified mid-IR features

From the *Spitzer* spectra we have identified several features in the range of 20 - 40 μm whose origins are still debated. These are in general very broad features compared to the molecular or PAH features. Tables C.9 and C.10 list these lines identified in PPNe and PAGB stars respectively.

5.6.4.1 The 21 μm feature:

Mid-IR spectra of a few PPNe and PAGB candidates in our sample display a broad feature near 21 μm . This feature has been detected earlier in some PAGB sources, C-rich, metal-poor and *s*-process enhanced stars by Kwok, Volk and Hrivnak (1999); Van Winckel and Reyniers (2000). The carrier candidates include TiC (von Helden *et al.*, 2000), SiS₂ grain (Goebel, 1993), doped-SiC dust

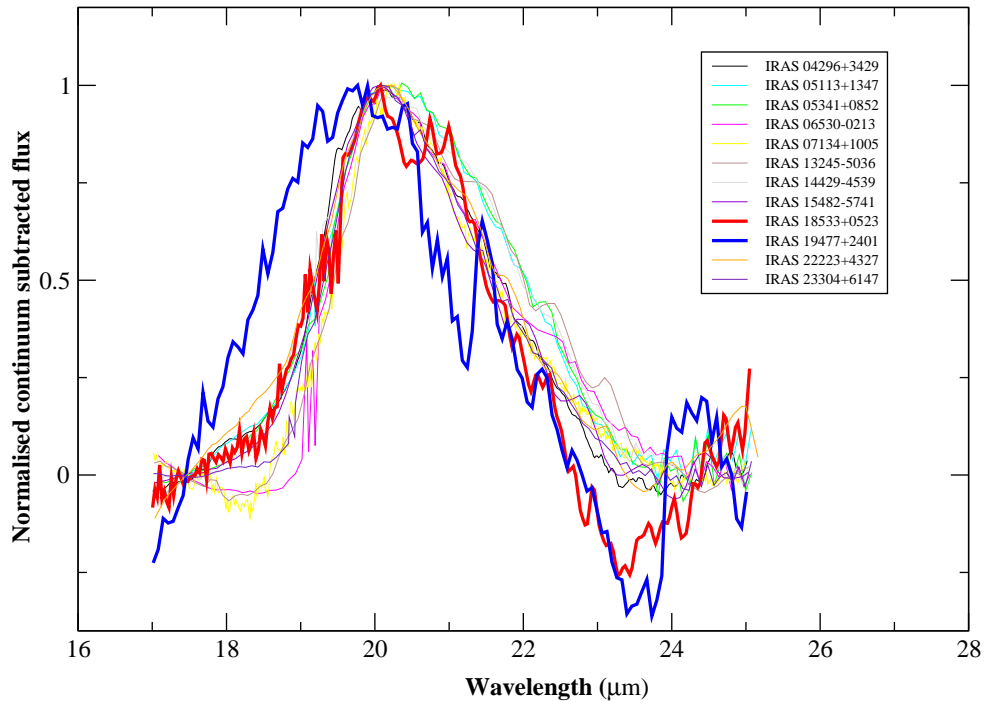


Figure 5.20: Morphology of the feature at 21 μm observed in 10 PAGB/PPNe objects; superposed on it are the profiles of two other PPNe sources IRAS 18533+0523 & IRAS 19477+2401 shown in red and blue respectively that depict different morphology.

(Speck and Hofmeister, 2004), carbon and silicon mixtures (Kimura, Nuth and Ferguson, 2005), FeO (Posch, Mutschke and Andersen, 2004) and PAH (Justanont *et al.*, 1996). Recently, Kwok and Zhang (2011) proposed an alternative grain type called mixed aromatic-aliphatic organic nanoparticles (MOANs) for explaining a number of unidentified features in the mid-IR including the 21 μm feature and those that are commonly attributed to PAH molecules.

We however, find two objects that show morphologically different profiles compared to those observed in 10 other PAGB/PPNe objects. Fig 5.20 shows the profiles for IRAS 18533+0523 and IRAS 19477+2401 that depict substructures not reported previously. It may be noted that the 21 μm feature

for IRAS 18533+0523 is reported for the first time in the present work. This object show split profile with two peaks (having sub-structures) ~ 20 and $21 \mu\text{m}$. In contrast IRAS 19477+2401 shows a split profile with the dominant half blue shifted with respect to the spectral morphology observed in 10 other PAGB/PPNe stars. Posch, Mutschke and Andersen (2004) showed that the presence of SiO_2 mantle on SiC surface could give rise to structures in the $21 \mu\text{m}$ profile in carbon stars. This may account for the structures observed at $\sim 20 \mu\text{m}$. The red-ward half of the profile in these objects shows an absorption-

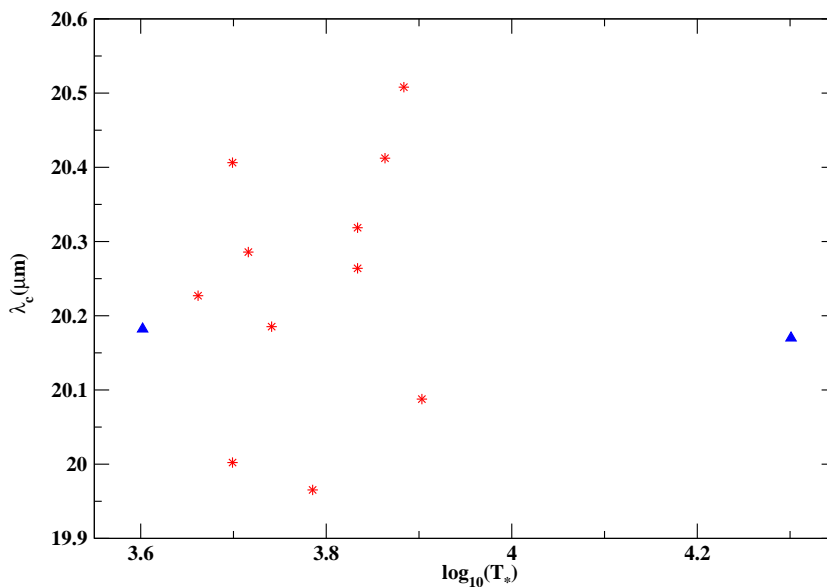


Figure 5.21: Plot of the peak wavelengths of the feature at $21 \mu\text{m}$ for PPNe (red asterisks) and PAGB stars (blue triangles) versus photospheric temperature T_*

like feature at $23.2 \mu\text{m}$ followed by an emission-like feature at about $24.5 \mu\text{m}$. We propose that the cause of this may be due to the combination of a core and mantle type dust grain configuration. We propose SiC (Speck and Hofmeister, 2004) and FeS (Keller *et al.*, 2002) as the candidate material for the core and the mantle respectively. The observed profile of the other 10 PAGB/PPNe objects in Fig 5.20 may be caused purely by the SiC core having negligible

mantle thickness. The morphology observed in IRAS 18533+0523 and IRAS 19477+2401 may be caused by an increase in the mantle thickness on the core grain.

Fig 5.21 shows the variation of the peak wavelength (λ_c) of the 21 μm feature with T_* . One may notice that the λ_c shows an increasing tendency with T_* for PPNe sources. We propose the increase in the mantle layer thickness of FeS with temperature to be the probable reason behind the red shift in the peak wavelength.

5.6.4.2 The 23- μm feature:

The 23.5 μm band is usually observed in circumstellar disks surrounding young stars and carbon rich evolved stars. The carrier of this broad feature has been attributed to iron sulfides (FeS) (Keller *et al.*, 2002). The IR reflectance of troilite (FeS) has four strong resonances with a broad feature at 23 μm and narrower features at 33, 38 and 43 μm (Begemann *et al.*, 1994). Warmer grains emit stronger towards the shorter wavelengths, thereby increasing the strength of the 23 μm relative to the other bands (Keller *et al.*, 2002). It may be recalled here that ISO spectra from comet Hale-Bopp show a significantly sharper feature at ~ 23.5 μm which has been attributed to forsterite (Mg_2SiO_4) by Crovisier *et al.* (1997) and Malfait *et al.* (1998). Oxygen rich crystalline silicates have peaks near 23.8, 27.5, 33.8 and 36.5 μm due to crystalline olivines ($\text{Mg}_x\text{Fe}_{1-x}$) $_2\text{SiO}_4$ [$0 \leq x \leq 1$], and peaks near 18.2, 23.2, 28, and 36.0 due to crystalline pyroxenes ($\text{Mg}_x\text{Fe}_{1-x}$) SiO_3 [$0 \leq x \leq 1$] (Jaeger *et al.*, 1998). Fig. 5.22 represents the typical continuum subtracted spectra in the region of 20-30 μm for PAGB (top panel) and PPNe (bottom panel) stars in our sample. The spectra can be attributed to (Mg_2SiO_4) owing to its sharp narrow spectral profile. The mixed chemistry is usually explained in the binary AGB evolution, in which a reservoir of oxygen-rich dust is stored in the system, and the star subsequently evolves to a carbon-rich phase. There are 19 PPNe and 13 PAGB sources with crystalline silicate emission. Carbon rich stars with crystalline olivines were observed earlier by Molster *et al.* (2001); Jiang *et al.* (2013) and

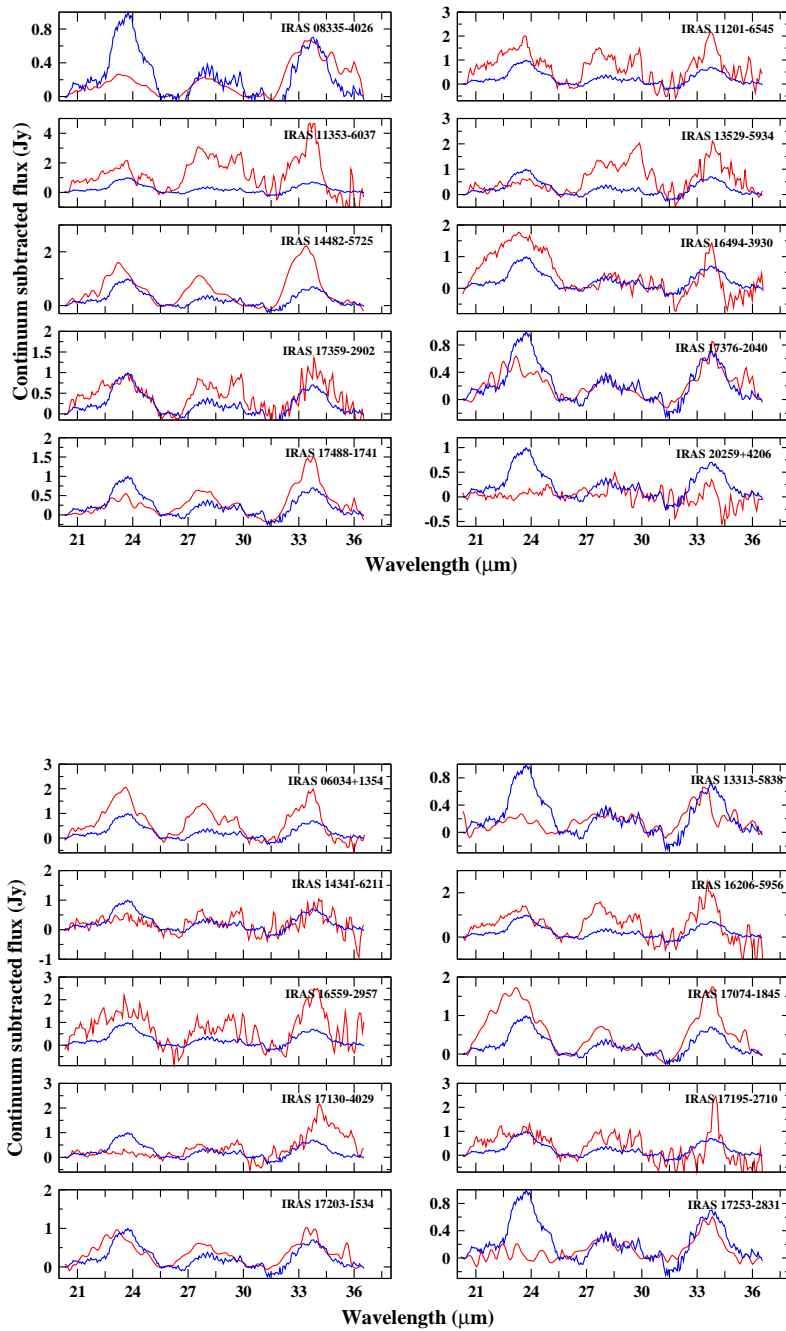


Figure 5.22: Typical continuum subtracted 23 & 30 μm features of PAGB stars (top panels) & PPNe candidates (bottom panels). The blue curve corresponds to the continuum subtracted ISO spectrum (normalised to unity) of comet Hale-Bopp attributed to crystalline forsterite is shown for comparison

Blommaert *et al.* (2014). The $23 \mu\text{m}$ feature is absent in the PAGB stars IRAS 20259+4206 and in the PPNe IRAS 17130-4029 & IRAS 17253-2831.

5.6.4.3 The $30\text{-}\mu\text{m}$ feature:

The unidentified very broad emission feature around $30 \mu\text{m}$ was first discovered by Forrest, Houck and McCarthy (1981) in carbon-rich stars. The feature

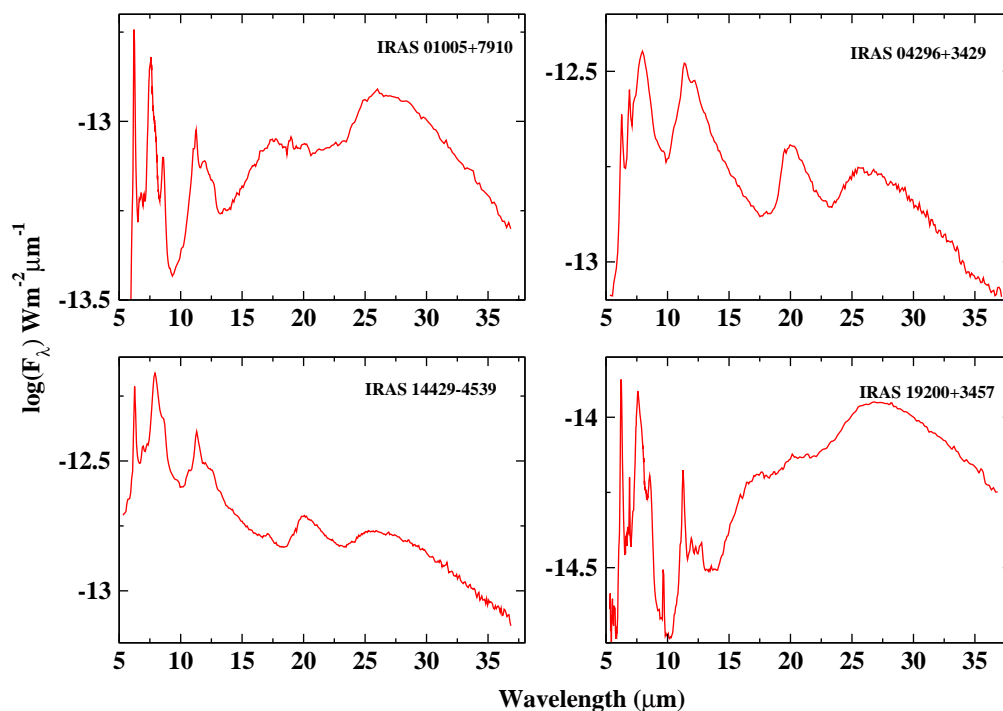


Figure 5.23: PPNe candidates with $30 \mu\text{m}$ feature possibly due to MgS

is commonly found with varying band shapes in C-rich AGB (Jiang, Szczerba and Deguchi, 1999), post-AGBs and PNe (Goebel and Moseley, 1985; Hrivnak, Volk and Kwok, 2000; Volk *et al.*, 2002). Goebel and Moseley (1985) proposed solid magnesium sulfide (MgS) as the possible carrier with the feature peaking in the range $30\text{-}35 \mu\text{m}$ depending on the temperature of the grain. The peak positions shift from $26 \mu\text{m}$ in the case of AGB stars to $35 \mu\text{m}$ in PNe.

Zhukovska and Gail (2008) suggested the formation of MgS on the surface of SiC grains as the most promising mechanism for MgS formation in the circumstellar shells of evolved stars. Duley (2000) suggested the carrier to be carbon-based linear molecules with specific side groups. Figure 5.23 represents the PPNe candidates in our sample with broad $30\ \mu\text{m}$ feature due to MgS. Earlier Hrivnak, Volk and Kwok (2000) and Volk *et al.* (2002) had used ISO spectra to study the $30\ \mu\text{m}$ feature. The ISO spectra appeared to have two separate features at 26 and $30\ \mu\text{m}$ at varying strengths. The *Spitzer* spectra of our samples do not support this claim. There are 18 PPNe and 5 PAGB sources with broad $30\ \mu\text{m}$ feature due to MgS. This feature is mostly observed in sources showing strong/blended PAH emissions. This supports the claim that MgS are formed in C-rich envelopes (Zhukovska and Gail, 2008).

5.7 Identification of transition objects

The transition from the PAGB to PNe phase remains an elusive stage in stellar evolution. After the termination of the high AGB mass loss, the circumstellar envelopes expand and cool, and the effective temperature of the central star increases to ionize the circumstellar material during the PAGB/PPNe phase (Kwok and Feldman, 1981; Kwok and Bignell, 1984). The PPNe also show fast bipolar outflows as well as slower components that are probably due to the ejected material during the previous AGB phase (Solf, 1994; Balick and Frank, 2002; Sahai *et al.*, 2007; Sahai, Sugerman and Hinkle, 2009). These outflows may be driven by an accretion disk around a binary companion (Morris, 1987). The effect of rotation, development of ionization front, bipolar outflows are considered as shaping agents to explain the observed aspherical morphologies (Sahai and Trauger, 1998; García-Segura *et al.*, 1999; Cerrigone *et al.*, 2008). As the temperature of the PAGB cores rises to 10^4 K, it ionizes the surrounding circumstellar material by emitting low-excitation atomic lines. This suggests that such lines predominantly arise from the PDRs.

Mid-IR fine structure lines suffer less dust extinction compared to the op-

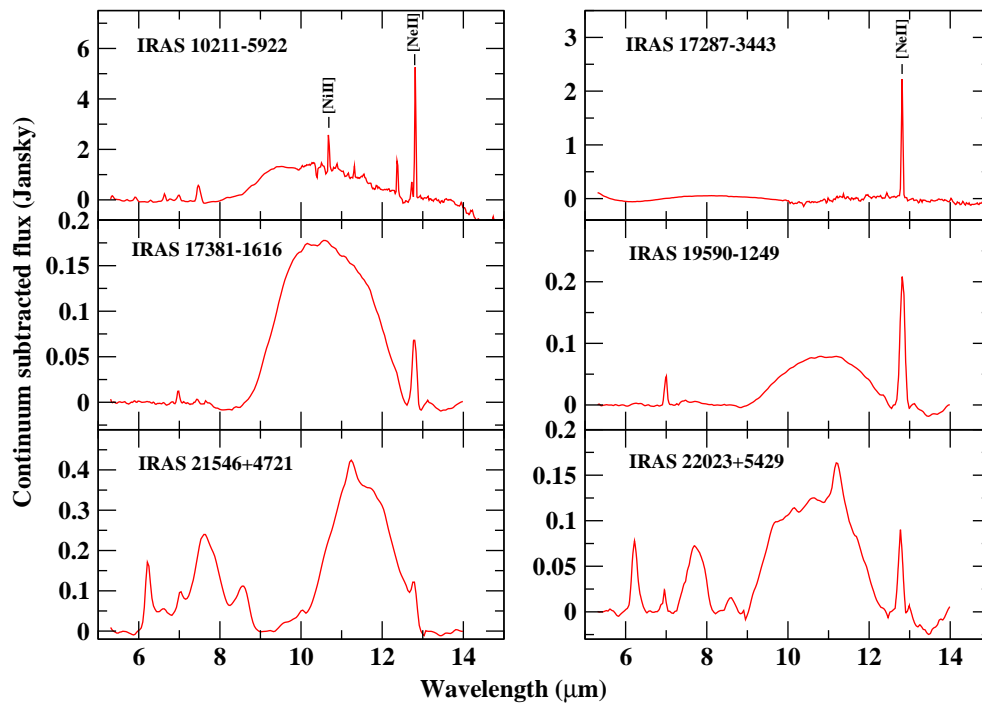


Figure 5.24: Continuum subtracted spectra of transition objects from PAGB/PPNe to PNe phase showing prominent [NeII] emission at 12.8 μm

tical and UV emission lines. The ground level configuration of such ions have energy levels separated by a small difference which is of the order of the electron thermal energy. Hence the thermal electrons populate these levels by collisions and the electronic transitions from excited levels give radiations. Collisionally excited lines may appear either in the electric dipole induced permitted transition or in the electric quadrupole or magnetic dipole induced forbidden transition. The forbidden lines are observed from PPNe due to low nebular density. The [NeII] ($^2P_{1/2} \rightarrow ^2P_{3/2}$) 12.814 μm line emission from singly ionized neon can be used as diagnostic tool to determine the physical properties of the ionized gas. This nebular emission has been observed in six candidates suggesting that the ionization of the circumstellar material may have already started in these evolved stars.

Figure 5.24 represents *Spitzer* IRS spectra of transition objects with hot cores ionizing the circumstellar materials thereby making a transition from PAGB/PPNe to PNe phase showing [NeII] emission at $12.8 \mu\text{m}$. Among these transition objects, IRAS 21546+4721 is a PAGB candidate with PAH emission in addition to [NeII]. IRAS 17287-3443, IRAS 17381-1616, IRAS 19590-1249 and IRAS 22023+5249 are PPNe candidates. Among the PPNe showing transition behavior only IRAS 22023+5249 showed PAH features. IRAS 17381-1616 and IRAS 19590-1249 show broad $11 \mu\text{m}$ feature of SiC. The effective temperature of all these sources are $\geq 10^4$ K. IRAS 10211-5922 is classified as Blue supergiant star with spectral type B3Iae. However Volk and Kwok (1989) classified it as a Proto-planetary nebula.

5.8 Identification of Fullerenes

Fullerene molecules (e.g. C_{60} and C_{70}) are large molecules made of carbon hexagons and pentagons that are organised in the shape of a hollow sphere or ellipsoid (Kroto *et al.*, 1985; Kroto, 1988; Curl and Smalley, 1988; Krätschmer *et al.*, 1990). It takes a shape of a soccer ball or a geodesic dome commonly referred to as "buckyball", named after the inventor of the geodesic dome, Buckminster Fuller. The C_{60} molecule consists of 60 carbon atoms arranged in the shape of a hollow sphere that is made of 20 hexagons and 12 pentagons. The excitation mechanism of fullerenes is similar to that of PAHs. They are generally thought to be excited by the absorption of a single UV photon. Rapid internal conversion excites the molecule in the electronic ground state to highly excited vibrational states. The molecule then de-excites back with the emission of IR photons. It has 174 vibrational modes, but due to its symmetry many modes are degenerate and only 4 modes are IR active. The mid-IR vibrational modes lie at 18.9, 17.4, 8.5, $7.0 \mu\text{m}$. Fullerenes were first synthesized in laboratory for understanding the formation mechanism of long-chain carbon molecules (Kroto *et al.*, 1985). Laboratory experiments have measured these IR vibrational modes wavelengths in the pure, solid state (Krätschmer *et al.*,

1990) as well as in the gas-phase (Frum *et al.*, 1991). Nemes *et al.* (1994) suggested that the difference in the observed peak wavelength from the standard IR modes is primarily due to temperature effects; higher temperatures shift the bands to higher wavelengths and causes broadening.

The model for the C_{70} geometry has a prolate top more like a rugby ball. It has 204 fundamental vibrational modes where 31 are IR active. Most of the C_{70} IR active bands are weak, and blends with C_{60} bands with isolated medium strength bands at 12.6, 14.8, 15.6 and 21.8 μm . It was suggested that fullerenes could also form in carbon star outflows and be injected into the interstellar medium.

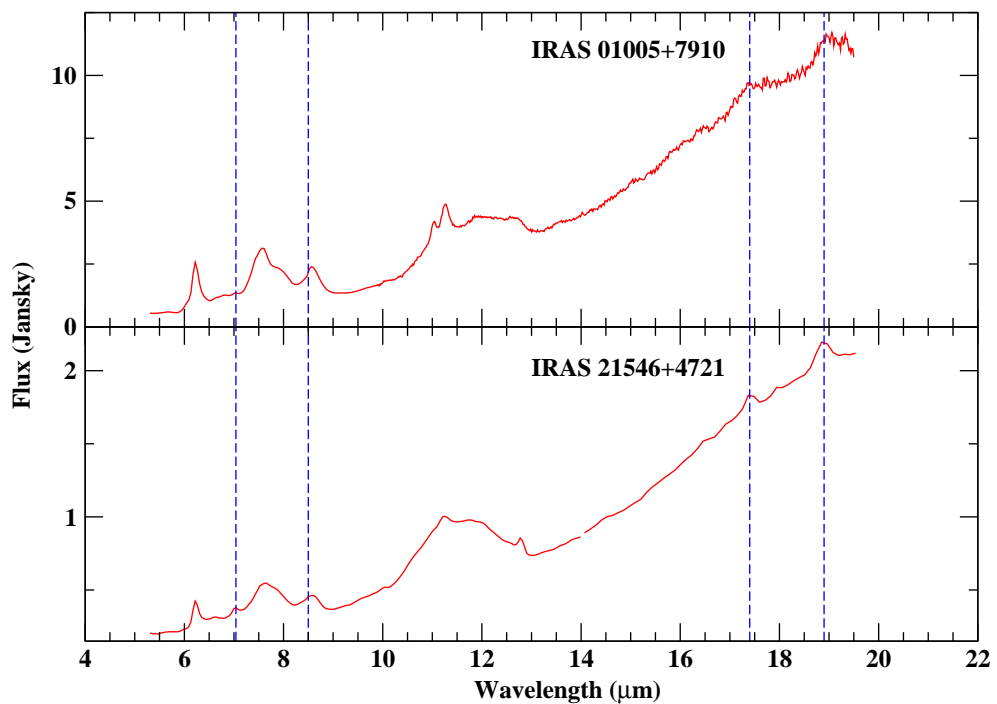


Figure 5.25: *Spitzer* IRS spectra of PPNe candidate IRAS 01005+7910 and PAGB candidate IRAS 21546+4721 showing vibrational modes of C_{60} fullerene

Clayton *et al.* (1995) searched for fullerenes in the IR wavelengths at 8.6 μm in R Coronae Borealis stars. Cami *et al.* (2010) reported the identification

of C_{60} bands from the *Spitzer* IRS spectrum of the planetary nebula Tc 1. García-Hernández *et al.* (2010) found C_{60} in carbon-rich PNe. Zhang and Kwok (2011) and Gielen *et al.* (2011) used *Spitzer* mid-IR spectrum to identify C_{60} in protoplanetary nebula and PAGB candidates. All in all there are very few detections of C_{60} in late type stars.

We carefully searched for C_{60} vibrational modes in the *Spitzer* IRS spectra of PPNe/PAGB candidates in our sample. We could successfully detect C_{60} vibrational modes at 7.0, 8.5, 17.4 and 18.9 μm in the PAGB candidate IRAS 21546+4721. To the best of our knowledge this is the first detection of C_{60} in this source and one of the very few detections reported yet. Figure 5.25 represents *Spitzer* IRS spectrum of IRAS 21546+4721. The spectrum of the PPNe candidate IRAS 01005+7910 with successful detection of C_{60} is shown for comparison.

5.9 Conclusions

We present here an extensive study of NIR and mid-IR spectra and SED modeling of a large sample of PAGB/PPNe candidates. The important conclusions of the study are as follows:

1. The sum of the EWs of Brackett series lines show a positive correlation with the photospheric temperature; while the sum of the EWs of the first and second overtone bands show a negative correlation with the photospheric temperature.
2. Our observations showed that several PAGB stars undergo short term spectral variability that is indicative of on-going episodic mass loss. Cooler PAGB stars showed variation in the CO first overtone bands. In contrast, the hot PAGB stars showed variation in HI lines.
3. The SED modelling shows consistent results: the temperature of the inner dust shell shows decreasing tendency with increasing dust shell inner

radius r_1 , where as the stellar photospheric temperature shows increasing tendency with the ratio of r_1/r_c ; the gas mass loss rate correlates negatively with dust temperature; further, gas mass loss rate shows an increasing tendency with $\tau_{0.55}$.

4. The PAGB mass loss rates obtained from the SED models are higher than the AGB mass loss rates and show a positive correlation with the mass loss index $[K - 12]$.
5. Archival *Spitzer* mid-IR spectra of the sample stars are classified based on the observed mid-IR features. The objects that show PAH emission features in the range 5-20 μm indicate the onset of UV radiation from the central star and hence their advanced stage of evolution. Variation in the observed strength of various PAH modes with the photospheric temperature (T_*) was established.
6. The observed split in the 21 μm morphology was explained by proposing a core and mantle configuration for dust grains. SiC and FeS are proposed as the preferred material for the core and mantle respectively.
7. The 23 μm feature observed in the PAGB/PPNe candidates are largely attributed to crystalline forsterite owing to their narrow width.
8. Sources with strong/blended PAH emission mostly show very broad emission feature due to MgS. Other sources in our sample also showed crystalline forsterite emission at 23.8, 27.5, 33.8 μm .
9. Six transition objects showed [NeII] emission at 12.8 μm , thus indicating their transition nature from PAGB/PPNe to PNe with the onset of ionisation.
10. The IR vibrational modes of Fullerenes at 18.9, 17.4, 8.5, 7.0 μm were observed for the first time in the PAGB star IRAS 21546+4721.

Chapter 6

Summary and Future Work

The work presented in this thesis deals with the study of circumstellar environment of sources that are in various stages of stellar evolution. Here, we summarize and highlight some of the important results obtained from the research presented here. We also briefly mention some future directions of the work that may be taken up during the post-doctoral period.

6.1 Summary

6.1.1 Infrared studies of V1647 Ori and five other eruptive young stellar objects

V1647 Ori is a young eruptive variable star known to be illuminating McNeil's nebula. It experienced two episodes of outbursts during 2004 and 2008. The 2004 outburst lasted for about 2 years and subsequently slowly faded to its quiescent brightness. In 2008, V1647 Ori experienced its second outburst in six years which is still on-going. The nature of the outburst and its similarity to the pre-main sequence eruptive events of FUors and EXors make V1647 Ori to be distinctive. NIR monitoring was done spanning the two outburst and

quiescent phases. The current, on-going outburst, shows higher amplitude of brightness and extinction A_v fluctuations than the earlier 2004 outburst. It also seems to show a slower fading at a rate of $\sim 0.06 - 0.18$ mag per year since 2012 which is reminiscent of a typical FUors light curve. The NIR spectra during the current on-going outburst showed variability in the Br γ and CO first overtone bands. The time scales of the outburst and observed spectral features suggest V1647 Ori to be a new class of object having both the properties of FU Ori and EX Lupi. Mid-IR spectra show silicate emission and CO₂ ice absorption feature during the 2004 outburst thus depicted its highly embedded nature. Modeling of the SEDs during the outburst and quiescent phases show that the disk mass and disk accretion rate much higher during the former than those in the latter. IR photometric and spectroscopic properties of V1647 Ori was compared with five other eruptive variables. The IR properties of V1331 Cyg showed a possible similarity to V1647 Ori.

6.1.2 Infrared studies on a sample of Asymptotic Giant Branch stars

NIR spectroscopy was used to study the signatures of mass loss processes during the AGB phase of evolution on a sample of M, SR, S type stars. NIR observations in the H and K bands showed first and second overtone bands of CO in absorption. In all the sources the hydrogen recombination lines were absent. The second overtone band of CO(3-0) show a trend of correlation with mass loss parameters like $[H - K]$ and $[K - 12]$ color for M and S type stars. The observed trend may be due to the fact that this line originates from the stellar photosphere where the effects of pulsation are more pronounced. Similarly a positive correlation of CO(3-0) with CO(4-1) and CO(2-0) with CO(3-1) is seen which is due to the population of the levels that are excited at equilibrium conditions. The SEDs of the AGB candidates show the absence of detached shells indicating its on going mass loss. The SED model of M-type stars showed higher mass loss rates compared to the SR and S type

stars in our sample. These mass loss rates were also evident from their higher opacities as revealed by SED models. The SED models also showed a warmer dust shell temperature for all the types in the range 450 - 700 K. The warm circumstellar envelopes in the AGB stars may be due to the presence of the expanding envelopes closer to the central source. The mass loss rate of M type stars also showed an increasing trend with the $[K - 12]$ color.

6.1.3 Infrared studies on a sample of Post-AGB/Proto-Planetary Nebulae

The episodic PAGB mass loss during the PAGB/PPNe stage was studied by monitoring its NIR spectroscopic variations. Repeated spectroscopic observations in the NIR wavelengths were done on a sample of a PAGB stars. Cooler PAGB stars showed spectral variation in CO first overtone bands while hot PAGB stars showed variation in HI lines. The sum of the EWs of Brackett series lines shows a positive correlation with stellar evolution of the central source (with the increase of photospheric temperature), while the sum of the EWs of the first overtone bands of CO show a negative correlation. Using the *Spitzer* mid-IR spectra, the PAGB & PPNe candidates were classified based on the observed spectral features. Modeling of the SEDs with a double shell configuration was done for sources with strong PAH emission in its mid-IR spectra. SEDs for all other sources were modeled using a single shell configuration. SED models of the PAGB candidates showed higher mass loss rates compared to the M, SR, S type sources. The temperature of the inner dust shell showed a decreasing tendency with increasing dust shell inner radius r_1 , where as the stellar photospheric temperature shows increasing tendency with the ratio of r_1/r_c . The mass loss rate showed a negative correlation with dust temperature; while it correlated positively with $\tau_{0.55}$. The observed strength of various PAH modes showed variation with the photospheric temperature (T_*). The mid-IR spectra of a few PAGB/PPNe candidates showed dust features at 21, 23 and 30 μm . We propose a core and mantle type configuration of dust

grains to explain the observed structures in the 21 μm feature. The observed structures may be explained by the varying thickness of the mantle material FeS on the SiC core grain. Some of the objects in our sample showed the presence of crystalline forsterite. The peak wavelength of the 21 μm feature was observed to move towards longer wavelength with the increase of T_* while the peak wavelength of 11 μm feature moves towards the shorter wavelength. A few PAGB/PPNe candidates showed prominent [NeII] emission at 12.8 μm indicating their transition nature to PNe with the onset of ionizing photons. The vibrational modes of fullerenes were detected for the first time in a PAGB candidate IRAS 21546+4721.

6.2 Future Work

One of the most exciting challenges facing theories of post-main sequence evolution is to understand how AGB stars and their circumstellar envelopes (CSEs) transform themselves to PNe with a variety of aspherical morphologies. Generalised Interacting Stellar Winds model is the most successful model for describing the shaping of PNe (Kwok, 1982; Kahn and West, 1985). The model consists of a fast ($\geq 1000 \text{ km s}^{-1}$) spherical stellar wind that interacts with an equatorially dense AGB CSE to produce an axisymmetric PNe. The fast wind is blocked by the torus in the equatorial plane of the AGB star, but may easily flow into the polar regions, creating a bipolar PPNe. However, this model is inadequate to explain the high-resolution imaging surveys with Hubble Space Telescope (HST) (Sahai *et al.*, 1999). Collimated fast winds (CFWs) have been proposed to operate during the PAGB phase and are considered to be the primary agents for shaping PPNe (Sahai and Trauger, 1998). Other models take into account the interaction of a companion object to explain the observed non-asymmetry structure (Soker and Rappaport, 2001).

As PAGB stars/PPNe evolve into early stages of PNe, part of the shell begins to be ionized by the central star. These ionization fronts observed in the envelope of PPNe objects acts as a shaping agent and could heavily influ-

ence the observed morphologies in the earlier part of the evolutionary phase. The physical processes associated with the observed morphologies during the formation of PNe can be studied by observing the radio continuum emissions from the ionised shells around these objects (Cerrigone *et al.*, 2008). The radio continuum emissions may be due to wind-shock interaction or ionisation from the central star. Since radio waves suffer much lesser extinction and could pass through high dust density it can be used as an excellent probe for understanding the physical processes taking place deep inside the circumstellar envelope. The radio-continuum observations of these transition sources with a hot central star will be proposed to be done using the Giant Meter wave Radio Telescope (GMRT) in the frequency bands of 150, 235, 327, 610 & 1280 MHz. The sample of sources will be so chosen as to have a negative spectral index that indicate a possible increase in the flux levels at these bands.

The presence of fast wind during the PAGB/PPNe phase can also be detected by observing molecular hydrogen at $2.121 \mu\text{m}$ and $2.248 \mu\text{m}$ in the NIR (Davis *et al.*, 2003). Molecular hydrogen can be excited by the interaction of fast wind with the circumstellar shell. These NIR observations will be made using a NIR imaging Fabry-Perot spectrometer coupled with the NICS at the cassegrain focus of the Mt.Abu 1.2 m telescope. This instrument is currently being designed and assembled by the author. The radio continuum observations coupled with the detection of molecular hydrogen in the NIR on a large sample of PAGB/PPNe candidates will lead to the understanding of the physical processes responsible for their shaping and their evolutionary status.

NIR monitoring of several FU Ori & EXor sources will continue to be pursued.

References

- Ábrahám, P., Kóspál, Á., Csizmadia, S., Kun, M., Moór, A., Prusti, T.: 2004, Long-term evolution of FU Orionis objects at infrared wavelengths. *Astron. Astrophys.* **428**, 89–97.
- Ábrahám, P., Mosoni, L., Henning, T., Kóspál, Á., Leinert, C., Quanz, S.P., Ratzka, T.: 2006, First AU-scale observations of V1647 Orionis with VLTI/MIDI. *Astron. Astrophys.* **449**, L13–L16.
- Acosta-Pulido, J.A., Kun, M., Ábrahám, P., Kóspál, Á., Csizmadia, S., Kiss, L.L., Moór, A., Szabados, L., Benkő, J.M., Barrena Delgado, R., Charcos-Llorens, M., Eredics, M., Kiss, Z.T., Manchado, A., Rácz, M., Ramos Almeida, C., Székely, P., Vidal-Núñez, M.J.: 2007, The 2004-2006 Outburst and Environment of V1647 Ori. *Astron. J.* **133**, 2020–2036.
- Adams, F.C., Shu, F.H.: 1986, Infrared spectra of rotating protostars. *Astrophys. J.* **308**, 836–853.
- Allamandola, L.J., Hudgins, D.M., Sandford, S.A.: 1999, Modeling the Unidentified Infrared Emission with Combinations of Polycyclic Aromatic Hydrocarbons. *Astrophys. J. Lett.* **511**, L115–L119.
- Allamandola, L.J., Tielens, A.G.G.M., Barker, J.R.: 1985, Polycyclic aromatic hydrocarbons and the unidentified infrared emission bands - Auto exhaust along the Milky Way. *Astrophys. J. Lett.* **290**, L25–L28.
- Allamandola, L.J., Tielens, A.G.G.M., Barker, J.R.: 1989, Interstellar polycyclic aromatic hydrocarbons - The infrared emission bands, the excita-

- tion/emission mechanism, and the astrophysical implications. *Astrophys. J. Supplement.* **71**, 733–775.
- Anandarao, B.G., Banerjee, D.P.K.: 2005, Proceedings of the Symposium "Infrared and Optical Astronomy at Mt. Abu Observoatry: The Past Decade and the Future". *Bulletin of the Astronomical Society of India* **33**, 67.
- Anandarao, B.G., Pottasch, S.R., Vaidya, D.B.: 1993, Circumstellar Dust in Mira Variables and the Mass Loss Mechanisms. *Astron. Astrophys.* **273**, 570.
- Anandarao, B., Richardson, E.H., Chakraborty, A., Epps, H.: 2008, A wide-field near-infrared camera and spectrograph for the Mt. Abu 1.2 m telescope. In: *Society of Photo-Optical Instrumentation Engineers (SPIE) Conference Series, Society of Photo-Optical Instrumentation Engineers (SPIE) Conference Series* **7014**.
- Andre, P., Ward-Thompson, D., Barsony, M.: 1993, Submillimeter continuum observations of Rho Ophiuchi A - The candidate protostar VLA 1623 and prestellar clumps. *Astrophys. J.* **406**, 122–141.
- Andre, P., Ward-Thompson, D., Barsony, M.: 2000, From Prestellar Cores to Protostars: the Initial Conditions of Star Formation. *Protostars and Planets IV*, 59.
- Andrews, S.M., Rothberg, B., Simon, T.: 2004, Mid-Infrared and Submillimeter Observations of the Illuminating Source of MCNeil's Variable Nebula. *Astrophys. J. Lett.* **610**, L45–L48.
- Anthony-Twarog, B.J.: 1982, The H-beta distance scale for B stars - The Orion association. *Astron. J.* **87**, 1213–1222.
- Appenzeller, I., Oestreicher, R., Jankovics, I.: 1984, Forbidden-line profiles of T Tauri stars. *Astron. Astrophys.* **141**, 108–115.
- Arellano Ferro, A.: 1981, A survey of variable yellow supergiants in the southern Milky Way. *Pub. Astron. Soc. Pac.* **93**, 351–360.

- Arlandini, C., Käppeler, F., Wisshak, K., Gallino, R., Lugaro, M., Busso, M., Straniero, O.: 1999, Neutron Capture in Low-Mass Asymptotic Giant Branch Stars: Cross Sections and Abundance Signatures. *Astrophys. J.* **525**, 886–900.
- Armitage, P.J., Livio, M., Pringle, J.E.: 2001, Episodic accretion in magnetically layered protoplanetary discs. *Mon. Not. Roy. Astron. Soc.* **324**, 705–711.
- Arndt, T.U., Fleischer, A.J., Sedlmayr, E.: 1997, Circumstellar dust shells around long-period variables. VI. an approximative formula for the mass loss rate of C-rich stars. *Astron. Astrophys.* **327**, 614–619.
- Aspin, C.: 2011, The Continuing Outburst of V1647 Orionis: Winter/Spring 2011 Observations. *Astron. J.* **142**, 135.
- Aspin, C., Reipurth, B.: 2009, V1647 Orionis: Optical Photometric and Spectroscopic Monitoring Through the 2003-2006 Outburst. *Astron. J.* **138**, 1137–1158.
- Aspin, C., Beck, T.L., Reipurth, B.: 2008, V1647 Orionis: One Year Into Quiescence. *Astron. J.* **135**, 423–440.
- Aspin, C., Barbieri, C., Boschi, F., Di Mille, F., Rampazzi, F., Reipurth, B., Tsvetkov, M.: 2006, The 1966-1967 Outburst of V1647 Orionis and the Appearance of McNeil’s Nebula. *Astron. J.* **132**, 1298–1306.
- Aspin, C., Reipurth, B., Beck, T.L., Aldering, G., Doering, R.L., Hammel, H.B., Lynch, D.K., Meixner, M., Pecontal, E., Russell, R.W., Sitko, M.L., Thomas, R.C., U, V.: 2009, V1647 Orionis: Reinvigorated Accretion and the Re-Appearance of McNeil’s Nebula. *Astrophys. J. Lett.* **692**, L67–L71.
- Audard, M., Ábrahám, P., Dunham, M.M., Green, J.D., Grosso, N., Hamaguchi, K., Kastner, J.H., Kóspál, Á., Lodato, G., Romanova, M.M., Skinner, S.L., Vorobyov, E.I., Zhu, Z.: 2014, Episodic Accretion in Young Stars. *Protostars and Planets VI*, 387–410.

- Bachiller, R.: 1996, Bipolar Molecular Outflows from Young Stars and Protostars. *ARA&A* **34**, 111–154.
- Bakes, E.L.O., Tielens, A.G.G.M., Bauschlicher, C.W. Jr.: 2001, Theoretical Modeling of Infrared Emission from Neutral and Charged Polycyclic Aromatic Hydrocarbons. I. *Astrophys. J.* **556**, 501–514.
- Balbus, S.A.: 2003, Enhanced Angular Momentum Transport in Accretion Disks. *ARA&A* **41**, 555–597.
- Balbus, S.A., Hawley, J.F.: 1991, A powerful local shear instability in weakly magnetized disks. I - Linear analysis. II - Nonlinear evolution. *Astrophys. J.* **376**, 214–233.
- Balbus, S.A., Hawley, J.F.: 1998, Instability, turbulence, and enhanced transport in accretion disks. *Reviews of Modern Physics* **70**, 1–53.
- Balick, B., Frank, A.: 2002, Shapes and Shaping of Planetary Nebulae. *ARA&A* **40**, 439–486.
- Bamberg, J.A., Zaun, N.H.: 1985, Design and performance of the cryogenic focal plane optics assembly for the Infrared Astronomical Satellite (IRAS). In: Melugin, R.K. (ed.) *Cryogenic optical systems and instruments, Society of Photo-Optical Instrumentation Engineers (SPIE) Conference Series* **509**, 94–102.
- Banwell, C.N., McCash, E.M.: 1994, *Fundamentals of Molecular Spectroscopy*.
- Begemann, B., Dorschner, J., Henning, T., Mutschke, H., Thamm, E.: 1994, A laboratory approach to the interstellar sulfide dust problem. *Astrophys. J. Lett.* **423**, L71–L74.
- Beletic, J.W., Blank, R., Gulbransen, D., Lee, D., Loose, M., Piquette, E.C., Sprafke, T., Tennant, W.E., Zandian, M., Zino, J.: 2008, Teledyne Imaging Sensors: infrared imaging technologies for astronomy and civil space. In:

- Society of Photo-Optical Instrumentation Engineers (SPIE) Conference Series, Society of Photo-Optical Instrumentation Engineers (SPIE) Conference Series* **7021**.
- Bell, K.R., Lin, D.N.C., Hartmann, L.W., Kenyon, S.J.: 1995, The FU Orionis outburst as a thermal accretion event: Observational constraints for protostellar disk models. *Astrophys. J.* **444**, 376–395.
- Benjamin, R.A., Churchwell, E., Babler, B.L., Bania, T.M., Clemens, D.P., Cohen, M., Dickey, J.M., Indebetouw, R., Jackson, J.M., Kobulnicky, H.A., Lazarian, A., Marston, A.P., Mathis, J.S., Meade, M.R., Seager, S., Stolovy, S.R., Watson, C., Whitney, B.A., Wolff, M.J., Wolfire, M.G.: 2003, GLIMPSE. I. An SIRTf Legacy Project to Map the Inner Galaxy. *Pub. Astron. Soc. Pac.* **115**, 953–964.
- Bessell, M.S., Brett, J.M.: 1988, JHKLM photometry - Standard systems, passbands, and intrinsic colors. *Pub. Astron. Soc. Pac.* **100**, 1134–1151.
- Bieging, J.H., Rieke, M.J., Rieke, G.H.: 2002, CO 1st overtone spectra of cool evolved stars: Diagnostics for hydrodynamic atmosphere models. *Astron. Astrophys.* **384**, 965–981.
- Biscaya, A.M., Rieke, G.H., Narayanan, G., Luhman, K.L., Young, E.T.: 1997, First-Overtone CO Variability in Young Stellar Objects. *Astrophys. J.* **491**, 359–365.
- Blöcker, T.: 1999, Structure and Evolution of AGB Stars. In: Le Bertre, T., Lebre, A., Waelkens, C. (eds.) *Asymptotic Giant Branch Stars, IAU Symposium* **191**, 21.
- Bloecker, T.: 1995a, Stellar evolution of low- and intermediate-mass stars. II. Post-AGB evolution. *Astron. Astrophys.* **299**, 755.
- Bloecker, T.: 1995b, Stellar evolution of low and intermediate-mass stars. I. Mass loss on the AGB and its consequences for stellar evolution. *Astron. Astrophys.* **297**, 727.

- Blommaert, J.A.D.L., de Vries, B.L., Waters, L.B.F.M., Waelkens, C., Min, M., Van Winckel, H., Molster, F., Decin, L., Groenewegen, M.A.T., Barlow, M., García-Lario, P., Kerschbaum, F., Posch, T., Royer, P., Ueta, T., Vandenbussche, B., Van de Steene, G., van Hoof, P.: 2014, Herschel/PACS observations of the 69 μm band of crystalline olivine around evolved stars. *Astron. Astrophys.* **565**, A109.
- Bonnell, I., Bastien, P.: 1992, A binary origin for FU Orionis stars. *Astrophys. J. Lett.* **401**, L31–L34.
- Boothroyd, A.I., Sackmann, I.J.: 1988, The production of low-mass stars. IV - Carbon stars. *Astrophys. J.* **328**, 671–679.
- Bowen, G.H.: 1988, Dynamical modeling of long-period variable star atmospheres. *Astrophys. J.* **329**, 299–317.
- Briceño, C., Vivas, A.K., Hernández, J., Calvet, N., Hartmann, L., Megeath, T., Berlind, P., Calkins, M., Hoyer, S.: 2004, MCNeil’s Nebula in Orion: The Outburst History. *Astrophys. J. Lett.* **606**, L123–L126.
- Brittain, S.D., Rettig, T.W., Simon, T., Gibb, E.L., Liskowsky, J.: 2010, Near-Infrared Spectroscopic Study of V1647 Ori. *Astrophys. J.* **708**, 109–116.
- Bujarrabal, V., Castro-Carrizo, A., Alcolea, J., Sánchez Contreras, C.: 2001, Mass, linear momentum and kinetic energy of bipolar flows in protoplanetary nebulae. *Astron. Astrophys.* **377**, 868–897.
- Burton, M.G., Hollenbach, D.J., Tielens, A.G.G.: 1992, Mid-infrared rotational line emission from interstellar molecular hydrogen. *Astrophys. J.* **399**, 563–572.
- Calvet, N., Hartmann, L., Kenyon, S.J.: 1991, On the near-infrared spectrum of FU Orionis. *Astrophys. J.* **383**, 752–756.
- Calvet, N., Magris, G.C., Patino, A., D’Alessio, P.: 1992, Irradiation of Accretion Disks around Young Objects. II. Continuum Energy Distribution. *Revista Mexicana de Astronomía y Astrofísica* **24**, 27.

- Cami, J., Bernard-Salas, J., Peeters, E., Malek, S.E.: 2010, Detection of C₆₀ and C₇₀ in a Young Planetary Nebula. *Science* **329**, 1180.
- Cataldo, F., Strazzulla, G., Iglesias-Groth, S.: 2009, Stability of C₆₀ and C₇₀ fullerenes toward corpuscular and γ radiation. *Mon. Not. Roy. Astron. Soc.* **394**, 615–623.
- Cerrigone, L., Umana, G., Trigilio, C., Leto, P., Buemi, C.S., Hora, J.L.: 2008, Radio continuum properties of young planetary nebulae. *Mon. Not. Roy. Astron. Soc.* **390**, 363–370.
- Cerrigone, L., Hora, J.L., Umana, G., Trigilio, C.: 2009, Spitzer Detection of Polycyclic Aromatic Hydrocarbons and Silicate Features in Post-AGB Stars and Young Planetary Nebulae. *Astrophys. J.* **703**, 585–600.
- Chen, P.S., Gao, H., Jorissen, A.: 1995, A catalogue of associations between IRAS sources and S stars. *Astron. Astrophys. Suppl.* **113**, 51.
- Clayton, G.C., Kelly, D.M., Lacy, J.H., Little-Marenin, I.R., Feldman, P.A., Bernath, P.F.: 1995, A Mid-Infrared Search for C₆₀ in R Coronae Borealis Stars and IRC + 10216. *Astron. J.* **109**, 2096.
- Clegg, P.E., Ade, P.A.R., Armand, C., Baluteau, J.P., Barlow, M.J., Buckley, M.A., Berges, J.C., Burgdorf, M., Caux, E., Ceccarelli, C., Cerulli, R., Church, S.E., Cotin, F., Cox, P., Cruvellier, P., Culhane, J.L., Davis, G.R., di Giorgio, A., Diplock, B.R., Drummond, D.L., Emery, R.J., Ewart, J.D., Fischer, J., Furniss, I., Glencross, W.M., Greenhouse, M.A., Griffin, M.J., Gry, C., Harwood, A.S., Hazell, A.S., Joubert, M., King, K.J., Lim, T., Liseau, R., Long, J.A., Lorenzetti, D., Molinari, S., Murray, A.G., Naylor, D.A., Nisini, B., Norman, K., Omont, A., Orfei, R., Patrick, T.J., Pequignot, D., Pouliquen, D., Price, M.C., Nguyen-Q-Rieu, Rogers A.J., Robinson F.D., Saisse M., Saraceno P., Serra G., Sidher S.D., Smith A.F., Smith H.A., Spinoglio L., Swinyard B.M., Texier D., Towlson W.A., Trams N.R., Unger S.J., White G.J.: 1996, The ISO Long-Wavelength Spectrometer. *Astron. Astrophys.* **315**, L38–L42.

- Cohen, M., Schwartz, R.D.: 1983, The exciting stars of Herbig-Haro objects. *Astrophys. J.* **265**, 877–900.
- Cohen, M., Allamandola, L., Tielens, A.G.G.M., Bregman, J., Simpson, J.P., Witteborn, F.C., Wooden, D., Rank, D.: 1986, The infrared emission bands. I - Correlation studies and the dependence on C/O ratio. *Astrophys. J.* **302**, 737–749.
- Cox, A.N.: 2000, *Allen's astrophysical quantities*.
- Crovisier, J., Leech, K., Bockelee-Morvan, D., Brooke, T.Y., Hanner, M.S., Altieri, B., Keller, H.U., Lellouch, E.: 1997, The spectrum of Comet Hale-Bopp (C/1995 01) observed with the Infrared Space Observatory at 2.9 AU from the Sun. *Science* **275**, 1904–1907.
- Curl, R.F., Smalley, R.E.: 1988, Probing C₆₀. *Science* **242**, 1017–1022.
- Dalgarno, A.: 2000, Astrophysical Importance of H₂. In: Combes, F., Pineau Des Forets, G. (eds.) *Molecular Hydrogen in Space*, 3–12.
- Davis, C.J., Smith, M.D., Stern, L., Kerr, T.H., Chiar, J.E.: 2003, Near-infrared spectroscopy of (proto)-planetary nebulae: molecular hydrogen excitation as an evolutionary tracer. *Mon. Not. Roy. Astron. Soc.* **344**, 262–282.
- de Graauw, T., Haser, L.N., Beintema, D.A., Roelfsema, P.R., van Aghoven, H., Barl, L., Bauer, O.H., Bekenkamp, H.E.G., Boonstra, A.J., Boxhoorn, D.R., Cote, J., de Groene, P., van Dijkhuizen, C., Drapatz, S., Evers, J., Feuchtgruber, H., Frericks, M., Genzel, R., Haerendel, G., Heras, A.M., van der Hucht, K.A., van der Hulst, T., Huygen, R., Jacobs, H., Jakob, G., Kamperman, T., Katterloher, R.O., Kester, D.J.M., Kunze, D., Kussendrager, D., Lahuis, F., Lamers, H.J.G.L.M., Leech, K., van der Lei, S., van der Linden, R., Luinge, W., Lutz, D., Melzner, F., Morris, P.W., van Nguyen, D., Ploeger, G., Price, S., Salama, A., Schaeidt, S.G., Sijm, N., Smoorenburg, C., Spakman, J., Spoon, H., Steinmayer, M., Stoecker, J., Valentijn, E.A.,

- Vandenbussche, B., Visser, H., Waelkens, C., Waters, L.B.F.M., Wensink, J., Wesselius, P.R., Wiezorrek, E., Wieprecht, E., Wijnbergen, J.J., Wildeman, K.J., Young, E.: 1996, Observing with the ISO Short-Wavelength Spectrometer. *Astron. Astrophys.* **315**, L49–L54.
- Duari, D., Cherchneff, I., Willacy, K.: 1999, Carbon molecules in the inner wind of the oxygen-rich Mira IK Tauri. *Astron. Astrophys.* **341**, L47–L50.
- Duley, W.W.: 2000, Chemical Evolution of Carbonaceous Material in Interstellar Clouds. *Astrophys. J.* **528**, 841–848.
- Dunham, M.M., Evans, N.J. II, Terebey, S., Dullemond, C.P., Young, C.H.: 2010, Evolutionary Signatures in the Formation of Low-Mass Protostars. II. Toward Reconciling Models and Observations. *Astrophys. J.* **710**, 470–502.
- Egan, M.P., Price, S.D., Kraemer, K.E.: 2003a, The Midcourse Space Experiment Point Source Catalog Version 2.3. In: *American Astronomical Society Meeting Abstracts, Bulletin of the American Astronomical Society* **35**, 1301.
- Egan, M.P., Price, S.D., Kraemer, K.E., Mizuno, D.R., Carey, S.J., Wright, C.O., Engelke, C.W., Cohen, M., Gugliotti, M.G.: 2003b, MSX6C Infrared Point Source Catalog. The Midcourse Space Experiment Point Source Catalog Version 2.3 (October 2003). *VizieR Online Data Catalog* **5114**, 0.
- Ehrenfreund, P., Foing, B.H.: 2010, Fullerenes and Cosmic Carbon. *Science* **329**, 1159–1160.
- Eisloffel, J., Mundt, R.: 1997, Parsec-Scale Jets From Young Stars. *Astron. J.* **114**, 280–287.
- Emerson, D.: 1996, *Interpreting Astronomical Spectra*.
- Evans, N.J. II, Balkum, S., Levreault, R.M., Hartmann, L., Kenyon, S.: 1994, Molecular outflows from FU Orionis stars. *Astrophys. J.* **424**, 793–799.
- Fazio, G.G., Hora, J.L., Allen, L.E., Ashby, M.L.N., Barmby, P., Deutsch, L.K., Huang, J.S., Kleiner, S., Marengo, M., Megeath, S.T., Melnick, G.J.,

- Pahre, M.A., Patten, B.M., Polizotti, J., Smith, H.A., Taylor, R.S., Wang, Z., Willner, S.P., Hoffmann, W.F., Pipher, J.L., Forrest, W.J., McMurty, C.W., McCreight, C.R., McKelvey, M.E., McMurray, R.E., Koch, D.G., Moseley, S.H., Arendt, R.G., Mentzell, J.E., Marx, C.T., Losch, P., Mayman, P., Eichhorn, W., Krebs, D., Jhabvala, M., Gezari, D.Y., Fixsen, D.J., Flores, J., Shakoorzadeh, K., Jungo, R., Hakun, C., Workman, L., Karpati, G., Kichak, R., Whitley, R., Mann, S., Tollestrup, E.V., Eisenhardt, P., Stern, D., Gorjian, V., Bhattacharya, B., Carey, S., Nelson, B.O., Glaccum, W.J., Lacy, M., Lowrance, P.J., Laine, S., Reach, W.T., Stauffer, J.A., Surace, J.A., Wilson, G., Wright, E.L., Hoffman, A., Domingo, G., Cohen, M.: 2004, The Infrared Array Camera (IRAC) for the Spitzer Space Telescope. *Astrophys. J. Supplement.* **154**, 10–17.
- Fedele, D., van den Ancker, M.E., Petr-Gotzens, M.G., Ageorges, N., Rafanelli, P.: 2007, Optical and infrared properties of V1647 Orionis during the 2003–2006 outburst. I. The reflection nebula. *Astron. Astrophys.* **472**, 199–205.
- Fleischer, A.J., Gauger, A., Sedlmayr, E.: 1992, Circumstellar dust shells around long-period variables. I - Dynamical models of C-stars including dust formation, growth and evaporation. *Astron. Astrophys.* **266**, 321–339.
- Forrest, W.J., Houck, J.R., McCarthy, J.F.: 1981, A far-infrared emission feature in carbon-rich stars and planetary nebulae. *Astrophys. J.* **248**, 195–200.
- Fouque, P., Le Bertre, T., Epchtein, N., Guglielmo, F., Kerschbaum, F.: 1992, Near-infrared photometry of a sample of IRAS point sources. *Astron. Astrophys. Suppl.* **93**, 151–171.
- Frum, C.I., Engleman, R., Hedderich, H.G., Bernath, P.F., Lamb, L.D., Huffman, D.R.: 1991, The Infrared Emission Spectrum of Gas Phase C₆₀ (buckminsterfullerene). *Chemical Physics Letters* **176**, 504–508.

- Galliano, F., Madden, S.C., Tielens, A.G.G.M., Peeters, E., Jones, A.P.: 2008, Variations of the Mid-IR Aromatic Features inside and among Galaxies. *Astrophys. J.* **679**, 310–345.
- García-Hernández, D.A., Manchado, A., García-Lario, P., Domínguez-Tagle, C., Conway, G.M., Prada, F.: 2002, Near-IR spectroscopy of planetary nebulae precursors. *Astron. Astrophys.* **387**, 955–968.
- García-Hernández, D.A., Manchado, A., García-Lario, P., Stanghellini, L., Villaver, E., Shaw, R.A., Szczerba, R., Perea-Calderón, J.V.: 2010, Formation of Fullerenes in H-containing Planetary Nebulae. *Astrophys. J. Lett.* **724**, L39–L43.
- García-Lario, P., Manchado, A., Pych, W., Pottasch, S.R.: 1997, Near infrared photometry of IRAS sources with colours like planetary nebulae. III. *Astron. Astrophys. Suppl.* **126**, 479–502.
- García-Segura, G., Langer, N., Różyczka, M., Franco, J.: 1999, Shaping Bipolar and Elliptical Planetary Nebulae: Effects of Stellar Rotation, Photoionization Heating, and Magnetic Fields. *Astrophys. J.* **517**, 767–781.
- Gauba, G., Parthasarathy, M., Kumar, B., Yadav, R.K.S., Sagar, R.: 2003, Photometry and low resolution spectroscopy of hot post-AGB candidates. *Astron. Astrophys.* **404**, 305–315.
- Gibb, E.L., Rettig, T.W., Brittain, S.D., Wasikowski, D., Simon, T., Vacca, W.D., Cushing, M.C., Kulesa, C.: 2006, Post-Outburst Infrared Spectra of V1647 Ori, the Illuminating Star of McNeil’s Nebula. *Astrophys. J.* **641**, 383–388.
- Gielen, C., Cami, J., Bouwman, J., Peeters, E., Min, M.: 2011, Carbonaceous molecules in the oxygen-rich circumstellar environment of binary post-AGB stars. C₆₀ fullerenes and polycyclic aromatic hydrocarbons. *Astron. Astrophys.* **536**, A54.

- Gilroy, K.K., Brown, J.A.: 1991, Carbon isotope ratios along the giant branch of M67. *Astrophys. J.* **371**, 578–583.
- Giridhar, S., Ferro, A., Parrao, L.: 1997, Elemental Abundances and Atmospheric Parameters of Seven F-G Supergiants. *Pub. Astron. Soc. Pac.* **109**, 1077–1084.
- Glass, I.S.: 1999, *Handbook of Infrared Astronomy*.
- Goebel, J.H.: 1993, SiS₂ in circumstellar shells. *Astron. Astrophys.* **278**, 226–230.
- Goebel, J.H., Moseley, S.H.: 1985, MgS grain component in circumstellar shells. *Astrophys. J. Lett.* **290**, L35–L39.
- Gorlova, N., Lobel, A., Burgasser, A.J., Rieke, G.H., Ilyin, I., Stauffer, J.R.: 2006, On the CO Near-Infrared Band and the Line-splitting Phenomenon in the Yellow Hypergiant ρ Cassiopeiae. *Astrophys. J.* **651**, 1130–1150.
- Grankin, K.N., Artemenko, S.A.: 2009, New Extreme Outburst of Z CMa. *Information Bulletin on Variable Stars* **5905**, 1.
- Greaves, J.: 2003, GSC 2139 2190 is a slowly changing Be variable and not a hot low mass post asymptotic giant branch star. *Information Bulletin on Variable Stars* **5472**, 1.
- Green, J.D., Hartmann, L., Calvet, N., Watson, D.M., Ibrahimov, M., Furlan, E., Sargent, B., Forrest, W.J.: 2006, Spitzer IRS Observations of FU Orionis Objects. *Astrophys. J.* **648**, 1099–1109.
- Groenewegen, M.A.T., de Jong, T.: 1998, CO observations and mass loss of MS- and S-stars. *Astron. Astrophys.* **337**, 797–807.
- Groenewegen, M.A.T., Marigo, P.: 2003, Synthetic AGB Evolution. In: Habing, H.J., Olofsson, H. (eds.) *Asymptotic giant branch stars*, by Harm J. Habing and Hans Olofsson. *Astronomy and astrophysics library*, New York, Berlin: Springer, 2003, p. 105, 105.

- Grosso, N., Kastner, J.H., Ozawa, H., Richmond, M., Simon, T., Weintraub, D.A., Hamaguchi, K., Frank, A.: 2005, Enhanced X-ray variability from V1647 Ori, the young star in outburst illuminating McNeil's Nebula. *Astron. Astrophys.* **438**, 159–168.
- Gullbring, E., Hartmann, L., Briceno, C., Calvet, N.: 1998, Disk Accretion Rates for T Tauri Stars. *Astrophys. J.* **492**, 323.
- Haas, M., Christou, J.C., Zinnecker, H., Ridgway, S.T., Leinert, C.: 1993, Sub-diffraction-limited infrared speckle observations of Z Canis Majoris, a 0.10 arcsec variable binary star. *Astron. Astrophys.* **269**, 282–290.
- Habing, H.J.: 1996, Circumstellar envelopes and Asymptotic Giant Branch stars. *Astron. Astrophys. Rev.* **7**, 97–207.
- Habing, H.J., Olofsson, H. (eds.): 2003, *Asymptotic giant branch stars*.
- Hamann, F., Persson, S.E.: 1992, Emission-line studies of young stars. III - Correlations with the infrared excess. *Astrophys. J.* **394**, 628–642.
- Hartmann, L.: 2009, *Accretion Processes in Star Formation: Second Edition*, Cambridge University Press, ???.
- Hartmann, L., Kenyon, S.J.: 1985, On the nature of FU Orionis objects. *Astrophys. J.* **299**, 462–478.
- Hartmann, L., Kenyon, S.J.: 1996, The FU Orionis Phenomenon. *ARA&A* **34**, 207–240.
- Hartmann, L., Heitsch, F., Ballesteros-Paredes, J.: 2009, Dynamic Star Formation. In: *Revista Mexicana de Astronomia y Astrofisica Conference Series, Revista Mexicana de Astronomia y Astrofisica, vol. 27* **35**, 66–67.
- Hartmann, L., Kenyon, S.J., Hewett, R., Edwards, S., Strom, K.M., Strom, S.E., Stauffer, J.R.: 1989, Pre-main-sequence disk accretion in Z Canis Majoris. *Astrophys. J.* **338**, 1001–1010.

- He, J.H., Szczerba, R., Hasegawa, T.I., Schmidt, M.R.: 2014, Observed Relationship between CO 2-1 and Dust Emission during the Post-asymptotic-giant-branch Phase. *Astrophys. J. Supplement.* **210**, 26.
- Helou, G., Walker, D.W. (eds.): 1988, *Infrared astronomical satellite (IRAS) catalogs and atlases. Volume 7: The small scale structure catalog* **7**.
- Henning, T., Burkert, A., Launhardt, R., Leinert, C., Stecklum, B.: 1998, Infrared imaging and millimetre continuum mapping of Herbig Ae/Be and FU Orionis stars. *Astron. Astrophys.* **336**, 565–586.
- Herbig, G.H.: 1977, Eruptive phenomena in early stellar evolution. *Astrophys. J.* **217**, 693–715.
- Herbig, G.H.: 1989, FU Orionis eruptions. In: Reipurth, B. (ed.) *European Southern Observatory Conference and Workshop Proceedings, European Southern Observatory Conference and Workshop Proceedings* **33**, 233–246.
- Herbig, G.H., Petrov, P.P., Duemmler, R.: 2003, High-Resolution Spectroscopy of FU Orionis Stars. *Astrophys. J.* **595**, 384–411.
- Herpin, F., Cernicharo, J., Heras, A.: 2000, H₂ Emission from CRL618. In: Combes, F., Pineau Des Forets, G. (eds.) *Molecular Hydrogen in Space*, 151.
- Herwig, F.: 2005, Evolution of Asymptotic Giant Branch Stars. *ARA&A* **43**, 435–479.
- Hillenbrand, L.A., Strom, S.E., Vrba, F.J., Keene, J.: 1992, Herbig Ae/Be stars - Intermediate-mass stars surrounded by massive circumstellar accretion disks. *Astrophys. J.* **397**, 613–643.
- Hinkle, K.H., Hall, D.N.B., Ridgway, S.T.: 1982, Time series infrared spectroscopy of the Mira variable Chi Cygni. *Astrophys. J.* **252**, 697–714.
- Hoffman, A.W., Love, P.J., Rosbeck, J.P.: 2004, Megapixel detector arrays: visible to 28 μm . In: Grycewicz, T.J., McCreight, C.R. (eds.) *Focal Plane*

- Arrays for Space Telescopes, Society of Photo-Optical Instrumentation Engineers (SPIE) Conference Series* **5167**, 194–203.
- Hoogzaad, S.N., Molster, F.J., Dominik, C., Waters, L.B.F.M., Barlow, M.J., de Koter, A.: 2002, The circumstellar dust shell of the post-AGB star HD 161796. *Astron. Astrophys.* **389**, 547–555.
- Houck, J.R., Roellig, T.L., van Cleve, J., Forrest, W.J., Herter, T., Lawrence, C.R., Matthews, K., Reitsema, H.J., Soifer, B.T., Watson, D.M., Weedman, D., Huisjen, M., Troeltzsch, J., Barry, D.J., Bernard-Salas, J., Blacken, C.E., Brandl, B.R., Charmandaris, V., Devost, D., Gull, G.E., Hall, P., Henderson, C.P., Higdon, S.J.U., Pirger, B.E., Schoenwald, J., Sloan, G.C., Uchida, K.I., Appleton, P.N., Armus, L., Burgdorf, M.J., Fajardo-Acosta, S.B., Grillmair, C.J., Ingalls, J.G., Morris, P.W., Teplitz, H.I.: 2004, The Infrared Spectrograph (IRS) on the Spitzer Space Telescope. *Astrophys. J. Supplement.* **154**, 18–24.
- Hrivnak, B.J., Biegging, J.H.: 2005, CO J = 2-1 and 4-3 Observations of Proto-planetary Nebulae: Time-variable Mass Loss. *Astrophys. J.* **624**, 331–351.
- Hrivnak, B.J., Kwok, S.: 1999, Discovery of Two New, Carbon-rich Proto-Planetary Nebulae: IRAS Z02229+6208 and IRAS 07430+1115. *Astrophys. J.* **513**, 869–878.
- Hrivnak, B.J., Kwok, S., Geballe, T.R.: 1994, Near-infrared spectroscopy of proto-planetary nebulae. *Astrophys. J.* **420**, 783–796.
- Hrivnak, B.J., Kwok, S., Volk, K.M.: 1989, A study of several F and G supergiant-like stars with infrared excesses as candidates for proto-planetary nebulae. *Astrophys. J.* **346**, 265–276.
- Hrivnak, B.J., Volk, K., Kwok, S.: 2000, 2-45 Micron Infrared Spectroscopy of Carbon-rich Proto-Planetary Nebulae. *Astrophys. J.* **535**, 275–292.

- Hunt, L.K., Mannucci, F., Testi, L., Migliorini, S., Stanga, R.M., Baffa, C., Lisi, F., Vanzi, L.: 1998, Northern JHK Standard Stars for Array Detectors. *Astron. J.* **115**, 2594–2603.
- Iben, I. Jr.: 1967, Stellar Evolution Within and off the Main Sequence. *ARA&A* **5**, 571.
- Iben, I. Jr.: 1975, Thermal pulses; p-capture, alpha-capture, s-process nucleosynthesis; and convective mixing in a star of intermediate mass. *Astrophys. J.* **196**, 525–547.
- Iben, I. Jr.: 1976, Further adventures of a thermally pulsing star. *Astrophys. J.* **208**, 165–176.
- Iben, I. Jr.: 1982, Low mass asymptotic giant branch evolution. I. *Astrophys. J.* **260**, 821–837.
- Iben, I. Jr.: 1995, Planetary nebulae and their central stars - origin and evolution. *Physics Reports* **250**, 2–94.
- Ishihara, D., Onaka, T., Kataza, H., Salama, A., Alfageme, C., Cassatella, A., Cox, N., García-Lario, P., Stephenson, C., Cohen, M., Fujishiro, N., Fujiwara, H., Hasegawa, S., Ita, Y., Kim, W., Matsuhara, H., Murakami, H., Müller, T.G., Nakagawa, T., Ohyama, Y., Oyabu, S., Pyo, J., Sakon, I., Shibai, H., Takita, S., Tanabé, T., Uemizu, K., Ueno, M., Usui, F., Wada, T., Watarai, H., Yamamura, I., Yamauchi, C.: 2010, The AKARI/IRC mid-infrared all-sky survey. *Astron. Astrophys.* **514**, A1.
- Ivezic, Z., Elitzur, M.: 1997, Self-similarity and scaling behaviour of infrared emission from radiatively heated dust - I. Theory. *Mon. Not. Roy. Astron. Soc.* **287**, 799–811.
- Ivezic, Z., Nenkova, M., Elitzur, M.: 1999, *DUSTY: Radiation transport in a dusty environment*. Astrophysics Source Code Library.

- Ivezic, Z., Groenewegen, M.A.T., Men'shchikov, A., Szczerba, R.: 1997, Benchmark problems for dust radiative transfer. *Mon. Not. Roy. Astron. Soc.* **291**, 121–124.
- Jaeger, C., Molster, F.J., Dorschner, J., Henning, T., Mutschke, H., Waters, L.B.F.M.: 1998, Steps toward interstellar silicate mineralogy. IV. The crystalline revolution. *Astron. Astrophys.* **339**, 904–916.
- Jiang, B.W., Szczerba, R., Deguchi, S.: 1999, IRAS 03313+6058: an AGB star with 30 micron emission. *Astron. Astrophys.* **344**, 918–922.
- Jiang, B.W., Zhang, K., Li, A., Lisse, C.M.: 2013, Crystalline Silicates in Evolved Stars. I. Spitzer/Infrared Spectrograph Spectroscopy of IRAS 16456-3542, 18354-0638, and 23239+5754. *Astrophys. J.* **765**, 72.
- Jorissen, A., Knapp, G.R.: 1998, Circumstellar shells and mass loss rates: Clues to the evolution of S stars. *Astron. Astrophys. Suppl.* **129**, 363–398.
- Joyce, R.R.: 1992, Observing With Infrared Arrays. In: Howell, S.B. (ed.) *Astronomical CCD Observing and Reduction Techniques*, *Astronomical Society of the Pacific Conference Series* **23**, 258.
- Jura, M.: 1986, RV Tauri stars as post-asymptotic giant branch objects. *Astrophys. J.* **309**, 732–736.
- Justtanont, K., Barlow, M.J., Skinner, C.J., Roche, P.F., Aitken, D.K., Smith, C.H.: 1996, Mid-infrared spectroscopy of carbon-rich post-AGB objects and detection of the PAH molecule chrysene. *Astron. Astrophys.* **309**, 612–628.
- Kaeppler, F., Gallino, R., Busso, M., Picchio, G., Raiteri, C.M.: 1990, S-process nucleosynthesis - Classical approach and asymptotic giant branch models for low-mass stars. *Astrophys. J.* **354**, 630–643.
- Kahn, F.D., West, K.A.: 1985, Shapes of planetary nebulae. *Mon. Not. Roy. Astron. Soc.* **212**, 837–850.

- Kastner, J.H., Richmond, M., Grosso, N., Weintraub, D.A., Simon, T., Frank, A., Hamaguchi, K., Ozawa, H., Henden, A.: 2004, An X-ray outburst from the rapidly accreting young star that illuminates McNeil's nebula. *Nature* **430**, 429–431.
- Kastner, J.H., Richmond, M., Grosso, N., Weintraub, D.A., Simon, T., Henden, A., Hamaguchi, K., Frank, A., Ozawa, H.: 2006, V1647 Orionis: The X-Ray Evolution of a Pre-Main-Sequence Accretion Burst. *Astrophys. J. Lett.* **648**, L43–L46.
- Keenan, P.C.: 1954, Classification of the S-Type Stars. *Astrophys. J.* **120**, 484.
- Keller, L.P., Hony, S., Bradley, J.P., Molster, F.J., Waters, L.B.F.M., Bouwman, J., de Koter, A., Brownlee, D.E., Flynn, G.J., Henning, T., Mutschke, H.: 2002, Identification of iron sulphide grains in protoplanetary disks. *Nature* **417**, 148–150.
- Kelly, D.M., Hrivnak, B.J.: 2005, A 2 Micron H₂ Spectral Survey of Protoplanetary Nebulae. *Astrophys. J.* **629**, 1040–1054.
- Kenyon, S.J., Hartmann, L.W.: 1991, The dusty envelopes of FU Orionis variables. *Astrophys. J.* **383**, 664–673.
- Kenyon, S.J., Hartmann, L., Hewett, R.: 1988, Accretion disk models for FU Orionis and V1057 Cygni - Detailed comparisons between observations and theory. *Astrophys. J.* **325**, 231–251.
- Kenyon, S.J., Hartmann, L.W., Kolotilov, E.A.: 1991, On the FU Orionis variable V1515 Cygni. *Pub. Astron. Soc. Pac.* **103**, 1069–1076.
- Kenyon, S.J., Hartmann, L.W., Strom, K.M., Strom, S.E.: 1990, An IRAS survey of the Taurus-Auriga molecular cloud. *Astron. J.* **99**, 869–887.
- Kenyon, S.J., Kolotilov, E.A., Ibragimov, M.A., Mattei, J.A.: 2000, Flickering in FU Orionis. *Astrophys. J.* **531**, 1028–1036.

- Kerschbaum, F., Hron, J.: 1994, Semiregular variables of types SRa and SRb. New JHKLM-photometry for 200 stars. *Astron. Astrophys. Suppl.* **106**, 397–411.
- Kessler, M.F., Steinz, J.A., Anderegg, M.E., Clavel, J., Drechsel, G., Estaria, P., Faelker, J., Riedinger, J.R., Robson, A., Taylor, B.G., Ximénez de Ferrán, S.: 1996, The Infrared Space Observatory (ISO) mission. *Astron. Astrophys.* **315**, L27–L31.
- Kholopov, P.N.: 1987, *General Catalogue of Variable Stars*..
- Kimura, Y., Nuth, J.A. III, Ferguson, F.T.: 2005, Is the 21 Micron Feature Observed in Some Post-AGB Stars Caused by the Interaction between Ti Atoms and Fullerenes? *Astrophys. J. Lett.* **632**, L159–L162.
- Kleinmann, S.G., Hall, D.N.B.: 1986, Spectra of late-type standard stars in the region 2.0-2.5 microns. *Astrophys. J. Supplement.* **62**, 501–517.
- Kohoutek, L., Wehmeyer, R.: 1999, Catalogue of H-alpha emission stars in the Northern Milky Way. *Astron. Astrophys. Suppl.* **134**, 255–256.
- Koresko, C.D., Beckwith, S.V.W., Ghez, A.M., Matthews, K., Neugebauer, G.: 1991, An infrared companion to Z Canis Majoris. *Astron. J.* **102**, 2073–2078.
- Kóspál, Á.: 2011, Millimeter interferometric observations of FU Orionis-type objects in Cygnus. *Astron. Astrophys.* **535**, A125.
- Kospal, A., Abraham, P., Acosta-Pulido, J., Csizmadia, S., Eredics, M., Kun, M., Racz, M.: 2005, The rapid fading of V1647 Orionis: the sudden end of a FUor-type eruption? *Information Bulletin on Variable Stars* **5661**, 1.
- Krätschmer, W., Lamb, L.D., Fostiropoulos, K., Huffman, D.R.: 1990, Solid C₆₀: a new form of carbon. *Nature* **347**, 354–358.
- Kroto, H.: 1988, Space, Stars, C₆₀, and Soot. *Science* **242**, 1139–1145.

- Kroto, H.W., Heath, J.R., O'Brien, S.C., Curl, R.F., Smalley, R.E.: 1985, C(60): Buckminsterfullerene. *Nature* **318**, 162.
- Kumar Dewangan, L., Anandarao, B.G.: 2010, Spitzer IRAC imaging photometric study of the massive star-forming region AFGL 437. *Mon. Not. Roy. Astron. Soc.* **402**, 2583–2590.
- Kun, M.: 2008, Early spectroscopy and photometry of the new outburst of V1647 Ori. *Information Bulletin on Variable Stars* **5850**, 1.
- Kwok, S.: 1982, From red giants to planetary nebulae. *Astrophys. J.* **258**, 280–288.
- Kwok, S.: 1993, Proto-planetary nebulae. *ARA&A* **31**, 63–92.
- Kwok, S.: 2000, *The Origin and Evolution of Planetary Nebulae*.
- Kwok, S.: 2004, The synthesis of organic and inorganic compounds in evolved stars. *Nature* **430**, 985–991.
- Kwok, S., Bignell, R.C.: 1984, Radio structure of the proto-planetary nebula GL 618. *Astrophys. J.* **276**, 544–550.
- Kwok, S., Feldman, P.A.: 1981, Discovery of radio brightening in AFGL 618. *Astrophys. J. Lett.* **247**, L67–L71.
- Kwok, S., Zhang, Y.: 2011, Mixed aromatic-aliphatic organic nanoparticles as carriers of unidentified infrared emission features. *Nature* **479**, 80–83.
- Kwok, S., Boreiko, R.T., Hrivnak, B.J.: 1987, Ground-based observations of IRAS candidates for late asymptotic giant branch stars. *Astrophys. J.* **312**, 303–313.
- Kwok, S., Volk, K., Hrivnak, B.J.: 1999, Chemical evolution of carbonaceous materials in the last stages of stellar evolution. *Astron. Astrophys.* **350**, L35–L38.

- Lachaume, R., Malbet, F., Monin, J.L.: 2003, The vertical structure of T Tauri accretion discs. III. Consistent interpretation of spectra and visibilities with a two-layer model. *Astron. Astrophys.* **400**, 185–202.
- Lada, C.J.: 1987, Star formation - From OB associations to protostars. In: Peimbert, M., Jugaku, J. (eds.) *Star Forming Regions, IAU Symposium* **115**, 1–17.
- Lada, C.J., Wilking, B.A.: 1984, The nature of the embedded population in the Rho Ophiuchi dark cloud - Mid-infrared observations. *Astrophys. J.* **287**, 610–621.
- Lambert, D.L.: 1991, The Chemical Composition of Asymptotic Giant Branch Stars - the S-Process. In: Michaud, G., Tutukov, A.V. (eds.) *Evolution of Stars: the Photospheric Abundance Connection, IAU Symposium* **145**, 299.
- Lamers, H.J.G.L.M., Cassinelli, J.P.: 1999, *Introduction to Stellar Winds*.
- Lançon, A., Wood, P.R.: 2000, A library of 0.5 to 2.5 μ m spectra of luminous cool stars. *Astron. Astrophys. Suppl.* **146**, 217–249.
- Lang, K.R.: 1999, *Astrophysical formulae*.
- Lattanzio, J., Forestini, M.: 1999, Nucleosynthesis in AGB Stars. In: Le Bertre, T., Lebre, A., Waelkens, C. (eds.) *Asymptotic Giant Branch Stars, IAU Symposium* **191**, 31.
- Lattanzio, J.C.: 1987, The formation of a 1.5-solar mass carbon star with $M_{\text{bol}} = -4.4$. *Astrophys. J. Lett.* **313**, L15–L18.
- Lattanzio, J.C., Wood, P.R.: 2003, Evolution, Nucleosynthesis, and Pulsation of AGB Stars. In: Habing, H.J., Olofsson, H. (eds.) *Asymptotic giant branch stars, by Harm J. Habing and Hans Olofsson. Astronomy and astrophysics library, New York, Berlin: Springer, 2003, p. 23, 23.*

- Lauterborn, D., Refsdal, S., Weigert, A.: 1971, Stars with Central Helium Burning and the Occurrence of Loops in the H-R Diagram. *Astron. Astrophys.* **10**, 97.
- Lebzelter, T., Hron, J.: 1999, A search for Technetium in semiregular variables. *Astron. Astrophys.* **351**, 533–542.
- Leger, A., Puget, J.L.: 1984, Identification of the 'unidentified' IR emission features of interstellar dust? *Astron. Astrophys.* **137**, L5–L8.
- Lewis, B.M.: 1989, Some effects of dust formation on O and C stars - Why carbon stars are underabundant. *Astron. J.* **98**, 1814–1819.
- Likkell, L., Forveille, T., Omont, A., Morris, M.: 1991, CO observations of cold IRAS objects - AGB and post-AGB stars. *Astron. Astrophys.* **246**, 153–174.
- Lodato, G., Bertin, G.: 2001, The spectral energy distribution of self-gravitating protostellar disks. *Astron. Astrophys.* **375**, 455–468.
- Lodato, G., Clarke, C.J.: 2004, Massive planets in FU Orionis discs: implications for thermal instability models. *Mon. Not. Roy. Astron. Soc.* **353**, 841–852.
- Loidl, R., Lançon, A., Jørgensen, U.G.: 2001, Spectra of carbon-rich asymptotic giant branch stars between 0.5 and 2.5 μ m: Theory meets observation. *Astron. Astrophys.* **371**, 1065–1077.
- Loidl, R., Höfner, S., Jørgensen, U.G., Aringer, B.: 1999, Dynamic model atmospheres of AGB stars. II. Synthetic near infrared spectra of carbon stars. *Astron. Astrophys.* **342**, 531–541.
- Loup, C., Forveille, T., Omont, A., Paul, J.F.: 1993a, CO and HCN observations of circumstellar envelopes. A catalogue - Mass loss rates and distributions. *Astron. Astrophys. Suppl.* **99**, 291–377.

- Loup, C., Forveille, T., Omont, A., Paul, J.F.: 1993b, CO and HCN observations of circumstellar envelopes. A catalogue - Mass loss rates and distributions. *Astron. Astrophys. Suppl.* **99**, 291–377.
- Luck, R.E., Lambert, D.L., Bond, H.E.: 1983, HR 4912 - A variable of the old-disk population. *Pub. Astron. Soc. Pac.* **95**, 413–421.
- Lynch, D.K., Rudy, R.J., Mazuk, S., Puetter, R.C.: 2000, 0.8-2.5 Micron Spectroscopy of Nova Ophiuchi 1998. *Astrophys. J.* **541**, 791–801.
- Malbet, F., Lachaume, R., Berger, J.P., Colavita, M.M., di Folco, E., Eisner, J.A., Lane, B.F., Millan-Gabet, R., Ségransan, D., Traub, W.A.: 2005, New insights on the AU-scale circumstellar structure of FU Orionis. *Astron. Astrophys.* **437**, 627–636.
- Malfait, K., Waelkens, C., Waters, L.B.F.M., Vandenbussche, B., Huygen, E., de Graauw, M.S.: 1998, The spectrum of the young star HD 100546 observed with the Infrared Space Observatory. *Astron. Astrophys.* **332**, L25–L28.
- Manteiga, M., García-Hernández, D.A., Ulla, A., Manchado, A., García-Lario, P.: 2011, IRAS 17423-1755 (Hen 3-1475) Revisited: An O-rich High-mass Post-asymptotic Giant Branch Star. *Astron. J.* **141**, 80.
- Martin, S.C.: 1997, A Funnel Flow Origin for CO Bandhead Emission in Young Stellar Objects. *Astrophys. J. Lett.* **478**, L33–L36.
- Mathis, J.S., Rumpl, W., Nordsieck, K.H.: 1977, The size distribution of interstellar grains. *Astrophys. J.* **217**, 425–433.
- McDonald, I., Sloan, G.C., Zijlstra, A.A., Matsunaga, N., Matsuura, M., Kraemer, K.E., Bernard-Salas, J., Markwick, A.J.: 2010, Rusty Old Stars: A Source of the Missing Interstellar Iron? *Astrophys. J. Lett.* **717**, L92–L97.
- McGehee, P.M., Smith, J.A., Henden, A.A., Richmond, M.W., Knapp, G.R., Finkbeiner, D.P., Ivezić, Ž., Brinkmann, J.: 2004, The V1647 Orionis (IRAS 05436-0007) Protostar and Its Environment. *Astrophys. J.* **616**, 1058–1064.

- McLean, I.S.: 2008, *Electronic Imaging in Astronomy: Detectors and Instrumentation (Second Edition)*, Praxis Publishing, ???.
- McNeil, J.W., Reipurth, B., Meech, K.: 2004, IRAS 05436-0007. *IAU Circ.* **8284**, 1.
- Meyer, M.R., Calvet, N., Hillenbrand, L.A.: 1997, Intrinsic Near-Infrared Excesses of T Tauri Stars: Understanding the Classical T Tauri Star Locus. *Astron. J.* **114**, 288–300.
- Millar, T.J.: 2003, Molecule and Dust Grain Formation. In: Habing, H.J., Olofsson, H. (eds.) *Asymptotic giant branch stars, by Harm J. Habing and Hans Olofsson. Astronomy and astrophysics library, New York, Berlin: Springer, 2003, p. 247, 247.*
- Millar, T.J., Williams, D.A.: 1993, Dust and Chemistry in Astronomy. *Science* **262**, 1462.
- Miroshnichenko, A.S., Bjorkman, K.S., Grosso, M., Levato, H., Grankin, K.N., Rudy, R.J., Lynch, D.K., Mazuk, S., Puetter, R.C.: 2005, MWC 930 - a new luminous blue variable candidate. *Mon. Not. Roy. Astron. Soc.* **364**, 335–343.
- Molster, F.J., Yamamura, I., Waters, L.B.F.M., Tielens, A.G.G.M., de Graauw, T., de Jong, T., de Koter, A., Malfait, K., van den Ancker, M.E., van Winckel, H., Voors, R.H.M., Waelkens, C.: 1999, Low-temperature crystallization of silicate dust in circumstellar disks. *Nature* **401**, 563–565.
- Molster, F.J., Yamamura, I., Waters, L.B.F., Nyman, L.Å., Käuffl, H.U., de Jong, T., Loup, C.: 2001, IRAS 09425-6040: A carbon star surrounded by highly crystalline silicate dust. *Astron. Astrophys.* **366**, 923–929.
- Morris, M.: 1987, Mechanisms for mass loss from cool stars. *Pub. Astron. Soc. Pac.* **99**, 1115–1122.
- Mowlavi, N.: 1999, On the third dredge-up phenomenon in asymptotic giant branch stars. *Astron. Astrophys.* **344**, 617–631.

- Mundt, R., Eisloffel, J.: 1998, T Tauri Stars Associated with Herbig-Haro Objects and Jets. *Astron. J.* **116**, 860–867.
- Muzerolle, J., Hartmann, L., Calvet, N.: 1998, A Br γ Probe of Disk Accretion in T Tauri Stars and Embedded Young Stellar Objects. *Astron. J.* **116**, 2965–2974.
- Muzerolle, J., Megeath, S.T., Flaherty, K.M., Gordon, K.D., Rieke, G.H., Young, E.T., Lada, C.J.: 2005, The Outburst of V1647 Orionis Revealed by Spitzer. *Astrophys. J. Lett.* **620**, L107–L110.
- Najita, J.R., Doppmann, G.W., Carr, J.S., Graham, J.R., Eisner, J.A.: 2009, High-Resolution K-Band Spectroscopy of MWC 480 and V1331 Cyg. *Astrophys. J.* **691**, 738–748.
- Nanda Kumar, M.S.: 1999, Near infrared investigation on regions of star formation. PhD thesis, Gujarat University.
- Nemes, L., Ram, S.R., Bernath, P.F., Tinker, M.C., Lowell, D.L., Donald, R.H.: 1994, Gas-phase infrared emission spectra of C60 and C70. Temperature-dependent studies. *Chemical Physics Letters* **218**, 295–303.
- Ninan, J.P., Ojha, D.K., Bhatt, B.C., Ghosh, S.K., Mohan, V., Mallick, K.K., Tamura, M., Henning, T.: 2013, Reappearance of McNeil’s Nebula (V1647 Orionis) and its Outburst Environment. *Astrophys. J.* **778**, 116.
- Norris, B.R.M., Tuthill, P.G., Ireland, M.J., Lacour, S., Zijlstra, A.A., Lykou, F., Evans, T.M., Stewart, P., Bedding, T.R.: 2012, A close halo of large transparent grains around extreme red giant stars. *Nature* **484**, 220–222.
- Ojha, D.K., Ghosh, S.K., Tej, A., Verma, R.P., Vig, S., Anupama, G.C., Bhatt, B.C., Parihar, P., Prabhu, T.P., Kamath, U.S., Anandarao, B.G.: 2005, Post-outburst phase of the McNeil’s nebula (V1647 Orionis). *Bulletin of the Astronomical Society of India* **33**, 370–371.

- Ojha, D.K., Ghosh, S.K., Tej, A., Verma, R.P., Vig, S., Anupama, G.C., Sahu, D.K., Parihar, P., Bhatt, B.C., Prabhu, T.P., Maheswar, G., Bhatt, H.C., Anandarao, B.G., Venkataraman, V.: 2006, Post-outburst phase of McNeil's nebula (V1647 Orionis). *Mon. Not. Roy. Astron. Soc.* **368**, 825–836.
- Olofsson, H.: 2003, Circumstellar Envelopes. In: Habing, H.J., Olofsson, H. (eds.) *Asymptotic giant branch stars, by Harm J. Habing and Hans Olofsson. Astronomy and astrophysics library, New York, Berlin: Springer, 2003, p. 325, 325.*
- Omont, A.: 1986, Physics and chemistry of interstellar polycyclic aromatic molecules. *Astron. Astrophys.* **164**, 159–178.
- Omont, A., Loup, C., Forveille, T., te Lintel Hekkert, P., Habing, H., Sivagnanam, P.: 1993a, Characterization and proportion of very cold C-rich circumstellar envelopes. *Astron. Astrophys.* **267**, 515–548.
- Omont, A., Lucas, R., Morris, M., Guilloteau, S.: 1993b, S-bearing molecules in O-rich circumstellar envelopes. *Astron. Astrophys.* **267**, 490–514.
- Origlia, L., Ferraro, F.R., Fusi Pecci, F., Rood, R.T.: 2002, ISOCAM Observations of Galactic Globular Clusters: Mass Loss along the Red Giant Branch. *Astrophys. J.* **571**, 458–468.
- Oudmaijer, R.D.: 1996, A search for hot post-AGB stars in the IRAS Point Source Catalog. *Astron. Astrophys.* **306**, 823.
- Oudmaijer, R.D., van der Veen, W.E.C.J., Waters, L.B.F.M., Trams, N.R., Waelkens, C., Engelsman, E.: 1992, SAO stars with infrared excess in the IRAS Point Source Catalog. *Astron. Astrophys. Suppl.* **96**, 625–643.
- Oudmaijer, R.D., Waters, L.B.F.M., van der Veen, W.E.C.J., Geballe, T.R.: 1995, Near-infrared spectroscopy of post-AGB stars. *Astron. Astrophys.* **299**, 69.

- Parmar, P.S., Lacy, J.H., Achtermann, J.M.: 1991, Detection of low-J pure-rotational emission from H₂ in the Orion Bar region - Evidence for small-scale clumpiness. *Astrophys. J. Lett.* **372**, L25–L28.
- Parthasarathy, M., Pottasch, S.R.: 1986, The far-infrared (IRAS) excess in HD 161796 and related stars. *Astron. Astrophys.* **154**, L16–L19.
- Parthasarathy, M., Vijapurkar, J., Drilling, J.S.: 2000, Low resolution spectroscopy of hot post-AGB candidates. *Astron. Astrophys. Suppl.* **145**, 269–274.
- Petrov, P.P., Kurosawa, R., Romanova, M.M., Gameiro, J.F., Fernandez, M., Babina, E.V., Artemenko, S.A.: 2014, Facing the wind of the pre-FUor V1331 Cyg. *Mon. Not. Roy. Astron. Soc.* **442**, 3643–3652.
- Popham, R., Kenyon, S., Hartmann, L., Narayan, R.: 1996, Spectra and Line Profiles of FU Orionis Objects: Comparisons between Boundary Layer Models and Observations. *Astrophys. J.* **473**, 422.
- Posch, T., Mutschke, H., Andersen, A.: 2004, Reconsidering the Origin of the 21 Micron Feature: Oxides in Carbon-rich Protoplanetary Nebulae? *Astrophys. J.* **616**, 1167–1180.
- Pottasch, S.R., Parthasarathy, M.: 1988, The far-infrared (IRAS) excess in luminous F-G stars. *Astron. Astrophys.* **192**, 182–186.
- Quanz, S.P., Henning, T., Bouwman, J., Ratzka, T., Leinert, C.: 2006, FU Orionis: The MIDI VLT Perspective. *Astrophys. J.* **648**, 472–483.
- Quanz, S.P., Henning, T., Bouwman, J., van Boekel, R., Juhász, A., Linz, H., Pontoppidan, K.M., Lahuis, F.: 2007, Evolution of Dust and Ice Features around FU Orionis Objects. *Astrophys. J.* **668**, 359–383.
- Racine, R.: 1968, Distance of the Cepheid SU Cassiopeae. *Astron. J.* **73**, 588–589.

- Ramstedt, S., Schöier, F.L., Olofsson, H., Lundgren, A.A.: 2006, Mass-loss properties of S-stars on the AGB. *Astron. Astrophys.* **454**, L103–L106.
- Reipurth, B., Aspin, C.: 1997, Infrared Spectroscopy of Herbig-Haro Energy Sources. *Astron. J.* **114**, 2700.
- Reipurth, B., Aspin, C.: 2004a, IRAS 05436-0007 and the Emergence of MC-Neil's Nebula. *Astrophys. J. Lett.* **606**, L119–L122.
- Reipurth, B., Aspin, C.: 2004b, The FU Orionis Binary System and the Formation of Close Binaries. *Astrophys. J. Lett.* **608**, L65–L68.
- Renzini, A.: 1981, Red giants as precursors of planetary nebulae. In: Iben, I. Jr., Renzini, A. (eds.) *Physical Processes in Red Giants, Astrophysics and Space Science Library* **88**, 431–446.
- Rettig, T.W., Brittain, S.D., Gibb, E.L., Simon, T., Kulesa, C.: 2005, CO Emission and Absorption toward V1647 Orionis (McNeil's Nebula). *Astrophys. J.* **626**, 245–252.
- Rieke, G.H.: 2007, Infrared Detector Arrays for Astronomy. *ARA&A* **45**, 77–115.
- Robitaille, T.P., Whitney, B.A., Indebetouw, R., Wood, K., Denzmore, P.: 2006, Interpreting Spectral Energy Distributions from Young Stellar Objects. I. A Grid of 200,000 YSO Model SEDs. *Astrophys. J. Supplement.* **167**, 256–285.
- Robitaille, T.P., Whitney, B.A., Indebetouw, R., Wood, K.: 2007, Interpreting Spectral Energy Distributions from Young Stellar Objects. II. Fitting Observed SEDs Using a Large Grid of Precomputed Models. *Astrophys. J. Supplement.* **169**, 328–352.
- Sahai, R., Liechti, S.: 1995, Circumstellar CO emission in S stars. I. Mass-loss with little or no dust. *Astron. Astrophys.* **293**, 198–207.

- Sahai, R., Trauger, J.T.: 1998, Multipolar Bubbles and Jets in Low-Excitation Planetary Nebulae: Toward a New Understanding of the Formation and Shaping of Planetary Nebulae. *Astron. J.* **116**, 1357–1366.
- Sahai, R., Sugerman, B.E.K., Hinkle, K.: 2009, Sculpting an Asymptotic Giant Branch Mass-Loss Envelope into a Bipolar Planetary Nebula: High-Velocity Outflows in V Hydrae. *Astrophys. J.* **699**, 1015–1023.
- Sahai, R., Dayal, A., Watson, A.M., Trauger, J.T., Stapelfeldt, K.R., Burrows, C.J., Gallagher, J.S. III, Scowen, P.A., Hester, J.J., Evans, R.W., Ballester, G.E., Clarke, J.T., Crisp, D., Griffiths, R.E., Hoessel, J.G., Holtzman, J.A., Krist, J., Mould, J.R.: 1999, The Etched Hourglass Nebula MYCN 18. I. HUBBLE SPACE TELESCOPE Observations. *Astron. J.* **118**, 468–476.
- Sahai, R., Morris, M., Sánchez Contreras, C., Claussen, M.: 2007, Preplanetary Nebulae: A Hubble Space Telescope Imaging Survey and a New Morphological Classification System. *Astron. J.* **134**, 2200–2225.
- Sánchez Contreras, C., Sahai, R., Gil de Paz, A., Goodrich, R.: 2008, Echelle Long-Slit Optical Spectroscopy of Evolved Stars. *Astrophys. J. Supplement.* **179**, 166–194.
- Sandell, G., Weintraub, D.A.: 2001, On the Similarity of FU Orionis Stars to Class I Protostars: Evidence from the Submillimeter. *Astrophys. J. Supplement.* **134**, 115–132.
- Schwarzschild, M., Härm, R.: 1967, Hydrogen Mixing by Helium-Shell Flashes. *Astrophys. J.* **150**, 961.
- Sedlmayr, E., Winters, J.M.: 2000, Grain Formation in the Winds of Cool Red Giant Stars. In: Wing, R.F. (ed.) *The Carbon Star Phenomenon, IAU Symposium* **177**, 337.
- Semkov, E.H., Peneva, S.P.: 2012, VR_cL_c optical light curves of V1647 Ori during the continuing second outburst. *Information Bulletin on Variable Stars* **6025**, 1.

- Shadick, S.J., Falk, H.J., Mitalas, R.: 1980, Theoretical surface abundances of Population I giants. *Mon. Not. Roy. Astron. Soc.* **192**, 493–502.
- Shull, J.M., Beckwith, S.: 1982, Interstellar molecular hydrogen. *ARA&A* **20**, 163–190.
- Siebenmorgen, R., Krügel, E.: 2010, The destruction and survival of polycyclic aromatic hydrocarbons in the disks of T Tauri stars. *Astron. Astrophys.* **511**, A6.
- Sipos, N., Ábrahám, P., Acosta-Pulido, J., Juhász, A., Kóspál, Á., Kun, M., Moór, A., Setiawan, J.: 2009, EX Lupi in quiescence. *Astron. Astrophys.* **507**, 881–889.
- Skrutskie, M.F., Cutri, R.M., Stiening, R., Weinberg, M.D., Schneider, S., Carpenter, J.M., Beichman, C., Capps, R., Chester, T., Elias, J., Huchra, J., Liebert, J., Lonsdale, C., Monet, D.G., Price, S., Seitzer, P., Jarrett, T., Kirkpatrick, J.D., Gizis, J.E., Howard, E., Evans, T., Fowler, J., Fullmer, L., Hurt, R., Light, R., Kopan, E.L., Marsh, K.A., McCallon, H.L., Tam, R., Van Dyk, S., Wheelock, S.: 2006, The Two Micron All Sky Survey (2MASS). *Astron. J.* **131**, 1163–1183.
- Sloan, G.C., Kraemer, K.E., Price, S.D., Shipman, R.F.: 2003, A Uniform Database of 2.4-45.4 Micron Spectra from the Infrared Space Observatory Short Wavelength Spectrometer. *Astrophys. J. Supplement.* **147**, 379–401.
- Sloan, G.C., Jura, M., Duley, W.W., Kraemer, K.E., Bernard-Salas, J., Forrest, W.J., Sargent, B., Li, A., Barry, D.J., Bohac, C.J., Watson, D.M., Houck, J.R.: 2007, The Unusual Hydrocarbon Emission from the Early Carbon Star HD 100764: The Connection between Aromatics and Aliphatics. *Astrophys. J.* **664**, 1144–1153.
- Sloan, G.C., Lagadec, E., Zijlstra, A.A., Kraemer, K.E., Weis, A.P., Matsuura, M., Volk, K., Peeters, E., Duley, W.W., Cami, J., Bernard-Salas, J., Kemper, F., Sahai, R.: 2014, Carbon-rich Dust Past the Asymptotic Giant

- Branch: Aliphatics, Aromatics, and Fullerenes in the Magellanic Clouds. *Astrophys. J.* **791**, 28.
- Smolders, K., Neyskens, P., Blommaert, J.A.D.L., Hony, S., van Winckel, H., Decin, L., van Eck, S., Sloan, G.C., Cami, J., Uttenthaler, S., Degroote, P., Barry, D., Feast, M., Groenewegen, M.A.T., Matsuura, M., Menzies, J., Sahai, R., van Loon, J.T., Zijlstra, A.A., Acke, B., Bloemen, S., Cox, N., De Cat, P., Desmet, M., Exter, K., Ladjal, D., Østensen, R., Saesen, S., van Wyk, F., Verhoelst, T., Zima, W.: 2012, The Spitzer spectroscopic survey of S-type stars. *Astron. Astrophys.* **540**, A72.
- Soker, N., Rappaport, S.: 2001, Departure from Axisymmetry in Planetary Nebulae. *Astrophys. J.* **557**, 256–265.
- Solf, J.: 1994, Long-slit spectroscopic study of the bipolar reflection nebula M 1-92: Detection of compact Herbig-Haro condensations in the lobes. *Astron. Astrophys.* **282**, 567–585.
- Speck, A.K., Hofmeister, A.M.: 2004, Processing of Presolar Grains around Post-Asymptotic Giant Branch Stars: Silicon Carbide as the Carrier of the 21 Micron Feature. *Astrophys. J.* **600**, 986–991.
- Stahler, S.W., Palla, F.: 2005, *The Formation of Stars*.
- Stancliffe, R.J., Izzard, R.G., Tout, C.A.: 2005, Third dredge-up in low-mass stars: solving the Large Magellanic Cloud carbon star mystery. *Mon. Not. Roy. Astron. Soc.* **356**, L1–L5.
- Stancliffe, R.J., Tout, C.A., Pols, O.R.: 2004, Deep dredge-up in intermediate-mass thermally pulsing asymptotic giant branch stars. *Mon. Not. Roy. Astron. Soc.* **352**, 984–992.
- Stasińska, G., Szczerba, R., Schmidt, M., Siódmiak, N.: 2006, Post-AGB stars as testbeds of nucleosynthesis in AGB stars. *Astron. Astrophys.* **450**, 701–714.

- Straizys, V., Meistas, E., Vansevicius, V., Goldberg, E.P.: 1989, Interstellar extinction in the area of the North America and Pelican Nebulae complex. *Astron. Astrophys.* **222**, 82–84.
- Suárez, O., García-Lario, P., Manchado, A., Manteiga, M., Ulla, A., Pottasch, S.R.: 2006, A spectroscopic atlas of post-AGB stars and planetary nebulae selected from the IRAS point source catalogue. *Astron. Astrophys.* **458**, 173–180.
- Szczerba, R., Siódmiak, N., Stasińska, G., Borkowski, J.: 2007, An evolutionary catalogue of galactic post-AGB and related objects. *Astron. Astrophys.* **469**, 799–806.
- Szeifert, T., Hubrig, S., Schöller, M., Schütz, O., Stelzer, B., Mikulášek, Z.: 2010, The nature of the recent extreme outburst of the Herbig Be/FU Orionis binary Z Canis Majoris. *Astron. Astrophys.* **509**, L7.
- te Lintel Hekkert, P.T.L., Chapman, J.M., Zijlstra, A.A.: 1992, Discovery of bipolar OH maser emission from the high-latitude supergiant star HD 101584. *Astrophys. J. Lett.* **390**, L23–L26.
- Teets, W.K., Weintraub, D.A., Grosso, N., Principe, D., Kastner, J.H., Hamaguchi, K., Richmond, M.: 2011, X-Ray Production by V1647 Ori during Optical Outbursts. *Astrophys. J.* **741**, 83.
- Tennyson, J.: 2005, *Astronomical spectroscopy : an introduction to the atomic and molecular physics of astronomical spectra.*
- Testi, L., Palla, F., Natta, A.: 1998, A search for clustering around Herbig Ae/Be stars. II. Atlas of the observed sources. *Astron. Astrophys. Suppl.* **133**, 81–121.
- Thi, W.F., Bik, A., Waters, R.: 2005, Molecular Chemistry in Gaseous Disks Around Young Hot Stars. In: Käuffl, H.U., Siebenmorgen, R., Moorwood, A. (eds.) *High Resolution Infrared Spectroscopy in Astronomy*, 260–263.

- Tielens, A.G.G.M.: 2005, *The Physics and Chemistry of the Interstellar Medium*.
- Tielens, A.G.G.M.: 2008, Interstellar Polycyclic Aromatic Hydrocarbon Molecules. *ARA&A* **46**, 289–337.
- Tokunaga, A.T., Simons, D.A., Vacca, W.D.: 2002, The Mauna Kea Observatories Near-Infrared Filter Set. II. Specifications for a New JHKL'M' Filter Set for Infrared Astronomy. *Pub. Astron. Soc. Pac.* **114**, 180–186.
- Vacca, W.D., Cushing, M.C., Simon, T.: 2004, Near-Infrared Spectroscopy of MCNeil's Nebula Object. *Astrophys. J. Lett.* **609**, L29–L32.
- van den Ancker, M.E., Blondel, P.F.C., Tjin A Djie, H.R.E., Grankin, K.N., Ezhkova, O.V., Shevchenko, V.S., Guenther, E., Acke, B.: 2004, The stellar composition of the star formation region CMa R1 - III. A new outburst of the Be star component in Z CMa. *Mon. Not. Roy. Astron. Soc.* **349**, 1516–1536.
- van der Veen, W.E.C.J., Habing, H.J.: 1988, The IRAS two-colour diagram as a tool for studying late stages of stellar evolution. *Astron. Astrophys.* **194**, 125–134.
- Van Genderen, A.M.: 1999, Book Review: Highlights of astronomy, Volumes 11A and 11B / Kluwer, 1999. *Space Sci. Rev.* **90**, 526–526.
- Van Winckel, H., Reyniers, M.: 2000, A homogeneous study of the s-process in the 21 μ m carbon-rich post-AGB objects. *Astron. Astrophys.* **354**, 135–149.
- Vassiliadis, E., Wood, P.R.: 1993, Evolution of low- and intermediate-mass stars to the end of the asymptotic giant branch with mass loss. *Astrophys. J.* **413**, 641–657.
- Venkat, V., Anandarao, B.G.: 2008, V1647 Orionis. *IAU Circ.* **1596**, 1.

- Venkat, V., Anandarao, B.G.: 2011, V1647 Orionis. *Central Bureau Electronic Telegrams* **2647**, 1.
- Venkata Raman, V., Anandarao, B.G.: 2008, Infrared spectroscopic study of a selection of AGB and post-AGB stars. *Mon. Not. Roy. Astron. Soc.* **385**, 1076–1086.
- Volk, K.M., Kwok, S.: 1989, Evolution of protoplanetary nebulae. *Astrophys. J.* **342**, 345–363.
- Volk, K., Kwok, S., Hrivnak, B.J., Szczerba, R.: 2002, Infrared Space Observatory Observations of the Unidentified 30 Micron Feature in Proto-Planetary Nebulae. *Astrophys. J.* **567**, 412–422.
- von Helden, G., Tielens, A.G.G.M., van Heijnsbergen, D., Duncan, M.A., Hony, S., Waters, L.B.F.M., Meijer, G.: 2000, Titanium Carbide Nanocrystals in Circumstellar Environments. *Science* **288**, 313–316.
- Vorobyov, E.I., Basu, S.: 2006, The Burst Mode of Protostellar Accretion. *Astrophys. J.* **650**, 956–969.
- Waelkens, C., Waters, R.B.F.M.: 2003, Post-AGB Stars. In: Habing, H.J., Olofsson, H. (eds.) *Asymptotic giant branch stars, by Harm J. Habing and Hans Olofsson. Astronomy and astrophysics library, New York, Berlin: Springer, 2003*, 519.
- Waelkens, C., Waters, L.B.F.M., Cassatella, A., Le Bertre, T., Lamers, H.J.G.L.M.: 1987, HD 213985 - A hot post-AGB star in the Galactic halo. *Astron. Astrophys.* **181**, L5–L8.
- Wahlgren, G.M.: 1993, The Rv-Tauri and SRD Variables. In: Sasselov, D.D. (ed.) *Luminous High-Latitude Stars, Astronomical Society of the Pacific Conference Series* **45**, 270.
- Wallerstein, G., Knapp, G.R.: 1998, Carbon Stars. *ARA&A* **36**, 369–434.

- Walter, F.M., Stringfellow, G.S., Sherry, W.H., Field-Pollatou, A.: 2004, V1647 Orionis (IRAS 05436-0007) in Outburst: The First Three Months. *Astron. J.* **128**, 1872–1879.
- Wang, H., Apai, D., Henning, T., Pascucci, I.: 2004, FU Orionis: A Binary Star? *Astrophys. J. Lett.* **601**, L83–L86.
- Wang, X.H., Chen, P.S.: 2002, Near-infrared observations of candidate extrinsic S stars. *Astron. Astrophys.* **387**, 129–138.
- Waters, L.B.F.M., Cami, J., de Jong, T., Molster, F.J., van Loon, J.T., Bouwman, J., de Koter, A., Waelkens, C., Van Winckel, H., Morris, P.W., Cami, J., Bouwman, J., de Koter, A., de Jong, T., de Graauw, T.: 1998, An oxygen-rich dust disk surrounding an evolved star in the Red Rectangle. *Nature* **391**, 868.
- Weintraub, D.A., Sandell, G., Duncan, W.D.: 1991, Are FU Orionis stars younger than T Tauri stars? Submillimeter constraints on circumstellar disks. *Astrophys. J.* **382**, 270–289.
- Welin, G.: 1971, V1057 Cygni. *Information Bulletin on Variable Stars* **581**, 1.
- Welin, G.: 1976, Possible properties of pre-outburst FU Orionis stars. *Astron. Astrophys.* **49**, 145–148.
- Werner, M.W., Roellig, T.L., Low, F.J., Rieke, G.H., Rieke, M., Hoffmann, W.F., Young, E., Houck, J.R., Brandl, B., Fazio, G.G., Hora, J.L., Gehrz, R.D., Helou, G., Soifer, B.T., Stauffer, J., Keene, J., Eisenhardt, P., Gallagher, D., Gautier, T.N., Irace, W., Lawrence, C.R., Simmons, L., Van Cleve, J.E., Jura, M., Wright, E.L., Cruikshank, D.P.: 2004, The Spitzer Space Telescope Mission. *Astrophys. J. Supplement.* **154**, 1–9.
- Whelan, E.T., Dougados, C., Perrin, M.D., Bonnefoy, M., Bains, I., Redman, M.P., Ray, T.P., Bouy, H., Benisty, M., Bouvier, J., Chauvin, G., Garcia, P.J.V., Grankvin, K., Malbet, F.: 2010, The 2008 Outburst in the Young

- Stellar System Z CMa: The First Detection of Twin Jets. *Astrophys. J. Lett.* **720**, L119–L124.
- Whitelock, P., Menzies, J., Feast, M., Marang, F., Carter, B., Roberts, G., Catchpole, R., Chapman, J.: 1994, High Mass Agb-Stars in the South Galactic CAP. *Mon. Not. Roy. Astron. Soc.* **267**, 711.
- Winters, J.M., Le Bertre, T., Jeong, K.S., Helling, C., Sedlmayr, E.: 2000a, A systematic investigation of the mass loss mechanism in dust forming long-period variable stars. *Astron. Astrophys.* **361**, 641–659.
- Winters, J.M., Keady, J.J., Gauger, A., Sada, P.V.: 2000b, Circumstellar dust shells around long-period variables. VIII. CO infrared line profiles from dynamical models for C-stars. *Astron. Astrophys.* **359**, 651–662.
- Woitke, P.: 2006, Too little radiation pressure on dust in the winds of oxygen-rich AGB stars. *Astron. Astrophys.* **460**, L9–L12.
- Woitke, P., Goeres, A., Sedlmayr, E.: 1996, On the gas temperature in the shocked circumstellar envelopes of pulsating stars. II. Shock induced condensation around R Coronae Borealis stars. *Astron. Astrophys.* **313**, 217–228.
- Wood, P.R.: 1979, Pulsation and mass loss in Mira variables. *Astrophys. J.* **227**, 220–231.
- Woodsworth, A.W., Kwok, S., Chan, S.J.: 1990, CO observations of protoplanetary nebulae exhibiting the unidentified feature at 21 microns. *Astron. Astrophys.* **228**, 503–505.
- Yoon, D.H., Cho, S.H., Kim, J., Yun, Y.j., Park, Y.S.: 2014, SiO and H₂O Maser Survey toward Post-asymptotic Giant Branch and Asymptotic Giant Branch Stars. *Astrophys. J. Supplement.* **211**, 15.
- Zhang, Y., Kwok, S.: 2011, Detection of C₆₀ in the Protoplanetary Nebula IRAS 01005+7910. *Astrophys. J.* **730**, 126.

- Zhang, Y., Kwok, S., Hrivnak, B.J.: 2010, A Spitzer/Infrared Spectrograph Spectral Study of a Sample of Galactic Carbon-rich Proto-planetary Nebulae. *Astrophys. J.* **725**, 990–1001.
- Zhukovska, S., Gail, H.P.: 2008, Condensation of MgS in outflows from carbon stars. *Astron. Astrophys.* **486**, 229–237.

Appendix A

Near-infrared monitoring of V1647 Ori

Table A.1: V1647 Ori: *JHK* Photometric Magnitudes and Colors and A_V (in mag) during 2004-2012

Date	JD	<i>J</i>	<i>H</i>	<i>K</i>	<i>J-H</i>	<i>H-K</i>	A_V
2004Mar20	2453084.5	10.85	8.83	7.71	2.02	1.12	11.76
2004Mar21	2453085.5	10.76	8.91	7.59	1.85	1.32	7.81
2004Apr11	2453106.5	11.09	9.01	7.49	2.08	1.52	9.38
2004Oct16	2453294.5	11.15	9.24	7.89	1.91	1.35	8.40
2004Oct17	2453295.5	11.18	9.23	7.87	1.95	1.36	8.87
2004Dec21	2453360.5	11.04	9.20	7.83	1.84	1.37	7.27
2004Dec22	2453361.5	11.03	8.98	7.76	2.05	1.22	11.37
2005Dec31	2453735.5	14.05	11.32	9.63	2.73	1.69	17.01
2006Jan05	2453740.5	14.01	11.47	9.73	2.54	1.74	13.98
2006Feb27	2453793.5	14.60	11.70	9.70	2.90	2.00	16.87
2006Nov03	2454042.5	14.21	11.67	10.01	2.54	1.66	14.62
2006Nov04	2454043.5	14.19	11.68	9.92	2.51	1.76	13.41
2006Nov20	2454059.5	14.11	11.69	9.99	2.42	1.70	12.64
2006Nov21	2454060.5	14.19	11.64	9.94	2.55	1.70	14.44
2006Dec23	2454092.5	14.23	11.74	10.17	2.49	1.57	14.65
2008Nov21	2454791.5	10.79	8.95	7.69	1.84	1.26	8.15

Continued on next page

Table A.1 – *continued from previous page*

Date	JD	<i>J</i>	<i>H</i>	<i>K</i>	<i>J-H</i>	<i>H-K</i>	<i>A_V</i>
2008Nov22	2454792.5	10.82	8.95	7.75	1.87	1.20	9.05
2008Dec04	2454804.5	10.73	8.98	7.66	1.75	1.32	6.42
2009Jan25	2454856.5	10.76	8.86	7.26	1.90	1.60	6.25
2009Jan26	2454857.5	10.74	8.85	7.23	1.89	1.62	5.95
2009Dec18	2455183.5	10.70	8.96	7.55	1.74	1.41	5.56
2009Dec21	2455186.5	10.72	8.96	7.47	1.76	1.49	5.20
2010Jan18	2455214.5	10.74	9.00	7.22	1.74	1.78	—
2010Feb27	2455254.5	10.77	8.95	7.37	1.82	1.58	5.31
2010Oct26	2455495.5	10.79	8.92	7.42	1.87	1.50	6.64
2010Nov07	2455507.5	10.36	9.14	7.85	1.22	1.29	—
2010Dec01	2455531.5	10.86	8.93	7.84	1.93	1.09	10.76
2010Dec19	2455549.5	10.83	9.77	7.51	1.06	2.26	—
2011Jan01	2455562.5	10.86	9.01	7.68	1.85	1.33	7.73
2011Jan02	2455563.5	10.88	9.01	7.21	1.87	1.80	—
2011Jan24	2455585.5	10.80	8.88	8.01	1.92	0.87	—
2011Feb04	2455596.5	10.74	8.96	7.50	1.78	1.46	5.72
2011Mar07	2455627.5	10.86	8.96	7.48	1.90	1.48	7.21
2011Oct20	2455854.5	10.82	8.96	7.46	1.86	1.50	6.50
2011Nov29	2455894.5	11.16	9.17	7.35	1.99	1.82	—
2011Dec16	2455911.5	10.97	9.03	7.78	1.94	1.25	9.61
2012Feb18	2455975.5	10.86	8.98	7.91	1.88	1.07	10.23
2012Mar19	2456005.5	10.80	8.91	7.32	1.89	1.59	6.19
2012Mar30	2456016.5	10.92	8.95	7.89	1.97	1.06	11.55
2012Apr26	2456043.5	11.09	9.16	7.95	1.93	1.21	9.80
2012Apr30	2456047.5	11.11	9.30	7.72	1.81	1.58	5.17
2012Oct19	2456219.5	11.12	9.09	7.78	2.03	1.31	10.38
2012Nov02	2456233.5	10.95	8.96	7.77	1.99	1.19	10.79
2012Nov18	2456249.5	11.16	9.07	7.70	2.09	1.37	10.72

Appendix B

Near-infrared spectroscopy of AGB stars

Table B.1: 2MASS, IRAS colors and Mt Abu EWs (in Å) of the spectral features observed in a sample of M type stars

Star	Sp. Type	ϕ	$H - K$	$K - I_2$	CO(3-0)	CO(4-1)	CO(H)	CO(2-0)	CO(3-1)	CO(K)	\dot{M} ($M_{\odot} \text{ yr}^{-1}$)
02234-0024	M4e	0.34	0.44	2.31	16.1	7.8	51.5	21.1	6.9	61.9	2.6(-6) [†]
03082+1436	M5.5e	0.33	0.45	1.99	11.3	9.2	64.2	25.1	13.3	62.3	9.8(-7) [†]
03489-0131	M4III	...	0.31	1.86	4.8	5.3	61.9	18.4	20.2	45.9	1.3(-6)
04352+6602	Sev	0.44	0.50	1.22	31.8	29.8	101.2	1.4(-7) [†]
05265-0443	M7e	0.57	0.49	1.32	13.6	10.1	53.1	15.1	7.8	22.9	4.6(-7) [†]
05495+1547	S7.5	0.49	0.59	2.79	11.6	8.4	47.4	11.9	16.0	47.6	3.5(-6)
06468-1342	S	...	0.52	1.03	14.5	16.6	85.0	32.9	31.2	110.6	...
06571+5524	Se	0.59	0.64	1.67	20.0	22.1	105.6	18.3	25.6	52.8	1.7(-6) [†]
07043+2246	S6.9e	0.36	0.18	1.17	11.6	13.9	77.0	34.3	28.8	98.8	3.1(-7) [†]
07092+0735	Se	0.30	0.71	3.02	16.4	15.4	72.1	20.5	25.8	81.0	2.9(-6)
07197-1451	S	0.26	0.55	2.32	11.8	8.0	65.0	22.3	9.7	43.5	4.6(-6)
07299+0825	M7e	0.57	0.36	1.90	16.2	10.5	64.1	26.8	14.1	65.3	8.5(-7) [†]
07462+2351	SeV	0.96	0.52	-0.90	12.3	13.8	68.8	28.1	33.9	108.0	...
07537+3118		0.09	0.53	1.40	13.7	9.9	76.5	22.8	25.0	77.5	...
07584-2051	S2.4e	0.19	0.44	1.00	12.6	11.0	78.4	21.2	17.9	39.1	...
08188+1726	SeV	...	0.41	2.28	14.3	13.6	66.1	22.2	24.8	71.3	...
08308-1748	S	...	0.43	0.72	10.1	15.9	72.6	25.7	19.1	92.9	1.7(-7)
08416-3220		...	0.41	0.97	12.2	14.2	75.8	33.0	35.0	105.3	...

Continued on next page

Table B.1 – continued from previous page

Star	Sp. Type	ϕ	$H - K$	$K - 12$	CO(3-0)	CO(4-1)	CO(H)	CO(2-0)	CO(3-1)	CO(K)	\dot{M} ($M_{\odot} \text{ yr}^{-1}$)
08430-2548		...	0.46	1.51	12.2	13.0	68.3	19.6	16.6	80.2	...
09411-1820	Me	0.31	0.49	1.63	5.1	7.3	33.2	8.5	5.7	22.1	7.9(-7) [†]
12372-2623	M4	0.92	0.40	1.39	9.9	14.8	64.2	20.2	23.8	50.8	...
17001-3651	M	0.70	0.58	2.17	9.6	8.9	57.0	11.3	8.9	35.8	1.9(-6) [†]
17186-2914	S	...	0.70	1.76	14.5	13.2	80.7	23.9	26.1	89.2	2.9(-6)
17490-3502	M	0.60	0.54	2.26	16.4	16.1	78.1	24.6	17.6	95.8	...
17521-2907	Se	0.11	0.56	1.64	18.9	19.5	88.4	20.1	21.9	71.8	4.6(-6)
18508-1415	SeV	0.44	0.38	1.00	3.4	5.1	64.3	8.8	5.5	31.1	...
19111+2555	S	0.57	0.80	4.36	19.1	17.6	66.8	13.3	11.2	24.5	4.6(-6) [†]
19126-0708	S..	0.90	0.79	3.81	21.6	19.1	102.0	21.5	23.5	59.4	2.9(-6) [†]
19354+5005	S..	0.24	0.52	2.28	26.6	22.8	108.0	30.2	33.8	98.2	1.5(-6) [†]
23041+1016	M7e	0.87	0.52	2.40	7.3	9.0	50.7	12.4	6.3	18.7	1.5(-6) [†]

Table B.2: 2MASS, IRAS colors and Mt Abu EWs (in Å) of spectral features observed in a sample of S type stars

Star	Sp. Type	$H - K$	$K - 12$	CO(3-0)	CO(4-1)	CO(H)	CO(2-0)	CO(3-1)	CO(K)	\dot{M} ($M_{\odot} \text{ yr}^{-1}$)
04599+1514	M0	0.49	0.96	12.8	17.3	80.8	24.2	28.6	99.4	1.4(-7) [†]
05036+1222		0.60	1.09	12.7	15.1	80.9	26.2	28.1	54.3	...
05374+3153	M2Iab	0.16	1.44	13.7	12.2	77.5	21.6	26.6	88.3	7.3(-7) [†]
07247-1137	Sv...	0.34	0.85	8.6	10.7	57.8	25.8	19.1	74.5	...
07392+1419	M3II-III	0.09	-1.44	5.3	8.4	38.9	16.7	14.7	55.3	7.3(-7)
09070-2847	S	0.25	0.91	10.7	12.8	74.1	22.1	37.1	59.2	...
09152-3023		0.47	1.21	4.0	9.4	44.2	18.1	14.4	39.1	...
10538-1033	M...	0.29	0.74	8.1	4.5	44.6	22.9	9.6	64.9	...
11046+6838	M...	0.40	0.39	3.7	9.5	41.1	15.0	10.4	54.7	...
12219-2802	S	0.30	0.72	9.2	9.4	57.0	22.1	17.8	69.8	...
12417+6121	SeV	0.41	0.95	16.7	18.0	82.4	28.2	29.5	92.2	1.0(-7) [†]
13421-0316	K5	0.22	0.57	...	8.3	40.9	20.0	14.9	59.8	...
13494-0313	M...	0.42	0.56	3.0	9.2	55.5	17.4	20.0	47.4	...
14251-0251	S...	0.34	0.71	3.7	9.1	45.8	20.2	16.7	60.0	...
15494-2312	S	0.38	0.62	5.1	8.1	46.1	19.8	17.2	59.3	...
16205+5659	M...	0.18	0.78	5.4	7.1	45.3	13.0	19.1	61.6	...
16209-2808	S	0.54	0.92	10.7	13.6	73.9	21.9	27.2	79.5	1.0(-7)

Table B.3: 2MASS, IRAS colors and Mt Abu EWs (in Å) of spectral features observed in a sample of SR type stars

Star	Sp. Type	ϕ	$H - K$	$K - I_2$	CO(3-0)	CO(4-1)	CO(H)	CO(2-0)	CO(3-1)	CO(K)	\dot{M} ($M_{\odot} \text{ yr}^{-1}$)
04030+2435	S4.2V	...	0.40	0.63	4.1	8.3	45.0	16.2	17.9	34.1	...
04483+2826	CII	...	0.38	1.04	7.0	10.9	60.3	24.5	17.6	58.3	1.4(-7)
05213+0615	M4	0.41	0.39	1.37	9.3	11.1	64.8	19.3	21.4	56.9	...
05440+1753	S0.V	0.33	0.66	1.89	22.7	19.5	99.5	33.2	30.3	88.1	1.4(-6)
06333-0520	M6	0.85	0.38	1.20	19.7	10.1	77.8	19.1	24.8	61.5	1.7(-7)
08272-0609	M6e	...	0.40	1.47	11.3	7.8	51.7	19.1	15.1	81.4	5.6(-7)
08372-0924	M5II	...	0.36	1.57	5.5	6.5	52.3	18.5	12.4	49.0	1.7(-7)
08555+1102	M5III	...	0.26	1.28	7.4	7.9	61.8	15.5	13.9	43.7	2.4(-7)
09076+3110	M6IIIaSe	...	0.31	1.20	13.5	11.6	65.9	18.5	18.8	56.7	3.8(-7)†
10436-3459	S	...	0.37	1.61	10.5	15.4	61.2	30.3	23.9	79.0	9.5(-7)†
15492+4837	M6S	0.77	0.40	1.58	12.7	13.0	63.8	19.9	24.5	44.4	9.5(-7)†
16334-3107	S4.7.:V	...	0.43	1.13	15.0	22.9	93.4	22.5	29.7	104.8	1.0(-7)†
17206-2826	M.	...	0.42	0.82	10.3	11.4	68.1	15.2	19.6	63.8	1.0(-7)†
17390+0645	SV	0.36	0.92	12.1	7.6	56.7	29.8	14.2	70.9	...
19497+4327		...	0.60	0.82	6.7	11.5	59.2	25.2	18.1	73.8	...

Appendix C

Infrared investigations of PAGB/PPNe candidates

Table C.1: NIR spectral variability observed in a sample of PAGB/PPNe stars

Star	Spectral type	Date of observation	Pa β	Br γ	Br (H)	CO (H)	CO (K)
04296+3429	G0Ia	3 Jan 2006	...	4.1	8.4
		15 Dec 2011	...	2.95	42.01	...	3.82
07134+1005	F5Iab	4 Feb 2007	...	5.1
		16 Dec 2011	3.24	6.63	52.52	...	0.51
		21 Mar 2012	1.62	4.1	47.78	5.39	...
07430+1115	G5Ia	4 Feb 2006	...	3.9	28.9
		21 Mar 2012	4.18	3.41	30.17	23.24	...
08005-2356	F5e	15 Dec 2011	2.0	0.94	12.15	-7.94	-22.41
		19 Mar 2012	...	1.59	13.35	-4.75	-40.65
10158-2844	B9.5Ib-II	18 Feb 2012	1.25	2.44	56.15	-0.5	-5.34
		18 Mar 2010	1.91	2.51	45.31	-4.97	-1.9
		19 Jan 2013	2.31	1.14	36.01
		19 Mar 2012	1.86	1.60	33.1	...	7.44
		30 Mar 2012	1.38	6.62	38.76
12538-2611	F3Ia	19 Mar 2012	2.14	2.72	32.05
		20 Jan 2013	0.89	2.71	36.3	-1.47	-15.71
		22 Jan 2014	0.88	4.1	25.36	...	-34.31

Continued on next page

Table C.1 – *continued from previous page*

Star	Spectral type	Date of observation	Pa β	Br γ	Br (H)	CO (H)	CO (K)
16476-1122	MII	19 Mar 2012	24.67	...
		30 Mar 2012	3.65	...	27.76	40.42	41.39
17423-1755	Be	29 May 2003	...	-5.6	...	-27.6	-11.5
		13 May 2007	...	-5.2	...	-25.4	-23.6
		26 Apr 2012	...	-5.3	-30.17	-28.65	-26.59
17436+5003	F3Ib	18 Mar 2010	2.16	6.75	52.13	...	1.2
18237-0715	Be	28 May 2004	...	-31.7	-42.3
		3 Nov 2006	...	-20.9	-27.4	...	-11.1
		14 May 2007	...	-8.9	-29.8	...	-7.7
19399+2312	Be	1 Nov 2005	20.1	11.8	87.4
		15 May 2007	-4.4	-8.8	-88.0
		6 Jun 2007	-6.2	-15.6	-94.0
		24 Apr 2008	-4.0	-13.8	-35.8
		1 Dec 2010	...	1.69	49.61
20004+2955	G7Ia	2 Nov 2012	2.01	3.97	31.5	-9.99	-12.36
22272+5435	G5Ia	4 Nov 2006	4.4	3.4	30.2
		21 Nov 2008	2.47	5.46	32.6	17.12	31.74
		2 Jan 2011	2.14	3.45	32.53	12.09	21.92
		28 Nov 2011	2.33	3.27	34.91	24.12	32.08
		15 Dec 2011	...	2.43	23.09	3.74	26.39
		2 Nov 2012	1.99	2.65	36.41	-8.08	-6.47
22327-1731	A0III	6 Nov 2006	3.8	28.7
		16 Dec 2011	2.15	1.95	58.38	...	-3.72

Table C.2: Mid-IR EWs (in μm) of PAH features (wavelengths in μm) observed in a sample of PPNe candidates

Object	5.7	6.2	6.7	7.2	7.6	7.8	8.3	8.6	10.7	11.2	12.0	12.6
01005+7910	-0.032	-0.459	-0.030	-	-0.329	-0.161	-	-0.164	-	-0.232	-0.028	-0.018
04296+3429	-0.002	-0.148	-0.064	-0.013	blend	-0.560	blend	blend	-0.006	-0.125	-0.009	-0.013
05089+0459 [†]	-	-	-	-	-	-	-	-	-	-0.355	0	0
05113+1347 [†]	-	-	-	-	-	-	-	-	-	-1.48	blend	blend
05341+0852 [†]	-	-	-	-	-	-	-	-	-	-0.175	0	-0.058
06034+1354 [†]	-	-	-	-	-	-	-	-	-	-0.165	blend	blend
06530-0213 [†]	-	-	-	-	-	-	-	-	-	-0.212	-0.053	0
07134+1005 [†]	-	-	-	-	-	-	-	-	-	-0.237	-0.081	0
08005-2356 [†]	-	-	-	-	-	-	-	-	-	-0.104	blend	blend
11339-6004	-	-	-	-	-	-	-	-0.258	-	-1.922	-	-
11387-6113	-	-0.043	-	-	-	-0.080	-	-	-	-3.236	blend	blend
13245-5036 [†]	-	-	-	-	-	-	-	-	-	-0.087	-	-
13313-5838	-	-0.024	-0.070	-	-	-	-	-0.638	-0.013	-0.009	-0.024	-
13500-6106	-	-	-	-	-2.088	-	-	-	-	-	-	-1.043
14341-6211 [†]	-	-	-	-	-	-	-	-	-	-	-0.204	-
14429-4539	-	-0.192	-	-0.005	-	-0.337	-	-0.030	-0.009	-0.152	-0.005	-0.022
16206-5956 [†]	-	-	-	-	-	-	-	-	-	-1.214	-	-
16559-2957	-	-	-0.003	-0.007	-	-0.741	-	-	-0.009	-0.513	blend	blend

Continued on next page

Table C.2 – continued from previous page

Object	5.7	6.2	6.7	7.2	7.6	7.8	8.3	8.6	10.7	11.2	12.0	12.6
17009-4154 [†]	-	-	-	-	-	-	-	-	-	-0.142	-	-0.087
17074-1845	-	-	-	-	-	-0.032	-	-	-	-8.542	blend	blend
17130-4029	-	-0.056	-	-	-	-	-0.260	-	-	-0.111	blend	blend
17195-2710	-	-	-0.002	-	-0.005	-	-0.761	-	-	-0.844	blend	blend
17203-1534 [†]	-	-	-	-	-	-	-	-	blend	-5.682	blend	blend
17234-4008	-	-	-	-	-	-	-0.597	-	blend	-0.217	blend	blend
17253-2831	-	-0.003	-0.003	-0.003	-	-0.026	-	-0.230	-	-1.063	blend	blend
17287-3443 [†]	-	-	-	-	-	-	-	-	-0.069	-	-0.013	-
17311-4924 [†]	-	-	-	-	-	-	-	-	-	-	-	-
17317-2743 [†]	-	-	-	-	-	-	-	-	-	-0.485	-	-
17381-1616	-	-	-0.604	-	-	-	-0.037	-	-	-5.955	blend	blend
17423-1755	-0.001	-	-0.009	-	-	-	-	-	-	-	-	-0.009
17542-0603	-0.002	-0.011	-0.001	-0.005	-	-	-	-0.002	-	-0.377	blend	blend
17580-3111	-	-	-0.035	-0.003	-	-	-	-1.040	-	-0.235	blend	blend
18023-3409 [†]	-	-	-	-	-	-	-	-	-	-3.225	blend	blend
18062+2410 [†]	-	-	-	-	-	-	-	-	-	-8.402	blend	blend
18533+0523	-	-0.116	-	-0.002	-	-1.557	blend	blend	-	-1.063	blend	blend
19024+0044	-	-0.177	-	-0.013	-	-0.077	-	-0.029	-0.039	-	-0.022	-
19157-0247	-	-	-0.001	-	-	-	-0.018	-	-	-0.860	blend	blend

Continued on next page

Table C.2 – continued from previous page

Object	5.7	6.2	6.7	7.2	7.6	7.8	8.3	8.6	10.7	11.2	12.0	12.6
19200+3457	-	-0.527	-	-	-0.996	-	-	-0.119	-	-0.291	-0.029	-0.050
19306+1407	-0.057	-0.437	-	-0.006	-	-0.509	-	-0.023	-	-1.908	blend	blend
19454+2920 [†]	-	-	-	-	-	-	-	-	-	-0.192	blend	blend
19477+2401 [†]	-	-	-	-	-	-	-	-	-	-0.094	-	-
19590-1249	-	-0.097	-	-	-	-	-	-0.069	-	-8.415	blend	blend
20462+3416	-	-0.153	-	-0.024	-	-0.883	-	-0.027	-	-1.241	blend	-0.019
20572+4919	-	-0.007	-0.003	-	-	-	-	-	-	-1.784	blend	-
21289+5815	-	-0.138	-	-	-	-0.142	-	-0.023	blend	-0.905	blend	blend
22023+5249	-	-0.467	-	-	-1.444	-	-	-0.035	-	-0.838	blend	-0.013
22036+5306 [†]	-	-	-	-	-	-	-	-	-	-	-	-
22223+4327	-	-0.036	-	-	-	-	-0.202	-	-	-0.853	blend	blend
F22327-1731	-	-	-	-	-	-0.026	-	-	-	-0.152	blend	blend
23304+6147 [†]	-	-	-	-	-	-	-	-	-	-0.145	blend	-0.067

Table C.3: Mid-IR EWs (in μm) of PAH features (wavelengths in μm) observed in a sample of PAGB candidates

Object	5.7	6.2	6.7	7.2	7.6	7.8	8.3	8.6	10.7	11.2	12.0	12.6
06556+1623 [†]	-	-	-	-	-	-	-	-	-	-0.030	-0.004	-0.005
08335-4026	-	-0.119	-0.013	-	-	-0.256	-	-0.046	-0.007	-0.054	-	-0.018
10211-5922	-0.004	-0.001	-0.006	-0.005	-0.019	-	-	-	-0.010	-0.004	-0.019	-0.040
11201-6545 [†]	-	-	-	-	-	-	-	-	-	-0.766	-	-
11353-6037	-	-0.471	-	-0.010	-	-0.919	-	-0.105	-0.012	-0.071	-0.005	-0.010
12145-5834	-0.067	-0.392	-	-	-0.658	-	-	-0.168	-	-0.109	-0.004	-0.020
13529-5934 [†]	-	-	-	-	-	-	-	-0.708	-	-	-0.115	-
14325-6428 [†]	-	-	-	-	-	-	-	-	-	-	-0.344	-
14346-5952 [†]	-	-	-	-	-	-	-	-	-	-0.762	-	-
14482-5725	-	-0.069	-	-0.022	-	-	-0.151	-	-	-0.176	-	-
15482-5741	-	-0.130	-	-	-	-	-0.920	-	-	-0.088	-0.025	-
sao243233	-	-	-0.273	-	-0.120	-	-	-	-	-	-	-
16494-3930 [†]	-	-	-	-	-	-	-	-	-	-0.239	-	-
17088-4221 [†]	-	-	-	-	-	-	-	-	-	-3.554	blend	blend
17168-3736 [†]	-	-	-	-	-	-	-	-	-	-4.577	blend	blend
17359-2902	-	-	-	-	-	-	-	-0.320	-0.042	-0.635	blend	blend
17364-1238	-	-0.101	-	-	-	-	-	-0.075	-	-2.516	blend	blend
17376-2040	-	-	-	-	-0.017	-	-	-0.033	-	-0.176	blend	blend

Continued on next page

Table C.3 – continued from previous page

Object	5.7	6.2	6.7	7.2	7.6	7.8	8.3	8.6	10.7	11.2	12.0	12.6
17488-1741 [†]	-	-	-	-	-	-	-	-	-	-	-	-
18246-1032	-	-0.001	-0.025	-0.079	-0.285	blend	blend	-	-	-	-	-
20259+4206 [†]	-	-	-	-	-	-	-	-	-	-	-	-0.111
21546+4721	-0.027	-0.193	-0.012	-0.027	-0.424	-	-	-0.123	-	-0.943	blend	blend

Table C.4: Parameters derived from SED modeling of PPNe candidates using DUSTY; the spectral types are from SIMBAD and Suárez *et al.* (2006) (with asterisks)

Object	Sp.Type	T _*	T _d	$\tau_{0.55}$	Grain type	r ₁ (cm)	r ₁ /r _c	\dot{M} (M _⊙ yr ⁻¹)
05089+0459	M3I	3500	200	6.0	AmC(1.0)	2.14E+16	1.13E+03	5.87E-05
06034+1354	–	5000	500	3.0	AmC(0.2)+Gr(0.8)	2.93E+15	3.16E+02	1.67E-05
08005-2356	F5e	6650	450	5.0	Gr(1.0)	5.38E+15	1.02E+03	3.09E-05
11339-6004	–	14000	200	8.0	AmC(1.0)	1.77E+16	4.75E+02	4.84E-05
11387-6113	A3I	8890	170	3.0	Gr(1.0)	4.36E+16	1.48E+04	7.21E-05
13245-5036	A7Ie	7650	200	7.0	AmC(1.0)	2.98E+16	7.52E+04	8.25E-05
13500-6106	–	11000	280	20.0	AmC(0.1)+Gr(0.1)+Sil(0.8)	8.23E+15	4.29E+03	1.08E-04
14341-6211	–	6000	190	10.0	AmC(1.0)	3.15E+16	4.88E+03	9.75E-05
16206-5956	A3Iab:e	8000	105	0.7	AmC(0.3)+Sil(0.7)	7.65E+16	2.11E+04	5.11E-05
16559-2957	F5Iab:e	6650	220	4.0	AmC(0.7)+Sil(0.3)	1.65E+16	3.15E+03	5.14E-05
17074-1845	B5Ibe	11000	140	3.0	Sil(1.0)	3.31E+16	1.72E+04	1.03E-04
17130-4029	–	14000	200	2.5	Gr(1.0)	3.80E+16	3.21E+04	6.50E-05
17195-2710*	em	8000	380	9.0	Gr(1.0)	8.90E+15	2.45E+03	5.17E-05
17203-1534	B1IIIpe	10000	130	2.5	Gr(0.3)+Sil(0.7)	5.00E+16	2.15E+04	9.06E-05
17234-4008	–	14000	200	10.0	Gr(1.0)	3.89E+16	3.29E+04	1.13E-04
17253-2831	–	5000	170	5.0	AmC(0.7)+Gr(0.3)	3.66E+16	3.95E+03	7.54E-05

Continued on next page

Table C.4 – continued from previous page

Object	Sp.Type	T_*	T_d	$\tau_{0.55}$	Grain type	r_1 (cm)	r_1/r_c	\dot{M} ($M_\odot \text{ yr}^{-1}$)
17287-3443	–	18000	150	20.0	AmC(0.3)+Gr(0.7)	7.45E+16	1.04E+05	2.08E-04
17311-4924	B1Iae	15000	200	3.0	Gr(0.4)+Sil(0.6)	2.36E+16	2.94E+04	6.77E-05
17317-2743	F5I	6640	160	7.5	Gr(1.0)	4.29E+16	8.15E+03	1.05E-04
17381-1616	B1Ibe	20700	400	1.0	AmC(1.0)	5.85E+15	1.08E+04	1.68E-05
17423-1755	Be	13000	170	5.0	Gr(0.8)+Sil(0.2)	4.00E+16	2.66E+04	8.69E-05
18023-3409	B2IIIe	10000	175	1.0	AmC(0.3)+Sil(0.7)	2.24E+16	9.65E+03	3.75E-05
18062+2410	B1IIIpe	18000	200	1.0	Sil(1.0)	1.91E+16	2.67E+04	4.59E-05
19024+0044	–	10000	200	10.0	Gr(1.0)	3.47E+16	1.50E+04	1.07E-04
19157-0247	B1III	15000	800	2.0	Gr(0.8)+Sil(0.2)	1.57E+15	1.53E+03	1.28E-05
19454+2920	–	10000	180	7.0	AmC(1.0)	4.26E+16	1.83E+04	9.79E-05
19477+2401*	F4I	6820	200	10.0	AmC(0.8)+Gr(0.2)	2.89E+16	5.78E+03	9.73E-05
19590-1249	B1Ibe	20000	125	0.1	Gr(0.3)+Sil(0.7)	7.12E+16	1.23E+05	1.84E-05
20572+4919*	F3Je	7700	265	2.0	Gr(0.85)+Sil(0.15)	1.28E+16	2.99E+03	2.99E-05
22036+5306*	em	8000	150	8.0	AmC(0.8)+Gr(0.2)	6.26E+16	1.73E+04	1.25E-04
F22327-1731	A0III	7600	600	0.35	Gr(0.85)+Sil(0.15)	2.22E+15	5.53E+02	4.63E-06

Table C.5: Parameters derived from SED modeling of PAGB candidates; the spectral types are from SIMBAD and Suárez *et al.* (2006) (with asterisks)

Object	Sp.Type	T_*	T_d	$\tau_{0.55}$	Grain type	$r_1(\text{cm})$	r_1/r_c	$\dot{M} (M_\odot \text{ yr}^{-1})$
11201-6545	A3Ie	6000	150	5.0	AmC(1.0)	5.86E+16	9.09E+03	9.74E-05
13529-5934	–	12000	200	13.0	AmC(0.2)+Gr(0.8)	3.65E+16	2.26E+04	1.21E-04
14325-6428*	F5I	6640	160	2.5	AmC(0.9)+Gr(0.1)	4.96E+16	9.41E+03	6.55E-05
14346-5952	–	16000	650	15.0	Gr(1.0)	3.45E+15	2.14E+03	3.43E-05
sao243233	B3II/III	18000	100	0.5	Gr(1.0)	1.37E+17	1.38E+05	5.15E-05
16494-3930	G2I	5160	200	8.0	AmC(0.7)+Gr(0.3)	2.53E+16	2.90E+03	7.85E-05
17088-4221	–	14000	250	15.0	AmC(0.1)+Gr(0.9)	2.49E+16	2.10E+04	1.06E-04
17168-3736	–	14000	240	12.0	Gr(1.0)	2.78E+16	2.35E+04	1.03E-04
17359-2902	–	8000	230	15.0	Gr(1.0)	2.44E+16	6.74E+03	1.07E-04
17364-1238	–	8000	130	1.0	AmC(0.1)+SiI(0.9)	3.25E+16	8.95E+03	4.64E-05
17376-2040	F6I	6460	280	4.0	AmC(0.5)+Gr(0.5)	1.26E+16	2.26E+03	4.17E-05
17488-1741	F7I	6280	260	6.5	Gr(1.0)	1.67E+16	2.83E+03	6.09E-05
18246-1032	–	20000	130	20.0	Gr(0.8)+SiI(0.2)	8.50E+16	1.34E+05	2.25E-04
20259+4206	F3I	6990	200	8.0	AmC(1.0)	2.90E+16	6.10E+03	8.57E-05

Table C.6: Parameters derived with two shells in the SED modeling using DUSTY for the PPNe candidates; the spectral types are from SIMBAD

Objects	Sp. Type	T_*	Sphere1			Sphere2				
			PAH type	T_d	r_1 (cm)	r_1/r_c	Grain type	T_d	r_1 (cm)	r_1/r_c
011005+7910	B2Iab:e	15000	ionised	700	3.19E+15	3.09E+03	Gr(1.0)	250	2.54E+16	2.46E+04
04296+3429	G0Ia	5510	ionised	600	1.98E+15	2.58E+02	AmC(0.9)+Gr(0.1)	200	2.65E+16	3.47E+03
05113+1347	G8Ia	4590	neutral	250	1.48E+16	1.34E+03	AmC(1.0)	200	2.40E+16	2.18E+03
05341+0852	F4Iab	6820	ionised	500	4.01E+15	8.04E+02	Gr(1.0)	250	1.87E+16	3.76E+03
06530-0213	F0Iab:	7300	neutral	250	2.45E+16	5.63E+03	Gr(1.0)	100	1.23E+17	2.83E+04
07134+1005	F5Iab:	6650	neutral	600	2.50E+15	4.76E+02	AmC(1.0)	150	6.11E+16	1.16E+04
13313-5838	K1III	4600	ionised	700	1.09E+15	9.90E+01	Gr(0.7)+AmC(0.3)	300	9.33E+15	8.51E+02
14429-4539	F4I	6820	ionised	400	7.08E+15	1.42E+03	Gr(0.6)+AmC(0.4)	320	9.72E+15	1.95E+03
17009-4154	-	4500	neutral	250	1.46E+16	1.27E+03	Gr(1.0)	100	8.99E+16	7.84E+03
17542-0603	em	5500	ionised	1000	5.05E+14	6.58E+01	Gr(1.0)	500	3.70E+15	4.82E+02
17580-3111	-	5000	ionised	600	1.79E+15	1.93E+02	Gr(1.0)	200	2.37E+16	2.55E+03
18533+0523	-	5000	ionised	400	5.06E+15	5.45E+02	Gr(0.7)+AmC(0.3)	100	1.09E+17	1.17E+04
19200+3457	B...	12000	ionised	500	6.75E+15	4.18E+03	Gr(1.0)	230	2.54E+16	1.58E+04
19306+1407	B0:e	15400	ionised	800	2.29E+15	2.34E+03	Gr(1.0)	100	1.62E+17	1.65E+05
20462+3416	B1Iae	20500	neutral	150	1.56E+17	2.92E+05	Gr(0.5)+AmC(0.5)	100	1.77E+17	3.30E+05

Continued on next page

Table C.6 – *continued from previous page*

Objects	Sp. Type	T_*	Sphere1				Sphere2			
			PAH type	T_d	r_1 (cm)	r_1/r_c	Grain type	T_d	r_1 (cm)	r_1/r_c
21289+5815	A2Ie	7000	ionised	700	1.70E+15	3.59E+02	Gr(0.7)+Sil(0.3)	300	8.63E+15	1.82E+03
22023+5249	Be	12000	ionised	200	6.15E+16	3.81E+04	Gr(0.2)+AmC(0.8)	160	5.91E+16	3.67E+04
22223+4327	F9Ia	6100	ionised	700	1.45E+15	2.32E+02	Gr(1.0)	180	3.25E+16	5.21E+03
23304+6147	G2Ia	5200	neutral	400	5.50E+15	6.41E+02	Gr(0.5)+AmC(0.5)	170	3.60E+16	4.19E+03

Table C.7: Parameters derived with two shells in the SED modeling using DUSTY for the PAGB candidates; the spectral types are from SIMBAD

Objects	Sp. Type	T_*	Sphere1			Sphere2				
			PAH type	T_d	r_1 (cm)	r_1/r_c	Grain type	T_d	r_1 (cm)	r_1/r_c
06556+1623	Bpe	15000	neutral	1100	9.45E+14	9.16E+02	Gr(1.0)	300	1.85E+16	1.80E+04
08335-4026	B8e	11500	ionised	700	2.73E+15	1.55E+03	Gr(0.95)+Sil(0.05)	100	1.39E+17	7.94E+04
11353-6037	B5Ie	13400	ionised	500	7.30E+15	5.65E+03	Gr(1.0)	220	3.05E+16	2.36E+04
12145-5834	-	10000	ionised	500	5.93E+15	2.56E+03	Gr(1.0)	100	1.34E+17	5.76E+04
14482-5725	A2I	9080	neutral	400	4.22E+15	2.91E+02	Gr(1.0)	300	9.10E+15	6.27E+02
15482-5741	F7I	4000	ionised	700	9.36E+14	6.45E+01	AmC(1.0)	150	4.91E+16	3.38E+03
21546+4721	-	10000	ionised	500	5.91E+15	2.54E+03	Gr(1.0)	200	3.46E+16	1.49E+04

Table C.8: EWs (in μm) of H₂ S(5) rotational line (wavelengths in μm) observed in a sample of PAGB and PPNe candidates

Object	S(6)	S(5)
	6.11	6.93
14429-4539	..	-0.021
17542-0603	-0.014	..
19024+0044	-0.125	..
19200+3457	..	-0.035
20462+3416	..	-0.055
22023+5249	..	-0.055
PAGB		
11353-6037	..	-0.034
15482-5741	..	-0.012

Table C.9: EWs (in μm) of the spectral features at 23, 27, 33 μm possibly due to crystalline forsterite and broad 30 μm feature possibly due to MgS (wavelengths in μm) observed in a sample of PPNe candidates

Object	21	23	27	33	30
01005+7910	-	-	-	-	-4.331
04296+3429	-1.222	-	-	-	-2.223
05089+0459	-	-	-	-	-
05113+1347	-0.658	-	-	-	-2.762
05341+0852	-0.359	-	-	-	-2.382
06034+1354	-	-0.138	-0.092	-0.312	-
06530-0213	-1.801	-	-	-	-1.884
07134+1005	-	-	-	-	-
08005-2356	-	-	-	-	-
11339-6004	-	-	-	-	-1.444
11387-6113	-	-	-	-	-3.266
13245-5036	-1.431	-	-	-	-0.231
13313-5838	-	-	-	-	-
13500-6106	-	-	-	-	-2.515

Continued on next page

Table C.9 – *continued from previous page*

Object	21	23	27	33	30
14341-6211	-	-	-	-	-
14429-4539	-0.329	-	-	-	-1.929
16206-5956	-	-0.641	-0.128	-0.316	-
16559-2957	-	-0.469	-	-0.105	-
17009-4154	-	-	-	-	-
17074-1845	-	-0.462	-0.070	-0.207	-
17130-4029	-	-0.163	-0.064	-0.091	-
17195-2710	-	-0.431	-	-	-
17203-1534	-	-0.275	-0.084	-0.095	-
17234-4008	-	-	-	-	-1.629
17253-2831	-	-0.043	-0.096	-0.270	-
17287-3443	-	-	-	-	-
17317-2743	-	-0.700	-0.130	-0.203	-
17381-1616	-	-0.357	-	-0.025	-
17423-1755	-	-	-	-	-3.579
17542-0603	-	-0.113	-	-0.051	-
17580-3111	-	-0.257	-0.014	-0.102	-
18023-3409	-	-0.380	-0.105	-0.279	-
18062+2410	-	-0.068	-	-	-
18533+0523	-0.394	-	-	-	-1.521
19024+0044	-	-0.427	-0.099	-0.252	-
19157-0247	-	-0.077	-0.084	-0.291	-
19200+3457	-	-	-	-	-1.585
19306+1407	-	-	-	-	-
19454+2920	-	-	-	-	-
19477+2401	-0.215	-	-	-	-0.850
19590-1249	-	-0.268	-0.051	-0.080	-
20462+3416	-	-0.442	-0.138	-0.223	-
20572+4919	-	-	-	-	-
21289+5815	-	-	-	-	-
22023+5249	-	-0.432	-0.220	-0.166	-
22036+5306	-	-	-	-	-1.484
22223+4327	-3.743	-	-	-	-4.096
F22327-1731	-	-0.020	-0.020	-0.146	-

Continued on next page

Table C.9 – *continued from previous page*

Object	21	23	27	33	30
23304+6147	-1.511	-	-	-	-2.774

Table C.10: EWs (in μm) of the spectral features at 23, 27, 33 μm possibly due to crystalline forsterite and broad 30 μm feature possibly due to MgS (wavelengths in μm) observed in a sample of PAGB candidates

Object	21	23	27	33	30
06556+1623	-	-	-	-	-
08335-4026	-	-0.089	-0.144	-0.681	-
10211-5922	-	-	-	-	-
11201-6545	-	-0.314	-0.089	-0.118	-
11353-6037	-	-0.840	-0.18	-0.268	-
12145-5834	-	-	-	-	-5.371
13529-5934	-	-0.213	-0.572	-0.181	-
14325-6428	-	-	-	-	-4.172
14346-5952	-	-	-	-	-1.270
14482-5725	-	-0.214	-0.313	-0.917	-
15482-5741	-1.484	-	-	-	-1.901
sao243233	-	-	-	-0.055	-
16494-3930	-	-0.493	-	-0.139	-
17088-4221	-	-	-	-	-
17168-3736	-	-	-0.298	-0.277	-
17359-2902	-	-0.438	-0.115	-0.495	-
17364-1238	-	-0.689	-	-	-
17376-2040	-	-0.010	-0.008	-0.057	-
17488-1741	-	-0.022	-0.177	-0.281	-
18246-1032	-0.046	-0.033	-0.531	-0.069	-
20259+4206	-	-0.013	-0.021	-0.021	-
21546+4721	-	-	-	-	-1.624

Appendix D

LIST OF PUBLICATIONS

A. Refereed journals

1. “Near-infrared monitoring and modeling of V1647 Ori in its ongoing 2008-2012 outburst phase”
Venkata Raman, Veeman; Anandarao, Boddapati G.; Janardhan, Padmanabhan.; Pandey, Rajesh
2013, Research in Astronomy and Astrophysics, 13, 1107
2. “Infrared photometric and spectroscopic study of a selection of post-AGB stars and Proto-Planetary Nebulae”
Venkata Raman, V.; Anandarao, B. G.; Janardhan, P.; Pandey, Rajesh
In preparation for Monthly Notices of Royal Astronomical Society
3. “The Peculiar Extinction Law of SN 2014J Measured with the Hubble Space Telescope”
Amanullah, R.; Goobar, A.; Johansson, J.; Banerjee, D. P. K.; **Venkataraman, V.**; Joshi, V.; Ashok, N. M.;....
2014, The Astrophysical Journal Letters, 788, L21

4. **“Near-IR Studies of Recurrent Nova V745 Scorpii during its 2014 Outburst”**
Banerjee, D. P. K.; Joshi, Vishal; **Venkataraman, V.**; Ashok, N. M.;
Marion, G. H.; Hsiao, E. Y.; Raj, A.
2014, The Astrophysical Journal Letters, 785, L11
5. **“The Rise of SN 2014J in the Nearby Galaxy M82”**
Goobar, A.; Johansson, J.; Amanullah, R.; Cao, Y.;.....Banerjee, D. P.
K.; **Venkataraman, V.**; Joshi, V.; Ashok, N. M.;.....
2014, The Astrophysical Journal Letters, 784, L12
6. **“Early Observations and Analysis of the Type Ia SN 2014J in M82”**
Marion, G.H.; Sand, D.J.; Hsiao, E.Y.;.....**Venkataraman, V.**,Ashok,
N. M.;....
2015, The Astrophysical Journal, 798, 39
7. **“Infrared spectroscopic study of a selection of AGB and post-AGB stars”**
Venkata Raman, V.; Anandarao, B. G.
2008, Monthly Notices of Royal Astronomical Society, 385, 1076
8. **“Near-infrared photometry and radio continuum study of the massive star-forming regions IRAS 21413+5442 and IRAS 21407+5441”**
Anandarao, B. G.; **Raman, V. Venkata**; Ghosh, S. K.; Ojha, D. K.;
Kumar, M. S. N.
2008, Monthly Notices of the Royal Astronomical Society, 390, 1185
9. **“Post-outburst phase of McNeil’s nebula (V1647 Orionis)”**
Ojha, D. K.; Ghosh, S. K.; Tej, A.;.....Anandarao, B. G.; **Venkata Raman, V.**
2006,Monthly Notices of Royal Astronomical Society, 368, 825

B. Conference proceedings

1. “Multi-Wavelength Study of the 2008-2009 Outburst of V1647 Ori”

Garca-Alvarez, D.; Wright, N. J.;.....Anandarao, B. G.;..... Venkat, V.;.....

2011, 16th Cambridge Workshop on Cool Stars, Stellar Systems, and the Sun. ASP Conference Series, Vol. 448, proceedings of a conference held August 28- September 2, 2010 at the University of Washington, Seattle, Washington, Astronomical Society of the Pacific, 2012, 609

C. CBETS and ATels related to the thesis

1. “V1647 Ori”

Venkat, V.; Anandarao, B. G.

2006, IAU Circulars, 8694

2. “V1647 Ori”

Venkat, V.; Anandarao, B. G.

2008, Central Bureau for Astronomical Telegrams, 1596

3. “V1647 Ori”

Venkat, V.; Anandarao, B. G.

2011, Central Bureau for Astronomical Telegrams, 2647

D. Presentation at Conferences and Symposia

1. “Infrared study of Circumstellar shells on a sample of post-AGB stars”

Venkataraman, V.; Anandarao, B. G.; Padmanabhan Janardhan; Rajesh Pandey

2012, Poster presentation in Committee on Space Research (COSPAR) at Mysore, INDIA. 14-22 July, 2012

2. **“Near-IR Observations of the eruptive variable V1647 Ori and Modelling of its Spectral Energy Distribution”**
Venkataraman, V.; Anandarao, B. G.; Padmanabhan Janardhan.; Rajesh Pandey
2012, Poster presentation in Committee on Space Research (COSPAR) at Mysore, INDIA. 14-22 July, 2012
3. **“Investigation of the behaviour of the eruptive young stellar object V1647 Ori since its outburst in 2008”**
Venkataraman, V.; Anandarao, B. G.; P. Janardhan.; R. Pandey
2013, Poster presentation in 31st Astronomical Society of India meeting at Trivandrum, INDIA. 20-22 February, 2013
4. **“Infrared investigation of the eruptive young stellar object V1647 Ori during its outburst and quiescent phases”**
Venkataraman, V.; Anandarao, B. G.
2014, Poster presentation in International Conference on Interstellar Dust, Molecules and Chemistry at Tezpur, Assam, INDIA. 15-18 December, 2014

Appendix E

Reprints of research
papers published in
refereed journals

Near-infrared monitoring and modeling of V1647 Ori in its ongoing 2008–2012 outburst phase

This content has been downloaded from IOPscience. Please scroll down to see the full text.

2013 Res. Astron. Astrophys. 13 1107

(<http://iopscience.iop.org/1674-4527/13/9/009>)

View [the table of contents for this issue](#), or go to the [journal homepage](#) for more

Download details:

IP Address: 210.212.155.232

This content was downloaded on 02/12/2013 at 05:23

Please note that [terms and conditions apply](#).

Near-infrared monitoring and modeling of V1647 Ori in its ongoing 2008–2012 outburst phase

Veeman Venkata Raman¹, Boddapati G. Anandarao¹, Padmanabhan Janardhan¹ and Rajesh Pandey²

¹ Physical Research Laboratory (PRL), Ahmedabad - 380009, India; vvenkat@prl.res.in

² Physics Department, Mohanlal Sukhadia University, Udaipur - 313001, India

Received 2013 January 10; accepted 2013 April 18

Abstract We present results of the Mt Abu *JHK* photometric and HI Brackett γ line monitoring of the eruptive young stellar object V1647 Orionis (McNeil’s Object) during its ongoing outburst phase in 2008–2012. We discuss *JHK* color patterns and extinction during the outburst and compare them with those from the previous outburst phase in 2004–2005 and in the intervening quiescent period that lasted about 2 yr. Commencing from early 2012, the object has shown a slow fading out in all the bands. We report brightness variations in the nearby Herbig-Haro object HH22 that are possibly associated with those in V1647 Ori. We also present modeling of the spectral energy distributions of V1647 Ori during both its recent outburst and its quiescent phase. The physical parameters of the protostar and its circumstellar environment obtained from the modeling indicate marked differences between the two phases.

Key words: stars: pre-main sequence — stars: formation — (stars:) circumstellar matter — stars: individual (V1647 Ori)

1 INTRODUCTION

It is believed that most low-mass pre-main-sequence (PMS) stars undergo a recurring active stage during which they show enhanced brightness or an ‘outburst’ lasting for a few years to a decade or longer (e.g., Stahler & Palla 2004 and references therein). Among the various mechanisms proposed (see Hartmann & Kenyon 1996), by which the rate of accreted mass substantially increases over a period of time causing the outburst, are the thermal instability in accretion disks (Bell et al. 1995), evolution from envelope accretion to disk magnetospheric accretion (Hartmann & Kenyon 1985), and gravitational or tidal triggering by the passage of a putative binary companion (Bonnell & Bastien 1992). Depending upon the duration of the outburst, PMS stars are sub-classified as FUors (prototype being FU Orionis) that last for over a decade or longer and EXors (prototype EX Lupis) that occur over shorter periods of about two years (Herbig 1977). V1647 Ori (IRAS 05436–0007), first discovered by McNeil et al. (2004) and since called McNeil’s object, showed an outburst akin to EXors, yet it seemed to be distinctive (e.g., Ojha et al. 2006; Aspin et al. 2008; Aspin & Reipurth 2009 and the references therein). While the duration of its outburst was similar to EXors, its spectral characteristics seemed to be so different from EXors that it may as well be a new class of object in itself (Kun 2008). However, in recent times the star showed a second outburst (currently ongoing) starting from mid-2008 (for a comprehensive study, see Aspin 2011 and references therein).

Reporting post-2008 outburst behavior, Aspin (2011) concluded that the object remained “in an elevated photometric state” till early 2011. It was also concluded that McNeil’s nebular morphology remained unchanged in its two recent outbursts. Furthermore, a large discrepancy in the accretion rates derived from $H\alpha$ and $Br\gamma$ emission line fluxes was reported. Using high resolution spectroscopy, Brittain et al. (2010) showed that the accretion rates derived from $Br\gamma$ emission were similar during the two outbursts (though varying) and a factor of ~ 16 higher than the smallest accretion rate during the quiescent phase. These studies showed that the current (ongoing) outburst was basically different from the earlier one and this deserves further investigation. Clearly, therefore, continued monitoring of the object is necessary to detect possible changes in its behavior post-2011.

In this work, we present a substantial volume of *JHK* photometric and some *K* band spectroscopic observations made from Mt Abu during 2008–2012. We discuss their possible implications on the nature of V1647 Ori, in comparison with the previous outburst and quiescent phases. Further, we attempt to model the spectral energy distribution (SED) using an online modeling tool developed by Robitaille et al. (2007) and compare the physical parameters including accretion rates of both disk and envelope for V1647 Ori during the two epochs (viz. quiescence and outburst). Section 2 gives the details of our observations and Section 3 presents the results and discussion, including SED modeling results. Section 4 gives important conclusions.

2 NEAR-INFRARED PHOTOMETRIC AND SPECTROSCOPIC OBSERVATIONS

JHK photometric observations were made using the Near Infrared Camera & Multi-object Spectrograph (NICMOS) (256×256 HgCdTe array) and the Near Infrared Camera & Spectrograph (NICS) (HAWAII-1 $1k \times 1k$ HgCdTe array), both mounted at the Cassegrain focus of the 1.2 m infrared telescope of the Physical Research Laboratory’s (PRL’s) Mt Abu Observatory.

The data consist of more than 40 sets of *JHK* observations during the period 2004–2012, a majority of which were made during the period 2008–2012. A part of the photometric data obtained between 2004–2005 appeared in Ojha et al. (2006). Single frame integration times were 40–60 s/20–30 s for *J*, 20–40 s/10–20 s for *H* and 2 s/10–15 s for *K* band with the NICMOS/NICS cameras. Several such frames were taken amounting to total integration times of 120–720 s for NICMOS and 120–400 s for NICS. A sufficient number of dithered frames were obtained for effective background subtraction and flat fielding. The seeing during the observations was typically $1.7'' - 2.5''$. Photometric flux calibration was done by observing a standard star in the AS 13 region (Hunt et al. 1998).

Data reduction was done using the Image Reduction and Analysis Facility (IRAF) software. The dark-subtracted and background-subtracted images were co-added to obtain the final image in each band. The photometric magnitudes of V1647 Ori were then found using the task APPHOT in IRAF. The magnitude of extended sources such as HH22 was also estimated using a larger sampling aperture (usually four times the FWHM of a star image). The integrated magnitude of the nebula surrounding V1647 Ori was estimated from the images after the star was subtracted using a $40''$ aperture. *K* band spectroscopic observations were made using the NICMOS array at a spectral resolution of ~ 1000 . The integration time for the spectra was 60 s per frame. Spectral reduction was done using standard spectroscopic tasks in IRAF. For sky background subtraction, a set of at least two spectra was taken with the object dithered to two different positions along the slit. The sky-subtracted spectra were then co-added resulting in a total exposure time of 480 s. The atmospheric OH vibration-rotation lines were used for wavelength calibration. The spectra of V1647 Ori were then ratioed with that of a spectroscopic standard star of AOV type, observed at a similar airmass, to remove the telluric absorption features. Prior to ratioing, the HI absorption lines from the standard star spectra were removed by interpolation. The ratioed spectra were then multiplied by a blackbody curve at the effective temperature of the standard star to yield the final spectra. The observed *K* band photometric flux of V1647 Ori was used for flux calibration of the spectra.

3 RESULTS AND DISCUSSION

3.1 Photometry

Table 1 gives the *JHK* magnitudes and colors for all the dates of our observations. The photometric errors are typically 0.02 to 0.05 magnitudes. For the ongoing 2008 outburst period (observations from Nov 2008 till Nov 2012), the average magnitude with standard deviation (σ) for 29 data sets are: 10.85 (0.17); 9.02 (0.18); 7.60 (0.24) for the *J*, *H* and *K* bands respectively. Occasional deviations of more than 3σ due to variability of the object were noticed in all the three bands. For the 2004 outburst period (observations from Mar 2004 till Dec 2004) the averages for seven data sets are 11.01 (0.16); 9.06 (0.17); 7.73 (0.15) for the *J*, *H* and *K* bands respectively; the deviations are within 2σ . For the quiescent phase during 2006–2007 (observations from Dec 2005 till Dec 2006), the averages for eight data sets are 14.2 (0.18); 11.61 (0.14); 9.89 (0.18) for the *J*, *H* and *K* bands respectively; occasional deviations seen are within 2σ . Thus the ongoing outburst shows higher amplitude fluctuations in brightness than the 2004–2005 outburst, especially in the *K* band (more than 0.5 mag). The light curves in the *J*, *H* and *K* bands are shown in Figure 1 covering the period between 2004–2012. For comparison, a few data points from other published work are also shown (from McGehee et al. 2004; Ojha et al. 2006; Acosta-Pulido et al. 2007 and Aspin 2011). It may be mentioned here that Acosta-Pulido et al. (2007) reported a 56 day periodic component in their optical light curves in the visible bands. Our *JHK* data do not clearly show this component.

Trend of decline of Outburst phase since early 2012: In comparison with its behavior till 2011 (e.g. Venkat & Anandarao 2011), the object seems to show a steady decline in the brightness beginning from Feb-Mar 2012 (cf. Semkov & Peneva 2012; Ninan et al. 2012) with an approximate rate of 0.16, 0.06 and 0.18 mag per year in the *JHK* bands respectively (see Fig. 1). It is necessary to confirm this declining trend by continued monitoring. The slow decline compared to the one noticed in the 2004 outburst is reminiscent of a typical FUor light curve, but it is premature to conclude that

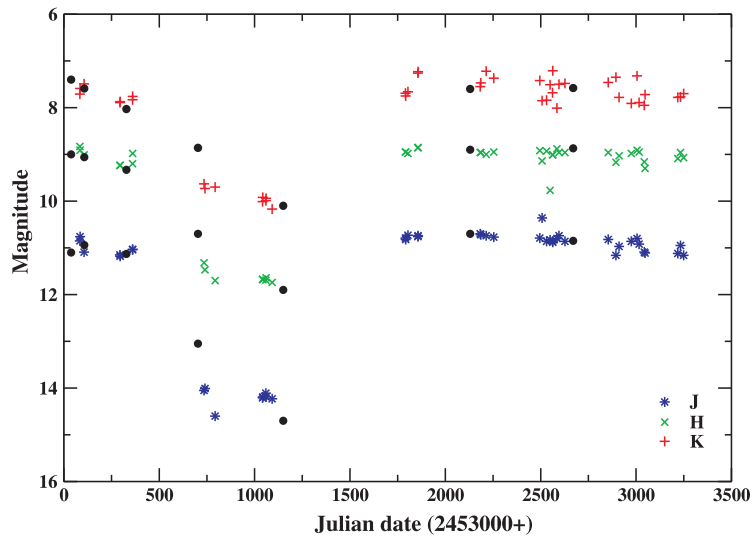


Fig. 1 V1647 Ori: Light Curves in the *J*, *H* and *K* bands from Mt Abu observations during 2004–2012 covering the two outbursts with the ~ 2 -yr quiescence in between. The asterisks represent the *J* band, crosses represent the *H* band and pluses represent the *K* band. Observations made elsewhere are shown in black filled circles (see text for references).

Table 1 V1647 Ori: *JHK* Photometric Magnitudes and Colors, and A_V (in mag) during 2004–2012

Date	JD	<i>J</i>	<i>H</i>	<i>K</i>	<i>J</i> – <i>H</i>	<i>H</i> – <i>K</i>	A_V
2004Mar20	2453084.5	10.85	8.83	7.71	2.02	1.12	11.76
2004Mar21	2453085.5	10.76	8.91	7.59	1.85	1.32	7.81
2004Apr11	2453106.5	11.09	9.01	7.49	2.08	1.52	9.38
2004Oct16	2453294.5	11.15	9.24	7.89	1.91	1.35	8.40
2004Oct17	2453295.5	11.18	9.23	7.87	1.95	1.36	8.87
2004Dec21	2453360.5	11.04	9.20	7.83	1.84	1.37	7.27
2004Dec22	2453361.5	11.03	8.98	7.76	2.05	1.22	11.37
2005Dec31	2453735.5	14.05	11.32	9.63	2.73	1.69	17.01
2006Jan05	2453740.5	14.01	11.47	9.73	2.54	1.74	13.98
2006Feb27	2453793.5	14.60	11.70	9.70	2.90	2.00	16.87
2006Nov03	2454042.5	14.21	11.67	10.01	2.54	1.66	14.62
2006Nov04	2454043.5	14.19	11.68	9.92	2.51	1.76	13.41
2006Nov20	2454059.5	14.11	11.69	9.99	2.42	1.70	12.64
2006Nov21	2454060.5	14.19	11.64	9.94	2.55	1.70	14.44
2006Dec23	2454092.5	14.23	11.74	10.17	2.49	1.57	14.65
2008Nov21	2454791.5	10.79	8.95	7.69	1.84	1.26	8.15
2008Nov22	2454792.5	10.82	8.95	7.75	1.87	1.20	9.05
2008Dec04	2454804.5	10.73	8.98	7.66	1.75	1.32	6.42
2009Jan25	2454856.5	10.76	8.86	7.26	1.90	1.60	6.25
2009Jan26	2454857.5	10.74	8.85	7.23	1.89	1.62	5.95
2009Dec18	2455183.5	10.70	8.96	7.55	1.74	1.41	5.56
2009Dec21	2455186.5	10.72	8.96	7.47	1.76	1.49	5.20
2010Jan18	2455214.5	10.74	9.00	7.22	1.74	1.78	—
2010Feb27	2455254.5	10.77	8.95	7.37	1.82	1.58	5.31
2010Oct26	2455495.5	10.79	8.92	7.42	1.87	1.50	6.64
2010Nov07	2455507.5	10.36	9.14	7.85	1.22	1.29	—
2010Dec01	2455531.5	10.86	8.93	7.84	1.93	1.09	10.76
2010Dec19	2455549.5	10.83	9.77	7.51	1.06	2.26	—
2011Jan01	2455562.5	10.86	9.01	7.68	1.85	1.33	7.73
2011Jan02	2455563.5	10.88	9.01	7.21	1.87	1.80	—
2011Jan24	2455585.5	10.80	8.88	8.01	1.92	0.87	—
2011Feb04	2455596.5	10.74	8.96	7.50	1.78	1.46	5.72
2011Mar07	2455627.5	10.86	8.96	7.48	1.90	1.48	7.21
2011Oct20	2455854.5	10.82	8.96	7.46	1.86	1.50	6.50
2011Nov29	2455894.5	11.16	9.17	7.35	1.99	1.82	—
2011Dec16	2455911.5	10.97	9.03	7.78	1.94	1.25	9.61
2012Feb18	2455975.5	10.86	8.98	7.91	1.88	1.07	10.23
2012Mar19	2456005.5	10.80	8.91	7.32	1.89	1.59	6.19
2012Mar30	2456016.5	10.92	8.95	7.89	1.97	1.06	11.55
2012Apr26	2456043.5	11.09	9.16	7.95	1.93	1.21	9.80
2012Apr30	2456047.5	11.11	9.30	7.72	1.81	1.58	5.17
2012Oct19	2456219.5	11.12	9.09	7.78	2.03	1.31	10.38
2012Nov02	2456233.5	10.95	8.96	7.77	1.99	1.19	10.79
2012Nov18	2456249.5	11.16	9.07	7.70	2.09	1.37	10.72

it is an FUor; as there have been spectroscopic indications to the contrary. In fact it could be a class in itself which shows characteristic features of both FUors and EXors (see Kun 2008).

We have computed the visual extinction A_V from the colors [*J*–*H*] and [*H*–*K*] for both epochs, using the formula for T Tauri stars derived from Meyer et al. (1997) and the extinction model of Bessell & Brett (1988),

$$A_V = 13.83 \times [J - H] - 8.02 \times [H - K] - 7.19. \quad (1)$$

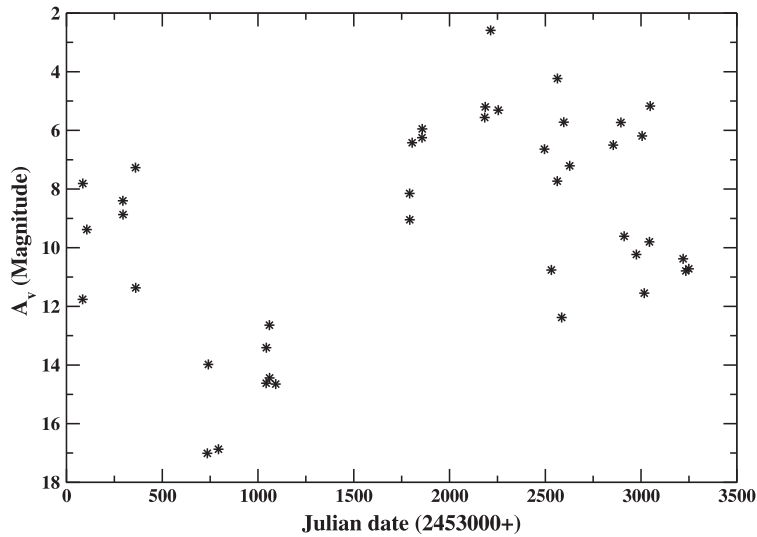


Fig. 2 V1647 Ori: Time variation of A_V from Mt Abu observations during 2004–2012 comprising two outbursts flanking the quiescent epoch (with larger extinction).

The computed A_V values are listed in Table 1. For comparison, the A_V corresponding to the 2MASS epoch (quiescent on 1998 October 7) is 13.3. The time evolution of A_V is shown in Figure 2. We find that there is ~ 6 mag difference in A_V between the two phases, with the outburst phase having a lower extinction. This can be attributed to the excess mass accreted by the envelope (from the environment) during the quiescent phase in comparison with the outburst phase during which the disk accretion (from the envelope) is expected to dominate (e.g. Aspin et al. 2008 and Aspin 2011).

A JHK color-color diagram constructed from Mt Abu data during 2004–2012 is shown in Figure 3. The A_V values computed using Equation (1) are in reasonable agreement (within 1 – 2 mag) with those obtained by de-reddening the JHK colors to the T Tauri locus in the color-color diagram. The color-color diagram demonstrates the variable nature of the source in the ongoing 2008 outburst phase in comparison with the 2004 outburst. The region occupied by the latest outburst (asterisks in Fig. 3) extends horizontally (i.e. with $[J-H] \sim 1.7-2.0$) beyond the T Tauri region; quite in contrast with the 2004 outburst phase (open circles). This tendency during the ongoing outburst indicates the presence of cold dust in the envelope/disk of the star compared to the 2004 outburst. Also, we found at least two occasions (in 2010 November 7 & 2010 December 19) in which the colors showed extreme values, as indicated by the magenta asterisks in Figure 3 around $[J-H] \sim 1.0-1.2$, with $[H-K]$ at 1.3 and 2.3. On another occasion (2011 January 24) the colors indicate a position to the left of the T Tauri region. The A_V could not be calculated for these cases falling well beyond the T Tauri regime (shown as dashes in Table 1). We suspect that such extreme fluctuations may have short duration (a few days) and be attributable to variation in circumstellar dust temperature.

3.2 Spectroscopic Variations

As may be seen in Figure 4, K band spectra taken at different times during the outburst phase show variability in hydrogen $\text{Br}\gamma$, indicating variable disk accretion rates. The $\text{Br}\gamma$ line shows a fluctuating trend that does not seem to be associated with photometric fluctuations (cf. $\text{H}\alpha$ line reported by Walter et al. 2004 and Aspin & Reipurth 2009). Quanz et al. (2007) reported molecular line

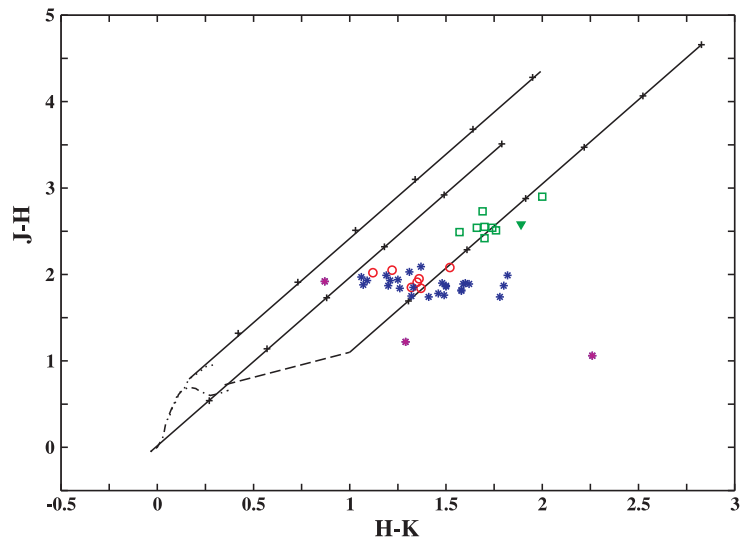


Fig. 3 V1647 Ori: Color-color diagram from Mt Abu observations. The 2MASS value is marked as an inverted *triangle* (corresponding to 1998 October 7). The *asterisks* correspond to the ongoing outburst period 2008–2012; while the *circles* correspond to the outburst period of 2004–2005. The *squares* are for the quiescent epoch of 2006–2007. The three “stray” magenta asterisks, with two appearing around $J - H \sim 1.0$ and the one appearing around $H - K \sim 0.8$, correspond to extremities in photometric magnitudes observed in our monitoring. See text for discussion. The *dot-dashed* curve represents the unreddened main-sequence stars; the *dotted* curve shows the unreddened giant stars. The black slanting parallel lines indicate the extinction vectors for $A_V = 30$ mag (the extinction law from Bessell & Brett 1988 was adopted). The pluses along the extinction vector correspond to an extinction interval of $A_V = 5$ mag. The T Tauri stars fall on the black dashed straight line, adopted from Meyer et al. (1997).

variability in the mid-IR region during the 2004 outburst. It may be noted that the width at zero-intensity and the ratio of peak to continuum intensity in Mt. Abu profiles are in reasonable agreement with those of Brittain et al. (2010) for the year 2009, in spite of the large differences in the resolving power employed and signal-to-noise values between the two observations. The accretion luminosities and disk accretion rates derived from the dereddened $\text{Br}\gamma$ line fluxes from our spectra (following the procedure described by Muzerolle et al. 1998) range from 20–60 L_\odot and 1.0×10^{-6} to $3.0 \times 10^{-6} M_\odot \text{ yr}^{-1}$ respectively, which are comparable with those reported by Brittain et al. (2010).

3.3 Variations in HH22 and the Nebula around V1647 Ori

Figure 5 shows a JHK color composite image of V1647 Ori and its associated nebula taken from Mt Abu on 2011 February 04 using NICS. Superposed on the image are the contours of isomagnitudes in the H band. The curved tail at the top left part of the nebular object is usually attributed to the ongoing accretion (cf. Reipurth & Aspin 2004). HH22 (knot A in Eisloffel & Mundt 1997), seen nearly to the north of V1647 Ori (see Fig. 5), is a Herbig-Haro type object (for the mid-IR counterpart, see Muzerolle et al. 2005). It happens to be located very close to V1647 Ori ($30''$ of separation at an assumed distance of 0.40 kpc) and its originating source has not yet been identified. It could possibly be a reflection nebula powered by V1647 Ori (see Briceño et al. 2004 and Aspin et al. 2008).

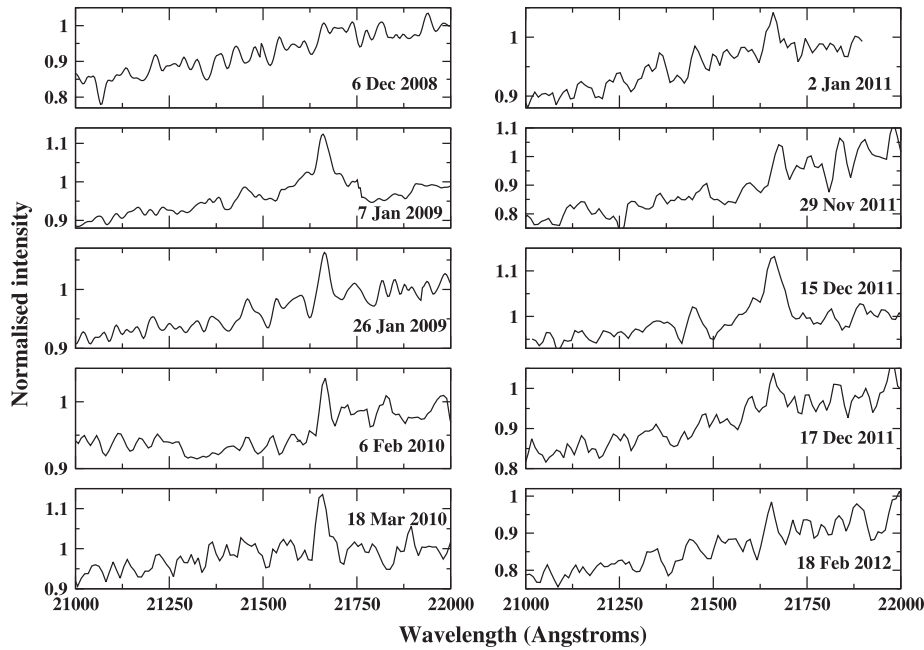


Fig. 4 V1647 Ori: Br γ line (at 2.16 μm) in the K band observed on a few occasions at Mt Abu. Variability is evident.

It may be expected therefore that the outburst from V1647 Ori could cause the nebulosity to show a corresponding brightening. The light travel time from the young stellar object (YSO) to HH22 is ~ 70 d. We analyzed images in the JHK bands obtained from Mt Abu to see if HH22 shows any variability in its brightness.

Figure 6 shows the integrated K magnitude of HH22 with time along with magnitudes of V1647 Ori. The plot indicates a possible correspondence between HH22 (knot A) and the outburst activity, as well as indication of a trigger from even short term fluctuations in V1647 Ori. We also noticed fluctuations in the brightness of the nebula around V1647 Ori, which typically follow those of V1647 Ori itself. Similar fluctuations were also noticed in the J and H bands.

3.4 Modeling of the Spectral Energy Distribution

Modeling the SED of V1647 Ori was done for three sets of data taken during: (i) the outburst phase 2004–2005; (ii) the quiescent phase 2006–2007 and (iii) the second (ongoing) outburst phase 2008–2012. For each of these three phases, the mean values of Mt Abu JHK magnitudes were considered. To the JHK data we added the visible, mid-infrared, far infrared and mm-wave data during quiescent and outburst epochs taken from Andrews et al. (2004) and Aspin et al. (2008). The SEDs given in Aspin et al. (2008) for the outburst and quiescent phases show that the fluxes of the PMS star in sub-mm and mm regions did not change more than 10% between the two phases. It is in the visible and infrared that a substantial change had taken place. The near-infrared region occurs right at the position of turn-over in the SED and hence is quite important. It was assumed that the small photometric variations, if present in the mid-infrared and far-infrared, are not significant in each phase. We used an online tool developed by Robitaille et al. (2007) for SED modeling. Using this tool, several authors have successfully modeled T Tauri stars and massive protostars with masses up

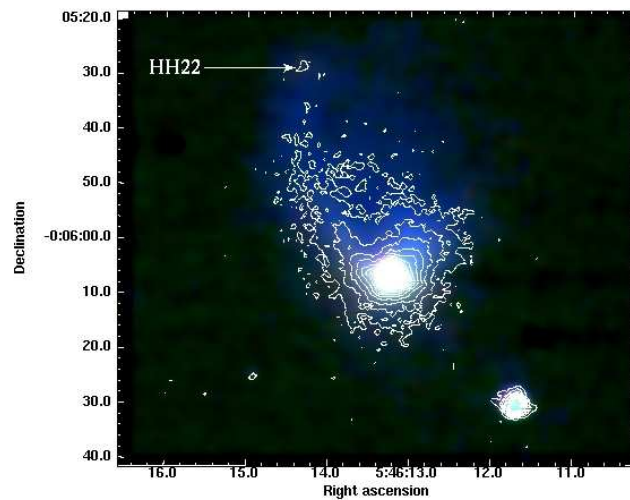


Fig. 5 Color composite image of V1647 Ori and the surrounding McNeil's nebula in the J (blue), H (green) and K (red) bands taken at Mt Abu using NICS on 2011 February 4; HH22 is seen nearly north of V1647 Ori. The H band contours (in white) are shown superposed on the image: the outermost contour is $20 \text{ mag arcsec}^{-2}$ with each contour brightening by $2 \text{ mag arcsec}^{-2}$ inwards.

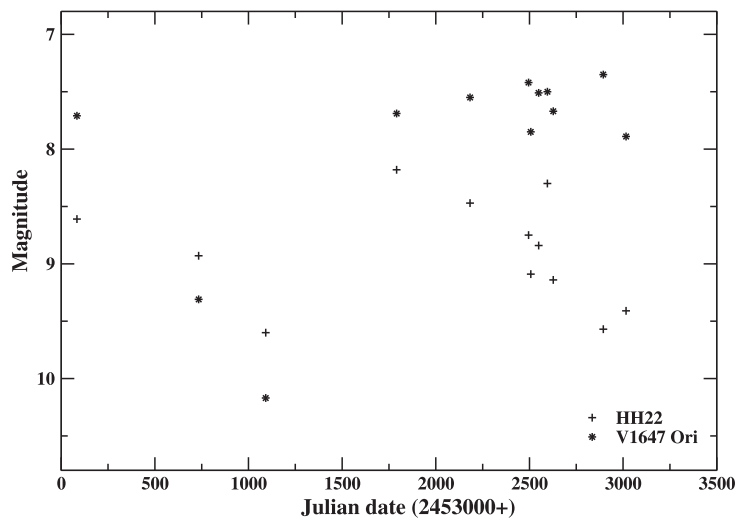


Fig. 6 Time variations of V1647 Ori in the K band seen against those in HH22. The asterisks correspond to V1647 Ori and pluses represent HH22. For HH22 the magnitudes are made brighter by subtracting five to facilitate a closer comparison.

to $25 M_{\odot}$ (e.g. Kumar Dewangan & Anandarao 2010). The online tool selects the best-fit solutions from 20 000 models (each with 10 different angles of inclination for the accretion disk, making a total of 200 000 models). The input parameters include, apart from a minimum of three data points in SED and their corresponding errors, a range of distances to the object and the visual extinction. The output parameters include stellar mass, temperature, radius, age and total luminosity; as well as

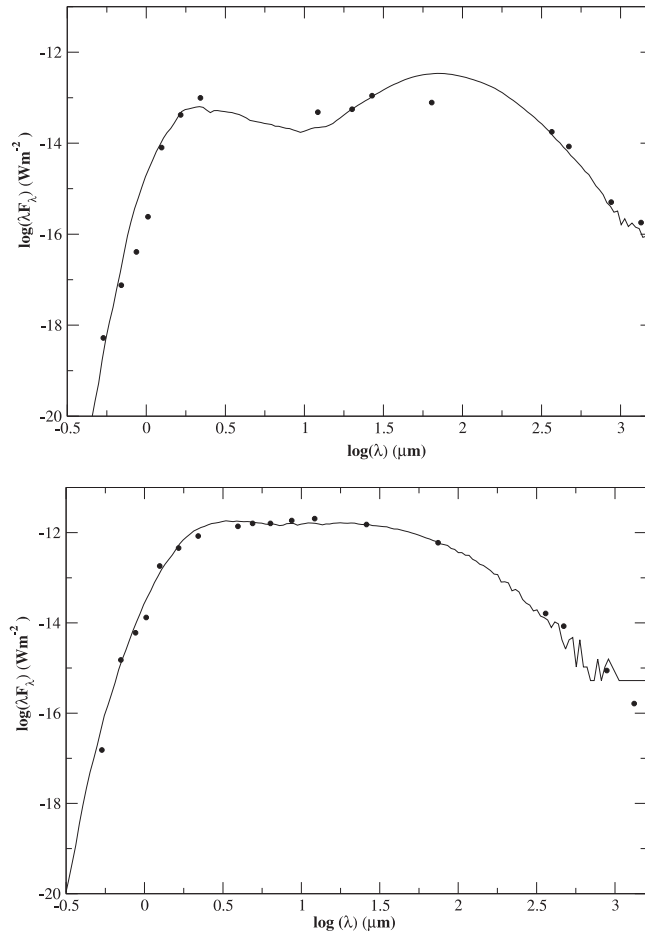


Fig. 7 SED models for V1647 Ori during (a) its quiescent phase (2006–2007) and (b) its outburst phase (2008–2012). The filled circles represent data points. The full dark curves show the best fits (see text for details).

disk inclination angle, masses of the disk and envelope and rates of accretion. In order to minimize the degeneracy of solutions, only those solutions that satisfy the criterion

$$(\chi^2 - \chi_{\text{best}}^2) \leq 3 \quad (2)$$

are chosen with χ^2 considered per data point (see Robitaille et al. 2006). Furthermore, in order to avoid ‘over-interpretation’ of SEDs, we provided a small range of visual extinction values (from the *JHK* photometry) for each phase, to account for the inherent uncertainties in their determination. In the present case, a distance of 0.40 kpc is adopted (from Anthony-Twarog 1982). The best fit models are displayed in Figure 7 along with the observed data (shown in filled circles) for the quiescent phase of 2006–2007 and the ongoing outburst phase of 2008–2012.

Table 2 lists the mean values and standard deviations of physical parameters derived from the models for the two epochs. The model parameters for the outburst phase 2004–2005 match quite well with those of the ongoing outburst phase of 2008–2012. In the quiescent phase one can notice the stellar parameters similar to those of a T Tauri star. But the outburst parameters mimic more

Table 2 Model Parameters for V1647 Ori in its Quiescent (2006–2007) and Outburst (2008–2012) Phases

Physical Parameter	Quiescent Phase	Outburst Phase
Stellar Age (yr)	$4.8 \pm 2.5 (\times 10^4)$	$6.3 \pm 3.1 (\times 10^5)$
Star Mass (M_{\odot})	0.34 ± 0.15	4.44 ± 0.34
Star Temperature (K)	3360 ± 170	7560 ± 1590
Star Radius (R_{\odot})	4.01 ± 0.12	7.08 ± 2.28
Total Luminosity (L_{\odot})	1.85 ± 0.24	156.5 ± 28.0
Envelope Mass (M_{\odot})	1.51 ± 0.02	$1.40 \pm 3.79 (\times 10^{-4})$
Envelope Accretion Rate ($M_{\odot} \text{ yr}^{-1}$)	$5.3 \pm 0.1 (\times 10^{-5})$	$3.7 \pm 0.0 (\times 10^{-6})$
Disk Mass (M_{\odot})	$6.8 \pm 8.00 (\times 10^{-5})$	$6.9 \pm 1.8 (\times 10^{-2})$
Disk Accretion Rate ($M_{\odot} \text{ yr}^{-1}$)	$5.5 \pm 3.3 (\times 10^{-9})$	$2.2 \pm 1.6 (\times 10^{-7})$

of an intermediate mass star rather than a low mass PMS star. In the outburst phase the disk mass and accretion rate are substantially enhanced when compared to the quiescent phase. The envelope accretion rate decreases by more than an order of magnitude in the outburst phase compared to the quiescence, but envelope mass decreases by several orders of magnitude. This may be due to the enhanced luminosity in the outburst phase which could prevent mass accretion from the envelope. In the quiescent phase, the envelope emission dominates in the mid-infrared and longer wavelength region, while in the outburst phase the disk emission contributes substantially in the region beyond $1 \mu\text{m}$.

It may be noted that the disk accretion rate for the outburst phase given in Table 2 matches well with those reported by Briceño et al. (2004), Aspin et al. (2008), Brittain et al. (2010) and Aspin (2011). However, the disk accretion rates in the quiescent phase derived from $\text{Br}\gamma/\text{Pa}\beta$ emission lines by Aspin et al. (2008) are much higher than the value derived from the model reported here. While this could be due to uncertainties in the SED model or emission line method, the important point to be noted is that the disk accretion rate during the outburst phase is much larger than that in the quiescent period. The total luminosity obtained here (which includes contributions from the star and its disk and envelope) matches well with those derived by Ábrahám et al. (2004) and Aspin et al. (2008) from the SEDs of the pre-outburst phase. The total outburst luminosity during the 2003 outburst as derived by Briceño et al. (2004) from the SED is $219 L_{\odot}$ which agrees well with that obtained from our model for the current ongoing outburst. Earlier, using a simpler model, Muzerolle et al. (2005) interpreted the *Spitzer* IRAC/MIPS (photometric bands between $3.5\text{--}70 \mu\text{m}$) data for the pre- and post-outburst phases. Their results are qualitatively similar to ours.

4 CONCLUSIONS

The important conclusions of this work are:

- (1) Monitoring of V1647 Ori in the *JHK* bands has shown that the object has been undergoing episodes of variation in mass accretion as indicated by small but significant variations in its *JHK* fluxes. This conclusion is also supported by its spectral variations in near-infrared;
- (2) Starting from early 2012, the object has seemed to show a slow fading out with a rate of $\sim 0.06\text{--}0.18$ mag per year. This may indicate that V1647 Ori is an intermediate type object falling between FUors and EXors, having characteristic features of both the prototypes;
- (3) The *JHK* color-color diagram indicates several occasions in the current, ongoing outburst in which the star displays positions beyond the T Tauri region, indicating the presence of colder dust compared to its 2004 outburst phase;
- (4) The Herbig-Haro object HH22, whose as yet unidentified energizing YSO is situated at about $30''$ from V1647 Ori, seems to show light fluctuations corresponding to those of the latter, thereby confirming that it is a reflection nebulosity triggered by the YSO;

- (5) The spectral energy distributions of V1647 Ori modeled for the epochs of quiescence and outburst, show that the disk mass and accretion rate in the outburst phase are significantly greater than those in the quiescent stage, but the envelope mass and accretion rates are much lower.

Acknowledgements The research work at PRL is supported by the Department of Space, Government of India. It is a pleasure to thank the Mt Abu Observatory staff for their cooperation in making observations. We gratefully acknowledge using the SEDFIT online software developed by Robitaille et al (2007). We thank the anonymous reviewer for useful comments.

References

- Ábrahám, P., Kóspál, Á., Csizmadia, S., et al. 2004, *A&A*, 419, L39
Acosta-Pulido, J. A., Kun, M., Ábrahám, P., et al. 2007, *AJ*, 133, 2020
Andrews, S. M., Rothberg, B., & Simon, T. 2004, *ApJ*, 610, L45
Anthony-Twarog, B. J. 1982, *AJ*, 87, 1213
Aspin, C. 2011, *AJ*, 142, 135
Aspin, C., Beck, T. L., & Reipurth, B. 2008, *AJ*, 135, 423
Aspin, C., & Reipurth, B. 2009, *AJ*, 138, 1137
Bell, K. R., Lin, D. N. C., Hartmann, L. W., & Kenyon, S. J. 1995, *ApJ*, 444, 376
Bessell, M. S., & Brett, J. M. 1988, *PASP*, 100, 1134
Bonnell, I., & Bastien, P. 1992, *ApJ*, 401, L31
Briceño, C., Vivas, A. K., Hernández, J., et al. 2004, *ApJ*, 606, L123
Brittain, S. D., Rettig, T. W., Simon, T., Gibb, E. L., & Liskowsky, J. 2010, *ApJ*, 708, 109
Eisloffel, J., & Mundt, R. 1997, *AJ*, 114, 280
Hartmann, L., & Kenyon, S. J. 1985, *ApJ*, 299, 462
Hartmann, L., & Kenyon, S. J. 1996, *ARA&A*, 34, 207
Herbig, G. H. 1977, *ApJ*, 217, 693
Hunt, L. K., Mannucci, F., Testi, L., et al. 1998, *AJ*, 115, 2594
Kumar Dewangan, L., & Anandarao, B. G. 2010, *MNRAS*, 402, 2583
Kun, M. 2008, *Information Bulletin on Variable Stars*, 5850, 1
McGehee, P. M., Smith, J. A., Henden, A. A., et al. 2004, *ApJ*, 616, 1058
McNeil, J. W., Reipurth, B., & Meech, K. 2004, *IAU Circ.*, 8284, 1
Meyer, M. R., Calvet, N., & Hillenbrand, L. A. 1997, *AJ*, 114, 288
Muzerolle, J., Hartmann, L., & Calvet, N. 1998, *AJ*, 116, 2965
Muzerolle, J., Megeath, S. T., Flaherty, K. M., et al. 2005, *ApJ*, 620, L107
Ninan, J. P., Ojha, D. K., Mallick, K. K., et al. 2012, *Central Bureau Electronic Telegrams*, 3164, 1
Ojha, D. K., Ghosh, S. K., Tej, A., et al. 2006, *MNRAS*, 368, 825
Quanz, S. P., Henning, T., Bouwman, J., et al. 2007, *ApJ*, 668, 359
Reipurth, B., & Aspin, C. 2004, *ApJ*, 606, L119
Robitaille, T. P., Whitney, B. A., Indebetouw, R., Wood, K., & Denzmore, P. 2006, *ApJS*, 167, 256
Robitaille, T. P., Whitney, B. A., Indebetouw, R., & Wood, K. 2007, *ApJS*, 169, 328
Semkov, E. H., & Peneva, S. P. 2012, *Information Bulletin on Variable Stars*, 6025, 1
Stahler, S. W., & Palla, F. 2004, *The Formation of Stars* (1st ed.; Weinheim: Wiley-VCH Verlag)
Venkat, V., & Anandarao, B. G. 2011, *Central Bureau Electronic Telegrams*, 2647, 1
Walter, F. M., Stringfellow, G. S., Sherry, W. H., & Field-Pollatou, A. 2004, *AJ*, 128, 1872

Infrared spectroscopic study of a selection of AGB and post-AGB stars

V. Venkata Raman[★] and B. G. Anandarao[★]

Physical Research Laboratory (PRL), Navrangpura, Ahmedabad 380009, India

Accepted 2008 January 3. Received 2007 December 3; in original form 2007 June 27

ABSTRACT

We present here near-infrared spectroscopy in the *H* and *K* bands of a selection of nearly 80 stars that belong to various asymptotic giant branch (AGB) types, namely S type, M type and SR type. This sample also includes 16 post-AGB (PAGB) stars. From these spectra, we seek correlations between the equivalent widths of some important spectral signatures and the infrared colours that are indicative of mass-loss. Repeated spectroscopic observations were made on some PAGB stars to look for spectral variations. We also analyse archival *Spitzer* mid-infrared spectra on a few PAGB stars to identify spectral features due to polycyclic aromatic hydrocarbon (PAH) molecules providing confirmation of the advanced stage of their evolution. Further, we model the spectral energy distributions (SEDs) of the stars (compiled from archival data) and compare circumstellar dust parameters and mass-loss rates in different types.

Our near-infrared spectra show that in the case of M- and S type stars, the equivalent widths of the CO(3–0) band are moderately correlated with infrared colours, suggesting a possible relationship with mass-loss processes. A few PAGB stars revealed short-term variability in their spectra, indicating episodic mass-loss: the cooler stars showed in CO first overtone bands and the hotter ones showed in H I Brackett lines. Our spectra on IRAS 19399+2312 suggest that it is a transition object. From the *Spitzer* spectra, there seems to be a dependence between the spectral type of the PAGB stars and the strength of the PAH features. Modelling of SEDs showed among the M and PAGB stars that the higher the mass-loss rates, the higher the [*K* – 12] colour in our sample.

Key words: techniques: spectroscopic – stars: AGB and post-AGB – circumstellar matter – stars: evolution – stars: mass-loss – dust, extinction.

1 INTRODUCTION

During their asymptotic giant branch (AGB) stage, intermediate-mass stars undergo substantial mass-loss triggered by pulsation shocks and radiation pressure (e.g. Willson 2000; van Winckel 2003). Near-infrared (near-IR) spectroscopy is one of the recognized tools to study the mass-loss process (e.g. Kleinmann & Hall 1986; Volk, Kwok & Hrivnak 1999; Lancon & Wood 2000; Bieging, Rieke & Rieke 2002; Winters et al. 2003). The near-IR *JHK* bands, contain several important diagnostic lines that can be used as signatures to probe the atmospheres of these stars (Hinkle, Hall & Ridgway 1982).

One of the most dramatic manifestations of the AGB stage is the high rate of mass-loss that is mainly attributed to pulsational levitation of atmosphere followed by expulsion of matter by the radiation pressure (Wood 1979; Bowen 1988; Gail & Sedlmayr 1988; Vassiliadis & Wood 1993; Habing 1996; Feast 2000; Willson 2000; Winters et al. 2000; Woitke 2003; Garcia-Lario 2006). One of the

issues that we would address is the possible signatures of pulsational mass-loss in the spectra of AGB stars. We would also like to study the IR spectral signatures that the intermediate-mass stars leave while evolving beyond AGB stage to become planetary nebulae (PNe) (e.g. Kwok 2000).

In this work we report near-IR (*H* and *K* bands) spectroscopy on a selection of about 80 AGB stars of different types, namely M type, S type, semiregular variables (SR) and post-AGB (PAGB) candidates (Section 2). In Section 3.1, we try to seek significant differences among these types and correlate spectral signature strengths with pulsation parameters or mass-loss indicators (such as the IR colour indices) in case of M, S and SR types.

Further, we present the *Spitzer* archival spectra in the mid-IR region on a few PAGB stars in order to find out the evolutionary stage of these stars in terms of the spectral features seen in the spectra (Section 3.2). Following this, using the DUSTY code, we model the IR spectral energy distributions (SEDs) of these sample stars, constructed from archival data in the visible, near- and far-IR regions to investigate basic differences in the photospheric and circumstellar parameters among the various types of AGB stars (Section 3.3). Some interesting aspects on variation of spectral lines in a few PAGB

[★]E-mail: vvenkat@prl.res.in (VVR); anand@prl.res.in (BGA)

stars are discussed in Section 4. Section 5 lists important conclusions of the present work.

2 NEAR-INFRARED SPECTROSCOPIC OBSERVATIONS

Near-IR spectroscopic observations were made in the J (only for some of the sample PAGB stars), H and K bands on the selection of stars, using the NICMOS-3 near-IR camera/spectrograph at the Cassegrain focus of the 1.2-m telescope at Mt Abu, Western India, during the period 2003–07. The observations were made at a spectral resolution of ~ 1000 . Spectrophotometric standard stars of A0V type were used for each programme star at similar air mass to remove the telluric absorptions and for relative flux calibration (cf. Lancon & Rocca-Volmerange 1992). For sky background subtraction, two traces were taken for each star for each cycle of integration at two spatially separated positions along the slit within 30 arcsec. Typical overall integration times varied between 0.6 and 160 s for the brightest and faintest stars in our sample (in each of the three bands). The atmospheric OH vibration–rotation lines were used to calibrate wavelength. The H I absorption lines from the standard star spectra are removed by interpolation. The resulting spectra of the standard star were used for the removal of telluric lines from the programme star by ratioing. The ratioed spectra were then multiplied by a blackbody spectrum at the effective temperature corresponding to the standard star to obtain the final spectra. Typically the signal-to-noise ratios (S/N values) at the strongest and the weakest spectral features varied between 100 and 3, respectively. Data processing

was done using standard spectroscopic tasks (e.g. APALL) inside IRAF.

2.1 The sample stars

The programme stars were selected from published literature/catalogues (Fouquet et al. 1992; Kerschbaum & Hron 1994; Chen, Gao & Jorissen 1995; Wang & Chen 2002; Stasinska et al. 2006). Our sample contains about 80 stars with the selection based on the observability at Mt Abu during the period November–May and JHK -band magnitudes brighter than 8–9. Among these stars, 30 are M type; 17 S type; 15 SR type and 16 are PAGB stars [some of which are known to be transition/proto-PNe (PPNe), see Ueta et al. 2003 and Kelly & Hrivnak 2005]. The greater bias towards M types in the sample is due to the fact that they are brighter in K band than the others. Tables 1–4 list all the stars in the four categories along with the $[H - K]$ and $[K - 12]$ colours computed from Two Micron All Sky Survey (2MASS) and IRAS photometric archival data. The phases (ϕ) of the variable stars of M and SR types, corresponding to the dates of our observations, are also listed in the tables (epochs taken from Kholopov et al. 1988). The spectral types are taken from SIMBAD data base.

3 RESULTS AND DISCUSSION

Fig. 1 shows some typical spectra for different types considered here. In general, we find in the AGB stars, the photospheric absorption lines of Na I doublet at $2.21 \mu\text{m}$, Ca I triplet at $\sim 2.26 \mu\text{m}$, as well as Mg I at $1.708 \mu\text{m}$ in all the sample stars. Brackett

Table 1. 2MASS and IRAS colours and Mt Abu EWs (in \AA) of the spectral features of the sample M stars.

Star	Spectral type	ϕ	$H - K$	$K - 12$	CO(3–0)	CO(4–1)	CO(H)	CO(2–0)	CO(3–1)	CO(K)	\bar{M}
02234–0024	M4e	0.34	0.44	2.31	16.1	7.8	51.5	21.1	6.9	61.9	2.6(–6) [†]
03082+1436	M5.5e	0.33	0.45	1.99	11.3	9.2	64.2	25.1	13.3	62.3	9.8(–7) [†]
03489–0131	M4III	–	0.31	1.86	4.8	5.3	61.9	18.4	20.2	45.9	1.3(–6)
04352+6602	Sev	0.44	0.50	1.22	–	–	–	31.8	29.8	101.2	1.4(–7) [†]
05265–0443	M7e	0.57	0.49	1.32	13.6	10.1	53.1	15.1	7.8	22.9	4.6(–7) [†]
05495+1547	S7.5	0.49	0.59	2.79	11.6	8.4	47.4	11.9	16.0	47.6	3.5(–6)
06468–1342	S	–	0.52	1.03	14.5	16.6	85.0	32.9	31.2	110.6	–
06571+5524	Se	0.59	0.64	1.67	20.0	22.1	105.6	18.3	25.6	52.8	1.7(–6) [†]
07043+2246	S6.9e	0.36	0.18	1.17	11.6	13.9	77.0	34.3	28.8	98.8	3.1(–7) [†]
07092+0735	Se	0.30	0.71	3.02	16.4	15.4	72.1	20.5	25.8	81.0	2.9(–6)
07197–1451	S	0.26	0.55	2.32	11.8	8.0	65.0	22.3	9.7	43.5	4.6(–6)
07299+0825	M7e	0.57	0.36	1.90	16.2	10.5	64.1	26.8	14.1	65.3	8.5(–7) [†]
07462+2351	SeV	0.96	0.52	–0.90	12.3	13.8	68.8	28.1	33.9	108.0	–
07537+3118		0.09	0.53	1.40	13.7	9.9	76.5	22.8	25.0	77.5	–
07584–2051	S2.4e	0.19	0.44	1.00	12.6	11.0	78.4	21.2	17.9	39.1	–
08188+1726	SeV	–	0.41	2.28	14.3	13.6	66.1	22.2	24.8	71.3	–
08308–1748	S	–	0.43	0.72	10.1	15.9	72.6	25.7	19.1	92.9	1.7(–7)
08416–3220		–	0.41	0.97	12.2	14.2	75.8	33.0	35.0	105.3	–
08430–2548		–	0.46	1.51	12.2	13.0	68.3	19.6	16.6	80.2	–
09411–1820	Me	0.31	0.49	1.63	5.1	7.3	33.2	8.5	5.7	22.1	7.9(–7) [†]
12372–2623	M4	0.92	0.40	1.39	9.9	14.8	64.2	20.2	23.8	50.8	–
17001–3651	M	0.70	0.58	2.17	9.6	8.9	57.0	11.3	8.9	35.8	1.9(–6) [†]
17186–2914	S	–	0.70	1.76	14.5	13.2	80.7	23.9	26.1	89.2	2.9(–6)
17490–3502	M	0.60	0.54	2.26	16.4	16.1	78.1	24.6	17.6	95.8	–
17521–2907	Se	0.11	0.56	1.64	18.9	19.5	88.4	20.1	21.9	71.8	4.6(–6)
18508–1415	SeV	0.44	0.38	1.00	3.4	5.1	64.3	8.8	5.5	31.1	–
19111+2555	S	0.57	0.80	4.36	19.1	17.6	66.8	13.3	11.2	24.5	4.6(–6) [†]
19126–0708	S...	0.90	0.79	3.81	21.6	19.1	102.0	21.5	23.5	59.4	2.9(–6) [†]
19354+5005	S...	0.24	0.52	2.28	26.6	22.8	108.0	30.2	33.8	98.2	1.5(–6) [†]
23041+1016	M7e	0.87	0.52	2.40	7.3	9.0	50.7	12.4	6.3	18.7	1.5(–6) [†]

Table 2. 2MASS and IRAS colours and Mt Abu EWs (in Å) of spectral features of the sample S stars.

Star	Spectral type	$H - K$	$K - 12$	CO(3-0)	CO(4-1)	CO(H)	CO(2-0)	CO(3-1)	CO(K)	\dot{M}
04599+1514	M0	0.49	0.96	12.8	17.3	80.8	24.2	28.6	99.4	1.4(-7) [†]
05036+1222		0.60	1.09	12.7	15.1	80.9	26.2	28.1	54.3	–
05374+3153	M2Iab	0.16	1.44	13.7	12.2	77.5	21.6	26.6	88.3	7.3(-7) [†]
07247-1137	Sv...	0.34	0.85	8.6	10.7	57.8	25.8	19.1	74.5	–
07392+1419	M3II-III	0.09	-1.44	5.3	8.4	38.9	16.7	14.7	55.3	7.3(-7)
09070-2847	S	0.25	0.91	10.7	12.8	74.1	22.1	37.1	59.2	–
09152-3023		0.47	1.21	4.0	9.4	44.2	18.1	14.4	39.1	–
10538-1033	M...	0.29	0.74	8.1	4.5	44.6	22.9	9.6	64.9	–
11046+6838	M...	0.40	0.39	3.7	9.5	41.1	15.0	10.4	54.7	–
12219-2802	S	0.30	0.72	9.2	9.4	57.0	22.1	17.8	69.8	–
12417+6121	SeV	0.41	0.95	16.7	18.0	82.4	28.2	29.5	92.2	1.0(-7) [†]
13421-0316	K5	0.22	0.57	–	8.3	40.9	20.0	14.9	59.8	–
13494-0313	M...	0.42	0.56	3.0	9.2	55.5	17.4	20.0	47.4	–
14251-0251	S...	0.34	0.71	3.7	9.1	45.8	20.2	16.7	60.0	–
15494-2312	S	0.38	0.62	5.1	8.1	46.1	19.8	17.2	59.3	–
16205+5659	M...	0.18	0.78	5.4	7.1	45.3	13.0	19.1	61.6	–
16209-2808	S	0.54	0.92	10.7	13.6	73.9	21.9	27.2	79.5	1.0(-7)

Table 3. 2MASS and IRAS colours and Mt Abu EWs (in Å) of spectral features of the sample SR stars.

Star	Spectral type	ϕ	$H - K$	$K - 12$	CO(3-0)	CO(4-1)	CO(H)	CO(2-0)	CO(3-1)	CO(K)	\dot{M}
04030+2435	S4.2V	–	0.40	0.63	4.1	8.3	45.0	16.2	17.9	34.1	–
04483+2826	CII	–	0.38	1.04	7.0	10.9	60.3	24.5	17.6	58.3	1.4(-7)
05213+0615	M4	0.41	0.39	1.37	9.3	11.1	64.8	19.3	21.4	56.9	–
05440+1753	S0.V	0.33	0.66	1.89	22.7	19.5	99.5	33.2	30.3	88.1	1.4(-6)
06333-0520	M6	0.85	0.38	1.20	19.7	10.1	77.8	19.1	24.8	61.5	1.7(-7)
08272-0609	M6e	–	0.40	1.47	11.3	7.8	51.7	19.1	15.1	81.4	5.6(-7)
08372-0924	M5II	–	0.36	1.57	5.5	6.5	52.3	18.5	12.4	49.0	1.7(-7)
08555+1102	M5III	–	0.26	1.28	7.4	7.9	61.8	15.5	13.9	43.7	2.4(-7)
09076+3110	M6IIIaSe	–	0.31	1.20	13.5	11.6	65.9	18.5	18.8	56.7	3.8(-7) [†]
10436-3459	S	–	0.37	1.61	10.5	15.4	61.2	30.3	23.9	79.0	9.5(-7) [†]
15492+4837	M6S	0.77	0.40	1.58	12.7	13.0	63.8	19.9	24.5	44.4	9.5(-7) [†]
16334-3107	S4.7:V	–	0.43	1.13	15.0	22.9	93.4	22.5	29.7	104.8	1.0(-7) [†]
17206-2826	M...	–	0.42	0.82	10.3	11.4	68.1	15.2	19.6	63.8	1.0(-7) [†]
17390+0645	SV...	–	0.36	0.92	12.1	7.6	56.7	29.8	14.2	70.9	–
19497+4327		–	0.60	0.82	6.7	11.5	59.2	25.2	18.1	73.8	–

Table 4. 2MASS and IRAS colours and Mt Abu EWs (in Å) of spectral features of the sample PAGB stars.

Star	Spectral type	$H - K$	$K - 12$	Pa β	Br γ	CO(K)	21 μ m	T_d	\dot{M}
Z02229+6208	G9a	0.44	6.38	–	9.2	8.4	–	300	2.9(-5)
04296+3429	G0Ia	0.49	7.34	–	4.1	17.7	-2.11	270	4.5(-5) [†]
05113+1347	G8Ia	0.25	5.98	–	6.5	12.9	–	350	2.1(-5)
06556+1623	Bpe	1.11	5.10	–	-52.4	–	–	1200/150	1.0(-5)
07134+1005	F5Ia	0.10	6.45	–	5.1	–	-1.73	280	2.3(-5) [†]
07284-0940	K0Ibvp	0.23	5.64	–	–	10.9	–	450	1.0(-5)
07430+1115	G5Ia	0.44	6.35	–	3.9	28.9	–	320	3.3(-5)
17423-1755	Be	1.48	5.30	–	-5.6	-23.6	–	125	4.9(-6) [†]
18237-0715	Be	0.55	2.29	-25.6	-14.9	–	–	70	5.8(-6)
19114+0002	G5Ia	0.27	4.84	–	5.4	–	–	120	4.9(-5) [†]
19157-0247	B1III	1.19	5.76	–	–	-10.8	–	270	1.1(-6) [†]
19399+2312	B1e	0.11	4.80	-6.2	-15.6	–	–	–	–
22223+4327	F9Ia	0.24	4.44	7.5	5.8	–	-1.31	125	1.0(-5) [†]
22272+5435	G5Ia	0.38	5.55	4.4	3.4	30.2	-0.83	250	1.6(-5) [†]
22327-1731	A0III	0.90	4.95	3.8	–	28.7	–	800	5.0(-6)
23304+6147	G2Ia	0.36	6.48	3.4	5.1	12.8	-2.53	250	3.5(-5) [†]

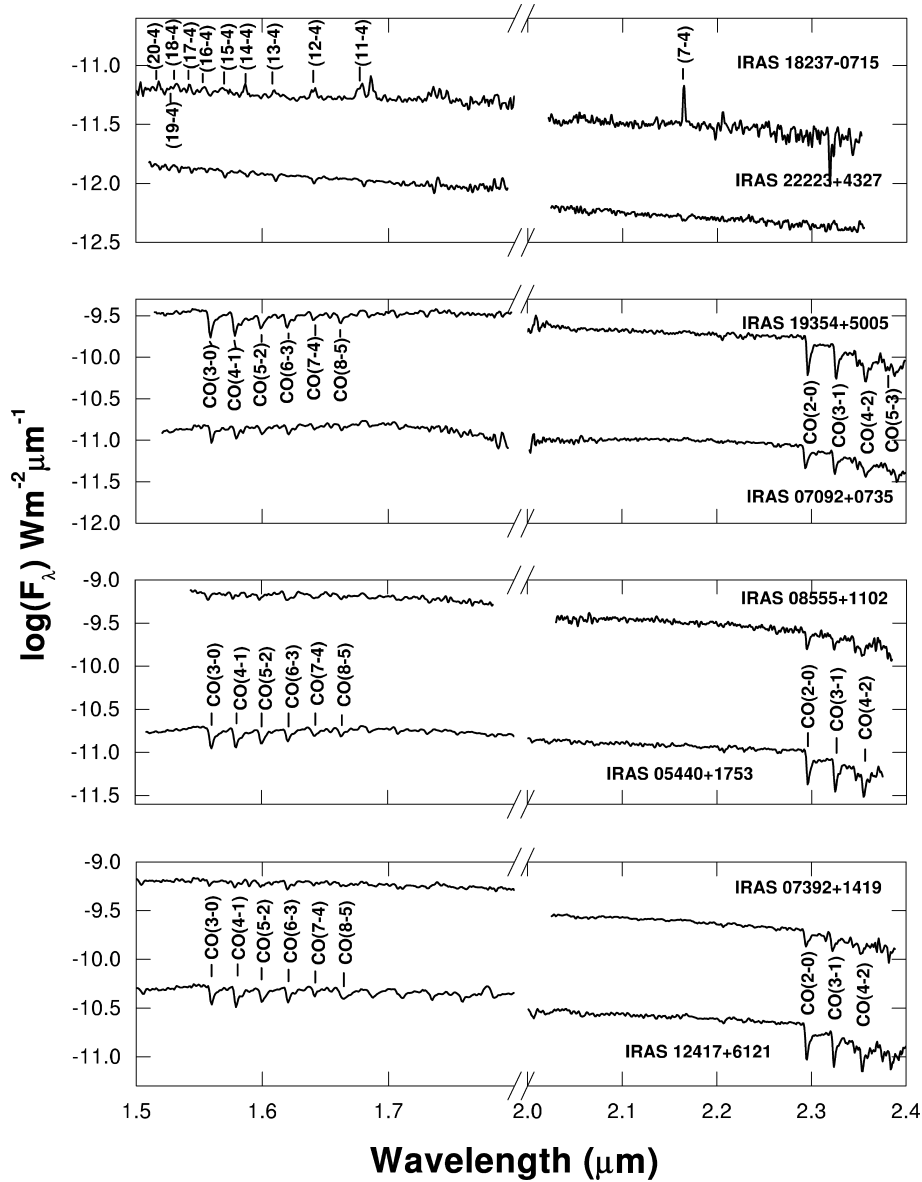


Figure 1. Mt Abu near-IR spectra of a selection of AGB and PAGB stars. From top to bottom the panels show PAGB, M, SR and S type stars giving two examples per category.

series lines of H I were found mostly among the PAGB stars where a hotter central source is believed to be present. In addition, the CO vibration–rotation lines of first and second overtone bands ($\Delta v = 2$ and 3, respectively) were seen in a large number of M, S and SR type stars and in a few PAGB stars. Some PAGB stars showed H I Brackett emission lines (IRAS 06556+1623, 17423–1755, 18237–0715 and 19399+2312 for the last one of which our spectra are new) and an indication of fainter emission in CO. This could be due to the fact that as the central star becomes hot, the CO lines become progressively weaker and finally disappear when CO dissociates (at 11.2 eV). Around this time the H I recombination lines start becoming prominent in emission. Our spectra on IRAS 06556+1623 and 17423–1755 are quite comparable to those of Garcia-Hernandez et al. (2002), with a faint detection of H₂ S(1) 1–0 line at 2.12 μ m. For the PAGB object IRAS 22327–1731, our spectra showed for the first time absorption in H I lines and CO bands. Some of the PAGB objects that showed variability are discussed in Section 4. Equiva-

lent widths (EWs) were computed for all the spectral features that are detected in our sample stars. The errors in the EWs are mainly from the S/N of the lines. To that extent the errors are estimated to be about 3 \AA , mostly applicable to the low-S/N (~ 3) line detections, such as the metallic lines; but for high-S/N (≥ 5) line/bands the errors are ≤ 1 \AA . Tables 1–4 list the EWs (in \AA , positive for absorption and negative for emission) of the CO(3–0, 4–1) second overtone bands in *H* band, CO(2–0, 3–1) first overtone bands in *K* band and H I Brackett series lines (only for PAGB stars), for the programme stars of each category.

3.1 Correlations and their implications

Based on physical processes, very interesting correlations were found among spectral features observed in AGB stars (Kleinmann & Hall 1986; Lancon & Wood 2000; Bieging et al. 2002). We tried to see if our sample too shows these. Kleinmann & Hall (1986) and

Bieging et al. (2002) have found that the CO(2–0) and CO(3–1) band head strengths are correlated. From the Tables 1–3, we can see this trend; in addition, one can see a correlation between CO(3–0) and CO(4–1) bands as well.

The first overtone bands of CO ($\Delta v = 2$) in the K band arise at $T \sim 800$ K partly in the photosphere and partly in the circumstellar envelopes; while the second overtone bands ($\Delta v = 3$) in the H band arise at $T \sim 3000$ – 4000 K entirely in the photospheric layers (e.g. Hinkle et al. 1982; Emerson 1996). As a result, the pulsational effects may be more pronounced in the $\Delta v = 3$ bands than in the $\Delta v = 2$ bands; while the former will reflect the circumstellar matter properties better. Thus we would expect a better correlation between EW of $\Delta v = 3$ bands with pulsation period P than the $\Delta v = 2$ bands. It should be noted here that for the CO bands the S/N is high (in many cases ≥ 5) and hence the errors in EW are ≤ 1 Å. Fig. 2 shows EWs of CO(3–0) and CO(2–0) plotted against the colour $[H - K]$ for M type stars. The phases of these variable stars are not necessarily the same between our observations and 2MASS or IRAS data acquisition (see Table 1 for phases during our observations). Also shown in Fig. 2 are the EWs of the CO lines from the S type stars (against the colour $[K - 12]$). The trend of correlation for CO(3–0) band is quite clear. For SR stars, we did not find any such trend.

In order to quantify the degree of correlation between two parameters, we have used the Spearman rank correlation method that does not assume any functional relationship between them (e.g. used by Loidl, Lancon & Jorgensen 2001). Fig. 2 shows only those correlations with CO(3–0) for which the rank coefficient (ρ) ≥ 0.50 and its significance (s) ≤ 0.01 (i.e. a chance occurrence of 1 in 100). We find that for M stars, for the CO(3–0) versus $[H - K]$, ρ is 0.50 with s of 0.008 (a chance occurrence of 8 in 1000); while for S stars, for CO(3–0) versus $[K - 12]$ ρ is 0.74 with s of 0.003. These are moderately significant correlations as may also be visually seen

from the plots. In comparison, the coefficients and their significance are quite poor for the CO(2–0) plots in Fig. 2. For M stars, one can also see a trend in the CO ($\Delta v = 3$) versus $\log P$ better than CO($\Delta v = 2$) versus $\log P$ (not shown). Usually the mass-loss is correlated well with the pulsation period; as also by the colour indices $[H - K]$ and $[K - 12]$ (Whitelock et al. 1994). While the trends in Fig. 2 are certainly beyond the errors in EW, we find that the scatter is rather significant in the correlation plot between the CO(3–0) band EWs and $[H - K]$ and other mass-loss indicators (not shown) such as $\log P$ and $[K - 12]$, although it is much less in comparison to the plots for CO(2–0) band (only $[H - K]$ is shown). Lancon & Wood (2000) and Loidl et al. (2001) argued that in the case of carbon-rich AGB stars, the CO lines arise deeper in side the atmospheres (close to the photospheres) and hence may not respond to dynamical effects such as pulsations as much as those lines that arise in the outer atmospheres. In our sample M stars, a large number of them are oxygen-rich and hence the pulsational phase effects may be significant and can possibly account for the scatter in our plots.

3.2 *Spitzer* spectra on a few post-AGB objects – PAH and 21 μm features

We have searched the *Spitzer* archival spectroscopic data in the mid-IR region of 6–30 μm and succeeded in obtaining seven PAGB stars for which the data were available and unpublished and are not in the list of sources presented originally by Hrivnak, Volk & Kwok (2000). The raw spectra (post-basic calibrated data) were analysed using the *Spitzer* IRS Custom Extraction (SPICE) task under *Spitzer* data processing software packages. Interesting spectra in the wavelength range of 10–18 μm from these objects are shown in Fig. 3 (where in addition to the seven *Spitzer* stars, we have shown one more PAGB star, namely IRAS 22272+5435, reanalysed from the *ISO*

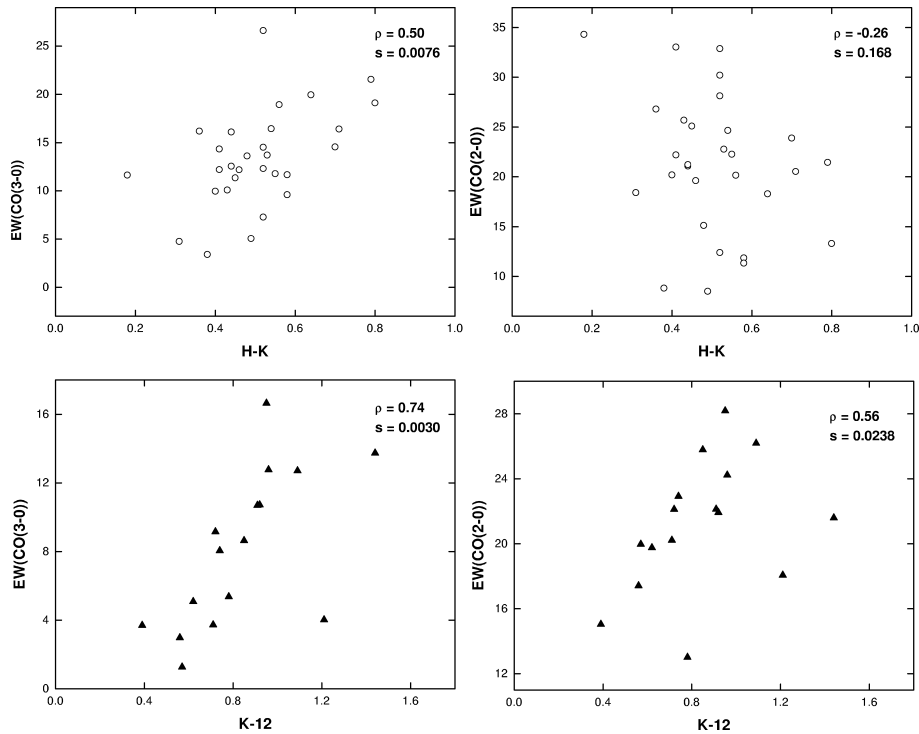


Figure 2. Plots of EWs (in Å) of the CO(3–0) line (left-hand panels) and CO(2–0) line (right-hand panels) with the IR colours $[H - K]$ for M stars (shown as open circles in top panels) and $[K - 12]$ for S type stars (filled triangles in bottom panels). The Spearman rank correlation coefficient (ρ) and its significance (s) are given in the corresponding figures.

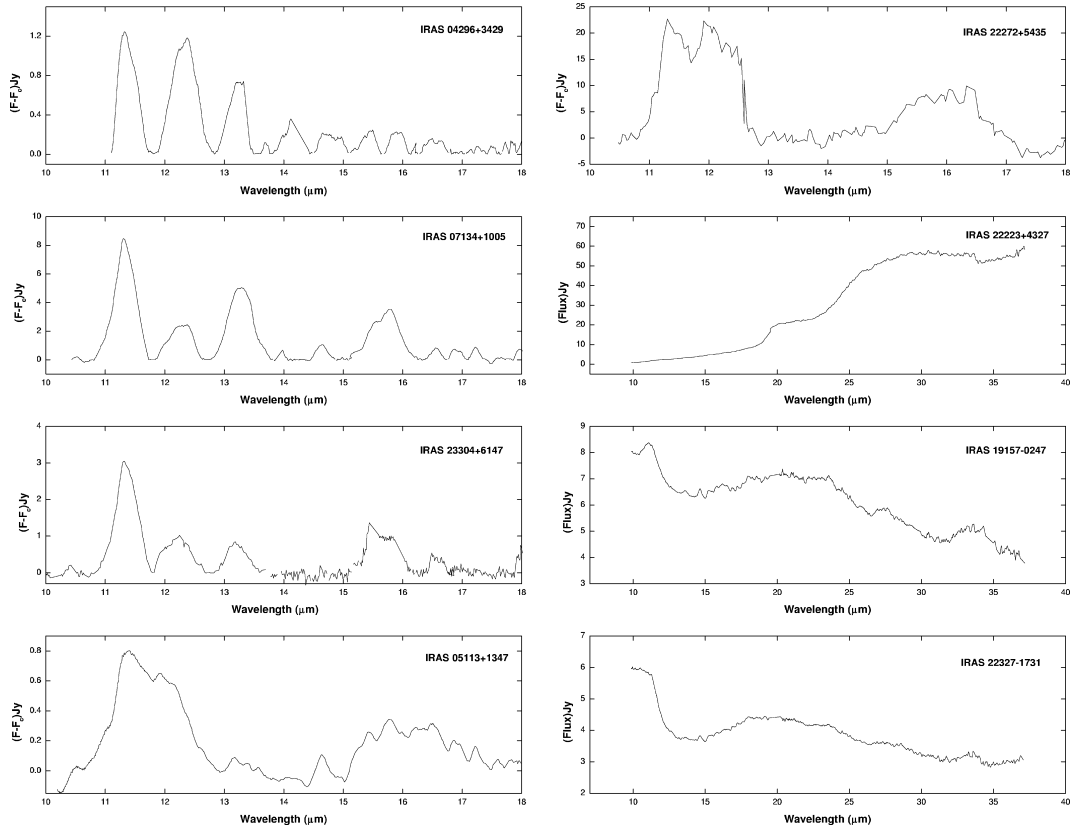


Figure 3. *Spitzer* spectra for some PAGB stars showing mid-IR PAH features in emission (for all the four spectra shown in the left-hand side panels and the one in the top right-hand panel, continuum was subtracted using (fifth-order) polynomial fitting in segments). The spectra for IRAS 22272+5435 were obtained by reanalysing the *ISO* data and shown here for comparison.

spectral archives). Of these eight stars, IRAS 19157–0247 and IRAS 22327–1731 are of early spectral types and showed nearly featureless continua (see Fig. 3). For the spectra of those stars that showed the in-plane and out-of-plane bending modes of C–H bonds in polycyclic aromatic hydrocarbon (PAH) molecules (e.g. Kwok 2004 and Tielens 2005), we have subtracted the continuum by (fifth-order) polynomial fitting in segments, in order to bring out the comparative strengths of the features. Fig. 4 shows the 6–10 μm spectra on two stars for which the data are available; these stars show the C–C stretching modes of 6.2 and 6.9 μm and the blended features around 8 μm due to C–C stretching and C–H in-plane bending modes. A comparison of the spectra in the region of 10–18 μm common to about six PAGB objects suggests that the intensity of the spectral features due to PAH molecules depends on the spectral type of the star – being weakest or shallowest for cooler stars than for relatively hotter stars. This can possibly be due to the ultraviolet (UV) radiation flux and the hardness that is available to excite the molecules (Tielens 2005).

We have computed the ratio of the EWs of the $F_{7.9}/F_{11.3}$ feature which is known to indicate whether the molecule is neutral or ionized (see Tielens 2005). We find that the PAGB star IRAS 04296+3429, having a ratio of 11.3, probably shows indications for ionized PAH molecules, while in IRAS 22272+5435, with a ratio of 0.8, neutrals may be predominant (see Figs 3 and 4). Further, the relative structure of PAHs may be inferred from the ratio of $F_{11.3}/F_{12.7}$: a large ratio indicates large compact PAHs, while a small ratio results when these molecules break up into smaller ir-

regular structures (Hony et al. 2001; Peeters et al. 2002; Sloan et al. 2005; Tielens 2005). In our sample PAGB stars, we find (see Fig. 3) that the objects IRAS 07134+1005 and 23304+5147 have ratios of 4.7 and 3.6, respectively, and hence may have large compact PAH molecules compared to IRAS 04296+3429 that has a ratio of 0.8. In IRAS 05113+1347 and 22272+5435 the *Spitzer* spectra show wide features at 7–8 and 11–12 μm regions. Such broad features are usually attributed to more complex structures in PAH molecules (see Kwok 2004).

Since the PAH modes arise by absorption of UV photons, their presence indicates the onset of substantial UV flux from the central star and hence the onset of transition/PPN phase. Mt Abu spectra taken on all these objects do not show the H α Brackett series in emission; they are seen in absorption. Thus it is possible that the UV radiation is soft (≤ 13.6 eV) as H ionization has not yet started in these objects.

Only three of our sample PAGB stars have *Spitzer* archival data beyond 18 μm , and all showed the 21- μm feature (Kwok, Volk & Hrivnak 1989, 1999; Volk, Kwok & Hrivnak 1999; Decin et al. 1998), which was attributed to TiC (von Helden et al. 2000) or SiC (Speck & Hofmeister 2004). Since these objects are already known to have the 21- μm feature (Volk et al. 1999), in Table 4 we give only the EWs of the feature (in μm), along with the EW for IRAS 07134+1005 computed from *ISO* archival data. All the properties of the observed feature (the peak wavelength, width and red-side asymmetry) resemble the SiC feature as shown by Speck & Hofmeister (2004).

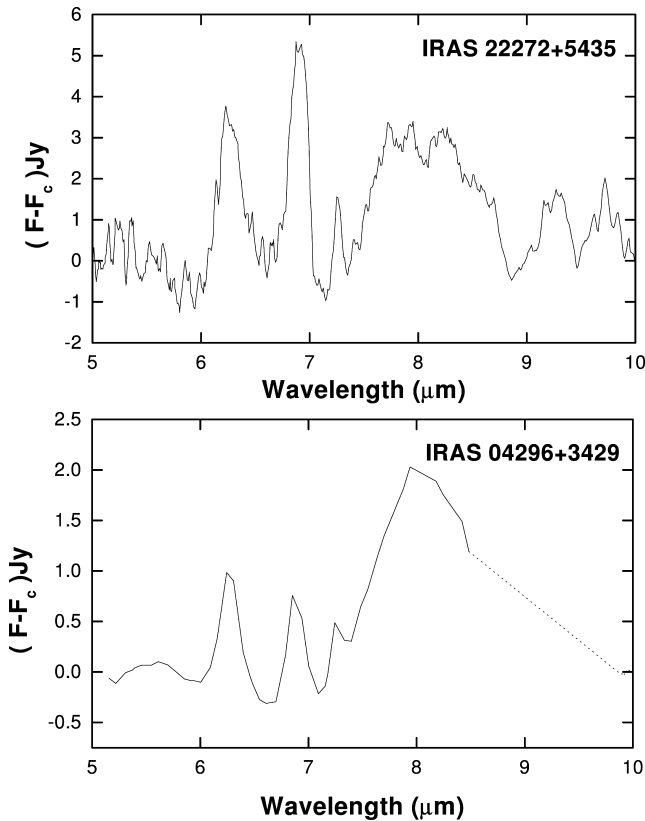


Figure 4. *Spitzer* spectra of IRAS 04296+3429 showing mid-IR (in the range 6–10 μm) PAH features in emission (continuum-subtracted as in Fig. 3). The spectra for IRAS 22272+5435 were obtained by reanalysing the *ISO* data and is shown here for comparison.

3.3 Modelling of infrared spectral energy distribution

Using the *DUSTY* code (Ivezic & Elitzur 1997), we have modelled the SEDs in the spectral region of 0.5–100 μm . This code incorporates full dynamical calculation for radiatively driven winds in AGB stars. The photometric data on all the programme objects were compiled mainly from 2MASS and IRAS archives. We have modelled the SEDs of all the programme stars except those that have upper limits (quality = 1) in IRAS data in more than one band. For a majority of the programme stars IRAS LRS data are not available. Even in the *ISO* archives we could get only a few stars. Therefore, we have modelled only the photometric fluxes, assuming silicate dust for M, S and SR types; while for most of the PAGB stars, we required carbonaceous dust. The dust grain data were taken from in-built tables in *DUSTY*. In a few cases we obtained data from DENIS and MSX archives as well. In the model that assumes spherical geometry, we fix stellar parameters like the photometric temperature (based on the visible and the near-IR data), inner dust shell temperature, type of dust and size distribution (MRN assumed) and opacity at 0.5 μm (usually taken value between 0.1 and 1.0). We have used density distribution relevant for modelling the radiatively driven winds in AGB stars as incorporated in to *DUSTY* by its authors. There would be 10–20 per cent uncertainties in all the model output parameters. We have generated nearly 150 models using several combinations of the above parameters. We then take the fluxes computed by the code and normalize with the observed 2- μm flux from each object and construct the model SEDs. A χ^2 test is performed to select the best fit model. In general the model shows that the

M types have lower effective temperatures than the S and SR types. M types show higher opacities by a factor of 2, than the S and SR types; S type being lowest. However, the inner dust shell temperature for all the types were found to be in the range 450–700 K. The SEDs of PAGB stars showed, in general, double-humped but flatter trend than their AGB counterparts, indicating detached circumstellar shells (see e.g. Hrivnak & Kwok 1999). Since some of these are transition objects their spectral classes are much earlier than M types. The inner dust shell temperatures for most of the PAGB stars, as listed in Table 4, are found to be in the range of ~ 100 –300 K, significantly cooler than the values for AGB stars. A warmer dust shell was required in addition to the cooler one in one of the PAGB stars (1200 K for IRAS 06556+1623). The dust parameters that we obtained are in good agreement with those in the published literature. A few examples of SEDs of M, S, SR and PAGB stars and their model fits are shown in Figs 5–7, respectively. The *DUSTY* AGB star model estimates mass-loss rate also but with larger uncertainty of 30 per cent. The mass-loss rates (in $M_{\odot} \text{yr}^{-1}$) thus obtained are listed in Tables 1–4 for all the types; the sign † shows stars for which the rates are independently available from CO rotational line observations by several authors, namely Loup et al. (1993), Sahai & Liechti (1995), Groenewegen & de Jong (1998), Jorissen & Knapp (1998), Winters et al. (2000) and Ramstedt et al. (2006) for M, S and SR stars; and Woodsworth, Kwok & Chen (1990), Likkel et al. (1991), Omont et al. (1993), Hrivnak & Kwok (1999), Bujarrabal et al. (2001), Hoogzaad et al. (2002) and Hrivnak & Bieging (2005) for PAGB stars. Our model mass-loss rates are in reasonably good agreement with those determined from CO rotational lines, for all cases. From Tables 1 and 4, one can see a clear trend of increase of mass-loss rate with increase of the colour $[K - 12]$ (e.g. Bieging et al. 2002). Basically most of our sample M type stars are in the ascending phase of their AGB stage and hence the mass-loss rate increases with the $[K - 12]$ index (see Whitelock et al. 1994 and Habing 1996); while the PAGB stars in our sample are already in the PPN stage, having just passed the superwind mass-loss event. Following this phase the mass-loss would decrease. In fact one can see (Table 4) that the mass-loss rates for hot PAGB stars are distinctly less than those for cooler ones, possibly indicating the decrease of mass-loss after a superwind event.

4 SPECTRAL VARIATIONS IN SOME PAGB OBJECTS

Most of the PAGB stars in our sample are identified as PPNe (see Ueta et al. 2003 and references therein). Repeated spectroscopic observations were made on a few selected stars IRAS 17423–1755, IRAS 18237–0715, IRAS 19399+2312 and IRAS 22272+5435 (see Table 4 for their spectral types). Our results on several sources are compared with those taken earlier by Hrivnak, Kwok & Geballe (1994), Oudmaijer et al. (1995) and recently by Kelly & Hrivnak (2005). Here we report spectral variations in the CO first overtone bands in IRAS 22272+5435; and in H I lines in stars of early spectral type (hot PAGB stars). In both cases the time-scales of variability are short and may be associated with episodic mass-loss.

4.1 Variability of CO first overtone bands in IRAS 22272+5435

The spectra of this object of spectral type G5Ia show signatures that are probably indicative of its advanced stage of evolution in the PAGB phase. It was shown by Hrivnak et al. (1994) that the object shows episodes of mass-loss that was evident from month-scale

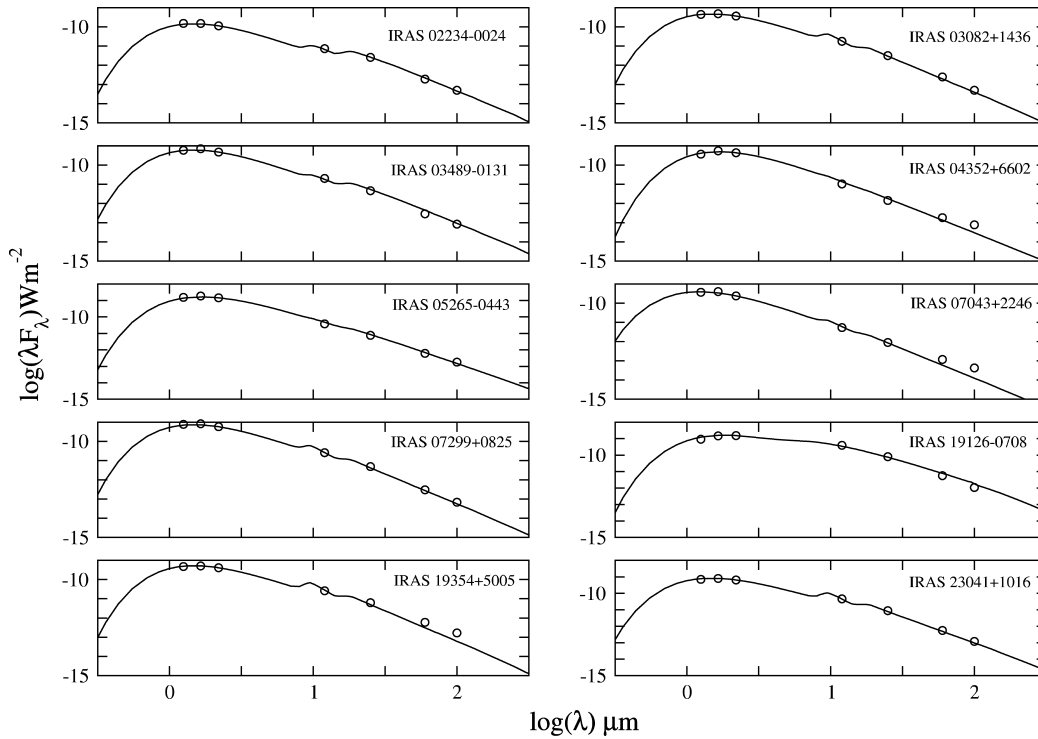


Figure 5. Model SEDs (full lines) of some M type stars compared with observed data from literature (open circles). See text for model parameters and explanation.

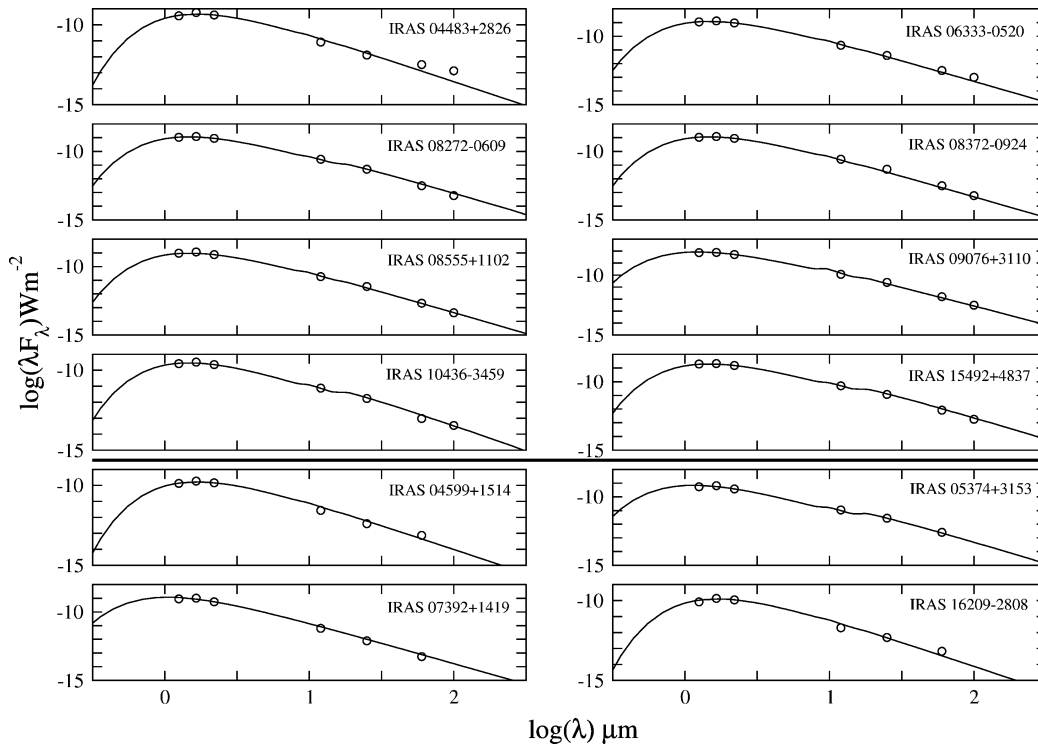


Figure 6. Model SEDs (full lines) of some SR type (in the top eight panels) and S type stars (in the bottom four panels below the horizontal line) compared with observed data from literature (open circles). See text for model parameters and explanation.

variability in its spectra. We obtained its spectra in *H* and *K* bands on two occasions separated by about 47 d (2006 November 4 and December 22). EWs for 2006 November 4 are given in Table 4. Fig. 8 shows the spectra and it is clear that the CO first overtone bands in

the *K* band seen on November 4 were absent on December 22. But the Brackett H1 absorption lines were seen in both *H*- and *K*-band spectra on both the observations. Interestingly the *H*-band second overtone bands of CO were *still present* in the spectra on

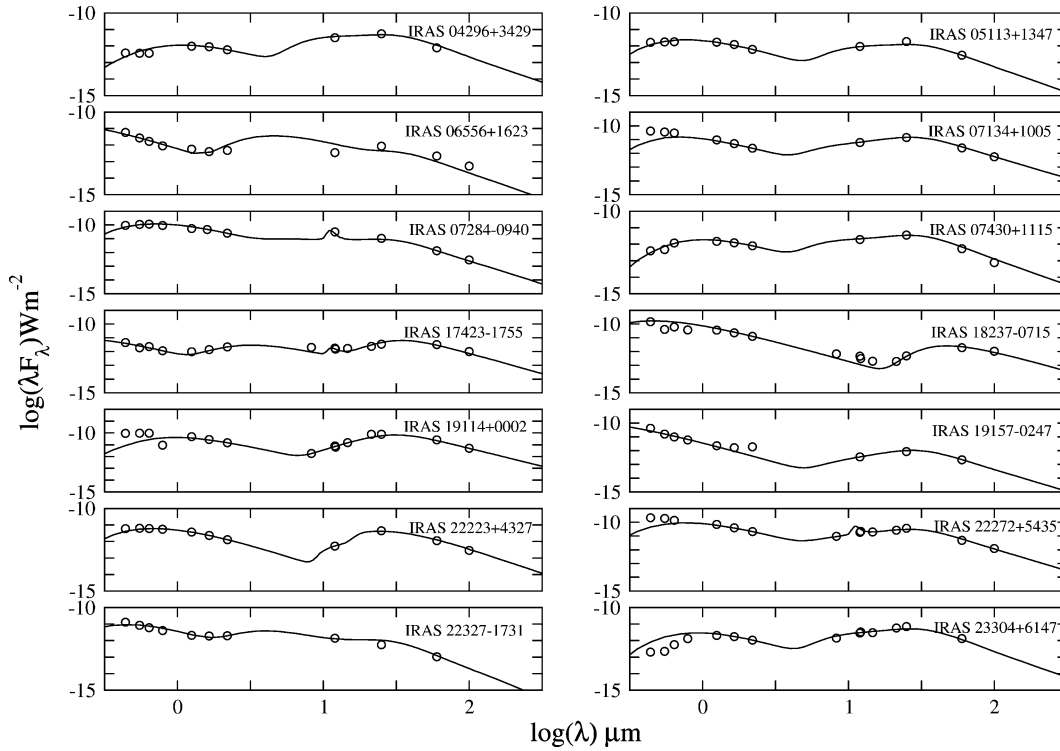


Figure 7. Model SEDs (full lines) of some PAGB stars compared with observed data from literature (open circles). See text for model parameters and explanation.

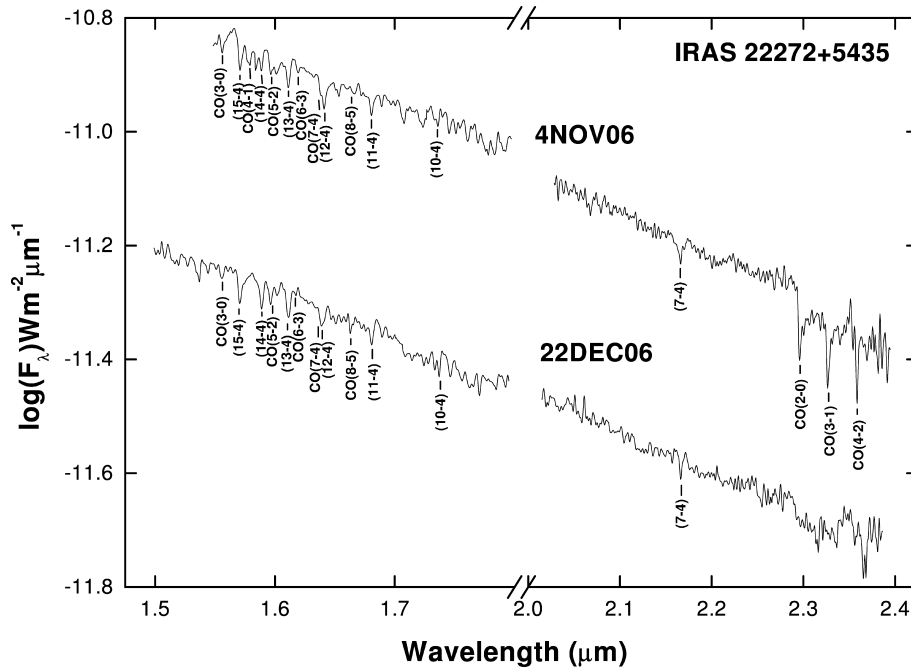


Figure 8. *H*- and *K*-band spectra of the PAGB star IRAS 22272+5435 taken on two dates from Mt Abu.

December 22. This shows that the mass-loss reached the outer regions of the atmosphere where the temperature is about a few hundreds of degree kelvin. The pulsations must be responsible for heating the matter in these regions resulting in the excitation of these lines and filling the absorption seen earlier.

We have found variability of spectra in a few other PAGB stars similar to IRAS 22272+5435. The *H*- and *K*-band spectra of IRAS 05113+1347, IRAS 19114+0002 and IRAS 22223+4327 were observed by Hrivnak et al. (1994). Our observations, made about 12 yr later, show clear indication of variability of CO in these stars which

might have occurred during the intervening period. In all these cases, the variations were found only in CO first overtone bands while the H I lines did not change. Oudmaijer et al. (1995) found CO second overtone bands in emission in the object IRAS 19114+0002 while our observations show near absence of these bands which can be attributed to mass-loss variations.

4.2 Variability of H I lines in IRAS 19399+2312

On the basis of the IRAS colours, Gauba et al. (2003) suggested that IRAS 19399+2312 (also known as V450 Vul) is a hot PAGB star possibly in transition to become a PPN. It was classified as a B1III star by Parthasarathy, Vijapurkar & Drilling (2000) but as B1IIIe by Kohoutek & Wehmeayer (1999). Recently, Greaves (2004) argued that being a possible member of the cluster NGC 6823, this star is unlikely to be a PAGB transition object but could be a spectroscopic type Be star. We made *JHK* band spectrometry at Mt Abu Observatory on this object on three occasions: first time on 2005 November 1 and then recently on 2007 May 15 and again on 2007 June 5–6 (the EWs obtained on 2007 June 6 are given in Table 4). The 2005 November 1 spectra showed some what shallow absorption in H I Paschen β and Brackett series lines. The later spectra however showed very prominent emissions in the H I lines, as well as a few permitted lines in He I and even forbidden lines in [Fe II] (1.60 μm) at relatively lower S/N (see Fig. 9). We also notice at a rather low S/N but still discernable CO ($\Delta v = 3$) lines in absorption. The appearance of the CO absorption lines is not usual in Be stars, as also the forbidden lines of metals ([Fe II]). In view of the appearance of forbidden lines (which was not reported earlier), and faint but significant CO lines, we believe that this object may as well be a transition object. To our knowledge, our observations are the first to show spectral variability in this object. From the ratios of the Brackett series lines which deviate from the Case B assumption

(see e.g. Lynch et al. 2000), we infer variations in electron density or opacity in the atmosphere of this object associated with the H I line ratio variations that occurred between 2007 May 15 and 2007 June 5/6.

We made repeated observations on two more PAGB stars of early spectral type: for IRAS 17423–1755 (Be) on 2003 May 29 and 2007 May 13 and for IRAS 18237–0715 (Be) on 2004 May 28, 2006 Nov 3 and 2007 May 14. In Table 4, the EWs for IRAS 17423–1755 are for the date 2003 May 29; and for IRAS 18237–0715 the EWs are for 2006 November 3. We find variations in the intensities of H I Brackett series emission lines in both these objects. In the case of IRAS 18237–0715 the Brackett line ratios matched well with the Case B assumption on 2004 May 28 and 2006 November 3; while on 2007 May 14 the ratios deviated from Case B. Earlier in a detailed study Miroshnichenko et al. (2005) found spectral line variations in this object. This star did not show CO lines (Table 4). In the case of IRAS 17423–1755 on both the days of our observations the ratios deviated from Case B. These observations indicate the changes in electron density or opacity. This star showed CO first overtone lines in emission (Table 4). While Gauba et al. (2003) found emission lines in the optical spectra of IRAS 17423–1755 and 18237–0715 and hence termed these as transition objects, the nature of the latter object is ambiguous and could be a luminous blue variable according to the study of Miroshnichenko et al. (2005). Our IR spectra of this object closely resemble those of Miroshnichenko et al. (2005) and show P-Cygni type profiles with double peaks (see Fig. 1, top panel). Since we do not find CO lines in the spectra of this object it is likely that this object cannot possibly be a PAGB/transition object; or CO must have been dissociated.

In the case of the object IRAS 22327–1731 (type A0III) Oudmaijer et al. (1995) found that the CO bands as well as the H I lines were absent; our results (Table 4) show that the object displays the CO bands and H I Paschen β and Brackett γ in absorption, thus showing variability.

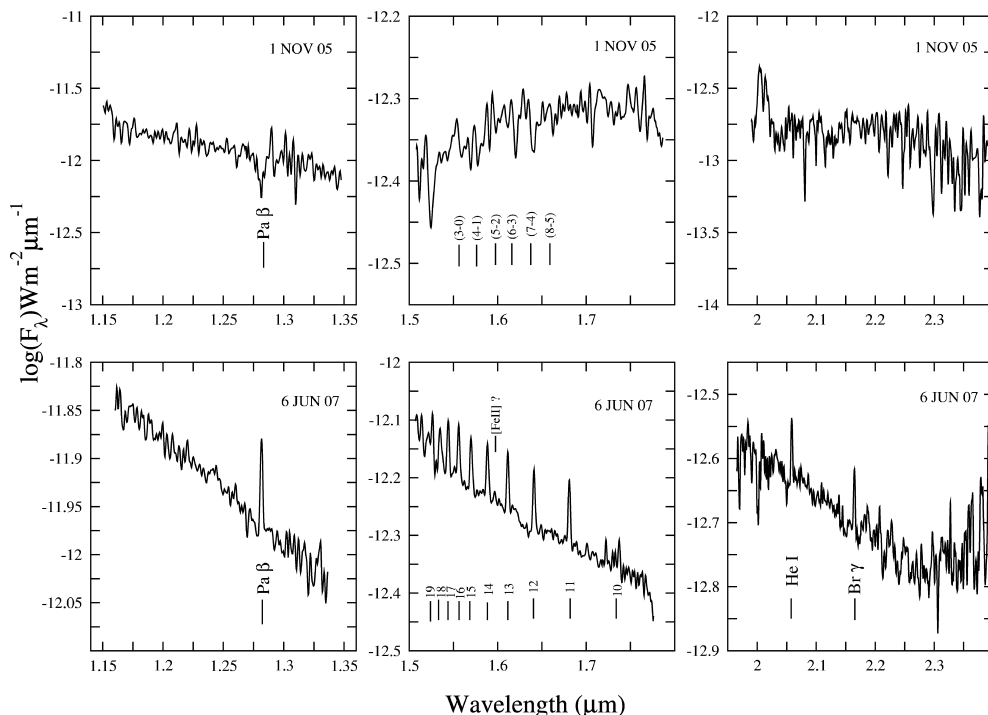


Figure 9. *J*-, *H*- and *K*-band spectra of the PAGB star IRAS 19399+2312 taken on two dates from Mt Abu.

5 CONCLUSIONS

(i) The EWs of CO(3–0) show a trend of correlation with $[H - K]$ in M type; while in S stars the CO(3–0) shows a positive correlation with $[K - 12]$.

(ii) The Mt Abu *H*- and *K*-band spectra also showed marked differences in the three types.

(iii) Archival *Spitzer* spectra of a few PAGB stars showing PAH emission features confirm their advanced stage of evolution into PPNs. There appears to be a dependence of the strength of the PAH features on the spectral type.

(iv) Modelling of SEDs of a number of the programme stars showed marked differences in various generic types. Model mass-loss rates for M and PAGB stars show an increasing trend with the colour $[K - 12]$ in our sample stars.

(v) Our observations showed that several PAGB stars undergo short-term spectral variability that is indicative of ongoing episodic mass-loss. Cooler PAGB stars showed variation in CO first overtone lines. In contrast, the hot PAGB stars showed variation in H I lines. The hot PAGB star IRAS 19399+2312 is identified as a transition object.

ACKNOWLEDGMENTS

The authors sincerely thank the anonymous referee for critical comments that led to substantial improvement over the original version. This research was supported by the Department of Space, Government of India. We thank the Mt Abu Observatory staff for help in observations with NICMOS. We thank the *Spitzer* archival facilities. We acknowledge the DUSTY team for making available the code for the astronomy community. This research has made use of *IRAS*, 2MASS and *ISO* data bases.

REFERENCES

Bieging J. H., Rieke M. J., Rieke G. H., 2002, *A&A*, 384, 965
 Bowen G. H., 1988, *ApJ*, 329, 299
 Bujarrabal V., Castro-Carrizo A., Alcolea J., Sanchez Conteras C., 2001, *A&A*, 377, 868
 Chen P. S., Gao H., Jorissen A., 1995, *A&AS*, 113, 51
 Decin L., van Winckel H., Waelkens C., Bakkar E. J., 1998, *A&A*, 332, 928
 Emerson D., 1996, *Interpretation of Astronomical Spectra*. Wiley, New York, p. 390
 Feast M. W., 2000, in Wing R. F., ed., *Proc. IAU Symp. 177, The Carbon Star Phenomenon*. Kluwer, Dordrecht, p. 207
 Fouquet P., Le Bertre T., Epchtein N., Guglielmo F., Kerschbaum F., 1992, *A&AS*, 93, 151
 Gail H.-P., Sedlmayr E., 1987, *A&A*, 177, 186
 Gail H.-P., Sedlmayr E., 1988, *A&A*, 206, 153
 Garcia-Hernandez D. A., Manchado A., Garcia-Lario P., Dominguez-Tagle C., Conway G. M., Prada F., 2002, *A&A*, 387, 955
 Garcia-Lario P., 2006, in Barlow M. J., Mendez R. H., eds, *Proc. IAU Symp. 234, Planetary Nebulae in Our Galaxy and Beyond*. Cambridge Univ. Press, Cambridge, p. 63
 Gauba G., Parthasarathy M., Kumar B., Yadav R. K. S., Sagar R., 2003, *A&A*, 404, 305
 Greaves J., 2004, *IBVS*, 5472, 1
 Groenewegen M. A. T., de Jong T., 1998, *A&A*, 337, 797
 Habing H., 1996, *A&AR*, 7, 97
 Hinkle K. H., Hall D. N. B., Ridgway S. T., 1982, *ApJ*, 252, 697
 Hony S., Van Kerckhoven C., Peeters E., Tielens A. G. G. M., Allamandola L. J., 2001, *A&A*, 370, 1030
 Hoogzaad S. N., Molster F. J., Dominik C., Waters L. B. F. M., Barlow M. J., de Koter A., 2002, *A&A*, 389, 547

Hrivnak B. J., Bieging J. H., 2005, *ApJ*, 624, 331
 Hrivnak B. J., Kwok S., 1999, *ApJ*, 513, 869
 Hrivnak B. J., Kwok S., Geballe T. R., 1994, *ApJ*, 420, 783
 Hrivnak B. J., Volk H., Kwok S., 2000, *ApJ*, 535, 275
 Ivezić Z., Elitzur M., 1997, *MNRAS*, 287, 799
 Jorissen A., Knapp G. R., 1998, *A&AS*, 129, 363
 Kelly D. M., Hrivnak B. J., 2005, *ApJ*, 629, 1040
 Kerschbaum F., Hron J., 1994, *A&AS*, 106, 397
 Kleinmann S. G., Hall D. N. B., 1986, *ApJS*, 62, 501
 Kholopov P. N. et al., 1988, *General Catalogue of Variable Stars*. Publishing House of the Academy of Sciences of the USSR, Moscow
 Kohoutek L., Wehmeayer R., 1999, *A&AS*, 134, 255
 Kwok S., 2000, *The Origin and Evolution of Planetary Nebulae*. Cambridge Univ. Press, Cambridge, p. 103, 151
 Kwok S., 2004, *Nat*, 430, 985
 Kwok S., Volk K., Hrivnak B. J., 1989, *ApJ*, 345, L51
 Kwok S., Volk K., Hrivnak B. J., 1999, in Le Bertre T., Lebre A., Waelkens C., eds, *ASP Conf. Ser. Vpl. 191, AGB Stars*. Astron. Soc. Pac., San Francisco, p. 297
 Lancon A., Rocca-Volmerange B., 1992, *A&AS*, 96, 593
 Lancon A., Wood P. R., 2000, *A&AS*, 146, 217
 Likkell L., Forveille T., Omont A., Morris M., 1991, *A&A*, 246, 153
 Loidl R., Lancon A., Jorgensen U. G., 2001, *A&A*, 371, 1065
 Loup C., Forveille T., Omont A., Paul J. F., 1993, *A&AS*, 99, 291
 Lynch D. K., Rudy R. J., Mazuk S., Puetter R. C., 2000, *ApJ*, 541, 791
 Miroshnichenko A. S. et al., 2005, *MNRAS*, 364, 335
 Omont A., Loup C., Forveille T., te Lintel Hekkert P., Habing H., Sivagnanam P., 1993, *A&A*, 267, 515
 Oudmaijer R. D., Waters L. B. F. M., van der Veen W. E. C. J., Geballe T. R., 1995, *A&A*, 299, 69
 Parthasarathy M., Vijapurkar J., Drilling J. S., 2000, *A&AS*, 145, 269
 Peeters E., Hony S., Van Kerckhoven C., Tielens A. G. G. M., Allamandola L. J., Hudgins D. M., Bauschlicher C. W., 2002, *A&A*, 390, 1089
 Ramstedt S., Schoier F. L., Olofsson H., Lundgren A. A., 2006, *A&A*, 454, L103
 Sahai R., Liechti S., 1995, *A&A*, 293, 198
 Sloan G. C. et al., 2005, *ApJ*, 632, 956
 Speck A. K., Hofmeister A. M., 2004, *ApJ*, 600, 986
 Stasinska G., Szczerba R., Schmidt M., Siodmiak N., 2006, *A&A*, 450, 701
 Tielens A. G. G. M., 2005, *The Physics and Chemistry of the Interstellar Medium*. Cambridge Univ. Press, Cambridge, p. 173
 Ueta T., Meixner M., Moser D. E., Pyzovskii L. A., Davis J. S., 2003, *AJ*, 125, 2227
 van Winckel H., 2003, *ARA&A*, 41, 391
 Vassiliadis E., Wood P. R., 1993, *ApJ*, 413, 641
 von Helden G., Tielens A. G. G. M., van Heijnsbergen D., Duncan M. A., Hony S., Waters L. B. F. M., Meijer G., 2000, *Sci*, 288, 313
 Volk K., Kwok S., Hrivnak B. J., 1999, *ApJ*, 516, L99
 Wang H., Chen P. S., 2002, *A&A*, 387, 129
 Whitelock P. A., Menzies J., Feast M. W., Marang F., Carter B., Roberts G., Catchpole R., Chapman J., 1994, *MNRAS*, 267, 711
 Willson L. A., 2000, *ARA&A*, 38, 573
 Winters J. M., Le Bertre T., Jeong K. S., Helling C., Sedlmayr E., 2000, *A&A*, 361, 641
 Winters J. M., Le Bertre T., Jeong K. S., Nyman L.-A., Epchtein N., 2003, *A&A*, 409, 715
 Woitke P., 2003, in Piskunov N. E., Weiss W. W., Gray D. F., eds, *Proc. IAU Symp. Vol. 210, Modelling of Stellar Atmospheres*. Astron. Soc. Pac., San Francisco, p. 387
 Wood P. R., 1979, *ApJ*, 227, 220
 Woodworth A. W., Kwok S., Chen S. J., 1990, *A&A*, 228, 503

This paper has been typeset from a $\text{\TeX}/\text{\LaTeX}$ file prepared by the author.